THE UNIVERSITY OF QUEENSLAND

AUSTRALIA

Applications of Tunable Diode Laser Absorption Spectroscopy to Aerospace Flows

Brad John Wheatley

BSc, BE(Aero)(Hons), GradDipMan, MSc(Thermal Power), MA(International Relations), GradDipMan, MSc(Physics)

A thesis submitted for the degree of Doctor of Philosophy at The University of Queensland in 2017

School of Mathematics and Physics

Abstract

Direct and wavelength modulated methods of tunable diode laser absorption spectroscopy (TDLAS) techniques were applied to hypersonic and rarefied gas environments. Three experimental campaigns are discussed including direct absorption spectroscopy of a steam ejector flow, wavelength modulated TDLAS of scramjet combustion in an expansion tunnel, and temperature measurement of atomic oxygen in a plasma generator. The literature relevant to TDLAS is reviewed and the theoretical bases for the two techniques are presented. Each campaign required innovative solutions to experimental problems but, in the end, TDLAS was successfully applied on a proof-of-concept basis in each environment.

The pressure and temperature in a 1 kms^{-1} steam ejector flow were measured using direct TDLAS. Three methods of analysing the data were compared for accuracy and ease of use. The best method was found to be using the Levenburg-Marquardt method to perform a non-linear least-squares minimisation of the residual between a Voigt fit of simulated and measured data. Absolute average residual errors of less than 0.1% were achieved together with pressure relative error of $\pm 2\%$ and temperature errors of ± 10 K.

Wavelength modulated TDLAS was investigated as a means to measure parameters in the combustor and nozzle of a scramjet in an expansion tunnel. The scramjet operated at an inlet Mach number of approximately 10 and a static pressure of 120 Pa simulating flight at approximately 30 km altitude. The test time was of the order of 1 ms. Hydrogen fuel was injected via five holes in the scramjet inlet ramp. Two laser diodes operating near 1392 nm were used to probe the scramjet nozzle flow. The lasers were simultaneously sinusoidally modulated in power and wavelength at a frequency near 1.0 MHz. Tests were conducted at various fuel injection pressures into both air and nitrogen test gas. Combustion was detected in the scramjet nozzle. Results are presented together with recommendations for future research.

The atomic oxygen concentration in a microwave generated plasma generated by an Evenson cavity was measured using TDLAS to probe the oxygen triplet at 844.6 nm. The oxygen atoms in the plasma were highly excited and emitted radiation that could have overwhelmed the laser absorption. Any spectral features were expected to be narrow as the plasma pressure was between 80 Pa and 300 Pa. The measured intensity ratios were used to calculate the number density of oxygen atoms in the upper states with a relative error of approximately 5%. The calculated number density, mole fraction of atomic oxygen and intensity ratio were highly sensitive to the temperature as was expected given the exponential form of Boltzmann's equation.

A brief analysis was also presented of a TDLAS system that could detect atomic oxygen in reflected shock or expansion tunnel experiments. Whilst the system was not implemented for this study, the information presented may assist future researchers to develop an atomic oxygen TDLAS system for free-piston hypersonic tunnels.

This research resulted in a modular TDLAS system that can be used to detect temperature, pressure and number density of water vapour or other species in a range of environments including hypersonic flows. The research was novel as it applied TDLAS to steam generator and ejector flows, atomic oxygen in a plasma, and scramjet tests in a free-piston expansion tunnel. A particular focus was placed

on making the system inexpensive with a high reliance on off-the-shelf products and components and the use of open-source software for control and data analysis. The experiments demonstrated that TDLAS could be successfully applied to flows of these types including the extreme conditions generated in an expansion tunnel. They also provide a basis for expanding the system to probe expansion tunnel flows for transient radicals and atoms such as hydroxyl, nitrous oxide and atomic oxygen and nitrogen. This research has shown that TDLAS has a strong future in hypersonic and rarefied gas applications.

Declaration by Author

This thesis is composed of my original work, and contains no material previously published or written by another person except where due reference has been made in the text. I have clearly stated the contribution by others to jointly-authored works that I have included in my thesis.

I have clearly stated the contribution of others to my thesis as a whole, including statistical assistance, survey design, data analysis, significant technical procedures, professional editorial advice, and any other original research work used or reported in my thesis. The content of my thesis is the result of work I have carried out since the commencement of my research higher degree candidature and does not include a substantial part of work that has been submitted to qualify for the award of any other degree or diploma in any university or other tertiary institution. I have clearly stated which parts of my thesis, if any, have been submitted to qualify for another award.

I acknowledge that an electronic copy of my thesis must be lodged with the University Library and, subject to the policy and procedures of The University of Queensland, the thesis be made available for research and study in accordance with the Copyright Act 1968 unless a period of embargo has been approved by the Dean of the Graduate School.

I acknowledge that copyright of all material contained in my thesis resides with the copyright holder(s) of that material. Where appropriate I have obtained copyright permission from the copyright holder to reproduce material in this thesis.

Publications during candidature

Zander, Fabian, Smart, Michael K., Drennan, John, Morgan, Richard G. and Wheatley, Brad (2013) Extreme materials in hypersonics. *Materials Australia*, *46* 1: 41-45.

Wheatley, Brad (2012). Tunable diode laser absorption spectroscopy of hypersonic flows. In: 28th Congress of the International Council of the Aeronautical Sciences 2012 (ICAS 2012). Proceedings. *ICAS 2012: 28th Congress of the International Council of the Aeronautical Sciences*, Brisbane, QLD, Australia, (2769-2778). 23-28 September, 2012.

Wheatley, B.J., McIntyre, T.J. and Buttsworth, D.R. (2014). Tunable diode laser absorption spectroscopy of hypersonic flows. In: Harun Chowdhury and Firoz Alam, Proceedings of the 19th Australasian Fluid Mechanics Conference. *19th Australasian Fluid Mechanics Conference*, Melbourne, VIC, Australia, (87.1-87.4). 8-11 December 2014.

Morgan, R.G. and Wheatley, B.J. (2015). An Intercontinental Rocket Plane Transport Network. In: 20th AIAA International Space Planes and Hypersonic Systems and Technologies Conference. Proceedings. *20th AIAA International Space Planes and Hypersonic Systems and Technologies Conference*, Glasgow, Scotland, 7-11 July, 2015.

Wheatley, B.J., Fulge, H. and McIntyre, T.J. (2015). Atomic oxygen concentration in a microwave plasma. In: 7th Australian Conference on Laser Diagnostics in Fluid Mechanics and Combustion. Proceedings. *7th Australian Conference on Laser Diagnostics in Fluid Mechanics and Combustion*, Melbourne, Australia, 9-11 December, 2015.

Publications included in this thesis

No publications included.

Contributions by Others to the Thesis

Peter Jacobs designed and built two electronics boxes that were used during experiments. He also provided guidance and advice on using the *L1D3* computational fluid dynamics (CFD) package and interpreting the outputs from the program.

Ghassan Al-Doori designed and taught me how to operate the Steam Generator at the University of Southern Queensland in Toowoomba. David Buttsworth made nitrogen purging components for use on the Steam Generator. Kavous Ariafar provided CFD results for the flow properties at the exit from the stream ejector.

Hannes Fulge from the Institute for Space Systems (IRS) at the University of Stuttgart collaborated in experiments using the microwave generator at IRS. Stefan Löhle and Martin Eberhart provided advice and experimental assistance at the University of Stuttgart.

Jorge Sancho Ponce designed and built the scramjet and fuel system used for the X3 expansion tube experiments at the University of Queensland. He also designed and performed experiments that were replicated in this research. David Gildfind, Andreas Andrianatos, Juan Llobet and Pierpaolo Toniato operated X3 during my experiments. Steve Kimball and Peter Bleakley helped to translate National Instruments Virtual Instruments across hardware models.

Pierpaolo Toniato wrote a Python program to analyse pressure sensor traces from the experiments in the X3 expansion tube. Vince Wheatley developed Matlab code for a scramjet which was then translated to Python and adapted to apply to the X3 scramjet.

Statement of Parts of the Thesis Submitted to Qualify for the Award of Another Degree

Chapters 2 and 4 contain information that was submitted in partial satisfaction of a subject for a coursework Master of Science degree awarded by the University of Queensland in 2011. The earlier literature review of tunable diode laser systems was extensively expanded and updated for this thesis. The laser diode and photo-detector data in tables 4.1 to 4.6 were included in the earlier work.

Acknowledgements

Thank you to my supervisors, Tim McIntyre and David Buttsworth for your support, patience and understanding. Thanks also to the members of the Centre for Hypersonics, especially Richard Morgan, Peter Jacobs and the X-lab people for your support and friendship over the past three years.

The financial support of the University of Queensland is gratefully acknowledged. This includes scholarships for a Research Higher Degree and X3 operation. Also, the award of a Graduate Student International Travel Award for travel to the University of Stuttgart is gratefully acknowledged.

Finally, thank you to my beautiful wife, Kay, and children, Ben and Kate, for your undying love, belief and support. Without that, I would never have had the opportunity or courage to undertake this work.

Keywords

Tunable diode laser, Laser absorption spectroscopy, hypersonic, scramjet, water vapour, atomic oxygen

Australian and New Zealand Standard Research Classifications (ANZSRC)

ANZSRC Code: 020502, Lasers and quantum electronics, 100%

Fields of Research (FoR) Classification

FoR Code: 0205, Optical Physics, 100%

Contents

List of Figures

List of Tables

Nomenclature

Abbreviation	Description
$1f$	First harmonic
$2f$	Second Harmonic
a	Half-amplitude of the sinusoidal time variation of the diode frequency
A	Area (m^2)
$\bar{A}$	Relative absorption
A_{21}	Einstein A coefficient (spontaneous emission)
A_{jk}	Transition coefficient between levels j and k
$A^{(j)}$	Integrated absorbance of the j^{th} feature
AC	Alternating current
AFRL	United States Air Force Research Laboratory
ANU	Australian National University
APR	After pressure rise
AR	Anti-reflective
B_{12}	Einstein B coefficient (stimulated absorption)
B_{21}	Einstein B coefficient (stimulated emission)
B	Intermediate frequency bandwidth of a detection system (Hz)
BJT	Bipolar junction transistor
c	Speed of light (299 752 529 ms^{-1})
C_d	Drag coefficient
C_d	Injector discharge coefficient
CEA	Chemical Equilibrium with Applications
CFD	Computational fluid dynamics computer model
CT	Compression tube
CW	Continuous wave
DC	Direct current
DFB	Distributed feedback diode laser
DFFT	Discrete fast Fourier transform

DLAS	Diode laser absorption spectroscopy
e	Elementary charge
$\vec{E}$	Electric field vector
E_i	Energy of the i^{th} state
E_{low}	Lower state energy
E_p	Perturber resonance-level excitation energy
f	Frequency (Hz)
FM	Frequency modulation
FWHM	Full width at half maximum
g_j	Degeneracy of state j
G	Gain of an amplifier circuit
G	Group statistical weight
GHz	Gigahertz
GPIB	General purpose interface bus
h	Planck's constant
$\hbar$	Planck's constant
HEG	High Enthalpy shock tunnel in Göttingen
(h_{fg})	Enthalpy change during condensation
HIFiRE	Hypersonic International Flight Research Experiment program
HITEMP	High-temperature spectroscopic absorption paramters
HITRAN	High-resolution transmission molecular absorption database
HR	Highly reflective
HWHM	Half width at half maximum
i	Laser diode current
i_a	Laser diode modulation current maximum amplitude
i_c	Centre injection current
i_{ref}	Reference photodiode current
i_sig	signal photodiode current
i_{th}	Laser diode threshold current
I	Intensity of transmitted radiation
I_0	Incident intensity
I_D	Detected power (in the absence of analytes)
I_L	Laser diode output power
I_{ld}	Laser diode current

$I_{ld_{Act}}$	Actual laser diode current in a direct TDLAS measurement
$I_{ld_{Start}}$	Starting laser diode current in a direct TDLAS measurement
$I_{ld_{Stop}}$	Stopping laser diode current in a direct TDLAS measurement
IM	Intermediate modulation
IRS	Institute for Spacecraft Systems at The University of Stuttgart
J	Rotational quantum number
k	Boltzmann's constant $\left(\mathrm{JK}^{-1}\right)$
k_0	Integration multiple for Voigt lineshape
l	path length of an absorbing medium (m)
LEL	Lower explosive limit
LO	Local oscillator
LOS	Line-of-sight
LTE	Local thermodynamic equilibrium
m	Mass (kg)
m	Modulation index
$\dot{m}_{air}$	Mass of air injected
$\dot{m}_{H_2}$	Mass of hydrogen injected
m^*_{ap}	Reduced mass of absorber and perturber
m_e	Electron mass
M_g	Molar mass of fuel
m_O	Atomic oxygen mass
M	Mass (atomic or molecular)
M	Mach number
M_0	Free stream Mach number
MHz	Megahertz
Msps	Mega samples per second
n	Harmonic number
n_e	Electron number density
n_j	Number density of particles in state j
n_O	Number density of atomic oxygen
n_{O_2}	Number density of molecular oxygen
N	Noise strength
N	Negative maximum of $2f$ signal
NA	Numerical aperture

NEA	Noise equivalent absorbance
NEP	Noise equivalent power
NIR	Near infrared
NIST	National Institute of Standards and Technology
n_l	Lower state number density
n_O	Number density of atomic oxygen
P	Power (W)
P	Positive maximum of $2f$ signal
P	Pressure (Pa)
p_0	Free stream static pressure
p_{air}	Air fill pressure
P_{H_2}	Hydrogen fill pressure
P_{high}	Laser diode upper output power
P_{low}	Laser diode lower output power
P_p	Partial pressure
P_p	Plenum pressure
P_s^{min}	Minimum detectable sign power
PN	Part number
ppb	parts per billion
psia	pounds per square inch - absolute
PZT	Piezoelectric transducer
Q	Rotational branch corresponding to $\Delta J = 0$
$Q\left(T\right)$	Rovibrational partition function
Q_O	Atomic oxygen partition function
q_0	Free stream dynamic pressure
r	Detector response
R	Universal Gas Constant
R	Ratio of positive to negative maxima of $2f$ signal
R	Resistance (Ω)
R_{LS}	Ratio of line strengths
R^2	Correlation coefficient
RF	Radio frequency
RMS	Root mean squared
RS232	Standard for serial communication transmission of data

S	Signal strength
$S^{(j)}$	Line strength of j^{th} absorption feature $(\text{cm}^{-2}\text{atm}^{-1})$
$S\left(\nu\right)$	Signal measured by a detector
$\tilde{S}_n^{in-phase}$	In-phase component of the n^{th} harmonic output of a lock-in amplifier
S_n^{even}	Even component of the n^{th} harmonic output of a lock-in amplifier
S_n^{odd}	Odd component of the n^{th} harmonic output of a lock-in amplifier
Scramjet	Supersonic combustion ramjet
SCPI	Standard commands for programmable instruments
SN	Serial number
SNR	Signal-to-noise ratio
SOT	Small outline transistor
Specair	A program for computing, manipulating and fitting spectra
t	Time
T	Absolute temperature
T_g	Gas temperature
T_0	Fuel stagnation temperature
T_s	Saturation temperature
$T_{TEC_{Act}}$	Actual TEC temperature
TDLAS	Tunable Diode Laser Absorption Spectroscopy
TEC	Thermoelectric controller
TPS	Thermal protection system
USB	Universal serial bus
USQ	The University of Southern Queensland
UQ	The University of Queensland
v	Velocity (ms^{-1})
V_λ	Oscilloscope wavelength voltage
V_{in_A}	Input A to signal comparator
V_{in_B}	Input B to signal comparator
VDC	Volts direct current
VLOG	Logarithmic output pin on AD8304 logarithmic converter
V_{out}	Output voltage from a circuit
V_p	Plenum volume
V_{PD}	Photodetector voltage
V_{p-p}	Peak-to-peak voltage

w	Non-dimensional line position
WM	Wavelength modulation
WMS	Wavelength modulation spectroscopy
x	Mole fraction of a species
x_p	Mole fraction of perturber
x	Integration factor for Voigt line shape
X3	The X3 expansion shock tunnel at the University of Queensland
y	Integration factor for Voigt line shape

Greek symbols

α	spectral absorbance
α	Most probable speed in a Maxwellian distribution
β	ballistic coefficient
$\frac{\partial P_s}{\partial \nu}$	Received signal power per unit frequency range in a single spatial mode
δ_{n0}	Kronecker delta
δV	Change in oscilloscope voltage
δV_P	Change in piezo voltage
$\frac{\delta \tau}{\tau}$	Relative error in tranmissivity
$\frac{\delta n_O}{n_O}$	Relative error in tomic oxygen number density
Δf	Photodiode bandwidth
Δ_{λ_D}	Doppler FWHM
$\Delta \nu_D$	Doppler HWHM
$\Delta \nu_L$	Lorentzian HWHM
$\Delta \nu_V$	Voigt HWHM
ΔT	Supercooling (at Wilson Point)
Δ_s	Ionisation cutoff energy
ϵ	Group energy
ϵ_0	Permittivity of free space
γ	Ratio of specific heats
γ_a	Air-broadened HWHM
γ_s	Self-broadened HWHM
κ_1	Linear power modulation coefficient
κ_2	Non-linear power modulation coefficient
$\kappa_{I,ic}^{'}$	Linear constant of proportionality

$\kappa_{I,ic}^{"}$	Non-linear constant of proportionality
$\kappa_{\nu,ic}$	Linear frequency-to-injection current response
λ	Wavelength (nm)
η	Efficiency
η	Instrumentation factor
ϕ	Phase angle (radians)
ϕ	Equivalence ratio
ν	Frequency, wavenumber
ν_a	Frequency modulation amplitude
$\bar{\nu}$	Width-normalised modulated detuning
$\bar{\nu_a}$	Width-normalised frequency modulation amplitude
$\bar{\nu_d}$	Width-normalised centre detuning for the laser
ω	Frequency (Hz or cm^{-1})
ρ	Density $\left(\text{kgm}^{-3}\right)$
ρL	Density-length scaling
σ	Absorption cross-section of an analyte
σ_0	Absorption cross-section at resonance
τ	Post-detection integration time
τ_j	Transition probability from level j
$\tau\left(\nu\right)$	Transmittance of monochromatic radiation with a wavenumber ν
$\bar{\chi}\left(\nu\right)$	Line shape function
$\bar{\chi}\left(\nu_0 - \nu\right)$	Intensity at a wavenumber of ν of a spectral line that has a centre wavenumber of ν_0
ω	Plasma frequency

Subscripts and superscripts

0	centre
0	standard conditions
$1, 2$	beam frequencies
a	amplitude
AS	Analytical (signal)
BG	Background (signal)
D	Doppler
DC	Direct current

$even$	Even component of Fourier coefficient
ic	Injection current
IF	Intermediate frequency
i, j, k	atomic or molecular energy levels
$in - phase$	In-phase component of detector signal
L	Lorentzian
$Meas$	Measured
n	Fourier coefficient of detector signal
odd	Odd component of Fourier coefficient
s	Static
t	Total
V	Voigt

1. Introduction

Hypersonic flight imposes significant heat loads on spacecraft during planetary entry and on air-breathing vehicles in flight through the Earth's atmosphere. Convective, radiative and conductive heat transfer processes contribute to heating the surfaces of such vehicles.

The specific enthalpy of a flow at a free stream velocity v is $\frac{1}{2}v^2$. Thus, at a free stream velocity of 7 kms^{-1}, the flow's specific enthalpy is 24.5 MJkg^{-1} and the air temperature downstream of a normal shock wave is of the order of 7000 K [4]. At this temperature, molecules dissociate, atoms ionise and radiation is emitted as particles relax from excited to lower states. Convective and radiative heat transfer to vehicles during atmospheric entry are primary design considerations for the vehicle shape, size and mass. They drive the design of spacecraft thermal protection systems which, in turn, can limit the allowable payload mass for a spacecraft.

Ground testing plays an important role in hypersonic vehicle development and spacecraft design. Free piston-driven shock tunnels such as the T4 facility at the University of Queensland and the high enthalpy shock tunnel in Göttingen (HEG) are capable of simulating flight conditions up to orbital velocity while continuous facilities can reach Mach 8 flight conditions [5]. Free piston-driven expansion tunnels such as the X2 and X3 facilities at the University of Queensland can simulate flight conditions at super-orbital velocities [6]. Plasma wind tunnels such as those at the Institut für Raumfahrsysteme (IRS) at the University of Stuttgart can simulate high specific enthalpies (up to 150 MJkg^{-1}) which can, for example, appear during return missions to Earth or during aero-braking manoeuvres in higher altitudes [7]. The choice of facility used in any particular experiment is a balance between flow enthalpy, test time, scaling method, desired test outcomes and model size.

Free-piston super-orbital expansion tunnels (such as the X2 and X3 facilities at the University of Queensland) were developed, amongst other reasons, to overcome the flow dissociation issue associated with reflected shock tunnels. The test gas in an expansion tunnel accelerates continuously as it travels to the test section. Thus, it does not stagnate and does not dissociate prior to reaching the test section. The steady flow duration for an expansion tube is of the order of $0.1 - 1$ ms; much less than for a reflected shock tunnel.

Instrumentation used for expansion tunnel tests includes pressure sensors, thin film heat transfer gauges, friction gauges, force balances and optics. Optical methods include high-speed photography, emission spectroscopy, laser-based techniques including Planar Laser Induced Florescence (PLIF), laser holography, and Coherent anti-Stokes Raman Spectroscopy (CARS). Each technique has advantages and disadvantages as discussed extensively in published literature. Emission spectroscopy methods have been stalwarts of expansion tunnel experiments because of the high temperatures and levels of radiation in the bow shock of the test articles. In recent years, Tunable Diode Laser Absorption Spectroscopy (TDLAS) techniques been developed to probe scramjet and other hypersonic

flows overseas and in Australia but they have not previously been used on expansion tunnels at the University of Queensland.
The nature of expansion tunnel flow precludes many types of sensors from being used in experiments. Total temperature and total pressure sensors can also affect the flow around the test article and may be quickly destroyed in these flows. TDLAS could be suitable for measuring expansion tunnel parameters without influencing the experiment.

1.1. Tunable Diode Laser Absorption Spectroscopy

Tunable diode laser absorption spectroscopy (TDLAS) relies on absorption of laser light by molecules and atoms as particles move from lower to higher energy states. TDLAS has been applied in various scenarios since it was first developed in the 1970s [8, 9, 10, 11]. The introduction of room temperature tunable laser diodes allowed researchers to determine species concentrations and properties in various environments by measuring the absorption profile of individual spectral lines. Over the past 30 years, researchers have developed systems that use low power, continuous wave, tunable diode lasers. Researchers can simultaneously measure multiple characteristics of the flow such as temperature, pressure, velocity and species concentrations. TDLAS systems can measure temperatures and mole fractions to within 4% and 10% respectively of the actual values in flows with uniform temperature [12].
TDLAS system have been deployed on scramjets in both ground and flight environments. Water vapour is present as a primary combustion product in scramjets. Its abundance, coupled with the large line strengths for the vibrational bands in the near infrared makes it suitable for absorption spectroscopy studies in scramjet isolators, combustors and exhausts.
Researchers in Australia and the United States have developed TDLAS systems for scramjet combustion monitoring [13, 14, 15, 16, 17, 18]. Stanford University researchers recently undertook wavelength-multiplexed two-colour TDLAS to measure H_2O temperature and column density in a model scramjet combustor under high enthalpy conditions generated in a reflected shock tunnel [19]. In Australia, Griffiths et al [13] constructed a TDLAS system for time-resolved temperature and water vapour concentration measurements in a scramjet combustor. Also, O'Byrne and Wittig [15] measured the Mach number, free stream velocity and angle of attack at the inlet of a scramjet using tunable diode laser absorption spectroscopy of oxygen.
TDLAS has been used to probe CO_2 in hypersonic flows at VKI's Longshot tunnel [20] but it has not previously been used to probe expansion tunnel flows to the author's knowledge. During their test times of less than 1 ms, expansion tunnel flows exhibit large changes in pressure, temperature, shock positions and compositions. Species dissociate, ionise and radiate as they pass through shock waves upstream of test articles. TDLAS systems have the potential to significantly improve understanding of expansion tunnel flows and the concentration of short-lived species such as OH, NO or atomic oxygen and nitrogen in those flows.

1.2. Research Aim

The aim of this research was to develop and test a TDLAS system that could perform measurements in expansion tunnels at The University of Queensland.

1.3. Methodology

Firstly, literature was researched to determine the state of the art for TDLAS systems and understand the theory behind TDLAS. Chapter 2 summarises the literature review whilst Chapter 3 discusses the basic theory underpinning TDLAS.

Considering the wide range of TDLAS applications (as discussed in Chapter 2), a multifaceted approach was taken to the research. Initially, a system was designed to measure temperature and pressure using spectral lines of water vapour. This system is described in Chapter 4 and was designed to be modular and allow flexible application of TDLAS techniques in various environments. The limited availability of TDLAS expertise at the University of Queensland demanded the author to develop techniques and software independently using guidance from published work. This led to TDLAS applications that have not been reported elsewhere in this thesis but were nevertheless extremely important in gained expertise at applying TDLAS to a wide-ranging set of flow conditions.

A series of laboratory experiments were undertaken to characterise the TDLAS system using direct absorption by water vapour in the atmosphere. These experiments are summarised in Chapter 4. Multiple tests were undertaken using heated water samples in different laboratory conditions with a wide range of diode currents and temperatures.

Next, the direct techniques were applied to a steam ejector system at the University of Southern Queensland where a quasi-steady-state flow was used to explore low temperature and low pressure measurements for water vapour. These experiments (reported in Chapter 5) highlighted the importance of stray radiation and atmospheric absorption on TDLAS experiments with water vapour. Four methods of spectral data analysis were compared for accuracy, ease of use and repeatability as reported in Chapter 5.

Wavelength modulation spectroscopic methods were next applied to flows in a cold reflected shock tunnel[1]. Whilst these experiments are not reported in this thesis, they highlighted issues in applying TDLAS to reflected shock flows. One problem was occultation of the laser beam by residual diaphragm pieces. This caused the TDLAS signal to be intermittent and unpredictable. Imaging using high-speed video and a strong flash showed the cause to be pieces of the mylar diaphragm striking the test piece during a shot. Following these experiments, the diaphragm material was changed to tracing paper eliminating the interference.

As an aside, Drummond Tunnel experiments were conducted using an ice test piece (to represent a meteor) with small particles of pepper used to accelerate erosion. During a 10 ms test, the entire meteor was eroded. High-speed video showed the erosion process. As TDLAS was not used during these tests, they are not reported in this thesis. In the author's opinion, TDLAS could probe the flow

[1] Known as The Drummond Tunnel

upstream of the eroding meteor to measure pressure, temperature and water vapour concentration.
Hypersonics researchers at The University of Queensland wanted to measure the number density and properties of atomic oxygen or nitrogen behind the bow shock in expansion tunnels. The author analysed whether TDLAS could be used in this scenario finding that a system could be developed to probe the oxygen triplet centred on 777.417 nm. These lines belong to the transition $3s - 3p$ and multiplet ${}^5S^0 - {}^5P$. Chapter 7 contains outcomes of this research. A search of diode manufacturers revealed that suitable diodes could be made at high cost and without any guarantee of suitability. These risks led the author to abandon this approach.
Instead, collaborators at The University of Stuttgart kindly allowed the author to use their laser diode system and an Evenson cavity to conduct experiments into the feasibility of using TDLAS to probe the atomic oxygen triplet centred on 844.64 nm. These lines belong to the transition $3s-3p$ and multiplet ${}^3S^0 - {}^3P$. This research was novel as it had not previously been undertaken at IRS. The author set up the Evenson cavity after some brief instructions and performed all of the TDLAS experiments and data analysis. The goal of these experiments was to measure the atomic oxygen concentration in a weak plasma generated by a Evenson cavity. Chapter 7 contains outcomes of these experiments. If the atomic oxygen concentration could be measured in a weak plasma, it may also be measurable behind bow shocks during expansion tunnel experiments.
An opportunity arose at short notice to use TDLAS to probe water vapour in the exhaust of a scramjet mounted in the X3 expansion tunnel. This work is disclosed in Chapter 6. There were limited opportunities to modify the test piece or to develop analysis techniques prior to the experiments because of the short timeframe. Nevertheless, this was viewed as an ideal opportunity to use TDLAS in a large (1.8 m) diameter test section of a Mach 10 expansion tunnel flow with a test time of approximately 1 ms. Because of the external limitations placed on the experiment, free space TDLAS methods were used instead of using fibre optics to probe only the combustor flow. Fibre optics were abandoned because:

- The test scramjet would have to be modified to protect the launch diode and capture photodetector. A constraint on the experiment was that the scramjet was not to be modified if possible as it was to be used in other experiments.

- The optics would have to be ported through the signal interface into the expansion tunnel test section and through the scramjet support to the scramjet exhaust. The fibres had to be protected from the free stream flow and any steel shrapnel that originated from the primary diaphragm. The space in the scramjet support was extremely limited due to the fuel system pipes and pressure transducer cables so the scramjet test model would have had to be removed from the tunnel and modified by technicians. Given the restricted timeframe and limitations on modifying the scramjet, this was not possible.

The physical size of the expansion tunnel test section imposed further restrictions on the experimental design. After each shot, the test section was moved approximately 4 m downstream during the tunnel turnaround. The TDLAS experimental layout had to accommodate this movement and allow the author access to the scramjet to remove damage. The author also cleaned the test section windows

with ethanol after each shot to remove carbon residue and debris. To do this, large (1.5 m long) aluminium doors were swung outwards from the test section to provide access to the windows and scramjet. After turnaround, the entire test section was moved back upstream to be positioned with ± 0.5 mm of its original position so that the TDLAS beams were correctly aligned with the exhaust.
The final experimental challenge was to manage timing and recording of data. The expansion tunnel, fuel system and TDLAS system all required specific data recording methodologies which had to be integrated together. If the fuel system was late opening, no combustion would occur; however, the fuel system initiation time was 200 ms whereas the time required for a shock to traverse the expansion tunnel was 20 ms. The TDLAS system had to record at 60 Msps[2] during the 1 ms when the established flow was traversing the scramjet exhaust but the fuel system had to be triggered about 200 ms earlier. This high signal bandwidth required a novel amplifier and signal mixing system to be developed. These issues are discussed in detail in Chapter 6.
After the expansion tunnel experiments, the data had to be analysed. Ideally, the analysis techniques would be been developed and tested using CFD prior to the experiments; however, the limited notice precluded this. Analytical simulations of the expansion tunnel flow, scramjet and combustion conditions were developed by the author to estimate the conditions in the scramjet exhaust. The outcomes of these simulations were validated against pressure transducer measurements in the expansion tunnel and scramjet.
The TDLAS analysis had to account for unsteady flow conditions with rapidly varying pressure, temperature and molecular concentrations that lasted for only 1 ms. TDLAS is usually applied in relatively steady-state conditions so this analysis was unique. Another unique aspect was that large amplitude wavelength modulation was used instead of the usual method of a combination of small amplitude sinusoidal modulation overlaying a large amplitude sawtooth modulation. A wide range of advanced signal processing methods were used to extract the TDLAS signals from the recorded data.
A number of unexpected phenomena and issues were encountered during the development and implementation of the system. For instance, the water vapour produced by the steam ejector was either super-cooled or had formed condensation nuclei depending on the operating conditions of the steam generator. Similarly, application of TDLAS to the other environments yielded results that have not been previously reported. In each application, there were specific issues that had to be overcome to successfully apply TDLAS requiring innovative problem solving and multiple trials before finding the best way to apply the technology.

1.4. Research Outcomes

This research extended the scientific knowledge of TDLAS applications to aerospace flows. A modular TDLAS system was developed to detect temperature, pressure and number density of water vapour or other species in a range of environments including hypersonic flows. A particular focus was placed on making the system inexpensive with a high reliance on off-the-shelf products and components and the use of open-source software for control and data analysis.

[2]Mega samples per second

The research applied TDLAS to steam generator and ejector flows, atomic oxygen concentration measurement in a plasma, and detection of combustion in a scramjet operated in an expansion tunnel. Complex control mechanisms were implemented to coordinate signal triggering and recording over timeframes spanning from nanoseconds to seconds. Bespoke amplifiers and other electronic devices were designed and implemented to process rapidly changing photodetector outputs. Advanced signal processing techniques were developed to extract TDLAS signals from unsteady, transient, noisy flows. The experiments demonstrated that TDLAS could be successfully applied to flows of these types including the extreme conditions generated in expansion tunnels. They also provide a basis for expanding the system to probe expansion tunnel flows for transient radicals and atoms such as hydroxyl, nitrous oxide and atomic oxygen and nitrogen.
Overall, this research showed that TDLAS has a wide range of applications to aerospace flows provided judicious thought is given to experimental design and data analysis. Novel designs and advanced signal processing techniques may be used to extend TDLAS to many aerospace applications.

1.5. Thesis Structure

Chapter 2 reviews literature with a focus on TDLAS applications for hypersonic flows. Chapter 3 summarises the theoretical background for TDLAS. Any experiment specific theory is discussed in the relevant experimental chapter. Chapter 4 describes the TDLAS system in detail and provides justification for design decisions such as laser diode and optics selection. Chapters 5 to 7 detail application of TDLAS to various hypersonic flows including:

- steam ejector flows at The University of Southern Queensland;
- combustion detection in the nozzle of a scramjet during hypersonic tests in a free-piston expansion tunnel at The University of Queensland;
- atomic oxygen measurements in a microwave generator at The University of Stuttgart and a discussion of the requirements of a TDLAS system to probe atomic oxygen in an expansion tunnel.

The final chapter summarises the outcomes and provides recommendations for future research.

2. Literature Review

Since the first TDLAS system was developed, advances in diode manufacturing techniques, optical arrangements, fibre optics, electronics and computing have significantly improved the capabilities of systems. Early diode lasers required cryogenic cooling [10] whereas today diodes may be used at room temperatures. Optical fibres have progressed from being expensive, delicate and having large losses to being cheap, flexible and extremely efficient. Today, high gain and bandwidth photodiodes are capable of detecting modulation frequencies in the megahertz range. Modern electronics are capable of recording signals at billions of samples per second range and desktop computers can simulate and analyse complex and data-intensive signals.
This chapter reviews TDLAS-related literature with a focus on hypersonic flows. To set the scene, early applications of TDLAS are summarised and reviews of TDLAS developments are cited. Next, the history of theory development is detailed including line-shape theory and wavelength modulation spectroscopy theory. Applications of TDLAS to combustion and scramjet research are then summarised.

2.1. Early Applications

In the early 1970s, there were practically no commercial laser spectroscopic instruments for routine elemental analysis [21]. There was, however, a great deal of interest in obtaining high-resolution absorption data for gases [22]. Researchers [22] had obtained spectra for SF_6 near 10.6 μm by tuning a CO_2 laser across spectral lines but the laser's continuous tuning range of 50 MHz was found to be inadequate . Hinkley et al [22] used a tunable diode laser for high-resolution absorption measurements because the diode laser had a narrow line width (50 kHz or smaller) and its continuous tuning range of approximately 50 GHz was much greater than that of a gas laser.
Following the success of the initial experiments, Hinkley et al [8] used tunable diode lasers to detect air pollutants. Their system used cryogenically cooled $Pb_{1-x}Sn_xTe$ semiconductor lasers to detect ammonia, sulphur hexafluoride and ethylene by either point sampling, long-path atmospheric transmission or remote sensing. The perceived advantages of using tunable diode lasers over other spectroscopic methods were:

- the compactness of the diodes,
- the ability to tune wavelength using laser diode current, and
- modulating the diode current then extracting an intermediate modulation (IM) signal.

In 1977, Hanson [23] applied tunable diode lasers to the spectroscopy of transient, high-temperature gases heated by a shock wave. He rapidly tuned the laser across the full width of a CO vibration-rotation absorption line during the test time available behind an incident shock wave in a shock tube. The experiment resulted in direct determination of the line strength at high temperature and an accurate comparison of the line shape with a calculated Voigt profile. Also in 1977, Hanson and Falcone [24] developed a technique that used two nearly coincident vibration-rotation lines from the same species to measure temperature in a laboratory flame using absorption by CO near 4.5 μm.
By 1978, Reid et al [9] had developed the technique sufficiently to measure SO_2 concentrations in the low parts per billion (ppb) range. Reid's group also investigated the advantages and theory of wavelength modulation spectroscopy with particular emphasis on first and second harmonic detection methods. These examples all used cryogenically cooled diodes as laser sources. By the 1980s, semiconductor laser diodes were being mass produced for compact disc players, laser printers and telecommunication equipment. To be useful for spectroscopy, laser diodes had to have good wavelength stability at their operating temperature; be free of mode hopping over the wavelengths of interest; have a narrow bandwidth; and have a precise and repeatable current to output power relationship [21]. Most importantly though, these diodes could be used at room temperature.

2.2. Reviews of TDLAS Advances

Niemax et al [25] provide an introductory summary of TDLAS and its applications while Werle [26] has published an extensive review of advances in semiconductor laser based gas monitors. Werle highlighted that, to improve sensitivity, various types of modulation spectroscopy have been employed where the diode laser wavelength was modulated while being scanned across an absorption line. These techniques allowed measurements of absorptions as low as one part in a million within a 1 Hz bandwidth. Figure 2.1 summarises the effects that mostly limit the ultimate sensitivity of TDLAS systems using frequency modulated (FM) detection. A minimum exists in the figure at 10 MHz and one minute of averaging. Werle states that the lasers must operate in a single longitudinal mode with low noise and high power output in order to achieve ultra-sensitive FM TDLAS. Hodgkinson et al [27] reviewed the field of gas detection methods including TDLAS and presented a performance comparison of different techniques. They highlighted that the performance achieved in the laboratory is rarely replicated in the field due to difficulties in precisely aligning optics and unknown variations in temperature and pressure within the sample. These factors can affect the line width and absorption strength of the sample, having a significant effect on TDLAS performance. The authors note that there may be a fivefold difference in the limit of detection between an optimised laboratory instrument and an airborne one. They found that directly scanned and second-harmonic wavelength modulation spectroscopic ($2f$ WMS) TDLAS techniques perform similarly at lower values of noise equivalent absorbance (NEA). The best performance for each technique is when balanced detection systems are used that compensate for laser intensity fluctuation and interference. If both techniques are limited by optical interference fringes, their limits should be the same. All of these advances mean that the potential applications of TDLAS are changing constantly. While TDLAS may not have been practical

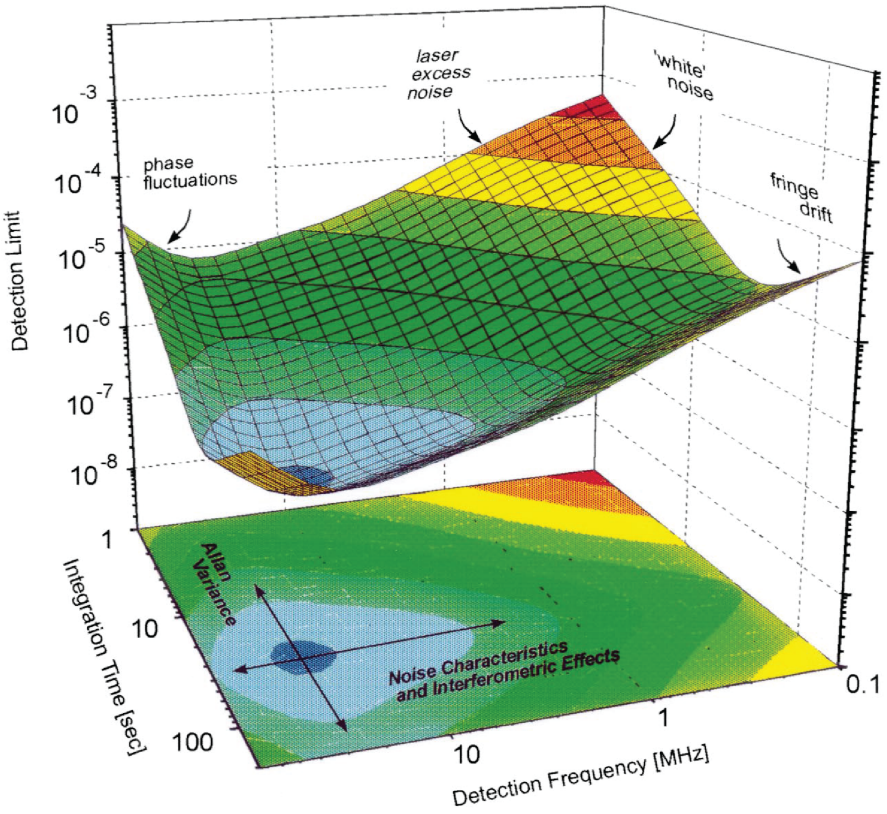

Figure 2.1.: Illustration of the influence of integration time and modulation frequency on spectrometer performance. (Source: [26])

for expansion tunnels in the past, it may be useful now.

2.3. Spectral Lines

TDLAS measures individual spectral lines and uses measured parameters to derive pressure, temperature and number density for the species being detected. As a result, the shape of a spectral line is of vital importance when using a TDLAS system. Thorne et al [28] state that four processes may contribute to the finite width of a spectral line: natural broadening, Doppler broadening, interactions with neighbouring particles and power broadening. Each of these processes will be considered below in light of their importance to TDLAS.

2.3.1. Natural broadening

Natural broadening is a consequence of the finite lifetime of the excited state due to spontaneous emission and occurs at a constant rate independent of external influences [28]. Natural broadening is due to the finite width of the discrete energy levels involved in transitions. In other words, the Einstein A_{21} coefficient determines the decay rate with a mean lifetime for a two-level atom of $\tau_2 = 1/A_{21}$. A real atom, in contrast to the two-level atom, has many levels. If an atom or molecule is initially in an upper level E_j, it may transition to any of several lower levels E_k. The transition probability from

level j is the sum of the individual transition coefficients A_{jk} and the lifetime for level j is:

$$\tau_j = \left[\sum_{k=0}^{j-1} A_{jk}\right]^{-1} \tag{2.1}$$

Also, the lower level will be broadened if it is not a ground state or a metastable state ($\tau_k \to \infty$) since it will also have a finite lifetime. The resulting Lorentzian profile has a full-width at half maximum (FWHM) of:

$$\Delta\nu_{jk} = \nu_j + \nu_k \tag{2.2}$$

$$= \frac{1}{2\pi\tau_j} + \frac{1}{2\pi\tau_k} \tag{2.3}$$

Naturally broadened line widths are of the order of $10^{-5} - 10^{-2}$ cm^{-1} [28]. Whilst this is narrow and of little relevance for 'normal' emission spectroscopic methods used in expansion tunnels, it is of the same order of magnitude as the line width of radiation emitted by a tunable diode laser and, as a result, may be important in TDLAS research.

2.3.2. Doppler broadening

The doppler broadened line shape derives from frequency differences due to atoms or molecules with velocities toward or away from the observer. For a gas at temperature T the fraction of atoms with velocity between v and $v + \mathrm{d}v$ is given by the Maxwell distribution:[1]

$$\frac{\mathrm{d}N\,(v)}{N} = \frac{1}{\sqrt{\pi}\alpha}\exp\frac{v^2}{\alpha}\mathrm{d}v \tag{2.4}$$

where α is the most probable speed given by:[2]

$$\alpha = \sqrt{\frac{2RT}{M}} \tag{2.5}$$

where R is the universal gas constant and M is the molar mass of the species. The most probable speed is $\sqrt{2}$ times the standard deviation of the velocity distribution. The doppler broadened half-width at half maximum (HWHM) of a spectral line $\Delta\nu_D$ is:

$$\Delta\nu_D = \sqrt{\ln 2}\frac{\nu_0\alpha}{c} \tag{2.6}$$

where ν_0 is the centre wavenumber of the spectral line and c is the speed of light.

[1] Also known as the Maxwell-Boltzmann distribution.

[2] This is not the mean speed. The mean speed is $\frac{2}{\sqrt{\pi}}\alpha$. See Ferziger et al [29] for a detailed discussion

2.3.3. Power broadening

Power broadening occurs when a line profile is affected by the intensity of radiation passing through a sample. A laser beam can cause power broadening due to its high intensity. As the excitation field becomes more intense, atoms spend a greater proportion of time in the excited state though never more than the saturation value of 50%. The line width is proportional to the range of detuning where saturation occurs which, in turn, increases with laser intensity [30]. The presence of power broadening depends critically on the nature of excitation and the type of measurement. Typical power broadening has a Lorentzian profile and is observed when the excited state population in a two-state system is driven by a continuous wave (CW) laser field whilst being continuously observed. Power broadening by pulsed excitation only occurs when an appreciable excited state population remains at the end of a pulse [30]. Power broadening may occur at laser intensities above 10 Wm^{-2} [31]. A 5 mW laser diode with a beam diameter of 2.5 mm has an intensity of more than 1 kWm^{-2} so power broadening could occur during TDLAS measurements if the frequency of the laser beam was constant and coincided with the centreline of a line. Given that the laser frequency changes constantly during TDLAS measurements, power broadening is unlikely to affect this research.

2.3.4. Collisional broadening

Spectral lines are broadened or narrowed and shifted by increasing gas pressure and in the presence of ions and electrons [28]; all of which are characteristics of hypersonic flows. Also, forbidden transitions may appear. Foley [32], Anderson [33] and Dicke [34] amongst many others performed seminal research on the effect of particle interactions on spectral lines. Breene [35] provides an excellent summary of the earlier research into collisional line broadening and shifting whilst Buldyreva [36] provides a more recent update on the topic.

Early theories of collisional broadening were based either on collisions causing a relative phase-shift of the radiation before and after the collision with no amplitude change (Fourier integral theory) or on transitions among the spatially degenerate quantum states (Debye's dielectric relaxation theory) [33]. The former gave good results at optical frequencies whilst the latter applied at the limiting case of zero frequency. Collisions that do not produce transitions between atomic states yield adiabatic approximations as they rely on the adiabatic hypothesis which states that transitions are due to radiation alone [37].

In 1949, Anderson [33] developed a generalised theory of collision broadening that was adequate for predicting line breadths in the microwave and infrared regions. Previously, van der Waals interactions were assumed to cause foreign gas broadening [33]. His theory differed from previous ones by accounting for transitions among quantum states caused by collisions. Anderson concluded that, in general, the van der Waals interaction was not adequate to cause the broadening observed. Anderson's formula included the effects of both phase shifts and transitions. Bloom and Margenau [37] extended Anderson's theory by using 'collision-smeared' atomic states.

2.4. Line Shapes

H.A. Lorentz provided the first treatment on the effects of interactions of radiating atoms and molecules on spectral lines [32]. In his treatment, Lorentz assumed that the atoms or molecules had a definite collision radius and each radiating system periodically suffered a sudden disruption to the radiation mechanism due to collisions [32]. These assumptions mean that the collisional durations are small compared to the intervals between them and collisions produce phase shifts in radiation. Other authors have refined and changed the theory over the years, however, the basic assumptions behind the 'hard sphere' theories of spectral broadening continue to apply [28]. In the hard sphere model, molecules are assumed to act as hard spheres that are perfectly elastic. The collisions are assumed to be fast and interactions between the molecules are short-range. Molecules are assumed to travel in straight lines before and after collisions making their motions uncorrelated. Based on these assumptions, the molecular velocity distribution has a Maxwellian form.

The gas medium is assumed to be optically thin making absorption weak so that non-linear terms in the Taylor-series expansion of the transmissivity equation can be ignored. Relating to this assumption, photons emitted anywhere in the gas are assumed to have negligible change of absorption before reaching the detector. The gas column is assumed to be homogeneous; comprising the same species, pressure and density throughout the entire column. Finally, the gas is assumed to be in local thermodynamic equilibrium (LTE) so that molecular populations and velocities are described by equilibrium relations. The molecular velocities have a Maxwellian distribution and the population among excited states has a Boltzmann distribution. Collisional processes must be more important than radiative processes so that there is no shortfall in radiative energy.

Given the broad range of these assumptions, it is perhaps not a surprise that some flows and environments do not comply with them. For instance, at high pressures (typically 10-100 atmospheres), spectral line narrowing is observed when blended lines such as those in Q branches begin to narrow due to mixing of the internal states of molecules by collisions [38]. In this environment, the population of excited states deviates from a Boltzmann distribution making the assumption of LTE invalid.

Dicke narrowing [34] is another case where the hard sphere model does not apply and the velocity probability distribution is not Maxwellian. This involves collisional narrowing of isolated spectral lines at pressures where Doppler broadening is important. Instead, Brownian motion models of molecular velocity should be used where soft collisions occur [38].

The theoretical understanding of spectral properties and line shapes underwent spectacular development throughout the 20^{th} century primarily due to the development of quantum theory. For example, Foley [32] investigated the pressure broadening of spectral lines using quantum radiation theory with an adiabatic collision approximation. Anderson [33] developed a generalised theory of collisional broadening that predicted line breadths. Bloom and Margenau [37] used radiation theory to derive Anderson's formula using an alternative method. Dicke [34] showed that Doppler broadened lines may be substantially narrowed by collisions that do not affect the internal state of the radiating system. These advancements alone were published in the seven years from 1946 and to 1953.

In 1957, Breene [35] published an extensive review of the causes of different line shapes. This

review provides an excellent basis for understanding the mechanisms of line broadening. Galatry [39] used classical Fourier integral theory to calculate the shape of a spectral line broadened by phase changes due to collisions and by the actual changes in velocity of the emitting particles resulting from collisions. He highlighted that the line-shape was not a simple Voigt-like profile but, instead, demonstrated Dicke narrowing. The resultant line shape is called a Galatry profile. Tsao and Cornutte [40] published a seminal work in 1962 on the line-widths of pressure broadened spectral lines as calculated using Anderson's impact theory [33]. In 1965, Arndt [41] developed general analytical expressions for the line shapes of Lorentzian signals broadened by modulation. He discussed the cases for first and second harmonics and calculated the line widths and signal intensities as functions of the modulation amplitude.

At low pressures, doppler broadening dominates and the absorption lines may be approximated by Gaussian line profiles or shapes [28]. At high pressures, pressure broadening dominates and Lorentzian line shapes approximate the absorption lines. Between these two limits, both Doppler and pressure broadening are important and Voigt profiles more closely match the line shapes. Spectral profiles recorded at high resolution are generally modelled as a Voigt function. They tend to a Gaussian in the low pressure limit and to a Lorentzian profile at higher pressures. The Voigt function may be expressed as the real part of the complex probability function [38]. The Voigt line shape was made accessible to electronic computation through the efforts of Whiting [42, 43] and Humlíček [44, 45] who developed algorithms to evaluate the function.

In 1984, Varghese and Hanson [38] showed that there were discrepancies of the order of a few percent between experimental data using TDLAS and the Voigt line shape. They stated that, for infrared transitions of typical molecules, Doppler broadening is important at pressures below approximately 13 kPa at room temperature and up to 100 kPa at flame temperatures. Varghese and Hanson found that velocity-changing collisions reduced the profile width and increased the line shape function at line centre [38]. This difference is important given that high resolution measurements are frequently made at line centre where the signal is maximum. The Voigt function under-predicts the absorption at line centre [38]. Notwithstanding this, Varghese and Hanson recommended that the Voigt profile is probably the best choice for fitting line shapes recorded at high resolution. More complex models may be employed if the plot of residual errors as a function of temperature reveals significant systematic discrepancies [38].

2.4.1. Curve fitting

Together with using the appropriate line shape for a particular application, TDLAS data must be correctly fitted to the profile to yield suitable results. This task is relatively straightforward for direct absorption where the detected line shape is the same as a modelled profile. Reid et al [10] and Cassidy et al [11] used least squares methods to fit curves. Later, non-linear techniques such as a modified Levenberg-Marquardt method [46] were used in conjunction with discrete fast Fourier transforms (DFFT) to reduce the computing time [47]. The use of an efficient optimal curve fitting routine was very important in the early years of TDLAS but has become less important as the computing capacity of personal computers has increased.

May and Webster [48] provide a clear description of spectral data analysis. The diode modulation amplitude and waveform are chosen to maximise the detected signal at some harmonic (usually the second) of the modulation frequency. The line shapes are only proportional to the derivative of the direct absorption line shapes if the modulation amplitude is small relative to the molecular line width. For a maximum signal to noise ratio (SNR), the modulation amplitude should be approximately twice the half width for an isolated line. In this case, the line shape differs markedly from the simple derivative.

The wavelength modulation technique is based on the concept that the wavelength of the light is modulated at a frequency f whereas the detector signal is de-modulated at a harmonic of the frequency nf [49]. The detected line shapes are not the same as those for direct absorption. Instead, the nf signal is given by the n^{th} coefficient of the Fourier series expansion of the wavelength-modulated line shape function. Westberg et al [49] developed a methodology for calculating a given Fourier coefficient of a wavelength modulated Voigt absorption function. Li et al [50] discuss a technique known as wavelet transform that can be used to get better time and frequency resolution based on Fourier transforms. Wavelet transform has multi-resolution characteristics meaning that it divides the frequency contents of a signal into low and high sub-bands. It provides access to information that can be obscured to other time-frequency methods such as Fourier analysis. Using the wavelet transform to improve spectral SNR, higher detection sensitivity and measurement precision can be achieved with a fast temporal response. This technique has potential to improve high speed TDLAS measurements. Readers should refer to reference [50] for details of the technique.

Skrtozki et al [51] developed an advanced integrative algorithm for fitting a Voigt function to data. Their algorithm is robust and fast and uses a novel iterative fitting process to achieve high accuracy. They state that their algorithm has advantages over the Levenberg-Marquardt [46] fitting algorithm. Readers should refer to reference [51] for details of the algorithm.

2.5. Wavelength Selection

A target species must be in sufficient concentration and must absorb radiation at a suitable wavelength to be a candidate for TDLAS monitoring. Each target species has numerous absorption or emission peaks depending on the reactions taking place and on the flow temperature and pressure. Wavelength choice also depends on the availability of laser diodes, photodetectors and optics. Choosing a strong absorption peak may be irrelevant if there are no commercially available laser diodes or photodetectors at that wavelength. This is particularly relevant for detecting water vapour as many of the cheapest and most readily available laser diodes have been developed for electronics or telecommunications and tend to avoid wavelengths where water vapour absorbs strongly. In the end, the wavelength choice may be a compromise between the best theoretically and one where optical components are commercially available.

After deciding on the species of interest and the wavelength for observation, the flow conditions, enthalpy and target species in the test area influence TDLAS system design and operation. As stated by Ouyang and Varghese [47], the level of resolution depends on the relative line positions, strengths,

density of data points, number of spectral lines and noise level of a particular dataset. Zhou et al [52] recommend that the following criteria be used to select wavelengths for probing:

- The lines must have sufficient strength over the intended temperature range.
- The line pairs must be close enough to be traversed in a single laser scan (spacing ≤ 1 cm^{-1}) but remain distinct at atmospheric pressure.
- The line pairs should have similar strength to maximise signal to noise and reduce overlap. Zhou et al imposed a line strength ratio of between 0.2 and 5.
- The line pairs must have sufficient relative sensitivity or change in line ratio with temperature.
- The two lines should be free of significant interference from nearby transitions.

These criteria have since been adopted by various authors [14, 13, 16, 17, 53, 54, 55] and are accepted for this study as being the state of the art.

2.6. Spectral Databases

The accuracy of TDLAS sensors relies on the ability to accurately simulate the absorbance spectra as a function of gas conditions. This requires accurate spectroscopic parameters (such as line centre frequency, line strength, lower state energy and line shape parameters) and line shape models. For high pressure applications, accurate collisional-broadening parameters are also required [56].
A spectral modelling program such as *HITRAN* [57], *Specair* [58] or *HITEMP* [59] is used to determine the optimal measurement wavelength. *HITRAN* is an excellent source for atmospheric spectra. *HITEMP* is analogous to the *HITRAN* database but encompasses many more bands and transitions than *HITRAN* for the absorbers H_2O, CO_2, CO, NO, and OH. Recently, *HITRAN* has been deployed on the internet via *Spectroscopy of Atmospheric Gases* [60]. This tool allows users to quickly and easily simulate atmospheric gas spectra using a variety of spectroscopic databases. Specair provides a user-friendly interface whilst modelling the absolute intensity of spectral radiation emitted by gases and plasmas.
HITRAN has been in development for more than 40 years [61] and is updated on a regular basis with the most recent update in 2012 [57]. Some researchers (such as those at Stanford University) place particular emphasis on validating spectroscopic parameters in their specific test conditions [53, 62, 63]. The NIST database [64] provides spectroscopic parameters for atomic species. Whilst the spectral databases have advantages, they also pose a number of potential risks including errors in the reported line strengths and missing or additional spectral lines at high temperature [13, 65].
This study relies primarily on the *HITRAN*, *HITEMP*, NIST and *Spectroscopy of Atmospheric Gases* tools. Where possible, spectroscopic parameters that have been experimentally validated are used. Any use of parameters that have not been experimentally validated is highlighted in the relevant chapter.

2.6.1. Spectral properties of water

Given water's importance to life, the environment and combustion, its spectral properties have been extensively researched. Somewhat surprising is the on-going investigation into the broadening and high temperature properties of spectral lines for water. This research is largely due to the accuracy and sensitivity requirements introduced by TDLAS techniques. This section reviews the developments in measuring line strengths, positions, pressure-shift coefficients and temperature ratios for water vapour spectral lines near 1.39 μm. This is included because researchers should not automatically assume that the information contained in spectral databases such as *HITRAN* is one hundred percent correct.[3]

Toth [66] made extensive measurements of line positions and strengths of water vapour in the region between 5750 cm^{-1} and 7965 cm^{-1} and compared the line strengths with those in the *HITRAN* 1986 database. He recommended improved line strengths and positions near 1.4 μm. Subsequent studies have found that Toth's results improved on those in the *HITRAN* 1986 database.

Nagali et al [67] measured half-widths for selected water transitions in the 1.4 μm region when perturbed by H_2O, N_2, and CO_2 at 298 K and over a temperature region $400 - 1000$ K. Self-broadening was measured over a pressure range of $4-18$ torr ($0.53-2.4$ kPa) whilst N_2 and CO_2 broadening were measured over $100-550$ torr ($13.3-73.3$ kPa) with a constant partial pressure of water vapour. Their work concentrated on bands near 7117 cm^{-1} and 7185 cm^{-1} and, as such, is applicable to this study which concentrates on the bands near 7181 cm^{-1} and 7185 cm^{-1}. Importantly, Nagali et al found that the measured values for most of the transitions were consistent with theoretical calculations based on the Robert and Bonamy model [67].

Lepere et al [68] studied the line profiles of water vapour near 7185.6 cm^{-1} at pressures below 1 torr (133 Pa). They found that the *HITRAN* 1996 database [69] line positions were very different from those found in their study. Lepere's results were more aligned with those of Toth [66]. The researchers also found that Rautian and Galatry profiles produced better results than the Voigt profile. Lepere's results agreed well with Nagali's [67] for water vapour diluted in nitrogen but were very different for pure water vapour. They also obtained satisfactory agreement with theoretical calculations of Delaye [70] using the Robert and Bonamy model.

In 1999, Nagali et al [71] reported on selected water vapour line strengths, positions and pressure-shift coefficients measured at pressures and temperatures to 65 atm (6.6 MPa) and 1800 K. The experiments were performed in a shock tube for spectral lines near 7117 cm^{-1}, 7185 cm^{-1} and 7462 cm^{-1}. They found that simulations using Toth's [66] line strengths and positions but *HITRAN's* broadening parameters gave the best agreement with experimental measurements and noted that *HITRAN* was to be updated to incorporate Toth's measurements.

Durry et al [65] measured the broadening coefficients of water vapour by nitrogen and oxygen in the wavelength region of interest to this study. They found that the ratio of nitrogen to oxygen coefficients is approximately 1.7. They also reported that measured broadening coefficients for some lines near 1392 nm were up to 20% different from those in *HITRAN* 2000 [72]. Durry's measurements for nitrogen and air broadening agreed well with theoretical calculations based on the Robert-Bonamy

[3] I found out this lesson the hard way when attempting to calibrate some laser diodes using data in *HITRAN* 1996. After spending considerable time trying to match experimental line positions with those in the database, I found that important lines were either not listed in *HITRAN* or had different parameters from those I measured.

formalism. Durry's values should be used where appropriate in this study.
Liu et al [73] provides an extensive listing of measured air broadening coefficients for water in the range $6940 - 7440$ cm^{-1}. The measured values are compared with those in *HITRAN* 2000 [72] and *HITRAN* 2004 [74]. They found large discrepancies between their measurements and *HITRAN* 2004 for the temperature exponent n for over half of the studied transitions. They also found discrepancies between measurements and *HITRAN* 2004 for 11 lines. Liu et al recommend using their results for combustion diagnostics with temperature variations between 300 K and 1000 K.
Fortunately, the 2012 release of *HITRAN* [57] is greatly extended in terms of accuracy, spectral coverage, additional absorption phenomena and validity. For instance, *HITRAN* 2012 includes 142,045 transition of H_2O isotopologue 161 compared with 37,432 transitions for the same isotopologue in *HITRAN* 2008 [57]. Both versions were used in this study with the 2012 version proving to be far superior.

2.7. Direct Detection

Direct detection TDLAS is not often used in research because the detectable SNR is usually less than that achievable using harmonic detection methods. Nevertheless, direct detection can provide good insights into TDLAS methods and is simple to implement and analyse. Direct TDLAS measures the relative transmissivity of a range of wavelengths or wavenumbers and requires scanning across the spectral lines. If the measurement steps are small enough, many points can be detected across a single line allowing the line strength and shape to be accurately measured. This makes direct absorption valuable in identifying line positions and strengths plus in calibrating diodes.The method was used in this study to calibrate laser diode wavelengths and to measure properties in a steam ejector flow.
When using direct detection, measurements must be corrected for changes in laser output power due to diode current. Also, the measurement steps must be small enough to be able to extract spectral properties. Multiple measurements can be made at each step to improve SNR but, in this case, the test gas properties must be constant during the test time. Finally, the combination of multiple measurements at each current step and small current steps mean the direct detection tests may take up to five minutes. All of these factors account for most researchers using harmonic detection methods for TDLAS.

2.8. Harmonic Detection

In 1901, Reginald Fessenden invented a signal modulation and demodulation technique called heterodyning whereby one frequency range is shifted into another range [75]. Teich [76] demonstrated that heterodyne methods could be used for coherent detection in the infrared region. Teich's work provides a good introduction to harmonic detection techniques. Figure 2.2 (adapted from [76]) shows the configuration of a generalised heterodyne receiver used by Teich. Two beams of different frequencies (ω_1 and ω_2) mix at the photo-detector to produce a signal at the difference frequency $\omega_1 - \omega_2$. When one of the beams is strong (a local oscillator (LO) beam), the sensitivity is much greater than that for

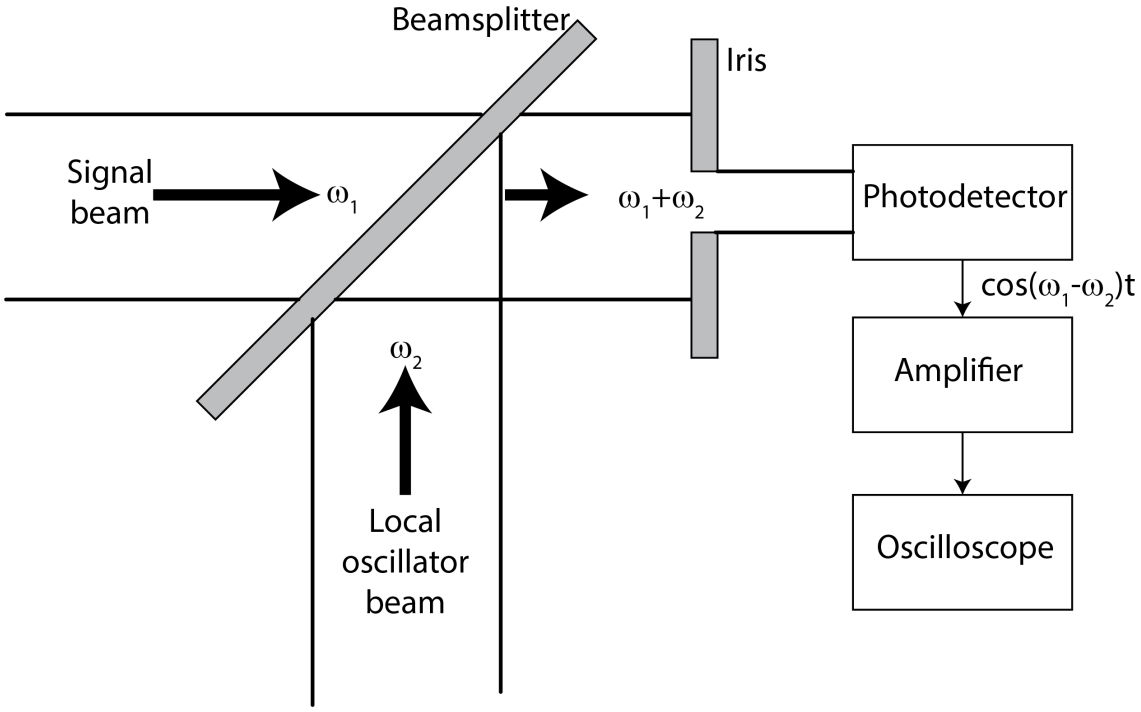

Figure 2.2.: Schematic layout of an infrared heterodyne receiver. Adapted from [76].

straight detection because of the high conversion gain between power at the input and at the difference frequency. The coherent detection process is extremely sensitive, preserves phase information and provides noiseless amplification [77]. The phase must be constant across the photo-detector surface which, in turn, requires careful alignment between the LO and signal beams. Let's now calculate the SNR at the detector output [76]. Consider two parallel electromagnetic waves of frequencies ν_1 and ν_2 impinging on the photo-detector as shown in figure 2.2. The total electric field vector $\vec{E_t}$ is given by:

$$\vec{E_t} = E_1 \cos \nu_1 t + E_2 \cos \nu_2 t \tag{2.7}$$

where E_1 and E_2 are the amplitudes of the incident waves. Assuming the two waves have the same polarisation, the response of the detector to the two incident waves r consists of a constant component r_{DC} and an intermediate frequency (IF) component r_{IF}:

$$r = r_{DC} + r_{IF} \tag{2.8}$$

$$= \left[1 + \frac{2E_1E_2 \cos\left(\nu_1 - \nu_2\right) t}{E_1^2 + E_2^2}\right] r_{DC} \tag{2.9}$$

For a strong LO beam $E_2 \gg E_1$ giving:

$$r_{IF} = 2\frac{E_1}{E_2} r_{DC} \cos(\nu_1 - \nu_2)t \tag{2.10}$$

The mean-square photo-detector response is:

$$\left\langle r_{IF}^2 \right\rangle = 2\frac{P_1}{P_2} r_{DC}^2 \tag{2.11}$$

where P_1 and P_2 are the radiation powers in the signal and LO beams respectively. The DC component of the photodiode response is primarily due to the LO beam power so:

$$r_{DC} = \frac{\eta e}{h\nu_1} P_2 \tag{2.12}$$

where η is the quantum efficiency of the photodiode, e is the elementary charge, h is Planck's constant and ν_1 is the radiation frequency. The mean-square shot noise in an ideal reverse-biased photodiode is:

$$\left\langle r_n^2 \right\rangle = 2er_{DC}\Delta f \tag{2.13}$$

where Δf is the bandwidth of the photodiode. The SNR is:

$$SNR = \frac{\left\langle r_{IF}^2 \right\rangle}{\left\langle r_n^2 \right\rangle} \tag{2.14}$$

$$= \frac{\eta P_1}{h\nu_1 \Delta f} \tag{2.15}$$

The minimum detectable power P_s^{min} is defined as the signal beam radiation necessary to achieve a unity SNR: [76]

$$P_s^{min} = \frac{h\nu_1 \Delta f}{\eta} \tag{2.16}$$

Assuming that $\eta = 1$ and $\nu_1 = 7181$ cm^{-1}, the minimum detectable power for a 1 Hz bandwidth is 1.4×10^{-19} W. An amplifier bandwidth of 100 kHz increases the minimum detectable power to 1.4×10^{-14} W. As may be seen from this example, heterodyne techniques can extract weak signals from noisy backgrounds. When using tunable diode lasers, the laser wavelength is sinusoidally modulated while the mean value of the wavelength is slowly ramped over the spectral line of interest. The sinusoidal modulation is used as the LO in this case.

Hinkley [22] used a $Pb_{0.88}Sn_{0.12}Te$ diode laser at 10.6 μm to measure the absorption spectrum of SF_6 at 0.1 Torr pressure. The 50 kHz line width of the laser was tunable across almost 7 GHz. Hinkley used heterodyne techniques with a CO_2 gas laser to produce a frequency scan with 1 GHz of a spectral line. In 1971, Hinkley and Kelley [8] extended their work to atmospheric pollution measurements using diode lasers as local oscillators. They stated that the signal (S) divided by the local oscillator generated noise (N) is given by:

$$\frac{S}{N} = \frac{1}{h\nu}\left(\frac{\partial P_s}{\partial \nu}\right)(B\tau)^{0.5} \tag{2.17}$$

where $h\nu$ is the photon energy, $\frac{\partial P_s}{\partial \nu}$ is the received signal power per unit frequency range in a single

spatial mode, B is the intermediate frequency (IF) bandwidth of the detection system, and τ is the post-detection integration time.

Ideally, the detected harmonic should produce a derivative of the signal shape function [41]; however, finite modulation amplitudes cause line distortions that become larger as the modulation amplitude increases. Arndt [41] used Fourier expansions to derive functions for the first and second harmonic amplitudes of Lorentzian line shapes modulated sinusoidally. While Arndt's work was directed toward detecting wide line nuclear magnetic resonance signals, the results also apply to wavelength modulated TDLAS signals.

Reid et al [10] initially developed the first and second harmonic detection methods that dramatically improved signal-to-noise (SNR) ratios above those possible using direct absorption methods. The general approach comprises modulating the laser wavelength, transmitting the laser beam through a gas sample and homodyne detecting the photo-current at the original modulation or some associated frequency [78]. Noise is reduced by shifting detection to higher frequencies where laser source noise is negligible and by removing the baseline slope found in direct absorption. Sensitivities of $10^{-4} - 10^{-5}$ fractional absorption can be achieved with wavelength modulation at kilohertz frequencies [78].

Cassidy et al [11] extended the analysis to include two-frequency modulation which aimed to improve the sensitivity of TDLAS systems. The second modulation was selected to minimise the effect of optical interference fringes[4] due to etalons that dominated high-sensitivity absorption measurements [11]. They showed that two-tone modulation could minimise the harmonic signal from optical interference fringes.

Silver [78] explored the relationships among frequency modulation techniques to provide guidelines for the best detection method for a given circumstance. He stated the second harmonic detection was probably employed because the noise is relatively low, the signal peaks at the absorption centre frequency, baselines are usually flat and most commercial lock-in amplifiers have a $2f$ detection capability. This last point is important because earlier TDLAS systems relied on analogue signal processing such as that available via lock-in amplifiers. The maximum WMS signal was obtained by adjusting the lock-in phase angle.

2.8.1. Wavelength Modulation Spectroscopy (WMS)

Kluczynski et al [79] provide an excellent overview of the theory behind WMS as at the year 2001. Their theoretical description includes the effect of the FM/IM phase shift, the non-linear IM associated with the sinusoidal modulation, and wavelength dependent transmission. Li et al [80] extended the theory to large modulation depth measurements in high pressure gases to account for real diode laser characteristics of FM/IM phase shift and non-linear IM. They found that, for optically thin measurements with characterised lasers, normalisation of the $2f$ signal with the $1f$ signal could remove the need for calibration [80].

In 2009, Rieker et al [81] presented an implementation of calibration-free WMS with second harmonic detection (WMS-$2f$) for measurements of gas temperature and concentration in harsh environments. Their study includes a table of potential sources of uncertainty in calibration-free WMS along with

[4] also known as Fabry-Perot fringes

Table 2.1.: Estimated uncertainty in calibration-free WMS measurements in a scramjet (Adapted from [82])

Source of Uncertainty	Estimated Uncertainty in T_{Meas}	Estimated Uncertainty in $P_{H_2O,Meas}$	Comment
Laser tuning characteristics	$\pm 4.2\%$	$\pm 2.7\%$	Estimated from laboratory validation in a controlled furnace and a uniform flame
Simulation and experiment wavelength matching	Negligible	Negligible	Accounted for by scanning absorption line peak and matching experiment/simulation at peak wavelength
Background absorption	Negligible	Negligible	Steady N_2 purge + background subtraction of residual
Etalon effects	Negligible	Negligible	Eliminated by angle-polished fibres and three wedges on all windows
WMS model	Negligible	Negligible	Model was properly matched to the experiment
Pressure deviation between simulation and experiment	$\pm 0.35\%$	$\pm 1.75\%$	Estimated from simulations based on actual measured pressure variation and CFD-predicted pressure non-uniformity
Optical depth and concentration deviation between simulation and experiment	$\pm 0.06\%$	$\pm 0.9\%$	Estimated from simulations based on CFD-predicted concentration non-uniformity
Total	$\pm 4.6\%$	$\pm 5.4\%$	

estimated uncertainties of measurements in a scramjet combustor (see table 2.1). Figure 2.3 shows how the calculated properties of the second-harmonic ($2f$) vary with modulation depth for Lorentzian, Gaussian and Voigt line shapes. The insert shows the variation in a typical $2f$ line shape as frequency is tuned across the absorption line. The values P and R are defined in the insert. They are plotted as a function of m for all three line shapes. P_{max} is normalised to unity for each line shape in the upper curves and occurs at $m = 2.2$ in each case and where m is defined as:

$$m = \frac{a}{\Delta\nu} \tag{2.18}$$

where a is the half-amplitude of the sinusoidal time variation of the diode frequency and $\Delta\nu$ is the HWHM of the absorption line. The $2f$ line shape has small systematic discrepancies at small and large values of modulation amplitude. At large modulation amplitudes, the modulated output becomes visibly distorted when observed directly on an oscilloscope. Also, the wavelength modulation can encroach on nearby weak lines and distort the $2f$ line shape [10]. The minimum absorption detectable by TDLAS using harmonic techniques is often limited by interference fringes generated by scattered light [11].

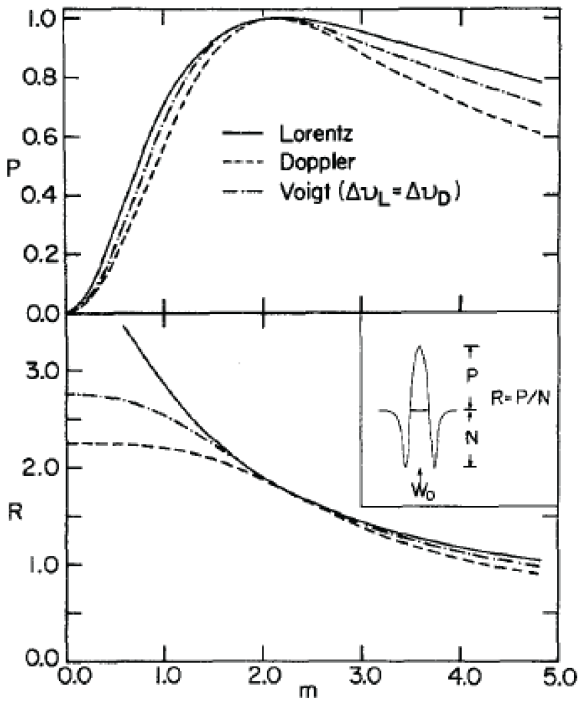

Figure 2.3.: Variation of $2f$ lineshapes with modulation index [10]

Not all near-IR diode lasers can be used with $2f$ techniques for sensitive detection of atmospheric pressure-broadened absorptions. Diodes should have a current tuning rate of approximately 0.1 cm^{-1}mA^{-1} and a temperature tuning rate of 0.4 cm^{-1}K^{-1} to provide good sensitivity. At lower tuning rates (ie closer to zero), the laser must be modulated over a considerable portion of its light versus current curve to detect an atmospheric broadened line [83]. Distributed Feedback (DFB) laser diodes, such as those used in this study, are susceptible to optical feedback and neutral density filters should be placed between optical elements to reduce the modulation noise. The limiting noise source is modulation noise caused by optical feedback to the laser diode and fringes from reflections off surfaces [83].

2.9. Applications of TDLAS

Let's now review some specific applications of TDLAS. Space limitations restrict the review to examples that highlight important aspects of system design relevant to this thesis including combustion, shock tube, expansion tunnel and scramjet instantiations.

2.9.1. Combustion

TDLAS has been widely applied to combustion of NO [84, 85, 86] and hydrocarbons [87, 88, 89]. Water vapour is one of the primary hydrocarbon combustion products and has a rich absorption spectrum throughout the infrared region [89]. This section reviews selected applications of TDLAS to combustion measurements. Flat-flame burners provide researchers with steady reproducible flames

with which they can develop TDLAS techniques in the laboratory. These burners are also used to verify the spectroscopic data in *HITRAN*, *HITEMP* and other databases.

In 1993, Arroyo and Hanson [90] applied laser spectroscopy techniques to detecting water vapour in a closed cell and above a methane-air flat flame burner. The system used a distributed feedback (DFB) InGaAsP diode laser emitting at approximately 1380 nm. The diode laser was tuned in wavelength using current modulation to achieve a 1 cm^{-1} tuning at 80 Hz repetition rate. Arroyo and Hanson directly measured absorptions to determine water vapour concentration and temperature as well as collision-broadening line shape. They used this method because the water vapour spectrum has doublets, triplets and other types of overlapping lines. The resultant mathematical transform relating the actual line shape to the wave form observed is more complicated than that for clear single lines.

Arroyo and Hanson reported that the strongest absorption lines for water vapour occur between 1350 and 1410 nm at room temperature and at 1340-1460 nm at 1500 K. They also reported that the line intensities were between 100 and 1000 times stronger than those at 820 nm and 1300 nm. They concluded that water vapour measurements in high temperature flows should be taken at wavelengths of 1340-1460 nm if possible [90].

One issue raised by Arroyo and Hanson was that optical communications laser diodes were available mostly at 1280-1340 nm and 1520-1580 nm ranges. They reported that single-mode DFB lasers have narrower wavelength dispersion than multi-mode (Fabry-Perot) lasers. Their measurements were taken at 1385 nm using a single-mode DFB laser. They used data from the 1992 *HITRAN* [91] database to obtain the line strengths and positions plus the lower energy of transition for water vapour at room temperature to derive the line strength at another temperature T.

Zhou et al [52] targeted a pair of water vapour transitions in the 1.8 μm region for water concentration and temperature measurement in flames. In 2008, Farooq et al [63] analysed water vapour absorption transitions in the $2.5 - 3.0$ μm region in a flat-flame burner. Cai et al [89] designed a sensor that used a single near infrared (NIR) diode laser operating at 1411 nm with second-harmonic detection wavelength modulated spectroscopy (WMS-$2f$) to measure the gas temperature and H_2O concentration in a heated cell containing H_2O-air mixtures over the expected temperature range of 500 to 1000 K [89]. Cai stated that the minimum detectable absorbance was 10^{-4} and the SNR was greater than 10.

Farooq et al [63] reported on in-situ combustion measurements of water vapour concentration and gas temperature using TDLAS near 2.5 μm. These bands have stronger absorption line strength compared to the overtone ($2\nu_1$ and $2\nu_2$) and combinational ($\nu_1 + \nu_2$) vibrational bands. Farooq states that the minimum detectable absorbance is 10^{-3} which is ten times greater than that proposed by Cai. Bolshov et al [92] measured temperature and water vapour concentrations in heated gases. The technique is based on the detection of the spectra of H_2O absorption lines with different energies of low levels. The following absorption lines of H_2O were used:

- 7189.344 cm^{-1} ($E_{low} = 142$ cm^{-1}),
- 7189.541 cm^{-1} ($E_{low} = 1255$ cm^{-1}),
- 7189.715 cm^{-1} ($E_{low} = 2005$ cm^{-1}).

Spectra were recorded using fast frequency scanning of a single DFB laser. A unique differential

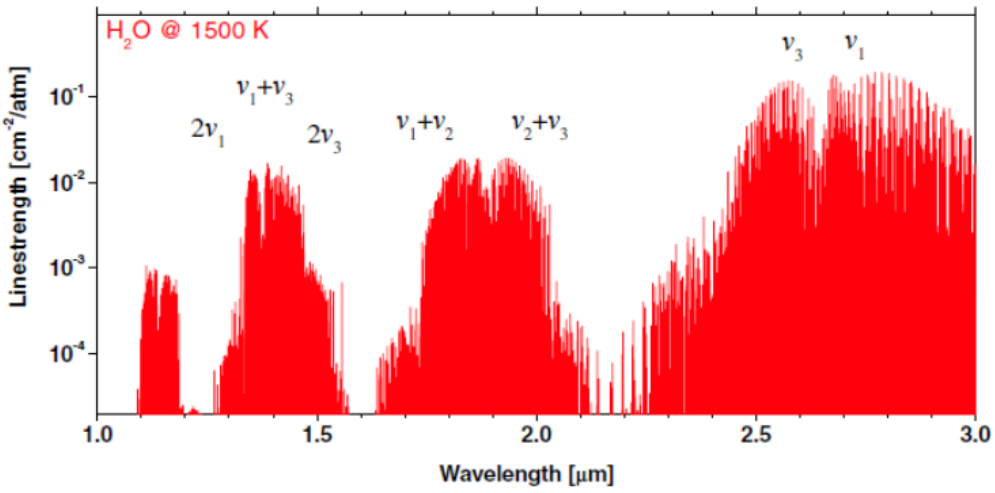

Figure 2.4.: Absorption line strengths of H_2O at 1500 K [63]

scheme was developed for recording the absorption spectra and an optimal technique was used for fitting the experimental spectra. The validated TDLAS technique was applied for detection of temperature and H_2O concentration in the post-combustion zone of a supersonic (Mach 2.0) air-fuel flow that used hydrogen and ethylene as the fuel. The combustion process was ignited and sustained by a pulsed electric discharge. The estimated precision of the temperature measurement was ± 40 K. The high signal-to-noise ratio enabled the reconstruction of the temporal behaviour of temperature with a resolution of similar to 1 ms.
In 2009, the Stanford team probed combustion flows at multiple wavelengths using calibration-free TDLAS [81]. The detected signals were fed into two lock-in amplifiers (one at the $1f$ and the other at $2f$) where the first and second harmonic signals were extracted. The system multiplexed laser signals before feeding them through a single mode optical fibre to the test area. The output from the test area was fed into a wavelength demultiplexer to extract the different wavelength signals. The demultiplexer used a reflection diffraction grating to direct the various wavelengths to their appropriate detectors.

2.9.1.1. Mass flux sensor

Chang et al [93] developed a mass flux sensor based on diode laser absorption to monitor water vapour absorption in air and combustion-driven facilities near 1.4 μm. The sensor achieved large signal-to-noise ratios via WMS-$2f$ for temperature measurement. WMS-$1f$ was used for velocity sensing. The system measured temperatures with 1% uncertainty and velocities between 2.5 ms^{-1} and 18 ms^{-1} with uncertainty of ± 0.5 ms^{-1}. Chang's paper highlights the importance of independently validating spectral data such as that presented in *HITRAN* [57].

2.9.2. Shock Tubes

In 1977, Hanson [23] applied TDLAS to transient, high temperature gases heated by a shock wave in a CO-H_2-Ar mixture. He calculated the post-shock pressure and temperature from measurements of the shock speed and initial shock tube conditions then compared the measured and calculated line

shape to derive the collision-broadening coefficient for CO-Ar. In 1992, Philippe and Hanson [94] probed high velocity and high temperature oxygen flows generated behind incident shock waves in a shock tube.

In 1999, Nagali, Hanson and other researchers [71] probed water vapour spectral absorption near 7117 cm^{-1}, 7185 cm^{-1} and 7462 cm^{-1} at pressures to 65 atm and temperatures to 1800 K in shock-heated mixtures of H_2O in N_2 and Ar with a diode laser source. Besides determining the accuracy of spectroscopic databases for pressures and temperatures typical of combustors, their experiments yielded temperature-dependent pressure-shift coefficients for H_2O transitions. Two TDLAS systems were used: one in the incident shock region and the other in the reflected shock region. The incident system probed at 7117 cm^{-1} whilst the other probed all three spectral lines. The beam in the incident region was directed through a 2 GHz free-spectral-range solid etalon before being incident on a photodiode. The etalon signal was used to convert all signals from the time to the frequency domain. The results were simulated using *HITRAN* and *HITEMP* 1992 spectroscopic databases [91]. The authors found that the simulations were almost identical at 1000 K but had differences of the order of 10% near line centres at 2000 K. The differences were larger in the wings of the vibrational band corresponding to absorption that is due to higher rotational levels.

Across the temperature range $600 - 1800$ K, Nagali et al found that calculations based on *HITEMP* and *HITRAN* were within 25% of the measured values with *HITEMP* being marginally better than *HITRAN*. They also compared the experimental results with those reported by Toth [66] finding better correlation with Toth's data with agreement to within 15% of the measured values. They attributed the improvement to the more accurate line positions and strengths reported by Toth.

2.9.3. Scramjets

TDLAS system have been deployed on scramjets in both ground and flight environments. Water vapour is present as a primary combustion product in scramjets. Its abundance, coupled with the large line strengths for the vibrational bands in the near infrared makes it suitable for absorption spectroscopy studies in scramjet isolators, combustors and exhausts. The flow in a scramjet isolator or combustor is inhomogeneous and highly reactive due to the presence of fuel, air, supersonic flows and high temperatures. The absorbance is difficult to calculate because the line shape and strength vary with temperature, pressure and species concentrations. In this section, we review four implementations that have been published.

In 2005, Liu et al [54] measured gas temperature and water concentration at the exit of a model scramjet combustor. Their system probed three absorption lines in the $1340 - 1470$ nm region and consisted of multiplexed, fibre-coupled, near-infrared DFB lasers. They used ratio thermometry to measure temperature at a 4 kHz rate. Figure 2.5 is a schematic layout of the TDLAS system used by Liu et al. To produce the test conditions, hot dry air at 500 K and 150 psia was fed into a vitiator where it was heated to 1200 K at 225 psia. The vitiator output was accelerated to Mach 2.5 using a Laval nozzle before being ingested into the scramjet combustor where it combusted with JP-7 fuel. The exhaust was probed using the TDLAS system. Integrated direct-absorbance area ratios were used to infer temperature and water vapour concentration at various engine conditions and at different vertical

path locations across the test region. At the Australian National University (ANU), Griffiths et al [13]

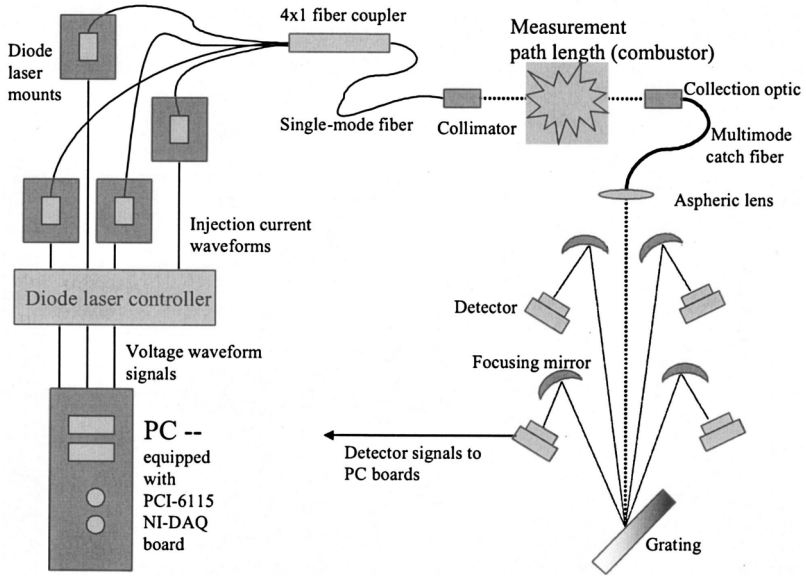

Figure 2.5.: Schematic of TDLAS system used by Liu et al [54]

constructed a TDLAS system for time-resolved temperature and water vapour concentration measurements in a scramjet combustor. Their system probed two absorption lines near 1390 nm at rates up to 20 kHz using two time-multiplexed lasers. Griffiths and Houwing [1, 13] probed two wavelengths at 1392.5335 nm $(7181.15578\,\mathrm{cm}^{-1})$ and 1392.8058 nm $(7179.7519\,\mathrm{cm}^{-1})$. Figure 2.6 shows the layout of the system. Two DFB laser diodes are modulated with their outputs passing through optical isolators into optical fibres. The enclosure for the laser diodes, isolators and collimating optics is purged with nitrogen to avoid absorption of the signal by atmospheric water vapour. The outputs from the lasers were time-multiplexed and were coupled together in the 50/50 fused-fibre coupler. One signal then passed through an interferometer to provide a time resolved signal that is observed with a linear detector. The test beam is compared with a reference beam using a log-ratio detector with the output signal recorded on a data acquisition system. As shown in figure 2.7, the strength of Line 1 decreases as flow temperature increase from room temperature to 2000 K. The strength of the second line increases from room temperature to approximately 900 K then gradually decreases as temperature increases further. The two lines have equal strength at approximately 1550 K. Below this crossing temperature, Line 1 is stronger than Line 2. At room temperature, Line 1 is 75 times stronger than Line 2. Above the crossing temperature, the strengths are approximately equal with Line 2 relatively stronger than Line 1 by up to 20%. Also in Australia, O'Byrne and Wittig [15] measured the Mach number and angle of attack at the inlet of a scramjet using tunable diode laser absorption spectroscopy of oxygen. They were able to accurately determine the free stream velocity in the inlet. The Mach number was measured to within ± 0.02 of the calculated value and the angle of attack to an uncertainty of $\pm 0.25^{\circ}$ at Mach 8 and 2° angle of attack.

At the United States Air Force Research Laboratory (AFRL), Lindstrom et al [16, 17] and Brown et al [14, 95] used 16 line-of sight (LOS) beams arranged to scan across the isolator and combustor

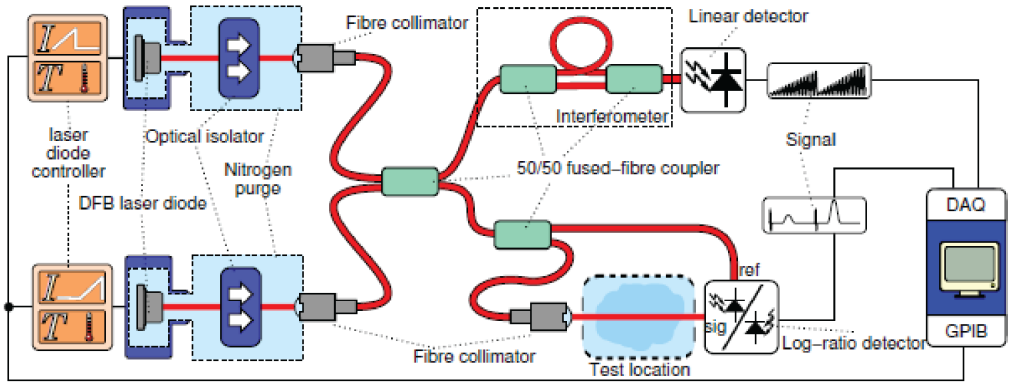

Figure 2.6.: Layout of ANU TDLAS system [1]

of a scramjet. Three DFB lasers were tuned to different wavelength regions and time multiplexed into a single period lasting 1 ms. The voltage of each diode was ramped from 0.5 V to more than 2.0 V in its multiplexing time. The outputs were combined into a single beam which was split by a 10/90 splitter with the weaker beam being used to provide a reference signal and frequency spectrum. The stronger beam was then split 50/50 with each of those outputs being split into eight beams. The diodes had an average power of 20 mW. The optical train attenuated the signal by -18.5 dB resulting in each LOS beam having an average power of 280 μW. Even with this low power output, the system had a good signal to noise ratio. The system also used nitrogen to purge enclosures that housed the optics to minimise unwanted absorption by atmospheric water vapour. Figure 2.8 shows the optical layout of the TDLAS system developed by Lindstrom et al as well as the time-multiplexed signal. The system required a circuit bandwidth of greater than 200 kHz to take measurements in approximately 5 μs as was required to scan across the absorption peak. The data acquisition system recorded each beam at 2.5 million samples per second (Msps) for a total recording rate of 90 MBs^{-1}. This high data rate limited the test protocol to having 0.2 s of data capture followed by 5 s of processing and data transfer before the next data capture sequence could start. Brown et al [14] examined the accuracy and precision of measurements, and discussed the propagation of uncertainties from the measured signals to the desired values of temperature, number density and pressure. The researchers used single mode, fibre-coupled DFB lasers to measure the line intensities of water vapour in the spectral regions $7184.2 - 7186.4$ cm^{-1}, $7159.5 - 7161.5$ cm^{-1} and $7179.5 - 7181.8$ cm^{-1}. They used the line intensities to determine the temperature, water concentration and static pressure in the isolator. The line intensities at different temperatures were derived from the line parameters in the *HITRAN* 2004 database [74]. The authors did not perform self-calibration of the system but relied on the work of earlier researchers to validate that the systematic errors in the *HITRAN* parameters were less than 5%. Using these intensities, the researchers measured the absorption of the laser radiation that passed through the isolator.

The path averaged static temperature was determined by measuring multiple absorption lines of the same molecule. The frequency integrated absorption was normalised by the cross-section and degeneracy for each transition then plotted against the initial state energy divided by Boltzmann's constant.

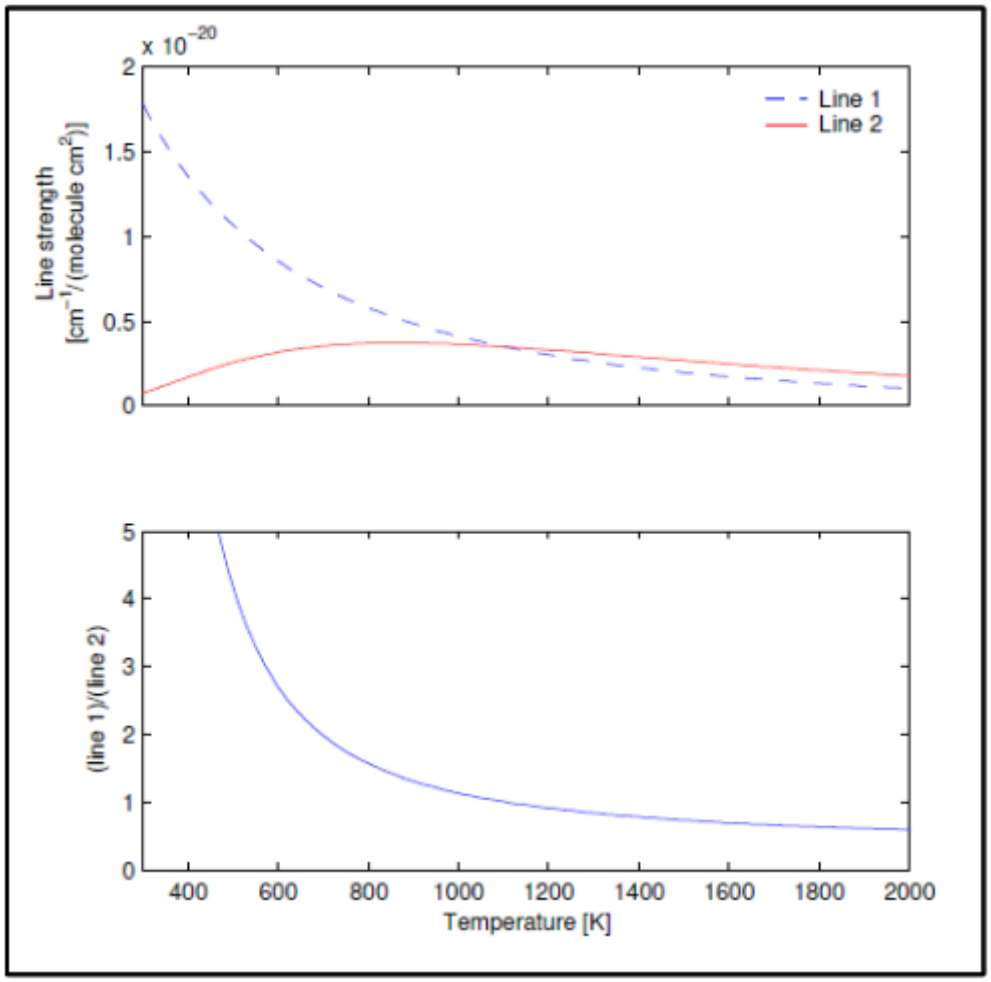

Figure 2.7.: Line strength (top) and line strength ratio for water vapour [1]

The flow temperature was derived from the curve slope. Figure 2.9 is a Boltzmann plot for a Mach 2 flow without any shock waves. The plot is linear because there were no disturbances in the flow. The flow static temperature was measured as 654 ± 1.2 K. The static temperature was then used to calculate the HWHM $(\Delta\nu_D)$ of a Gaussian line shape at that temperature. Once this width was known, the collisional broadening was determined from the Voigt fit. Static pressure was calculated from the collisional broadening of the absorption line. This calculation assumed that the line shape was represented by a single Voigt peak. If the flow has shock waves, boundary layer effects may impact on the accuracy of the pressure measurement.The gas mixture in the isolator comprised water vapour, nitrogen, oxygen and carbon dioxide. Thus, the collisional broadening depended on each of these molecules and their quantum states. The authors discuss a method of calculating species concentrations considering the molar concentrations of each species, the gas temperature, broadening parameters for each species and temperature coefficients for each species. The AFRL scramjet test rig was also used to detect combustor instabilities [82, 96]. The researchers found that fluctuations in temperature non-uniformity preceded back pressure-induced unstarts in the isolator.

In parallel with the AFRL test rig experiments AFRL and Arnold Engineering Development researchers developed a TDLAS system for flight tests [97, 98, 99, 100]. The Hypersonic International

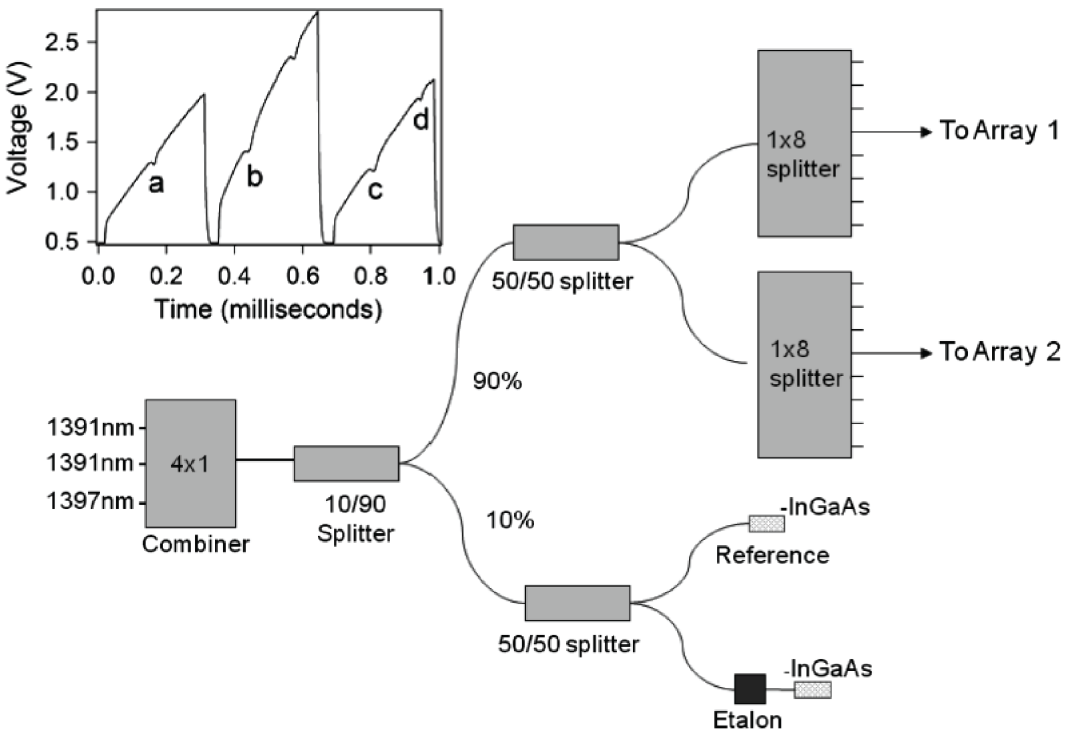

Figure 2.8.: Optical layout of multiplexed TDLAS system and time-multiplexed signal (inset). Refer to Lindstrom et al [16] for details on signals.

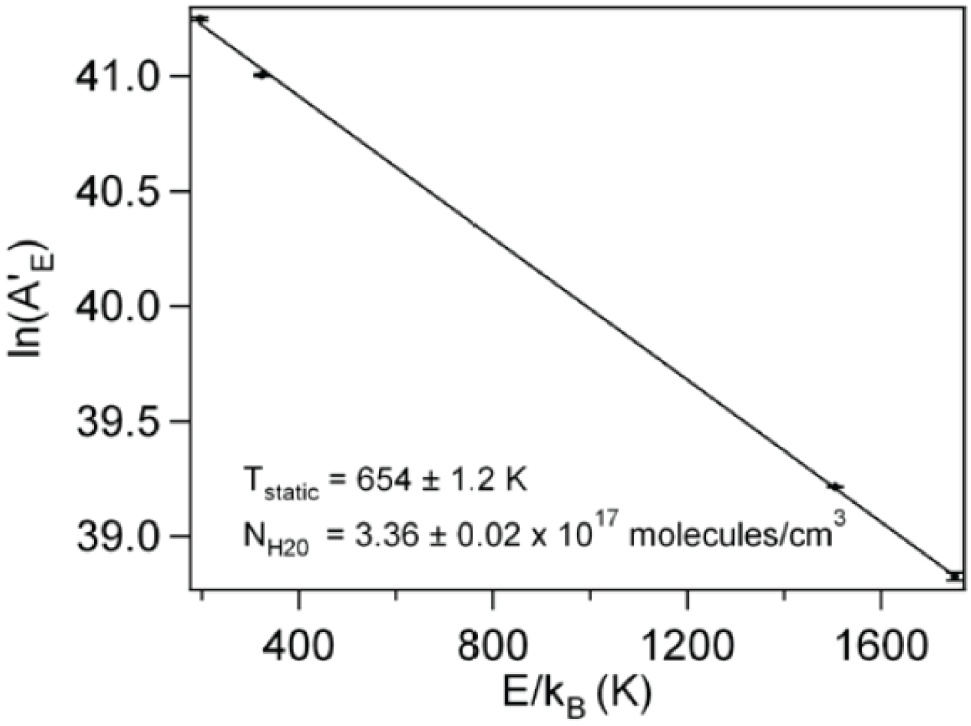

Figure 2.9.: Boltzmann plot using LOS average data from a single beam path [14]

Flight Research Experiment (HIFiRE) program is a collaborative international project that extends hypersonic research through flight experimentation. The primary objective of HIFiRE Flight 2 was to evaluate hydrocarbon-fuelled scramjet performance over the transition from dual-mode to scramjet operation near Mach 5.5 up to full scramjet operation at Mach 8 [98].
A mixture of 64% ethylene and 36% methane was used to fuel the scramjet. The exhaust static pressure and temperature were expected to be $2.0 - 3.0$ atm and $1560 - 2531$ K respectively and the exhaust gas composition for ideal stoichiometric combustion was anticipated to be 72.2% N_2, 14.8% O_2, 12.0% CO_2 and 0.9% Ar.
Sappey et al [98] state that the exhaust gases for a scramjet combustor contain roughly 10% water concentration at temperatures from 1000 K to 2500 K. They also state that a sensor must be able to measure temperature and concentration with sensitivity near 20 K and 0.5% respectively. Readers are directed to Sappey et al [98] for details of the TDLAS design, principles of operation and expected performance.
In 2014, Schultz et al reported on testing a scramjet with hydrocarbons in a reflected shock tube [19, 101, 102]. Both direct and WMS absorption were used in three conditions: an H_2O-seeded non-combustion case and H_2-Air combustion at fuel-air equivalence ratios of 0.17 and 0.46. The researchers found good agreement between TDLAS measurements and CFD predictions for temperature and velocity but there were substantial differences in water vapour column density measurements.
In 2011, Li et al [103] measured temperature, water vapour concentration and velocity simultaneously in the inlet, combustor and exhaust of a scramjet. The system was similar to that developed by Liu et al [53]; however, Li's team used direct absorption methods in lieu of WMS-2f because a satisfactory SNR was obtained and direct absorption was simpler to implement and interpret. Readers are directed to the paper [103] for details of the scramjet. At the inlet, the average temperature was 798 K, the average velocity was 1335 ms^{-1}, the average partial pressure of water vapour was 0.139 atm and the mole fraction of water was 23%. These values were within $2 - 3\%$ of the designed values. The water vapour concentration was high due to the method used to prepare the intake flow for the scramjet. The scramjet overall combustion efficiency was calculated to be between 76.2% and 81.5% depending on the method used to calculate the efficiency. Heat loss through the wall was approximately 15%. The paper lists measurement uncertainties as being $2.7-3.8\%$ for temperature, $4.7-9.8\%$ for water vapour partial pressure and $2.1 - 8.7\%$ for velocity with the largest uncertainties being in the combustor measurements.

2.10. Impact on Experiments

The experimental TDLAS design was intended to reflect the state of art from this literature review. The ultimate goal was to develop a system to measure products of combustion in a scramjet exhaust operated in X3 expansion tunnel. Ideally, a system similar to that developed at AFRL and reported by Lindstrom et al [16, 17] and Brown et al [14, 95] would be developed. However, financial restrictions meant that this was not possible. Instead, a system similar to that developed at ANU by Griffiths and Houwing [13, 1] was considered to be achievable.

After reviewing the equipment available commercially, the system was based on using a Thorlabs PRO8000 laser controller with three control modules fitted so that three laser diodes could be operated simultaneously. The controller provided precise temperature and current control of the laser diodes. Spectroscopic laser diodes were selected to probe water vapour near 1392 nm.
Based on the literature review, laser diodes were investigated to probe atomic oxygen. More than ten laser diode manufacturers were approached for price and availability of diodes to probe the atomic oxygen triplet centred on 777.4 nm. None of those approached could guarantee their diodes would operate even though some diode would cost over $20,000. Based on this the diodes were not procured. Six very low cost ($5 each) diodes were bought on an opportunity basis to probe the oxygen triplet but were found to operate at a minimum wavelength 0.2 nm above the desired wavelength when the TEC was operated at its temperature limit.
Given the lack of suitable laser diodes operating at 777 nm, an alternative solution was sought to meet the requirement of probing atomic oxygen. The author visited The University of Stuttgart to use their New Focus laser diode to probe atomic oxygen lines near 844.6 nm. Ideally, the experiments would based on laboratory tests using an Evenson tube to generate a weak oxygen plasma before progressing to using the system in an arc jet plasma. Unfortunately, the visit duration was limited to four weeks which were consumed in developing the experimental setup and techniques for the Evenson cavity.
The literature provided guidance when writing Python software to control multiple devices including the laser controller, TEC mounts, power meter, fuel solenoids, oscilloscopes and NI databoxes. The diverse range of equipment used precluded adaptation of existing NI LabVIEW software to control the experiments. Software was also written based on the surveyed literature to extract HITRAN data from the database, model spectra and analytically model the expansion tunnel, fuel system and scramjet. A lock-in amplifier and advanced signal processing techniques were implemented into custom-designed Python software based on information surveyed in the literature.
In short, the surveyed literature was essential to this research especially because of the broad scope of applications and methods.

2.11. Summary

TDLAS systems have improved enormously in the 45 years since the first system was trialled by Hinkley [22]. Advances in electronics, optics, computing algorithms, spectral databases and curve fitting have all impacted TDLAS.
This chapter has reviewed the advances in TDLAS theory and application related to the scope of this thesis. Developments in line shapes, harmonic detection, curve fitting, wavelength selection and wavelength modulation spectroscopy were reviewed. Applications of TDLAS in the areas of combustion, shock tube flows and scramjets were summarised. The literature review was an essential element of this research especially because of the broad scope of applications and methods.

3. Theoretical Background

This chapter provides a summary of the theory behind TDLAS. Absorption spectroscopy and line profiles are initially discussed before laser diode injection current modulation is explained. The theory is expanded to encompass the form of the detected signal and Fourier series analysis of signals [79].

3.1. Absorption of radiation

TDLAS differs fundamentally from emission spectroscopy in that the latter relies on particles in the flow being initially in excited states and relaxing to lower states. Instead, in TDLAS particles are excited from lower to higher states by the laser radiation.

3.1.1. Planck Distribution

The spectral energy density (per unit frequency) of radiation in a gas at thermodynamic equilibrium is given by Planck's blackbody distribution:

$$\rho\left(\nu, T\right) = \frac{8\pi h\nu^3}{c^3} \frac{1}{\exp^{\frac{h\nu}{kT}} - 1} \tag{3.1}$$

where h is Planck's constant, ν is the frequency of the radiation, c is the speed of light, k is Boltzmann's constant and T is the absolute temperature of the gas.[1] Thermodynamic equilibrium means that the radiating gas is enclosed in a blackbody cavity and is neither gaining nor losing net energy. This distribution is continuous as shown in figure 3.1.
The photon energy for radiation at frequency ν is:

$$E = h\nu \tag{3.2}$$

Since the spectral energy density of blackbody radiation is continuous, the energy of the sources of the radiation must also vary continuously. The predominant sources of blackbody radiation are molecular vibrations or rotations rather than electronic transitions within atoms. Planck's blackbody distribution was originally derived using thermodynamics and applies where a radiating mass of gas is optically thick at all frequencies. In this case, collisional process are more important than radiative ones and an excited state has a higher probability of de-excitation by collision than by spontaneous radiation [28].

[1] The units of ρ are $\mathrm{Jm^{-3}Hz^{-1}}$.

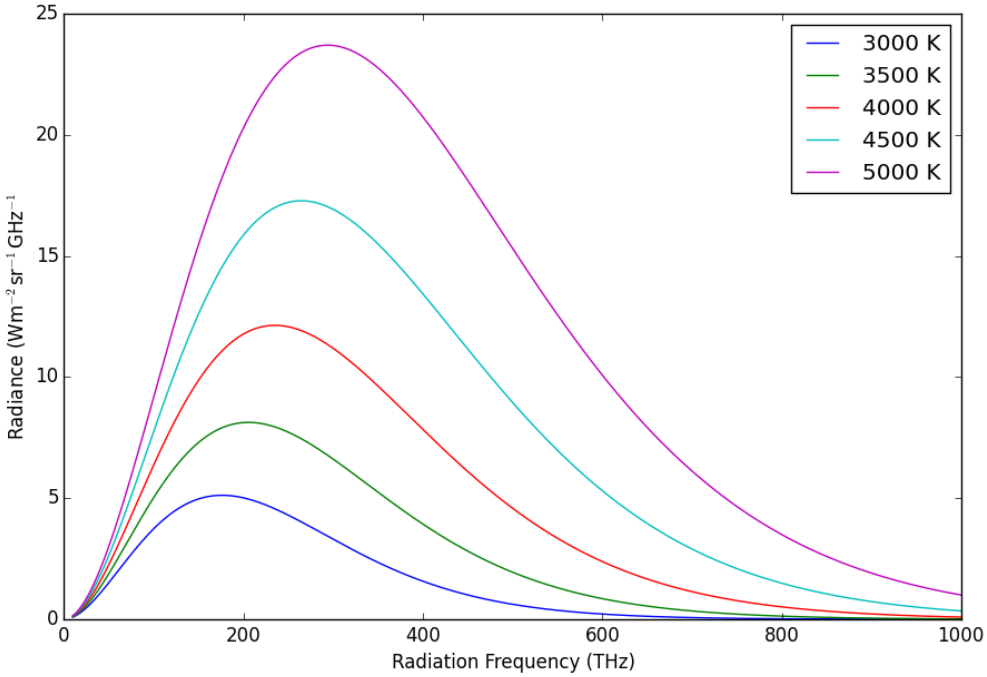

Figure 3.1.: Spectral distribution of blackbody radiation (Adapted from [28])

3.1.2. Boltzmann Population Distribution

The Boltzmann equation gives the ratio of the numbers of atoms occupying two energy states E_1 and E_2 for a system in local thermodynamic equilibrium (LTE) at temperature T:

$$\frac{n_1}{n_2} = \frac{g_1}{g_2} \exp^{\frac{E_1 - E_2}{kT}} \tag{3.3}$$

where n is the number density in atoms per m^3 and g is the statistical weight or degeneracy of a level. LTE differs from complete thermodynamic equilibrium in that the states are populated and depopulated predominantly by collisions, not radiation. In LTE, the allowable energy states are discrete or quantised and the emitted radiation is in the form of a line spectrum.

3.1.3. Einstein Probability Coefficients

In 1917, Einstein [104] used thermodynamic considerations to derive the relationship between absorption and emission probabilities for a two-level atom in a blackbody enclosure. The relationship is reproduced here for completeness.

Consider a two-level atom as shown in figure 3.2 with upper state E_2 and lower state E_1 and population densities in each state of n_2 and n_1 respectively. That atom is in the presence of radiation at frequency ν_{12} of density ρ. The probability per unit time of an atom in the higher level transitioning spontaneously to the lower level is A_{21}. This transition occurs by emission of a photon of energy $E_{21} = h\nu_{21}$. An atom may transition from the lower to the upper level by absorbing a photon of

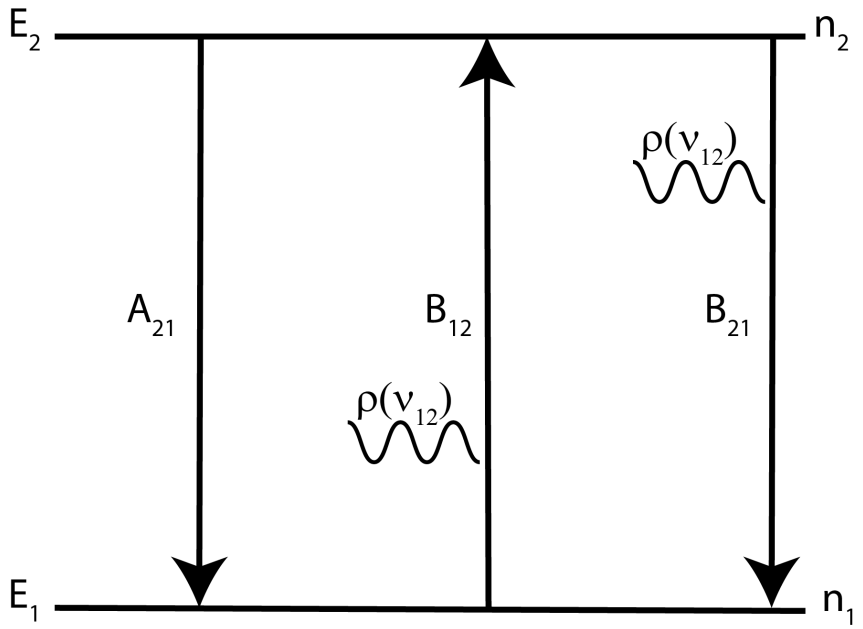

Figure 3.2.: Energy levels for a two-level atom in a blackbody enclosure (Adapted from [28])

energy $E_{12} = h\nu_{12}$, equal to E_{21} making $\nu_{21} = \nu_{12}$. This probability per unit time is $B_{12}\rho$. A photon interaction may also stimulate emission of another photon with the same phase and propagation direction as the interacting photon with a probability per unit time of $B_{21}\rho$.
The number of transitions per second for spontaneous absorption is $A_{21}n_2$; that for absorption is $B_{12}\rho n_1$; and the number for stimulated emission is $B_{21}\rho n_2$. Because the atom is in thermodynamic equilibrium, the rates of downward and upward transitions are related by:

$$A_{21}n_2 + B_{21}\rho n_2 = B_{12}\rho n_1 \tag{3.4}$$

The radiation density is then:

$$\rho = \frac{A_{21}}{B_{12}\left(\frac{n_1}{n_2}\right) - B_{21}} \tag{3.5}$$

Using Boltzmann's equation, this can be written as:

$$\rho = \frac{A_{21}}{B_{21}}\left[\left(\frac{B_{12}g_1}{B_{21}g_2}\right)\exp^{h\nu_{12}/kT} - 1\right]^{-1} \tag{3.6}$$

Comparing this with Planck's equation (3.1) gives:

$$B_{21} = \frac{B_{12}g_1}{g_2} \tag{3.7}$$

$$A_{21} = \frac{8\pi h\nu_{12}^3}{c^3}B_{21} = \frac{8\pi h\nu_{12}^3}{c^3}\frac{B_{12}g_1}{g_2} \tag{3.8}$$

Equation 3.8 states the spontaneous emission probability per unit time as a function of radiation frequency, the degeneracy of the two states and the absorption probability per unit time. These are intrinsic atomic properties [28] that show the direct relationship between spontaneous emission and absorption. Since TDLAS relies on absorption, let's consider B_{12} in more detail.

3.1.4. Absorption Coefficient

Hilborn [105] contains a succinct explanation of the relationship between the absorption coefficient and absorption cross-section along with the relationship of both to the Einstein coefficients. The absorption coefficient $\alpha(\nu)$ is defined as the fractional decrease in flux density at frequency ν per unit path length through an absorbing medium [28, 105]:

$$-\delta I(\nu) = I(\nu)\,\alpha(\nu)\,\delta x \tag{3.9}$$

where $I(\nu)$ is the flux density incident on the layer of thickness δx.[2]
Consider a sample of gas of unit cross-sectional area and thickness δx. Using the two-level atomic model, this sample contains $n_1\delta x$ atoms in level one so it will absorb $n_1\delta x\rho B_{12}$ photons per second of radiation at a frequency of ν_{12}. For collimated radiation, the relationship between the flux density I and energy density ρ is:

$$I = \rho c \tag{3.10}$$

3.2. Partition Function

The fraction of atoms or molecules in any given state depends on the total number in all possible states. The partition function is a normalisation factor that takes this into account. Using Boltzmann's equation, the population of state j measured relative to the ground state is:

$$n_j = \frac{n_0 g_j}{g_0}\exp\left(\frac{-E_j}{kT}\right) \tag{3.11}$$

[2] We will later use this as the Beer-Lambert relation

where n_0 and g_0 are ground state quantities. The sum of populations in each state must equal the total number density giving:

$$\begin{aligned} n &= \sum_{j=0}^{\infty} n_j \\ &= \frac{n_0}{g_0} Q\left(T\right) \end{aligned} \tag{3.12}$$

where the partition function $Q\left(T\right)$ is defined as:

$$Q\left(T\right) = \sum_{j=0}^{\infty} g_j \exp\left(\frac{-E_j}{kT}\right) \tag{3.13}$$

The population of level j is:

$$n_j = \frac{n g_j}{Q\left(T\right)} \exp\left(\frac{-E_j}{kT}\right) \tag{3.14}$$

The internal Helmholtz free energy A_s^{int} is related to the partition function by the equation:

$$A_s^{int} = kT \ln Q_s \tag{3.15}$$

The translational contribution U_s^t to the internal energy U_s is:

$$U_s^t = \frac{3}{2} kT \tag{3.16}$$

The internal contribution U_s^{int} to the internal energy U_s is:

$$U_s^{int} = T^2 \frac{\mathrm{d} \ln Q_s}{\mathrm{d}T} \tag{3.17}$$

$$= \frac{1}{Q_s} \sum_{l=0}^{N_s} g_{sl} \epsilon_{sl} \exp^{-\epsilon_{sl}/kT} \tag{3.18}$$

$$= \ll \epsilon \gg_s \tag{3.19}$$

where $\ll \epsilon \gg_s$ is the statistical thermodynamic mean of the energy over the Boltzmann distribution. The partition function is important when deriving temperature using TDLAS. Sources of useful data for partition functions are Rothman et al [57], Babou et al [106], Hansen [107], Fischer et al [108] and Goldman et al [109].

3.2.1. Partition Function for Atomic Species

The calculation of the internal partition function of atomic species presents some problems since the number of levels is infinite for an infinite space containing a single atom [110]. Interactions with other particles limits the number of levels. Colonna et al [110] developed a few-level approach for the electronic partition function of atomic systems. Their model groups the atomic states into a few virtual levels with suitable average energy and global statistical weight.
For a species s in gas or plasma phase, the internal partition function at temperature T is given by:

$$Q_s = \sum_{l=0}^{N_s} g_{sl} \exp -\frac{\epsilon_{sl}}{kT} \tag{3.20}$$

where N_s is the number of levels, g_{sl} is the statistical weight of the l^th level and ϵ_{sl} is the energy of the l^th level. Colonna et al [110] truncate the partition function to a given energy limit ϵ_s^M where:

$$\epsilon_s^M = I_s - \Delta_s \tag{3.21}$$

with I_s being the ionisation potential and Δ_s being the energy cutoff. The truncated partition function is then:

$$Q_s = \sum_{l=0}^{\epsilon_{sl}<\epsilon_s^M} g_{sl} \exp -\frac{\epsilon_{sl}}{kT} \tag{3.22}$$

The cutoff energy in real systems is not constant but depends on some quantity such as particle density (Fermi criterion) or electron density Griem criterion [110]. The cutoff can be determined after the gas or plasma composition is known; however, this approach increases computational time, particularly for complex CFD codes that couple with kinetic or thermodynamic calculations.

3.2.2. Partition Function of Water

As this study focusses on TDLAS of water vapour, the partition function of water is vitally important. This section compares three algorithms that have been used in TDLAS literature and selects an algorithm for use in this study. The partition function of a rigid-rotor, harmonic-oscillator is [28]:

$$\begin{aligned} Q\left(T\right) &= 2.0\left[\left(\frac{\pi}{ABC}\right)\left(\frac{kT}{hc}\right)^3\right]^{0.5}\left[1-\exp\left(\frac{-hc\nu_1}{kT}\right)\right]^{-1}\times \\ &\quad \left[1-\exp\left(\frac{-hc\nu_2}{kT}\right)\right]^{-1}\left[1-\exp\left(\frac{-hc\nu_3}{kT}\right)\right]^{-1} \end{aligned} \tag{3.23}$$

where A, B, C are the three rotational constants of an asymmetric top rotor. For water, $A = 27.0$

Coefficient	Value
a_0	-14.087 469 157 417 9
a_1	37.924 324 853 988 2
a_2	-42.681 797 873 178 9
a_3	25.330 244 851 791 6
a_4	-8.108 512 629 355 32
a_5	1.331 068 717 205 35
a_6	-0.087 298 105 109 575 7

Table 3.1.: Coefficients of Vidler's partition function for water vapour. (Source: [111])

Coefficient	$70 < T < 405$ K	$400 < T < 1500$ K	$1500 < T < 3005$ K
a	-4.4405	-94.327	-1172.7
b	0.27678	0.81903	2.9261
c	1.2536×10^{-3}	7.4005×10^{-5}	-1.3299×10^{-3}
d	-4.8938×10^{-7}	4.2437×10^{-7}	7.4356×10^{-7}

Table 3.2.: Coefficients of Zhou's partition function for water vapour. (Source: [52])

cm^{-1}, $B = 14.4$ cm^{-1} and $C = 9.4$ cm^{-1}. The three fundamental vibration frequencies for water are $\nu_1 = 3657.05$ cm^{-1}, $\nu_2 = 1594.75$ cm^{-1} and $\nu_3 = 3755.93$ cm^{-1}.

Vidler et al [111] provided calculations and estimates of the partition function for gas phase water as a function of temperature up to 6000 K. Table 3.1 reproduces Vidler's coefficients for the internal partition function of water vapour Q_{int} using the functional form:

$$\log Q_{int} = \sum_{i=0}^{6} a_i \left(\log_{10} T\right)^i \tag{3.24}$$

Zhou et al [52] used the following polynomial expression coupled with the coefficients presented in table 3.2 for the partition function of H_2O at temperatures between 70 K and 3005 K.

$$Q\left(T\right) = a + bT + cT^2 + dT^3 \tag{3.25}$$

Thorne et al [28] and Vidler et al [111] used the astromoner's convention for spin degeneracy factor where g_i was taken as $\frac{1}{4}$ for para states and $\frac{3}{4}$ for ortho states. This results in the partition function being $\frac{1}{4}$ that calculated using Zhou's algorithm. Zhou's approach is adopted in this thesis.

Figure 3.3 compares the partition function for water as calculated using the three algorithms for temperatures between 100 K and 2900 K having corrected for the difference in spin degeneracy factor. The agreement between all three methods is excellent across this temperature range. Zhou's method is used in this study as it is simple and applies across the range of water vapour temperatures to be

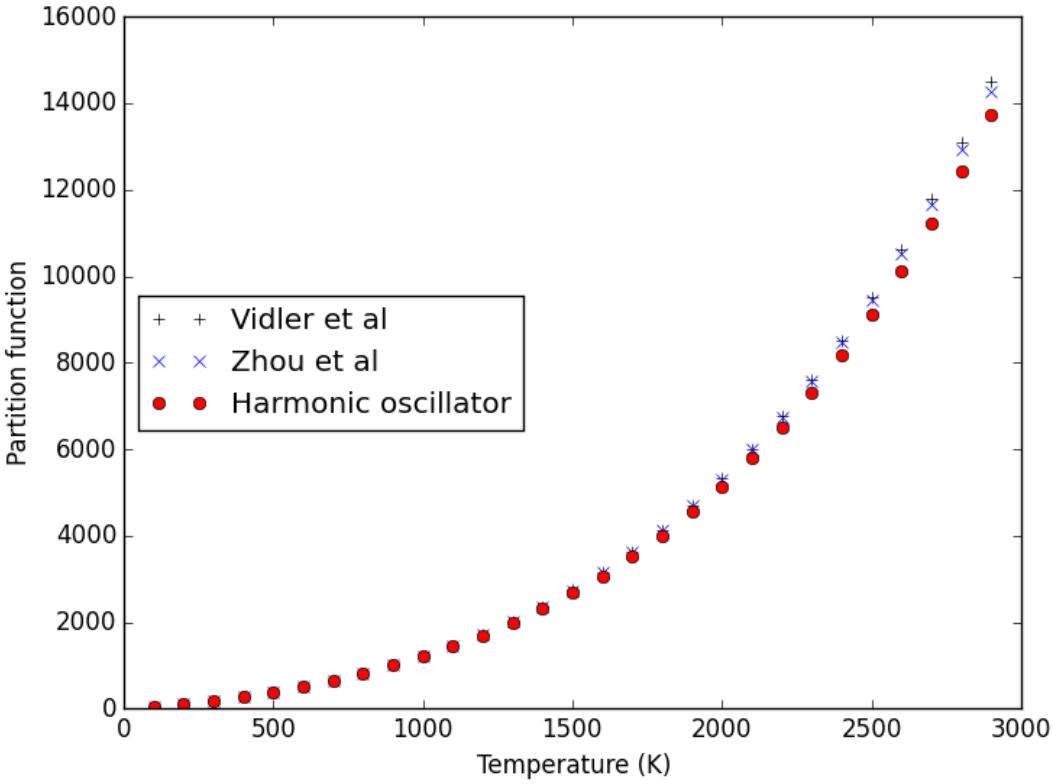

Figure 3.3.: Water vapour partition function calculated using the rigid-rotor harmonic oscillator model, Zhou's [52] method and a modified version of Vidler's [111] method.

measured using the TDLAS system.

3.3. Absorption spectroscopy

This section discusses the theory behind absorption spectroscopy. While this analysis is based on optically thin samples, it can be extended to thick cases as described in reference [79]. A fraction of the light that traverses a gaseous medium is absorbed if the light wavelength corresponds to an optical transition of a species in the medium. The transmittance $\tau(\nu)$ of monochromatic radiation of wavenumber ν through a uniform gas is given by the Beer-Lambert relation:

$$\begin{aligned} \tau(\nu) &= \left(\frac{I}{I_0}\right)_\nu \\ &= \exp\left[-\alpha(\nu)\right] \end{aligned} \tag{3.26}$$

where I_0 is the incident intensity, I is the intensity of the transmitted radiation and $\alpha(\nu)$ is the spectral absorbance of the sample at a wavenumber of ν. The transmittance is used in conventional absorption techniques. Alternatively, the relative absorption $\bar{A}$ may be used where:

$$\bar{A} = \frac{I_0 - I}{I_0} \tag{3.27}$$

In terms of the transmittance:

$$\bar{A} = 1 - \tau(\nu) \tag{3.28}$$

An optically thin sample has a spectral absorbance $\alpha(\nu) \ll 0.1$ so the exponential term may be approximated using a Taylor-series expansion to the first order as follows:

$$\tau(\nu) \approx 1 - \alpha(\nu) \tag{3.29}$$

The relative absorbance becomes:

$$\bar{A} = \alpha(\nu) \tag{3.30}$$

The absorbance is a function of the path length of the absorbing medium, l, the absorption cross-section of the analyte, σ, and the analyte density, ρ:

$$\alpha = \sigma l \rho \tag{3.31}$$

Absorbance is a strong function of wavenumber (or wavelength). If the resonance wavenumber for a transition is ν_0, the absorption cross-section is a function of that on resonance, σ_0, and a line shape function, $\bar{\chi}(\nu)$:

$$\sigma(\nu) = \bar{\chi}(\nu)\,\sigma_0 \tag{3.32}$$

Consider a gaseous sample of total pressure P (atm) and path length l (m) with a mole fraction x of the absorbing species. The spectral absorbance $\alpha(\nu)$ at wavenumber ν due to j absorption lines each centred at $\nu^{(j)}$ and with line strength $S^{(j)}$ (cm^{-2} atm^{-1}) may be written as:

$$\alpha(\nu) = Pxl\sum_{j} S^{(j)}(T)\,\bar{\chi}\left(\nu^{(j)} - \nu\right) \tag{3.33}$$

where $\bar{\chi}\left(\nu^{(j)} - \nu\right)$ is the intensity at wavenumber ν of a spectral line that has a centre wavenumber of $\nu^{(j)}$

The integrated absorbance of a single spectral line is:

$$\begin{aligned} A^{(j)} &= PxlS^{(j)}(T) \\ &= \int_{-\infty}^{\infty}\left[-\ln\left(\frac{I}{I_0}\right)\right]\mathrm{d}\nu \end{aligned} \tag{3.34}$$

The line shape function has been peak-normalised so that $\bar{\chi}(\nu_0) = 1$. The absorbance $\alpha(\nu)$ can then be written as a function of $\bar{\chi}(\nu)$ and the absorbance on resonance α_0 as:

$$\alpha(\nu) = \bar{\chi}(\nu)\,\alpha_0 \tag{3.35}$$

The ratio of the integrated absorbance of two transitions in direct absorption is equal to the ratio of the two line strengths $R_{LS}(T)$ [112]:

$$R_{LS}(T) = \frac{A^{(1)}}{A^{(2)}} = \frac{S^{(1)}}{S^{(2)}} \tag{3.36}$$

For a system in thermodynamic equilibrium at temperature T the ratio of number densities of particles occupying two energy states E_1 and E_2 is given by the Boltzmann equation [28]:

$$\frac{n_2}{n_1} = \frac{g_2}{g_1} \exp\left(-\frac{E_2 - E_1}{kT}\right) \tag{3.37}$$

where n is the number density (cm^{-3}) and g is the degeneracy of a level.
The line strength $S^{(j)}(T)$ is a function of the gas temperature T. The line strength at temperature T $\left(\text{in } \mathrm{cm}^{-2}\mathrm{atm}^{-1}\right)$ may be derived from the line strength plus the lower energy of transition at room temperature using the equation [112]:

$$\begin{aligned} S(T,\nu_0) &= S(T_0,\nu_0)\left(\frac{T_0}{T}\right)\left(\frac{Q(T_0)}{Q(T)}\right)\exp\left[\frac{-\hbar c E_{low}}{k}\left(\frac{1}{T}-\frac{1}{T_0}\right)\right] \\ &\quad \left[1-e^{\frac{-\hbar c\nu_0}{kT}}\right]\left[1-e^{\frac{-\hbar c\nu_0}{kT_0}}\right]^{-1} \end{aligned} \tag{3.38}$$

where $T_0 = 296$ K, $\hbar$ is Planck's constant (Js), k is Boltzmann's constant (JK^{-1}), c is the speed of light $(\mathrm{cm\ s}^{-1})$, ν_0 is the resonant frequency of the line (cm^{-1}), E_{low} is the energy of the lower state of the transition (cm^{-1}) and $Q(T)$ is the ro-vibrational partition function.
During an experiment using direct absorption, the temperature may be calculated from the measured ratio of integrated absorbance for two different temperature-dependent transitions that are close to each other. In this case, the last ratio terms in equation 3.38 may be ignored since the exponential terms are approximately equal. The two integrated absorbances are obtained at the same pressure, water concentration and path length. Thus, the ratio of the two integrals reduces to a ratio of the line strengths R_{LS} given by:

$$\begin{aligned} R_{LS} &= \frac{S^{(1)}(T)}{S^{(2)}(T)} \\ &= \frac{S\left(T_0,\nu^{(1)}\right)}{S\left(T_0,\nu^{(2)}\right)}\exp\left[-\left(\frac{\hbar c}{k}\right)\left(E_{low}^{(1)}-E_{low}^{(2)}\right)\left(\frac{1}{T}-\frac{1}{T_0}\right)\right] \end{aligned} \tag{3.39}$$

The relative sensitivity of this ratio to temperature is [52]:

$$\left|\frac{\mathrm{d}R_{LS}/R_{LS}}{\mathrm{d}T/T}\right| = \left(\frac{\hbar c}{k}\right)\frac{\left|\left(E_{low}^{(1)}-E_{low}^{(2)}\right)\right|}{T} \tag{3.40}$$

The absolute temperature sensitivity is [112]:

$$\left|\frac{\mathrm{d}R_{LS}}{\mathrm{d}T}\right| = \left(\frac{\hbar c}{k}\right)\frac{\left|\left(E_{low}^{(1)}-E_{low}^{(2)}\right)\right|}{T^2}R_{LS} \tag{3.41}$$

If the two transitions have lower states with dissimilar energy, the gas temperature can be calculated from the ratio of integrated absorbance of the lines provided the line strengths are sufficient to give an adequate signal-to-noise ratio [112].

3.4. Line Profiles

Let us now review the different line profiles along with their mathematical forms and, when necessary, approximations that are used for TDLAS calculations. The profiles are presented in terms of both wavelength and frequency for completeness.

3.4.1. Gaussian Line Profile

The Gaussian line profile as a function of wavelength λ is [43]:

$$I_\lambda = I_{\lambda_0} \exp^{-x^2} \tag{3.42}$$

where I_λ is the intensity at λ, I_{λ_0} is the intensity at centre wavelength λ_0 and

$$x = \sqrt{\ln 2}\frac{\lambda - \lambda_0}{w_g} \tag{3.43}$$

where w_g is the HWHM for the profile in nanometers. In terms of frequency, the HWHM is [28]:

$$\Delta\nu_g = \sqrt{\ln 2}\frac{\nu_0 \alpha}{c} \tag{3.44}$$

where ν_0 is the centre frequency, c is the speed of light and α is:

$$\alpha = \sqrt{\frac{2RT}{M}} \tag{3.45}$$

where R is the universal gas constant and M is the molar mass of the species. The line profile is then:

$$I_\nu = I_{\nu 0} \exp^{-x^2} \tag{3.46}$$

where I_ν is the intensity at ν, I_{ν_0} is the intensity at the centre frequency ν_0 and

$$x = \sqrt{\ln 2}\frac{\nu - \nu_0}{\Delta\nu_g} \tag{3.47}$$

Note the similarity between the wavelength and frequency representations of the Gaussian line profile. This stems from the Fourier transform of a Gaussian also being a Gaussian and is a unique property of the Gaussian line profile. The area-normalised Gaussian line profile is narrower and has weaker wings than the Lorentzian profile at the same temperature. The width of a Gaussian profile in the visible range is of the order of $0.4 - 40$ pm or $0.01 - 1.0$ cm^{-1}. In the infra red region, the wavenumber range

decreases to $0.001 - 0.1$ cm^{-1} [28]. Whilst thermal motion of atoms has been used in the discussion above, turbulence or mass diffusion of an emitting or absorbing gas can also produce a Gaussian line profile.

3.4.2. Lorentzian Line Shape

Spectral lines may be broadened and shifted in the presence of ions and electrons or by increasing gas pressure. Interactions between emitting and absorbing molecules or other particles in the flow can cause these perturbations. The Lorentzian line width varies linearly with respect to pressure up to several atmospheres. The Lorentzian HWHM is [28]:

$$\Delta\nu_L = \frac{\gamma}{4\pi} \tag{3.48}$$

where $\gamma = A_{21} = 1/\tau_2$ for a two level atom. At high pressures, the line shape may exhibit pressure broadening resulting in a Lorentzian profile described by:

$$\bar{\chi}(\nu) = \frac{1}{\pi} \frac{\Delta\nu_L}{(\nu_0 - \nu)^2 + \Delta\nu_L^2} \tag{3.49}$$

where $\Delta\nu_L$ is the HWHM. The Lorentzian HWHM is a linear function of pressure and varies with temperature as a power relationship [113]:

$$\Delta\nu_L(T, p) = \Delta\nu_L(T_0, p_0) \frac{p}{p_0} \left(\frac{T_0}{T}\right)^r \tag{3.50}$$

where $\Delta\nu_L(T, p)$ is the Lorentz halfwidth of the line at temperature T and pressure p, r is the temperature ratio power for a collision half-width of the line, $T_0 = 296$ K and $p_0 = 101.325$ kPa.

3.4.3. Voigt Line Shape

Earlier spectroscopic studies of gases used either Lorentzian of Gaussian profiles rather than the more accurate Voigt profile because the Voigt function was very difficult and time consuming to calculate, and the calculations were required at each wavelength [43]. In this section, we review the literature related to the Voigt profile in considerable depth because of the importance of this line shape to TDLAS.

Whiting [43] gives the following approximation[3] of the Voigt HWHM:

$$\Delta\nu_V = \frac{\Delta\nu_L}{2} + \sqrt{\left(\frac{\Delta\nu_L^2}{4} + \Delta\nu_D^2\right)} \tag{3.51}$$

Olivero [114] provides a review of the various empirical fits to the Voigt profile. An important aspect of the early work was the theoretical application of Humlíček's algorithm [44, 45] for calculating the Voigt/Faddeeva function. The value of Humlíček's algorithm was that it included a simple Fortran

[3] Accurate to about one percent

coding for the Voigt profile. This algorithm has been widely applied to later TDLAS systems and has been further developed [115]. The Voigt line shape is a convolution of the Doppler and Lorentzian profiles and is defined as [45]:

$$\bar{\chi}(\nu) = \frac{k_0 y}{\pi} \int_{-\infty}^{\infty} \frac{e^{-t^2}}{y^2 + (x-t)^2} dt \tag{3.52}$$

where $k_0 = \sqrt{\ln 2}/\left(\sqrt{\pi}\Delta\nu_D\right)$, $y = \sqrt{\ln 2}\Delta\nu_L/\Delta\nu_D$, $x = \sqrt{\ln 2}\left(\nu_0 - \nu\right)/\Delta\nu_D$.
Durry et al [65] incorporate the effects of self-broadening and broadening by a foreign gas when calculating the collisional half-width $\Delta\nu_V$:

$$\Delta\nu_V = \Delta\nu_{Self} p x + \Delta\nu_{Gas} p\left(1 - x\right) \tag{3.53}$$

where $\Delta\nu_{Self}$ is the self-broadening coefficient obtained from *HITRAN* [57], p is the gas pressure, x is the molar concentration of the target species and $\Delta\nu_{Gas}$ is the broadening coefficient of the perturbing gas (for example nitrogen or oxygen).
The algorithm provided by Humlíček [45] can be used to approximate the Voigt profile. When using this algorithm, x is the real component and y is the imaginary component. The symmetrical Voigt profile is the real component of the algorithm's output. More generally, any spectral profile is a function of the frequency, ν, the resonance frequency, ν_0, and the HWHM, $\Delta\nu$ such that:

$$\bar{\chi}(\nu, \nu_0, \Delta\nu) = fn(\nu_0, \Delta\nu) \tag{3.54}$$

with the line shape normalised such that:

$$\int_{-\infty}^{\infty} \bar{\chi}(\nu, \nu_0, \Delta\nu)\, \mathrm{d}\nu = 1 \tag{3.55}$$

Westberg et al [49, 116] demonstrated that a given Fourier coefficient of a wavelength-modulated Voigt absorption function can be calculated as a convolution of one or several Fourier coefficients for a modulated Lorentzian line shape function, for a given velocity group of molecules and the Maxwell-Boltzmann velocity distribution. Their method does not introduce any approximation and reduces calculation time by approximately three orders of magnitude.

3.5. Laser diode modulation

This section reviews the theory behind wavelength modulation spectroscopy building on the discussion in section 2.8. A laser diode emits narrow bandwidth coherent radiation at a certain power and wavelength[4] depending on the diode temperature and the injection current [117]. Laser diodes have narrow bandwidths and can be tuned rapidly over a limited range in frequency by changing the injection current, i_{ic}. If a small amplitude sinusoidal modulation current, i_a, at frequency f is applied to a

[4] frequency or wavenumber

diode with centre injection current of i_c, the modulated injection current is [79]:

$$i_{ic}(t) = i_c + i_a \cos(2\pi f t) \tag{3.56}$$

The instantaneous diode light frequency, $\nu(t)$, is:

$$\nu(t) = \nu_c + \nu_a \cos(2\pi f t) \tag{3.57}$$

where ν_c is the laser centre frequency and ν_a is the frequency modulation amplitude. Note that this analysis assumes there is no phase shift between the injection current and frequency modulations. All phases of the system are related making this assumption applicable without loss of generality [79].
As well as changing the laser light frequency, injection current modulation also affects the power output by the laser I_L. This effect depends on the type of laser diode but, for small i_a can be considered to comprise a strong linear part and a small non-linear contribution as follows:

$$I_L(t) = \kappa'_{I,ic}(i_{ic}(t) - i_{th}) + \kappa''_{I,ic}(i_{ic}(t) - i_{th})^2 \tag{3.58}$$

where $\kappa'_{I,ic}$ and $\kappa''_{I,ic}$ are linear and non-linear constants of proportionality and i_{th} is the threshold injection current for the laser diode. The laser centre power, $I_{L,0}(\nu_c)$ at frequency ν_c is solely a function of the frequency.

3.5.1. Detector signal

The light power impinging on a detector at wavenumber ν in the absence of analytes is defined as $I_D(\nu)$. This depends on the laser emitted power, $I_L(\nu)$, and the transmission of the optical system, $\tau(\nu)$. The laser power may depend on the wavenumber of the emitted radiation and the optical system may have losses due to mismatch of numerical apertures between optical components scattering, etalons or absorption by the atmosphere.

$$I_D(\nu) = \tau(\nu) I_L(\nu) \tag{3.59}$$

The laser power impinging on a detector, $I(\nu)$, after traversing a sample containing analytes is:

$$I(\nu) = I_D(\nu)[1 - \bar{\chi}(\nu)\alpha] \tag{3.60}$$

The signal measured by a detector, $S(\nu)$, is related to the light intensity at the detector $I(\nu)$ by an instrumentation factor, η.

$$S(\nu) = \eta I(\nu) \tag{3.61}$$

The detector signal consists of two parts: a background signal $S_{BG}(\nu)$ and an analytical detector signal $S_{AS}(\nu)$ where:

$$S(\nu) = S_{BG}(\nu) + S_{AS}(\nu) \tag{3.62}$$

The background signal is:

$$S_{BG}(\nu) = \eta I_D(\nu) \tag{3.63}$$

The analytical signal is:

$$S_{AS}(\nu) = -\eta I_D(\nu)\,\bar{\chi}(\nu)\,\alpha \tag{3.64}$$

The analytical signal is used in direct detection experiments such as those in chapter 5.

3.6. Wavelength modulation spectroscopy

The laser frequency modulation varies proportionally to the injection current modulation amplitude with the linear frequency-to-injection current response, $\kappa_{\nu,ic}$, as the proportionality constant. Defining the frequency modulation amplitude as $\nu_a = \kappa_{\nu,ic} i_a$, the time-dependent laser power is:

$$\begin{aligned} I_L(\nu_c, \nu_a, t) &= I_{L,0}(\nu_c) + \frac{\kappa'_{I,ic}}{\kappa_{\nu,ic}}\nu_a \cos(2\pi f t + \phi_1) + \frac{\kappa''_{I,ic}}{2\kappa^2_{\nu,ic}}\nu_a^2 \cos(2\pi 2 f t + \phi_2) \\ &= I_{L,0}(\nu_c) + \kappa_1 \nu_a \cos(2\pi f t + \phi_1) + \kappa_2 \nu_a^2 \cos(2\pi 2 f t + \phi_2) \end{aligned} \tag{3.65}$$

where $\kappa_1 = \kappa'_{I,ic}/\kappa_{\nu,ic}$ and $\kappa_2 = \kappa''_{I,ic}/2\kappa^2_{\nu,ic}$ are the linear and non-linear power modulation coefficients respectively. Phase components ϕ_1 and ϕ_2 have been included because the laser power modulation does not follow the frequency modulation instantaneously.
Increasing the injection current increases the laser power but decreases the frequency so ϕ_1 is slightly less than π. The non-linear power modulation amplitude is small and not necessarily related to the linear power modulation amplitude by a constant factor [79].

3.6.1. Time-dependent peak-normalised line functions

The spectral profile and the laser modulation can be related by introducing a width-normalised centre detuning for the laser, $\bar{\nu_d} = (\nu_c - \nu_0)/\Delta\nu$ where ν_0 is the wavenumber of the centre of a spectral line. The width-normalised frequency modulation amplitude is $\bar{\nu_a} = \nu_a/\Delta\nu$. Define the width-normalised modulated detuning as:

$$\bar{\nu}(t) = \bar{\nu_d} + \bar{\nu_a}\cos(2\pi f t) \tag{3.66}$$

The time-dependent peak-normalised Lorentzian lineshape function exposed to modulated laser light is then [79]:

$$\bar{\chi}_L\left(\bar{\nu}_d, \bar{\nu}_a, t\right) = \frac{1}{1+\bar{\nu}^2\left(t\right)} \tag{3.67}$$

Similarly, the time-dependent peak-normalised Gaussian line shape function exposed to modulated laser light is [79]:

$$\bar{\chi}_G\left(\bar{\nu}_d, \bar{\nu}_a, t\right) = 2\mathrm{e}^{-\bar{\nu}^2(t)} \tag{3.68}$$

The Fourier series is a set of orthogonal trigonometric functions that describe periodic functions. The modulated injection current and detector signal are both periodic functions so they can be represented by Fourier series. Kluczynski et al [79] show that, for small frequency modulation amplitudes, the in-phase component of the n^{th} harmonic output of a lock-in amplifier is:

$$\tilde{S}_n^{in-phase}\left(\bar{\nu}_c, \bar{\nu_a}\right) \approx -\eta I_D \frac{2-\delta_{n0}}{2^n n} \bar{\nu}_s^n \bar{\chi}^{(n)}\left(\bar{\nu}_c\right) \alpha_0 \tag{3.69}$$

where $\bar{\chi}^{(n)}\left(\bar{\nu}_c\right)$ is the n^{th} derivative of the line shape function with respect to $\bar{\nu}$ evaluated at the laser centre frequency $\bar{\nu}_c$ and δ_{n0} is the Kronecker delta. The first three harmonics of a lock-in amplifier for a WMS setup with small frequency amplitudes are [79]:

$$\tilde{S}_2^{in-phase}\left(\bar{\nu}_c, \bar{\nu_a}\right) \approx -\eta I_D \frac{1}{4} \bar{\nu}_s^2 \bar{\chi}^{(2)}\left(\bar{\nu}_c\right) \alpha_0 \tag{3.70}$$

$$\tilde{S}_3^{in-phase}\left(\bar{\nu}_c, \bar{\nu_a}\right) \approx -\eta I_D \frac{1}{24} \bar{\nu}_s^3 \bar{\chi}^{(3)}\left(\bar{\nu}_c\right) \alpha_0 \tag{3.71}$$

and

$$\tilde{S}_4^{in-phase}\left(\bar{\nu}_c, \bar{\nu_a}\right) \approx -\eta I_D \frac{1}{192} \bar{\nu}_s^4 \bar{\chi}^{(4)}\left(\bar{\nu}_c\right) \alpha_0 \tag{3.72}$$

The detected signal is proportional to α_0 making the method linear. Also, the even harmonics decrease rapidly as the order increases. This latter fact does not necessarily apply for larger modulation amplitudes. All odd harmonics of a single symmetrical line shape function are zero on resonance. In other words, $\tilde{S}_1^{in-phase}$ and $\tilde{S}_3^{in-phase}$ are zero on resonance for small modulation amplitudes. The odd-order harmonics are used to lock the frequency of the laser diodes. The Fourier series for the time-dependent detector signal is an infinite series of linear combinations of the even and odd components of the n^{th} Fourier coefficients of the detector signal:

$$S\left(\bar{\nu}_d, \bar{\nu}_a, t\right) = \sum_{n=0}^{\infty} S_n^{even}\left(\bar{\nu}_d, \bar{\nu}_a\right) \cos 2\pi n f t + \sum_{n=1}^{\infty} S_n^{odd}\left(\bar{\nu}_d, \bar{\nu}_a\right) \sin 2\pi n f t \tag{3.73}$$

where

$$S_n^{even}\left(\bar{\nu}_d, \bar{\nu}_a\right) = \frac{2-\delta_{n0}}{\tau}\int_0^{\tau} S\left(\bar{\nu}_d, \bar{\nu}_a, t\right)\cos\left(2\pi n f t\right)\mathrm{d}t \tag{3.74}$$

and

$$S_n^{odd}\left(\bar{\nu}_d, \bar{\nu}_a\right) = \frac{2}{\tau}\int_0^{\tau} S\left(\bar{\nu}_d, \bar{\nu}_a, t\right)\sin\left(2\pi n f t\right)\mathrm{d}t \tag{3.75}$$

Here, τ is an integration time that is proportional to the inverse of the modulation frequency. The detector signal harmonics are the sums of the analytical and background signals so the detector signal Fourier coefficients are the sums of the relevant Fourier coefficients [79]. For example:

$$S_n^{even}\left(\bar{\nu}_d, \bar{\nu}_a\right) = S_{AS,n}^{even}\left(\bar{\nu}_d, \bar{\nu}_a\right) + S_{BG,n}^{even}\left(\bar{\nu}_d, \bar{\nu}_a\right) \tag{3.76}$$

The even component of the n^{th} Fourier coefficient of the detector signal is equivalent to the in-phase component of the n^{th} harmonic output of a lock-in amplifier. The same applies for the odd components and out-of-phase output. Moreover, the background signal S_{BG} is not modulated making the Fourier coefficients of that signal zero. Thus, the Fourier coefficients of the detector signal are equal to those of the analytical signal.
Thus, the WMS signal is proportional to the absorption of light $I_0 - I$ rather than the transmission I/I_0 or the absorbance $-\log\left(I/I_0\right)$. Kluczynski et al [79] provide expressions for the Fourier coefficients of harmonics of Lorentzian and Gaussian line shapes.

3.7. Extracting Conditions

Ideally, the laser centre frequency, ν_c, would exactly coincide with the spectral line resonance frequency, ν_0. Consider a gaseous sample of total pressure P (atm) and path length l (m) with a mole fraction x of the absorbing species. The spectral absorbance $\alpha\left(\nu\right)$ at wavenumber ν due to the j^{th} absorption line which is centred at ν_j and has a strength $S^{(j)}$ (cm^{-2} atm^{-1}) may be written as:

$$\alpha\left(\nu\right) = Pxl\sum_j S^{(j)}\left(T\right)\Phi\left(\nu^{(j)} - \nu\right) \tag{3.77}$$

The line strength $S^{(j)}\left(T\right)$ is a function of the gas temperature T (K) and $\Phi\left(\nu^{(j)} - \nu\right)$ is the line shape. The line shape function is normalised such that:

$$\int \Phi\left(\nu^{(j)} - \nu\right) d\nu = 1 \tag{3.78}$$

The static temperature may be derived from the Doppler HWHM using:

$$T = \left(\frac{\alpha^{(j)}}{\nu^{(j)}}\right)^2 \frac{mc^2}{2k\ln 2} \tag{3.79}$$

The line strength at a temperature T may be derived from the line strength plus the lower energy of transition at room temperature using the equation:

$$S\left(T,\nu_0\right)=S\left(T_0,\nu_0\right)\frac{T_0Q\left(T_0\right)}{TQ\left(T\right)}\frac{\left[1-e^{\frac{-\hbar c\nu_0}{kT}}\right]}{\left[1-e^{\frac{-\hbar c\nu_0}{kT_0}}\right]}\exp\left[\frac{-\hbar c}{E"}\left(\frac{1}{T}-\frac{1}{T_0}\right)\right] \tag{3.80}$$

where $T_0 = 296$ K, $\hbar$ is Planck's constant (Js), k is Boltzmann's constant (JK^{-1}), c is the speed of light (ms^{-1}), ν_0 is the resonant frequency of the line, $E"$ is the energy of the lower state of the transition (cm^{-1}) and $Q\left(T\right)$ is the partition function. This theoretical derivation of the gas number density is complicated practically by uncertainties in the gas temperature, absorption by species other than the target, chemical reactions in the flow, atmospheric absorption and other sources of noise in the detection electronics.

3.8. Application to these experiments

Wavelength modulated spectroscopy was used for the expansion tunnel experiments. The test time was approximately 1 ms and the flow properties changed rapidly during that test time. The laser current was modulated at a frequency of about 1 MHz and 60 points were sampled each modulation cycle. A software lock-in amplifier was developed to extract the analytical signal as described above. The short test time and rapidly changing test conditions precluded use of a low-frequency wavelength ramp with the sinusoidal modulation as was typical of other studies. Instead, a larger amplitude sinusoidal wavelength modulation signal as implemented and the analytical signal was extracted using the software lock-in amplifier.

As another innovation, the modulation frequency was calculated using a high-order discrete fast Fourier transform (FFT). This frequency was used to tune the lock-in amplifier and reduce unwanted signals. Also, small packets of signals (typically 20-60 modulation cycles) were fed into the lock-in amplifier to find the maximum signal and optimal phase since these could change significantly as the test conditions in the scramjet changed. This meant that each packet sampled $20-60$ μs of test time. Further details of how harmonic detection was implemented are contained in chapter 6.

3.9. Summary

This chapter has briefly outlined the theory of direct and wavelength modulated absorption spectroscopy. The theory is applied and modified as necessary in the chapters on experiments.

4. TDLAS System Design

This chapter discusses the TDLAS system that was designed based on the outcomes of the literature review. This system was designed to be modular, accommodate up to eight simultaneous channels, target multiple species, allow direct or wavelength modulation spectroscopy, and use either free-space or fibre-coupled TDLAS. The components necessary to build this system were procured and assembled in the laboratory; however, ironically, the fibre-coupled components were not used for the experiments disclosed in this thesis. The experimental opportunities that arose were considered to be achievable using free-space methods without the added complexity introduced by used optical fibres. Thus, free-space techniques were applied in the reported experiments as discussed in chapters 5, 6 and 7.
The functional and physical design disclosed in this chapter is included for the benefit of future researchers who are anticipated to use this system for follow-on experiments in the expansion tunnels.

4.1. Functional Design

This section discusses the functional design of the TDLAS system resulting from the literature review. The physical design is discussed in the next section. The system comprises five sub-systems:

- transmitter,
- receiver,
- data recorder,
- control, and
- analysis.

The test area lies between the transmitter and receiver sub-systems and, for the purposes of functional design, is outside of the system. Figure 4.1 shows the functional layout of the TDLAS system. Each sub-system will be discussed separately to better understand its design requirements.

4.1.1. Transmitter

The transmitter sub-system is shown schematically in Figure 4.2. It provides radiation of appropriate wavelength, power, modulation and beam area to probe the target area for desired measurements. One part of the transmitter is independent of the wavelength of radiation to be emitted whilst the other part depends on wavelength.

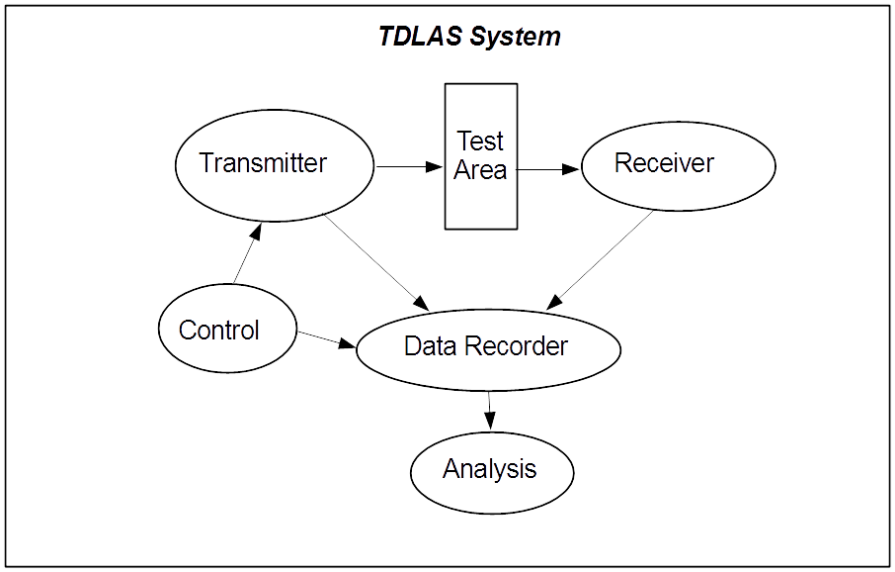

Figure 4.1.: Functional diagram of the TDLAS system

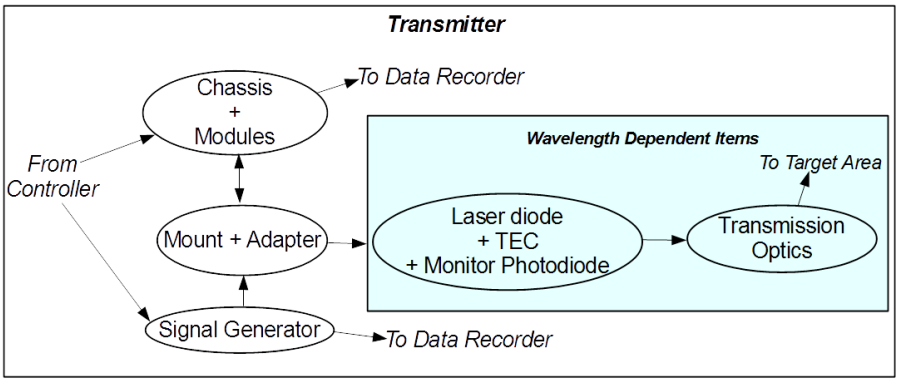

Figure 4.2.: Schematic diagram of transmitter

The laser diode controller chassis and modules, mounts and their adapters, and a signal generator comprise the wavelength independent part of the transmitter. These items provide the physical and electrical environment to transmit modulated radiation to the target area.

The chassis provides a physical interface for the controller modules, conditions power to the modules, controls the modules, and passes data to external interfaces. The controller modules provide signals to each mount and receive feedback signals from the mounts via electrical cables. One function of a module is to control the laser diode temperature via a thermo-electric controller. This maintains the laser diode temperature within strict limits which ensures that the laser diode wavelength and output power are as desired. The second function of a module control the laser diode current.

A mount provides a physical mounting for, and an electrical interface to, a laser diode. If the diode has an integral thermoelectric controller and monitor photodiode, the mount provides a hardware and electrical interface. If a laser diode does not have an integral temperature controller and monitor diode, the mount incorporates these items. Thus, the mount design depends on the form, fit and function of the laser diode selected to transmit the radiation into the target area. The laser diode selection, in

turn, depends on the size of the target area as well as the wavelengths, species and properties to be measured.
The signal generator provides modulation signals to the controllers and mounts. Based on the literature review, the laser diode modulation signals for $2f$ WMS would be low frequency (less than 100 kHz) sawtooth signals coupled with high frequency (500 kHz-500 MHz) sinusoids. It was originally intended that the laser diode controller could provide the sawtooth waveform whilst the sinusoidal waveforms would be taken from a signal generator and fed directly into the laser diode mounts. When the laser controller was tested after receipt, it was not able to generate sawtooth waveforms. Instead, it was able to step through laser diode currents very slowly. This meant that the modulation schema had to be changed.

4.1.1.1. Wavelength dependent components

The design of the wavelength dependent components depends on both the wavelength of interest and the type of measurement to be made. The wavelength determines the type of laser diode to be used as well as the form of the components in the optical path. The type of measurement determines whether a single diode is used or dual laser diodes are used. A single diode may be used to measure the absorbance of the flow in one wavelength region or the flow velocity. Zhou et al [52] simultaneously measure relative species concentration at flow temperature using a single wavelength to simplify the sensor system and reduce cost.
Alternatively, Griffiths and Houwing [13, 1] recommend using dual laser diodes to simultaneously measure flow temperature and relative species concentration in pulsed flows. Their design time-division multiplexed the laser signals across two absorption lines by alternatively scanning each diode input signal from low injection current to high injection current with the aid of a multiplexing box between the signal generator and the laser diodes. with this arrangement, they were able to achieve a scan rate of 10 kHz across a wavenumber range of 0.5 cm^{-1}. Importantly, only one laser was operating at any time.
At the highly complex end of the design scale, Lindstrom et al [14, 16, 17] probed 16 separate time-division multiplexed line of sight laser signals. Each laser was observed by a specific photodetector. The outputs from the photodetectors were amplified and recorded.

Optical Interference The following guidelines were adopted to avoid optical interference of the transmitted signals due to unintentional etalons:[13]

1. Where possible, angled fibre-optic connectors and wedged windows were used.

2. If the fibre-optic cable has flat-polished ends, the cable length should be approximately 2 m so that the modulation frequency of the detected signal is well above the laser scanning rate.

3. If possible, the Target Area windows should have anti-reflective coatings and the alignment between the laser and windows should be detuned slightly.

Other Losses. To avoid other losses, the wavelength dependent group design incorporated the following guidelines:

1. An aspheric lens was used to collimate the laser diode output.
2. The numerical aperture (NA) of a patch cable should be greater than or equal to the NA of the input collimator.
3. The diameter of a focussed beam should be less than the Mode Field Diameter (MFD) of the fibre into which it passes.
4. The output waist diameter of a patch cable should be matched to the cross-sectional area of the Target Area. The maximum waist diameter is defined as the maximum distance from the lens at which a Gaussian beam's waist can be placed.
5. Certain fibre-optic cables can be used at wavelengths up to 200 nm above the cut-off wavelength whilst others are limited to lower wavelength ranges. The wavelength range of each cable should be confirmed as part of the system design.

4.1.2. Single Wavelength Variant

Figure 4.3 shows a schematic of the wavelength dependent components for a single wavelength measurement. The TEC and laser diode feed into an optical isolator, collimators, a beam splitter, a photodetector, fibre optic cables and (if needed) atmospheric isolators.

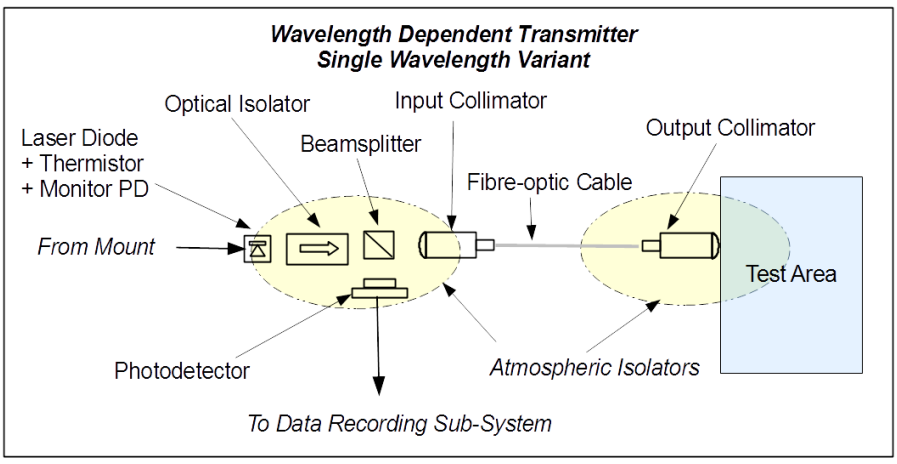

Figure 4.3.: Schematic Layout of a Single Wavelength WDT Group

Controller functions. The control signals to the mount are in the form of thermoelectric controller (TEC) currents and laser currents. The TEC current controls the laser diode temperature which, in turn controls the wavelength of radiation emitted by the diode. Typically, emissions may be varied of a range of approximately 4-5 nm by changing the diode temperature from $20°C$ to $40°C$. The actual rate of change depends on the diode and mount thermal characteristics. Given the thermal inertia of a typical mount, the TEC temperature and wavelength control is relatively steady-state.

Low frequency modulation. Once the diode centre wavelength is set, the wavelength can be modulated at a low frequency by varying the diode injection current. This current variation also changes the emitted power so either a monitor photodiode is required to provide feedback or the power changes must be compensated by some other means.

High frequency modulation. Whilst the controller provides steady-state and low-frequency control of a laser diode's wavelength and power, high frequency modulation can be applied by adjusting the injection current using high frequency signals fed into a bias-T junction on the mount. These signals are injected directly into the diode to reduce ohmic losses in the cabling. Care is required is setting the signal amplitude since this modulation could exceed the diodes capabilities and destroy it.

Optical path. The output from the laser diode i collimated by an aspheric lens before passing through an optical isolator. The isolator prevents reflected radiation from damaging the diode. After the optical isolator, the light enters a beamsplitter with a typical transmission:reflection ratio of 90:10. The weaker reflected signal from the beamsplitter is incident on a photodetector whose signal compared with the received photodetector signal.

Fibre port. The beam that is transmitted through the beamsplitter is then incident on a fibre port that couples it to a fibre-optic cable. The fibre port has a collimator that focuses the beam so that its diameter is less than the mode field diameter of the fibre. The signal is transmitted via a single-mode fibre optic cable to the target.

Atmospheric isolators. The transmission optics may, if necessary, use atmospheric isolators to minimise absorption of the radiation by the atmosphere. This function is particularly important for wavelengths that are absorbed strongly by water vapour. In this case, the atmospheric isolators should be purged by nitrogen. The atmospheric isolators take the form of air-tight containers surrounding the optical components.

Fibre-optic cable. The choice of fibre-optic cable can drive other design decisions for the transmitter. Single mode fibres were used in this layout. Where possible, the connectors were standardised as Fixed Connectors/Physical Contact (FC/PC). Figure 4.4 shows the differences between FC/PC and FC/APC (angled PC) connectors. FC/APC connectors have lower back reflections and return losses than FC/PC connectors but need to be aligned correctly. When coated with an anti-reflective coating, FC/PC connectors have higher free-space return loss than uncoated FC/PC connectors.
The output collimator should be mounted near the window to the target area ensuring that there is a small angle (approximately 1°) between the centreline of the output collimator and the perpendicular to the window. This angle will help to eliminate etalons. Also, if possible, a 1° wedge window should be used for viewing the test area to further reduce etalons.

Dual Wavelength Variant Dual laser diodes may be used to measure the flow temperature as well as the relative species concentration. The design of this variant is based on those of Griffiths and

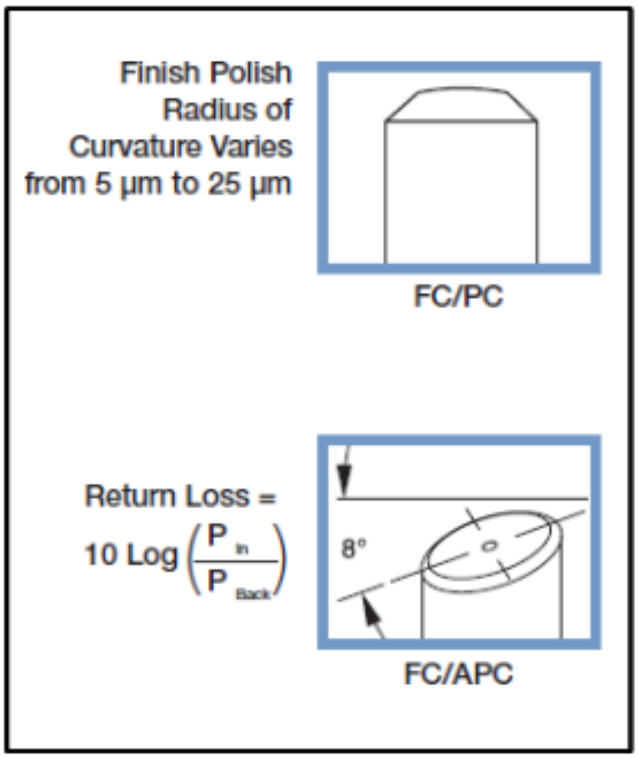

Figure 4.4.: Schematic diagrams of FC/PC and FC/APC Connector Ends (Source: Thorlabs)

Houwing [13] and Liu et al [54]. Figure 4.5 shows a schematic of the WDT Group for dual wavelength measurement. Two laser diodes produce modulated output at two absorption wavelengths for the species of interest.

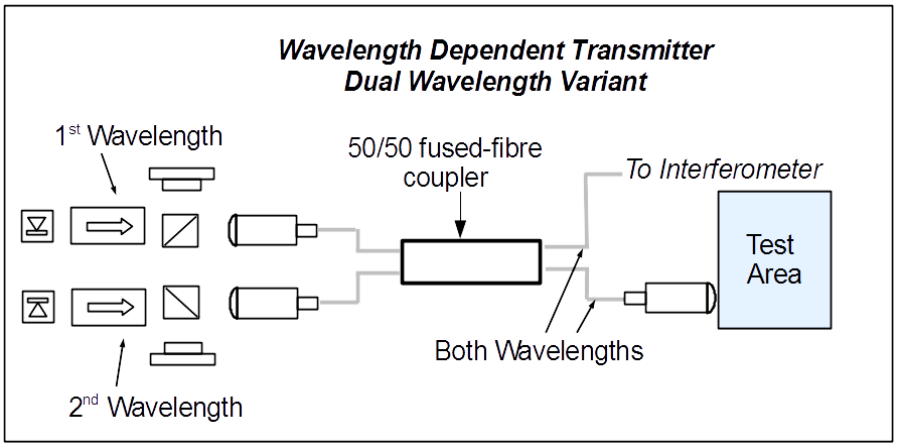

Figure 4.5.: Schematic Layout of Dual Wavelength WDT Group

The front end of the dual wavelength variant (that is, near the mount) is the same as for the single wavelength variant except that two LDs are used. Provided the LD wavelengths are similar, the outputs may be coupled via a 50/50 fused-fibre coupler. This technique does not automatically work for wavelengths that are widely separated as the couplers typically have narrow wavelength ranges.

Time-Division Multiplexing (TDM) With a TDM system, only one wavelength at a time is transmitted through the fibre and the test area. The laser emissions are multiplexed by transmitting from

each diode alternatively. Griffiths [1] provides details of a system that multiplexes signals from two diodes. Figure 4.6 reproduces the circuit from Griffiths' thesis. The circuit converts the output from a signal generator to be alternating inputs to the two laser diodes. Figure 4.7 shows the circuit input and outputs for a 10 kHz modulation. The negative half of the input signal drives the first diode whilst the second half drives the other diode. The input signal is specially designed to drive from low to high injection current to ensure the laser wavelength ramps from low wavelength to high wavelength in each cycle.

Griffiths explains that driving the injection current from high current to low causes the wavelength to scan up as the laser is turned on then it would reverse direction and scan down after about one-third of the scan. Driving from high injection current to low wastes much of the scan time [1, p 55-6].

A negative aspect of using TDM is that each laser is active for only half of the modulation cycle. As may be seen in Figure 4.7, the first laser emits for 450 μs then the second emits for 450 μs . This is particularly important in experiments with short test times such as those in shock and expansion tubes. If a TDM modulation frequency of 10 kHz is used in a test that lasts for 50 μss, there is a 50% likelihood that one of the diodes will not transmit during the test. In this case, the laser scanning modulation frequency should be at least 20 kHz.

An advantage of a TDM system is that the receiver sub-system detects only one wavelength at a time. The interferometer in Figure 4.5 is used to provide a time/wavelength correlation for the detected test signal. Readers are encouraged to refer to Griffiths for more details of the interferometer.

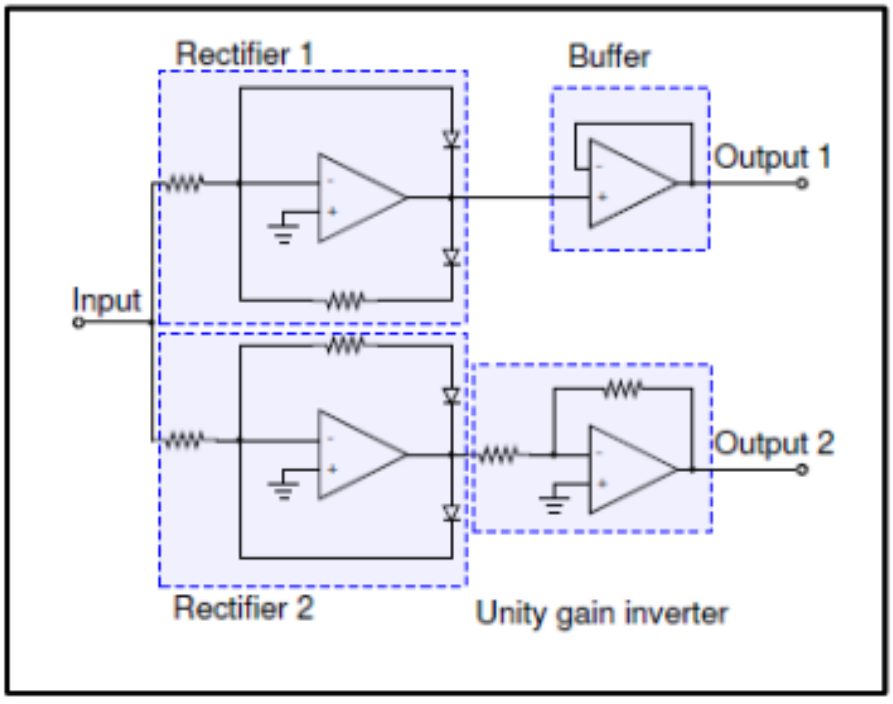

Figure 4.6.: Time-division multiplexing circuit (Source: [1])

Wavelength division multiplexing As an alternative to time division multiplexing, the outputs from the laser diodess may be wavelength division multiplexed (WDM). In this case, both wavelengths are simultaneously transmitted through the Test Area. This method of multiplexing overcomes the

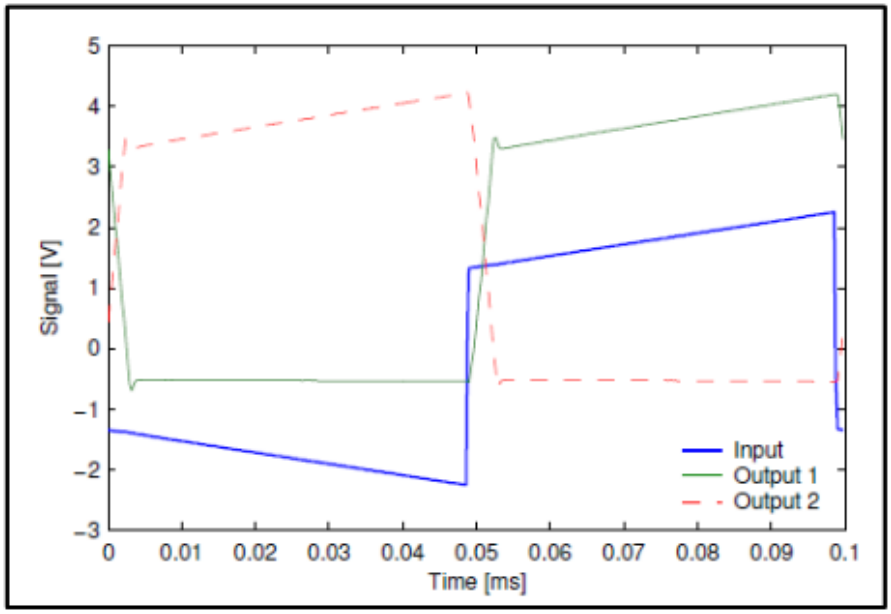

Figure 4.7.: Time-division multiplexing modulation scheme (Source: [1])

problem of lasers being active for only half of the signal modulation cycle; however, it also introduces additional complexities to the entire TDLAS system design, especially in the receiver sub-system. The individual beams must be extracted from the received multiplex signal before being recorded and analysed.

4.1.3. Receiver

The receiver, shown schematically in Figure 4.3, receives radiation from the Target Area, separates the radiation into desired wavelength region and measures the power received in each wavelength region. The wavelength dependent components provide electrical signals to amplifiers and a signal processor. Its design depends on the wavelengths to be measured as well as the type of multiplexing (either time-domain or wavelength domain) used by the transmitter. The signals are recorded after being processed by the receiver.

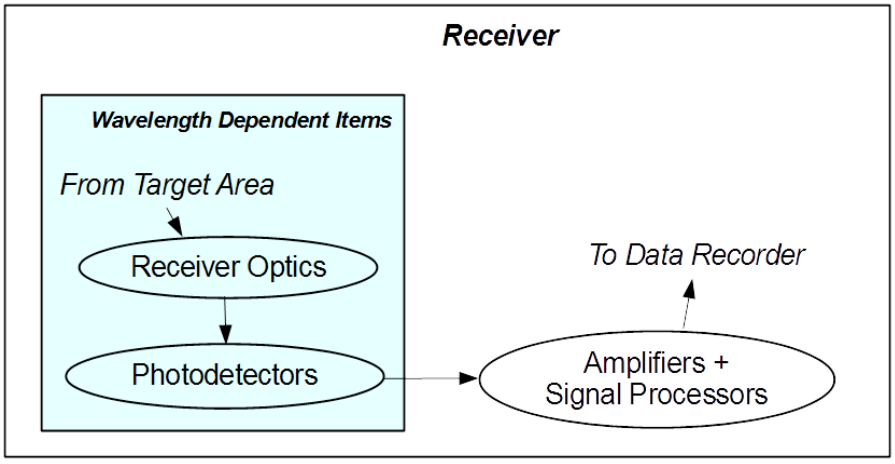

Figure 4.8.: Schematic layout of the receiver

Design guidelines. The following design guidelines apply to the receiver:

1. An atmospheric isolator should enclose the optical train if the laser wavelength is susceptible at room temperature to absorption by atmospheric species such as water vapour.

2. Unwanted sources of radiation, such as background emissions from the Test Area, should be filtered out.

3. The photodetector active area should be larger than the laser beam cross-section to ensure as much of the signal as possible is detected. If the photodetector area is smaller than the laser beam cross-section, additional optics may be needed to focus the beam onto the active area.

4. The photodetector should have a fast rise-time to ensure that rapid changes in intensity are detected. This is particularly important for pulsed hypersonic test facilities where the test time may be as short as 50 μs.

5. The optical train should accommodate variations in the path of the beam as it passes through the Test Area. This is because changes in refractive index, density and other flow parameters are expected in the Test Area.

6. The Test Area windows, the filter and the photodetector should be tuned to reduce etalons in the optical path.

Single wavelength. Figure 4.9 shows the schematic layout of a single wavelength receiver. After passing through the Test Area, the laser signal passes through a narrow-band filter to prevent broad-band radiation from being detected. The signal is detecting using a photodetector. The output is amplified and processed before being recorded. If the laser wavelength is susceptible at room temperature to absorption by atmospheric species such as water vapour, an atmospheric isolator may be needed to enclose the test window, filter and photodetector.

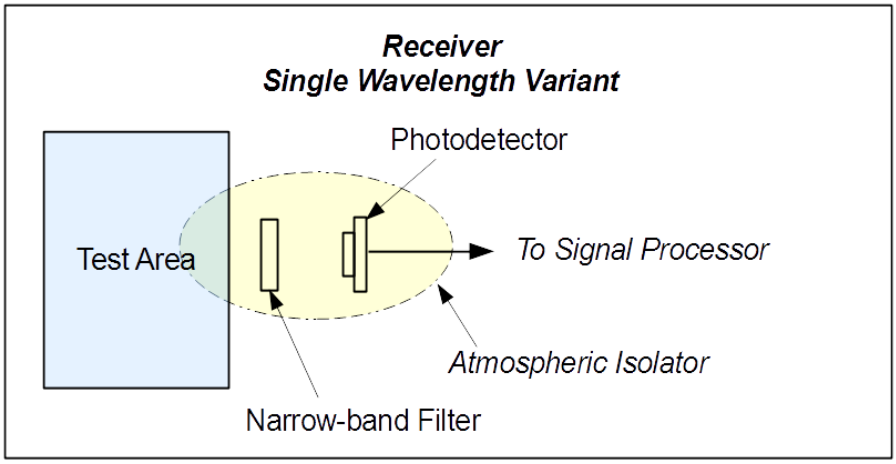

Figure 4.9.: Schematic layout of single wavelength receiver

Signal processor. The signal processor receives signals from the receiver, compares the signals, amplifies the output and sends it to the data recorder. Its design is based on that developed by Griffiths [1] which, in turn, built on the work of Hobbs [118] and Allen et al [87]. Griffiths [1] provides an excellent precis of the advantages and disadvantages of various detection and signal processing methods for TDLAS of transient hypersonic flows.

4.2. Physical Design

Laser controller. A Thorlabs PRO8000 Laser Controller with ITC8102DS15 modules provided power to two Thorlabs TCLDM9 thermo-electric control (TEC) mounts. The laser controller interfaced with a control computer via a General Purpose interface Bus (GPIB) connection allowing it to be controlled via SCPI[1] commands. The mount uses an Analog Devices AD590 integrated circuit temperature transducer to control laser diode temperature. Table 4.1 lists the specifications for the ITC8102DS15 laser diode and TEC controller.
The Thorlabs PRO8000 laser controller specification stated that the unit could be remotely controlled via either RS232 or GPIB connections. An Ines GPIB-USB-2 interface was used to provide a General Purpose Interface Bus (GPIB) that connected instruments to a desktop computer. This interface was compatible with IEEE 488.1 and IEEE 488.2, could control up to 15 devices and operated at up to 480 MBs^{-1}.

Table 4.1.: Laser diode controller specifications [119]

Parameter	Value
Injection current range	0 to ± 1 A
Resolution	15 μA
Accuracy (Full scale)	$\pm 0.1\%$
Noise without ripple (10 Hz to 10 MHz, RMS)	< 10 μA
Ripple (50 Hz, RMS typical)	< 1.5 μA
TEC current range	-2 to 2 A
Maximum output power	16 W
AD590 control range	-12.375 to 90 °C
AD590 resolution	0.0015 °C
AD590 accuracy	± 0.1 °C
AD590 temperature stability	< 0.001 °C

TEC mount. The TEC mount has a radio frequency (RF) modulation input that allows the laser to be modulated through a bias-T network. The manual for the TCLDM9 TEC mount stated that the

[1] Standard Commands for Programmable Instruments

Table 4.2.: Laser diode specifications [120]

Parameter	Minimum	Typical	Maximum
Temperature (°C)	15	25	35
Bias current (mA)		50	100
Injection current (mA)	15	100	200
Output power (mW)	0	2.5	5
Bandwidth (MHz)		10	20
Far-field FWHM - Lateral		27°	30°
Far-field FWHM - Vertical		55°	60°

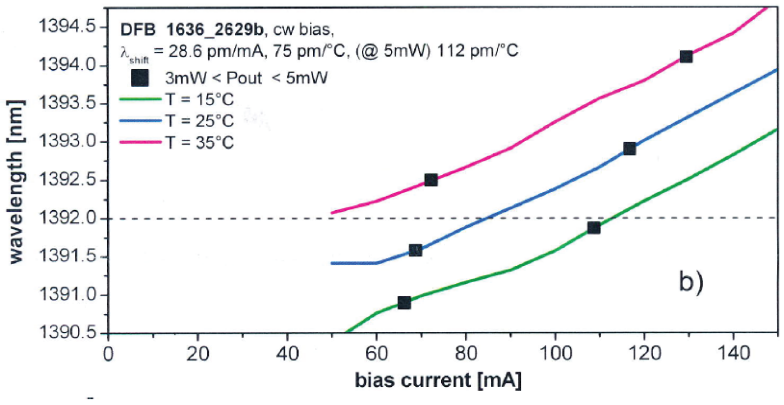

Figure 4.10.: Laser diode SN 1636 - wavelength versus current calibration [121]

RF modulation frequency range was 100 kHz to 500 MHz with an input impedance of 50Ω and a maximum RF power of 200 mW.[2]

Laser diodes. Specdilas DFB1392 distributed feedback laser diodes in small outline transistor (SOT) 5.6 packages were fitted to the mounts. Table 4.2 lists the laser diode specifications. The manufacturer provided calibration curves for each laser diode. Figures 4.10 to 4.15 show the manufacturer's calibration data for laser diodes SN 1636, 1243 and 1743 respectively. Typically, $3-4$ mW output power was achieved at wavelengths used for this study. The laser diodes were tunable across wavelength ranges of $1391.5-1393.0$ nm at diode temperatures of $15-35$ °C.

[2]During the laboratory experiments, I was not able to detect modulation at 100 kHz. Technical staff at Thorlabs later advised that the minimum RF modulation frequency was 500 kHz. This limitation considerably influenced the experiments because it restricted the equipment that could be used to extract harmonic signals.

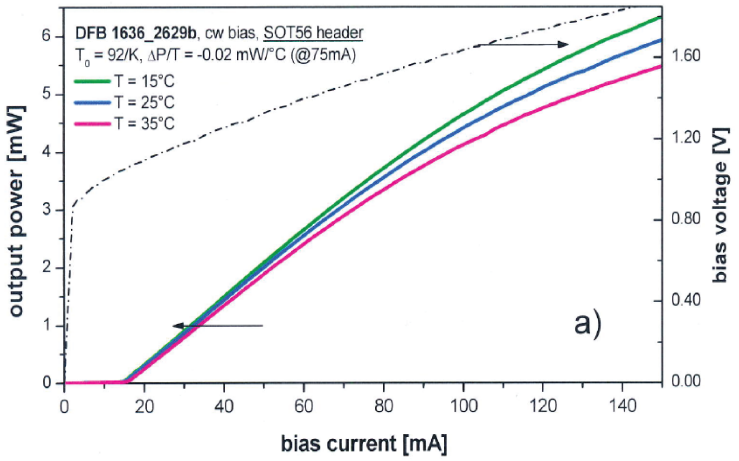

Figure 4.11.: Laser diode SN 1636 - output power versus current calibration [121]

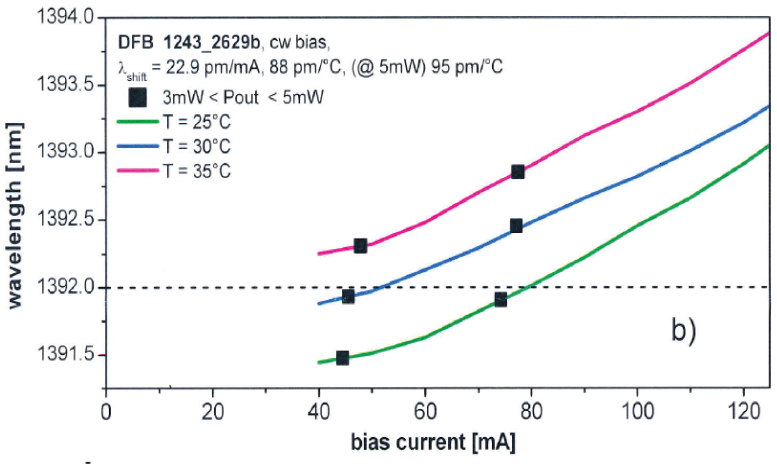

Figure 4.12.: laser diode SN 1243 - wavelength versus current calibration [122]

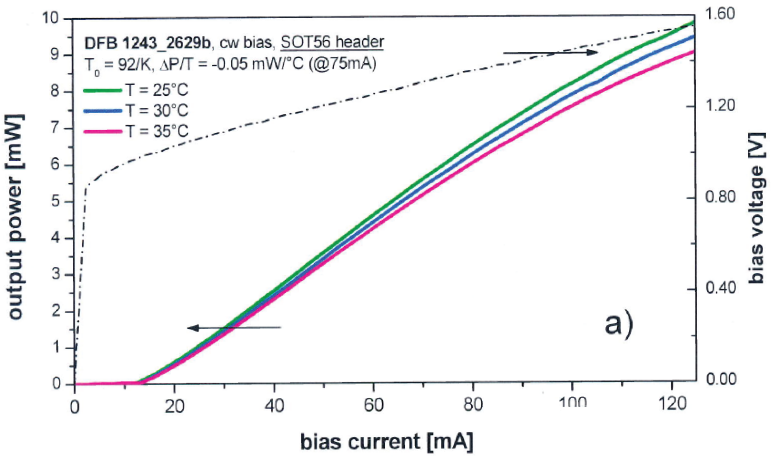

Figure 4.13.: Laser diode SN 1243 - output power versus current calibration [122]

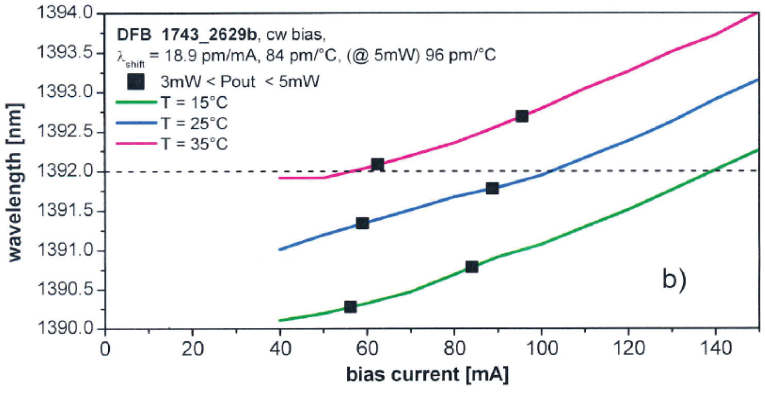

Figure 4.14.: Laser diode SN 1743 - wavelength versus current calibration [123]

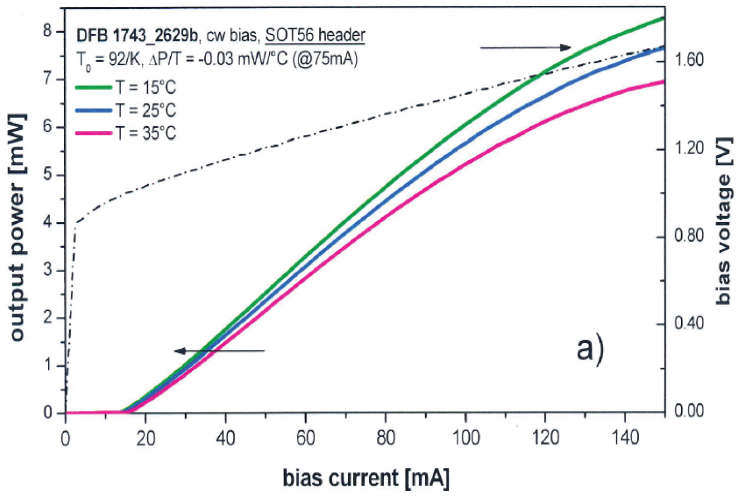

Figure 4.15.: Laser diode SN 1743 - output power versus current calibration [123]

Collimating lens, Laser diode output was collimated using Thorlabs C230TMD-C mounted aspheric lenses. The lens properties are listed in table 4.3.

Optical isolator. An OFR IO-4-1392-VLP narrow band adjustable isolator with a 4.0 mm aperture, more than 95% transmittance and more than 40 dB isolation was used. The isolator could be tuned within $\pm 5\%$ of the wavelength and was in a type VIIa form.

Beam-splitter. Thorlabs BP108 pellicle beam-splitters with a clear aperture of 25.4 mm and split ratio of 8% reflectance and 92% transmittance were used to split the laser beams when required.

Table 4.3.: Aspheric lens PN C230-TMD-C specifications [124]

Parameter	Value
Material	D-ZLaF52LA
Refractive index	1.793 ± 0.002
Design wavelength	780 nm
Clear aperture	5.07 mm
Effective focal length	4.51 mm $\pm$ 1%
Numerical aperture	0.55
Working distance from mount to laser window	2.43 mm
Focal shift at 1400 nm	0.95 mm

Fibre ports and cables. Tables 4.4 and 4.5 list the specifications of the Thorlabs fibre ports and optical fibres that were used in this system.

Table 4.4.: Fibre Port Characteristics (Source: Thorlabs)

	Model	
Parameter	**PAF-X-11-PC-C**	**PAF-X-15-PC-C**
Equivalent Focal length (mm)	11.0	15.4
Input Mode-field diameter (μm)	10.4	
Output Waist Diameter (mm)	2.1	2.9
Maximum Waist Distance (mm)	1100	2200
Divergence (mrad)	0.95	0.68
Clear Aperture (mm)	4.4	5.0
Numerical Aperature	0.20	0.16
Anti-reflective coating wavelength (nm)	1050-1600	
Length (mm)	22.8	

Table 4.5.: Fibre-optic cable characteristics (Source: Thorlabs)

Parameter	**P1-980A-FC-2**	**P1-SMF28-FC-2**
Wavelength (nm)	980	1260-1625
Connector Type	FC/PC	FC/PC
Mode-field diameter (μm)	5.8 μm @ 980 nm	9.2 μm@1310 nm
	6.2 μm @ 1064 nm	10.5 μm@1550 nm
Numerical Aperture	0.64	0.14
Jacket Part No	FT030-Y	FT900SM
Length (m)	2	2

Figure 4.16 shows how the end reflectivity of anti-reflective coated cable varies with wavelength. At 1392 nm, the reflectivity is approximately 0.7% making the return loss:

$$\text{Return Loss} = 10\log\left(\frac{1}{0.007}\right) = 21.5 \text{ dB}. \tag{4.1}$$

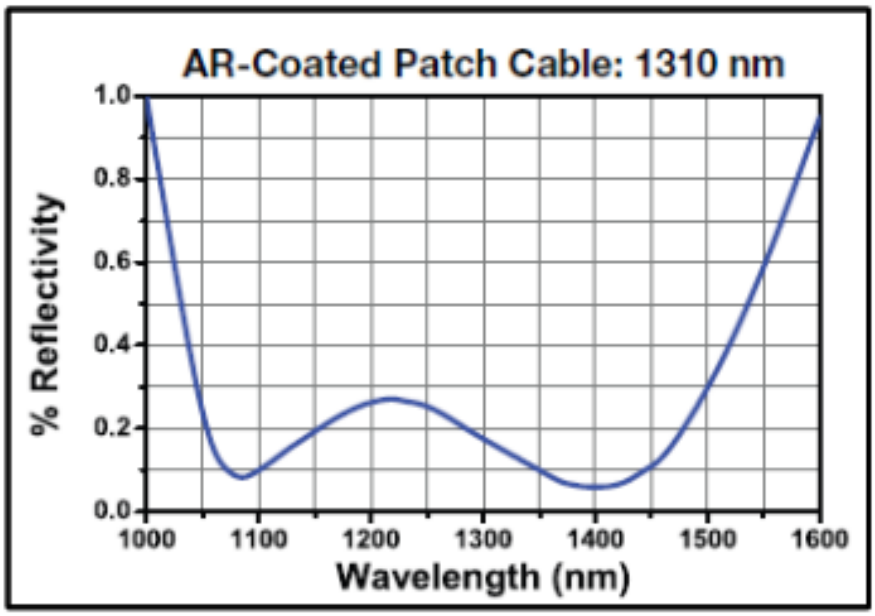

Figure 4.16.: End reflectivity of anti-reflective coated cable PN P1-SM28-FC-1-13 (Source: Thorlabs)

Photodetectors. Thorlabs FGA21 photo-diodes were used to detect the laser beams during wavelength modulation spectroscopy measurements. Table 4.6 lists the relevant specifications for the photo-diodes.

Power meter and sensor. For direct absorption measurements, a Thorlabs PM100D power meter coupled with an S122C sensor was used to measure the laser power. The Thorlabs S122C is a compact photodiode power sensor that uses a germanium (Ge) detector to measure power in the range 50 nW to 40 mW across the wavelength range $700 - 1800$ nm with an aperture diameter of 9.5 mm. A non-volatile memory in the sensor connector contains sensor information data and the sensor's NIST traceable calibration data. Other relevant specifications for the sensor are listed in table 4.7. The PM100D power meter is designed to interface with the S122C sensor to measure the optical power of laser light. Table 4.8 lists the relevant specifications for the PM100D power meter. The power meter can interface with a control computer via a USB[3] connection.

Receiver. The remainder of the receiver components were used in the scramjet experiments. They are described in appendix E sections E.10 to E.12 for the amplifier, data recording and signal extraction respectively.

4.3. Laser diode calibration

Each laser diode was calibrated to determine the relationships between TEC temperature, laser diode current, output power and wavelength. The PRO8000 controller was interfaced with a computer via a GPIB cable. This allowed remote control of the laser diode operating parameters and ensured

[3]Universal Serial Bus

Table 4.6.: Thorlabs FGA21 photodiode specifications [125]

Parameter	Value
Wavelength range	$800 - 1800$ nm
Active area	2.0 mm diameter
Rise time	66.0 ns
Bandwidth	5.3 MHz
Noise equivalent power (NEP)	3.0×10^{-14} WHz$^{-\frac{1}{2}}$
Maximum dark current	200 nA
Maximum capacitance	500 pF
Maximum bias voltage	3 V
Responsivity (1392 nm)	0.9 AW^{-1}

Table 4.7.: Thorlabs S122C photodiode power sensor specifications [126]

Parameter	Value
Linearity	$\pm 0.5\%$
Resolution	1 nW
Measurement uncertainty[4]	$\pm 5\%$
Response time	< 1 μs

repeatability of tests. A Thorlabs PM100D power meter and Thorlabs S122C photodetector sensor were used to measure the laser intensity. The power meter interfaced with a computer via a USB cable allowing remote control of the power meter. A locally developed Python program was used to control the laser diode controller, obtain measurements from the power meter and analyse data. The TCLDM9 TEC mounts were set up so that the actual temperature was within $0.05°$ C of the set temperature across the range of anticipated TEC temperatures ($15 - 35°$C).

Figure 4.17 shows a schematic diagram of the calibration layout. The laser diodes were calibrated against wavelength by detecting water vapour features within the operating range of the diode. Fortuitously, the relative humidity in the laboratory was regularly above 50% making water vapour features quite prominent. The features were detected by setting the diode temperature then varying its current across the operating range. Any water feature would reduce the power received by a photo-detector. Table 4.9 lists the *HITRAN* properties of candidate water vapour features used for calibration of the laser diodes [57]. Initially, TEC temperature was varied from $15°$C to $35°$C in steps of $0.5°$C. For each run, the starting laser diode current ($I_{LD_{Start}}$), ending laser diode current ($I_{LD_{Stop}}$), number of current steps and TEC temperature were set. The TEC temperature was allowed to stabilise then the program stepped through the laser diode currents and measured the actual laser diode current $I_{ld_{Act}}$ and TEC temperature $T_{TEC_{Act}}$ as well as the power received after transit through the atmosphere.

The actual TEC temperature was plotted to confirm its stability. Power received was plotted against laser diode current for constant TEC temperature. *HITRAN* features were fitted to the observed features to derive wavelength-current calibration charts. Figure 5.4 shows the wavelength calibration

Table 4.8.: Thorlabs PM100D power meter specifications when used with an S122C sensor [127]

Parameter	Value
Analogue to digital converter	16 bit
Accuracy	$\pm 0.2\%$ full-scale (5 μA-5 mA) $\pm 0.5\%$ full-scale (50 nA)
Bandwidth	DC - 100 kHz

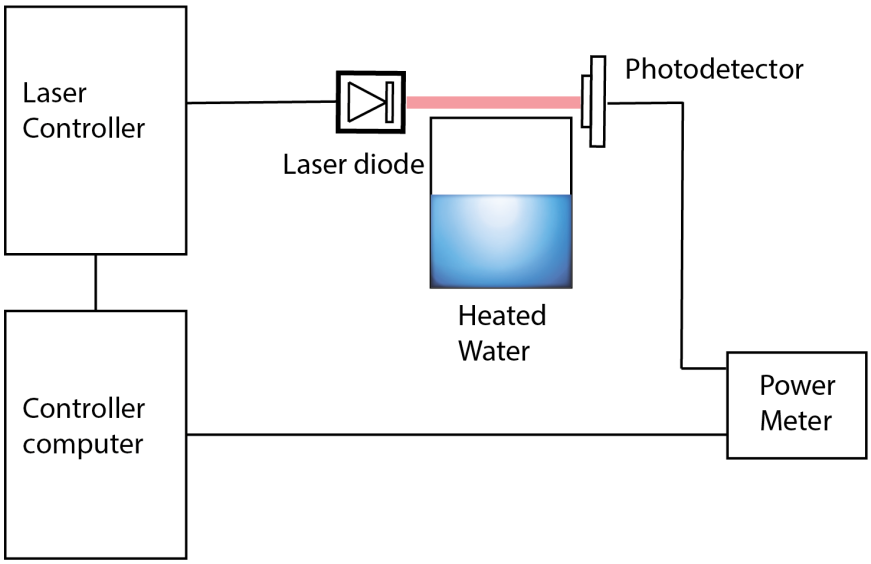

Figure 4.17.: Schematic diagram of laboratory test setup

curve for diode SN 1636 at a set TEC temperature of 19.5°C. The current-wavelength calibration equation is:

$$\lambda = 33.606 I_{ld} + 1388.9 \tag{4.2}$$

where λ is in nm and I_{ld} is in amperes. A linear least-squares regression between the current and wavelength produced a correlation coefficient of $R^2 = 0.9968$ indicating the linearity of laser diode current versus wavelength at constant laser diode temperature. Figure 4.19 shows the wavelength calibration curve for diode SN 1243 at a set TEC temperature of 19.5°C. The results from four tests are shown to demonstrate the repeatability of the results. The current-wavelength calibration equation is:

$$\lambda = 33.517 I_{ld} + 1389.0 \tag{4.3}$$

where λ is in nm and I_{ld} is in amperes. A linear least-squares regression between the current and wavelength produced a correlation coefficient of $R^2 = 0.9992$. Figures 4.20 and 4.21 show the power

Table 4.9.: Properties of water features used for wavelength calibration [57]

Wavenumber (cm^{-1})	Wavelength (nm)	Intensity ($cm\ molecule^{-1}$)	γ_a (cm^{-1})	γ_S (cm^{-1})	E_{low} (cm^{-1})	r
7179.75201	1392.8058	1.802×10^{-22}	0.0456	0.265	1216.1945	0.61
7180.39972	1392.6801	5.608×10^{-22}	0.098	0.500	225.8384	0.69
7181.15578	1392.5335	1.505×10^{-20}	0.1008	0.488	136.7617	0.71
7182.20911	1392.32927	1.541×10^{-21}	0.107	0.375	42.3717	0.76
7182.94962	1392.1857	3.752×10^{-21}	0.097	0.51	142.2785	0.71
7185.596571	1391.6729	1.995×10^{-22}	0.0342	0.371	1045.0583	0.62
7185.596909	1391.6728	5.984×10^{-22}	0.0421	0.195	1045.0577	0.62

versus current calibrations for laser diodes SN 1243 and SN 1636 respectively. A TEC temperature of 19.5°C was selected for all experiments. At this temperature, each laser diode was able to target a feature of interest at an acceptable power level. Power versus current and wavelength versus current polynomials were recorded. These calibration charts were used in later experiments to set the TEC temperature and laser diode current to accurately target individual features. The calibration charts in figures 4.13 to 4.14 were found to be accurate representations of the current-wavelength relationships. The current-power relationships in the figures accurately depicted laser diode performance provided allowance was made for collimation losses.

4.4. Summary

This chapter provided information on the hardware and software used for TDLAS experiments conducted as part of this research. It also provided information on wavelength calibration and presented the calibration charts for the laser diodes used in later experiments. The process of calibrating and collimating the laser diodes, mounts and lens combinations provided valuable training and experience in operating the system and optimising its optical performance.

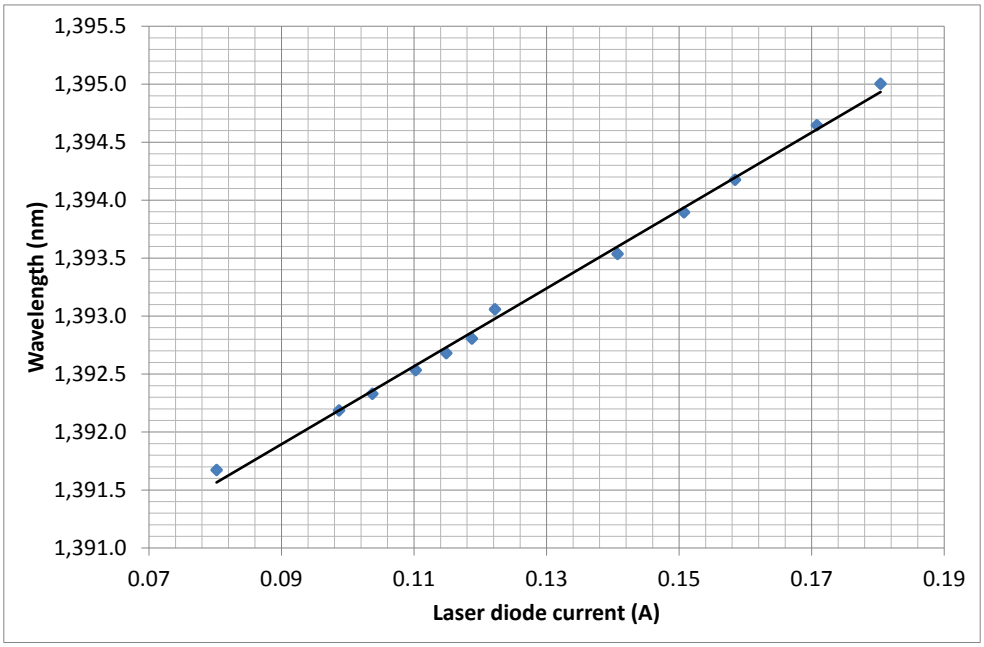

Figure 4.18.: Wavelength calibration chart for laser diode SN 1636 at a set TEC temperature of 19.5°C

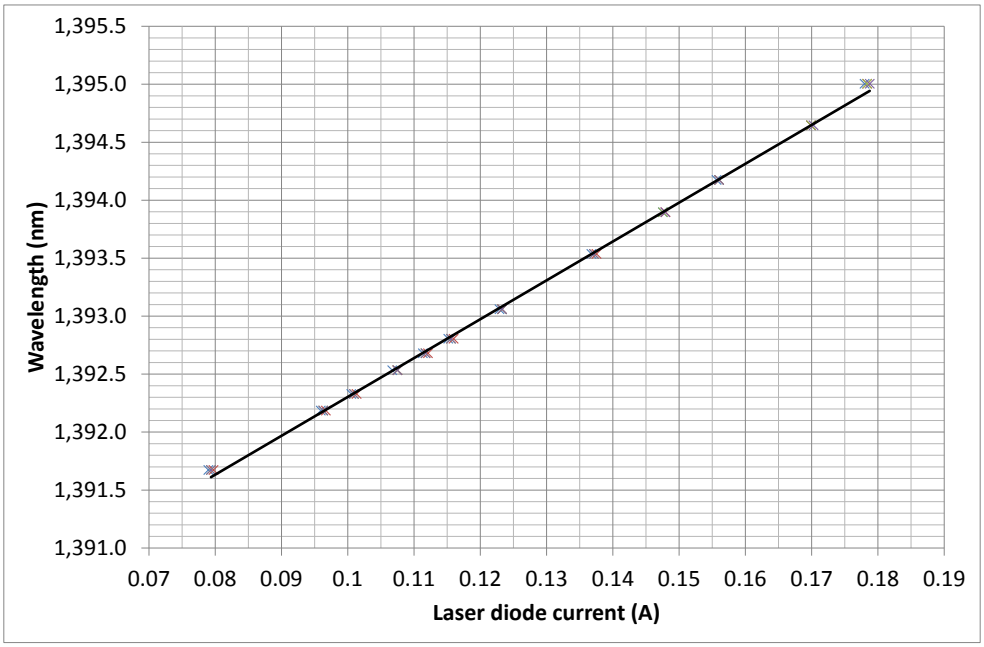

Figure 4.19.: Wavelength calibration chart for laser diode SN 1243 at a set TEC temperature of 19.5°C

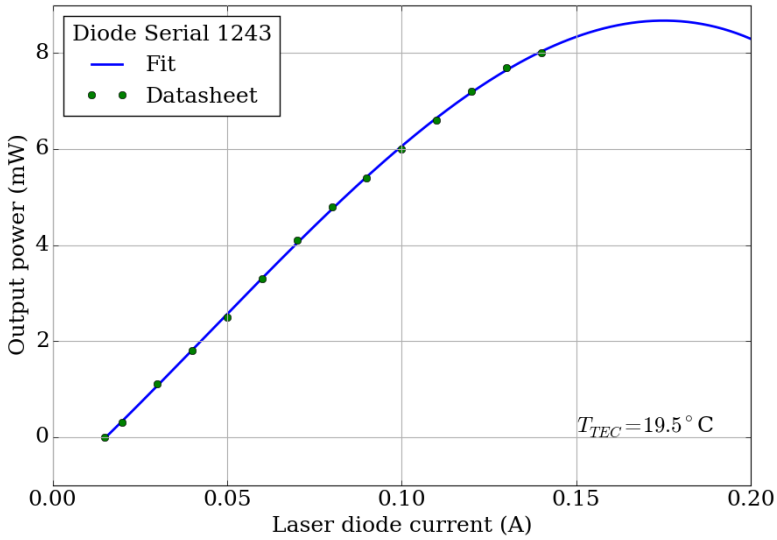

Figure 4.20.: Power calibration plot for laser diode SN 1243 at a set TEC temperature of $19.5°$C

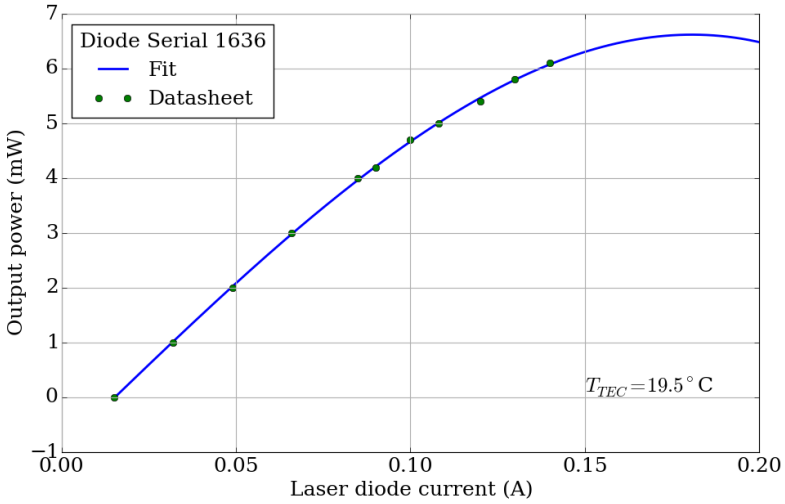

Figure 4.21.: Power calibration plot for laser diode SN 1636 at a set TEC temperature of $19.5°$C

5. Steam Ejector Experiments

Before using it in short test-time experiments, the TDLAS system was used to measure the properties of the flow at the exit from a steam ejector located at the University of Southern Queensland (USQ). The steam ejector produced a continuous, high-speed water vapour flow that was easily accessible and operated in a workshop environment. This made it suitable for developing direct absorption test procedures and techniques. This chapter begins by describing the TDLAS system and target spectral lines. Next, steam ejectors and their flows together with the rig at USQ are discussed. The experimental results are presented along with three methods of extracting the flow properties from the experimental data. These techniques are compared for accuracy and ease of use.

5.1. Experimental Setup

During his PhD candidature at the University of Southern Queensland, Ghassan Al-Doori developed a steam ejector to provide refrigerated air in hot climates [128]. Al-Doori measured the ejector exit flow total pressure with a traversing pitot probe but did not measure the temperature of the flow. The author was asked to devise a method of using TDLAS to measure the flow temperature at the ejector nozzle exit. For the initial experiments, the laser diode and photodetector viewed the flow through perspex windows of the test section. This layout was not successful as the windows absorbed the laser, atmospheric pressure broadened the spectral lines and stray light from the laboratory influenced the signal received by the photodetector. The setup was changed incrementally to eliminate these sources of uncertainty. The TDLAS system was covered by a blackout curtain to eliminate stray light. Sight tubes were placed through the perspex windows and these tubes were purged with dry gaseous nitrogen to eliminate atmospheric absorption.

The sight tubes did not influence the ejector flow as they terminated outside of the flowstream. The tubes were capped with perspex windows near the ejector. To avoid etalon effects due to these windows, the TDLAS beam was not fully collimated. This reduced the power received by the photodetector slightly but eliminated any etalon effects. The beam diameter was measured using a luminescent card as being approximately 2.0 ± 0.5 mm at the photodetector and 1.5 ± 0.5 mm at the nozzle centreline. Given that the nozzle diameter was 17 mm, the laser beam diameter had a minimal effect on measurements.

Al-Doori reported [128, Figure 7.18] that the flow at the exit of the nozzle was extremely uniform with a shear layer of approximately 2.0 mm thickness there. Thus, flow property variation along the laser beam line of sight was anticipated to have some influence on the TDLAS measurements. This influence was expected to affect the measured temperature but not the pressure. The sight tube

windows were aligned with the nozzle outlet in an attempt to minimise this influence.
The nitrogen purging system was validated by operating the system with and without purging. When there was no purging, the wings of the spectral lines were broadened significantly. With purging, the wings were much smaller and the spectral lines accurately reflected the pressure and temperature conditions in the test section when there was no flow present. These conditions were measured independently via a pressure transducer and thermocouple when there was no flow present.

5.2. TDLAS Equipment

The TDLAS equipment included a Thorlabs PRO8000 Laser Diode Controller fitted with Thorlabs ITC8052 combined laser diode/thermoelectric controller (LD/TEC) modules, a Thorlabs TCLDM9 laser diode mount with Laser Components DFB1392 laser diode, and a Thorlabs PM100D Power Meter fitted with a Thorlabs S-122C Power sensor.
The power emitted and wavelength of the laser diode depend on the thermoelectric controller (TEC) temperature and the laser diode bias current. The laser diode used in the experiment has a wavelength range of approximately $1392.0\text{ nm} - 1393.0\text{ nm}$ $(7189.07260\text{ cm}^{-1} - 7168.45878\text{ cm}^{-1})$ when the TEC temperature is set in to $19.5°$C. The experiment layout is shown in figure 5.1. Copper sight tubes with diameters of 12.7 mm were used to reduce the water vapour absorption path length through the test section. These tubes were sealed at the test section by 1 cm thick polycarbonate windows. There was a 15 mm gap between the polycarbonate windows at the nozzle. The sight tubes were purged with gaseous dry nitrogen to eliminate absorption by atmospheric water vapour. Retractable covers were used to protect the polycarbonate windows from water droplet contamination during steam flow establishment. The covers were raised when there were no droplets visible in the ejector flow. The ejector was operated for up to one hour without any condensation accumulating in the test section. The laser diode mount was placed so that the laser radiation was normal to and directed across the mid-point of the ejected flow. The laser beam had a waist diameter of approximately 2 mm. The sensor for the power meter was positioned opposite the laser diode mount across the test section. The sensor was positioned to maximise the power received from the laser with no flow through the test rig. The distance between the mount and the sensor was 160 ± 2 mm.
The diode temperature of $19.5°$C was selected as it provided a moderate output power whilst spanning the wavelengths of interest. The TEC in the laser diode mount maintained the laser diode temperature within a range of $\pm 0.005°$C. The laser diode current was previously calibrated against wavelength at the operating temperature as discussed in chapter 4.
To avoid etalons and interference due to the windows, the laser was not fully collimated. The beam divergence angle was estimated to be approximately $10°$. This simple technique reduced interference fringes and improved the system performance over a wide range of laser diode currents for a relatively small cost in laser power transmitted through the test section.

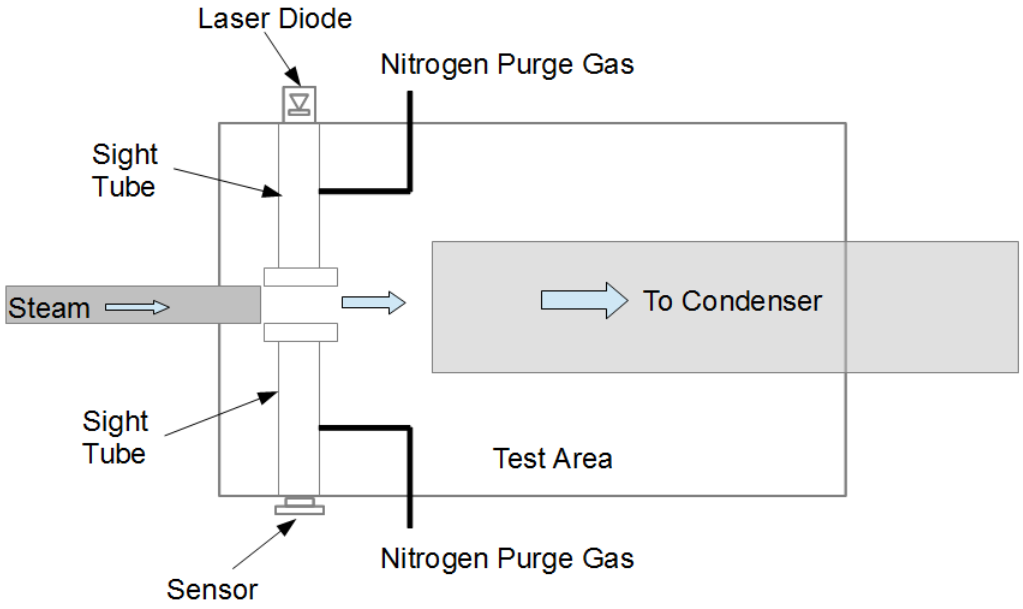

Figure 5.1.: Schematic diagram of the test section showing the steam flow direction, sight tubes, nitrogen purge gas lines, laser diode and photodiode.

5.2.1. Target Features

Table 4.9 lists *HITRAN* [57] data for the features at and near the target wavelength. The data includes the wavenumber of the centreline, the centreline wavelength, the intensity, the air-broadened HWHM (γ_a) of the lineshape, the self-broadened HWHM (γ_s), the energy of the lower transition level (E_{low}) and the coefficient of the pressure-shift (r). The target feature for this experiment was the strong absorption peak at 7181.156 cm^{-1} 1392.533 nm.

For a given pair of lines, the intensity ratio is a function of temperature only. The peak sensitivity for a specific pair of lines occurs at:

$$\begin{aligned} T &= \left(\frac{hc}{2k}\right)\left(E_{low}^{(1)} - E_{low}^{(2)}\right) \\ &= 0.72\Delta E \end{aligned} \tag{5.1}$$

where T is in kelvin and ΔE is the difference in the energies of the lower transition states for the lines (in cm^{-1}). The most sensitive line pair for a temperature range does not necessarily correspond to a line pair with a relative maximum in that range as the sensitivity depends also on the ratio of the transition probabilities of both lines. The partial pressure of water vapour can be found once the temperature, line strength and path length are known. The mole fraction of water vapour, x, can then be found using the total pressure, P, and the partial pressure of water vapour P_p [90]:

$$x = \frac{P_p}{P} \tag{5.2}$$

5.3. Steam ejectors

Cooling and heating systems typically use natural or synthetic working fluids that contribute to global warming. Refrigeration and air conditioning systems are also often driven by electricity further contributing to fossil fuel consumption and global warming. As an alternative to these systems, ejectors or jet pumps can be used in conjunction with waste energy or solar energy in refrigeration or air conditioning systems. Whilst ejectors have very low efficiencies when compared with conventional pumping systems, they can be cheaper to operate than mechanical pumps due to the absence of moving parts, high reliability and stable operation [128].
An ejector expands steam through a convergent-divergent nozzle to develop high-speed, low pressure flow that is used to entrain a secondary flow. The ejector design significantly affects the performance of a refrigeration system. There have been varying levels of success in computationally simulating the pressure and temperature distributions within the mixing region of ejectors. The flow there is complex due to strong turbulent mixing, high speed compressible vapour, large pressure gradients and the presence of shock waves. These factors also contribute to uncertainty in the measurement of pressures, temperatures and mixture concentrations in the mixing region.
A steam ejector consists of a steam generator, an ejector and a condenser plus the associated control equipment. The steam generator produces steam at pre-determined conditions. The ejector in turn consists of a convergent-divergent primary nozzle that ejects the steam flow within an axi-symmetric nozzle containing a second flow. The flow conditions at the nozzle exit depend on whether the flow is supercooled or has some amount of condensation.

5.3.1. USQ steam ejector rig

The steam ejector rig is described in detail in reference [128]. It consists of a steam generator, an ejector, a condenser and a control panel. The steam generator generates super-heated steam at stagnation pressures between 200 kPa and 300 kPa and stagnation temperatures up to $150°$C. The steam flows to the test section where it forms the primary flow. This primary flow entrains a secondary flow of air or other fluid when it is ejected from the nozzle into the test section. The test section consists of the nozzle, a pitot probe, a bellmouth inlet to a diffuser and observation windows. The ejected flow is condensed in the condenser.
Figure 5.2 shows the steam generator and ejector rig at the University of Southern Queensland with the important components indicated. Figure 5.3 is a schematic diagram of the ejector nozzle. The nozzle has a throat diameter of 3.2 mm and an axi-symmetric expansion with a semi-angle of $5°$, a length of 59.5 mm and an exit diameter of 13.9 ± 0.3 mm. The nozzle area ratio is approximately 18.9.

5.3.2. Steam ejector flow

During expansion, steam may be treated as either an ideal gas [129], an isentropic expansion of the mixture [130] or a sudden expansion of the water vapour-air mixture [131, 132]. The outlet conditions from the ejector lie between the limits of the ideal gas model and the isentropic expansion model.

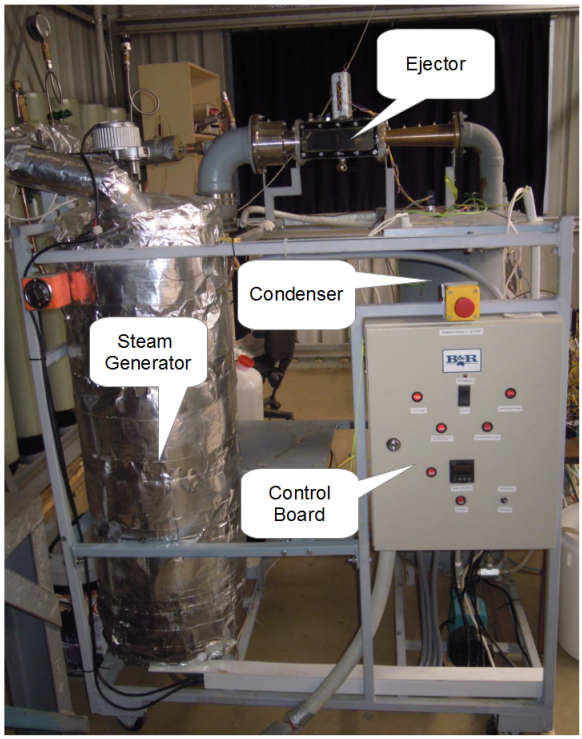

Figure 5.2.: USQ Steam Generator and Ejector Rig.

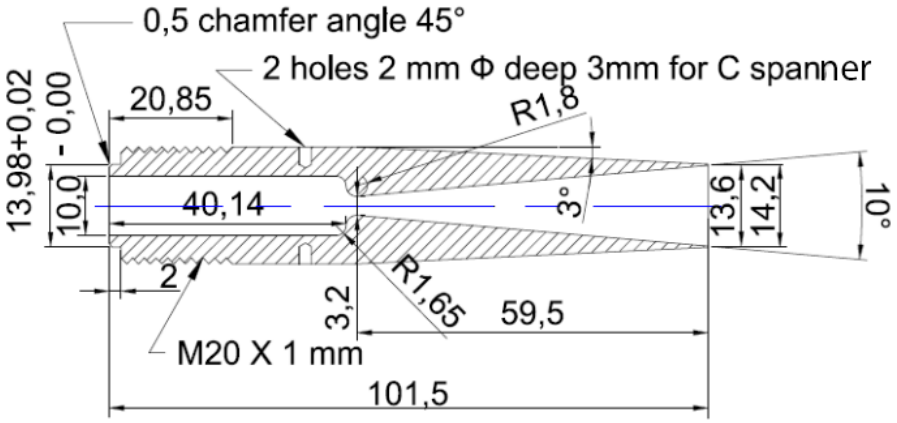

Figure 5.3.: Schematic diagram of the ejector nozzle design showing the principle dimensions. [128]

Whilst steam ejector flow appears to be simple and uncomplicated, it is, in fact, very complex due to supercooling of the water vapour and subsequent condensation. Condensation increases the rotational temperature due to the latent heat of vaporisation [133]. The released condensation energy increases the translational temperature and then the rotational temperature due to the translational-rotational relaxation [133].

Ejector flow consists of a primary nozzle with convergent and divergent sections and a secondary flow that is induced by the primary flow. The flow in the convergent section may be modelled using ideal gas assumptions because the steam is in the superheated state everywhere in this section. The throat properties can be calculated using a fixed ratio of specific heats (γ) or by changing γ with temperature. Depending on the value of γ and the generator pressure, the throat conditions vary considerably with consequent impact on the nozzle performance.

The steam in the ejector is initially dry superheated before becoming dry supercooled in the nozzle, condensing then being in wet equilibrium. Water vapour has a wide range of stagnation states from which an expansion isentrope intersects the vapour-liquid coexistence line. Expansion in supersonic nozzles is typically so rapid that the fluid departs radically from the equilibrium phase distribution and forms metastable phases that lie at local (but not global) minima of free energy and are resistant to small fluctuations [134].

Figure 5.4 shows the process of steam expansion and spontaneous condensation in a convergent-divergent nozzle. On entering the nozzle, the steam is dry superheated steam at condition $(\mathbf{1})$. The flow is sonic at the throat of the nozzle $(\mathbf{2})$ then expands as, initially, dry superheated vapour until the saturation point $(\mathbf{3})$ is reached.

On reaching the saturation point, the flow continues to expand as a dry supercooled vapour. The dry supercooled state is a metastable phase of the steam where the density of the vapour is higher than the density of the saturated vapour at the same pressure and the temperature is less than the saturation temperature at that pressure. The dry supercooled vapour expands until the onset of nucleation at the Wilson Point $(\mathbf{4})$ where the supersaturated condition ends. The Wilson Point is the point of maximum supercooling and is defined as [135]:

$$\Delta T = T_s\left(P\right) - T_G \tag{5.3}$$

where $T_s\left(P\right)$ is the saturation temperature at pressure P and T_g is the local vapour temperature.

Following the Wilson Point, the vapour stops expanding isentropically as it enters a zone of rapid condensation due to homogeneous nucleation. When the flow condenses, a portion of the vapour phase is removed and the remaining flow is heated by the energy extracted from the condensed phase [134]. Usually, the enthalpy change during condensation (h_{fg}) is larger than the product of the specific heat and local temperature so the heat transfer due to condensation has a larger effect on the stream properties than the vapour removal. As a result, condensation in supersonic flow increases the stream pressure and temperature.

The condensate particles are usually less than $1\ \mu$m in diameter making velocity slip between the vapour and liquid phases negligible [134]. This process continues until the flow reaches the wet equilibrium state $(\mathbf{5})$ after which the flow again expands isentropically until the nozzle exit $(\mathbf{6})$ [136].

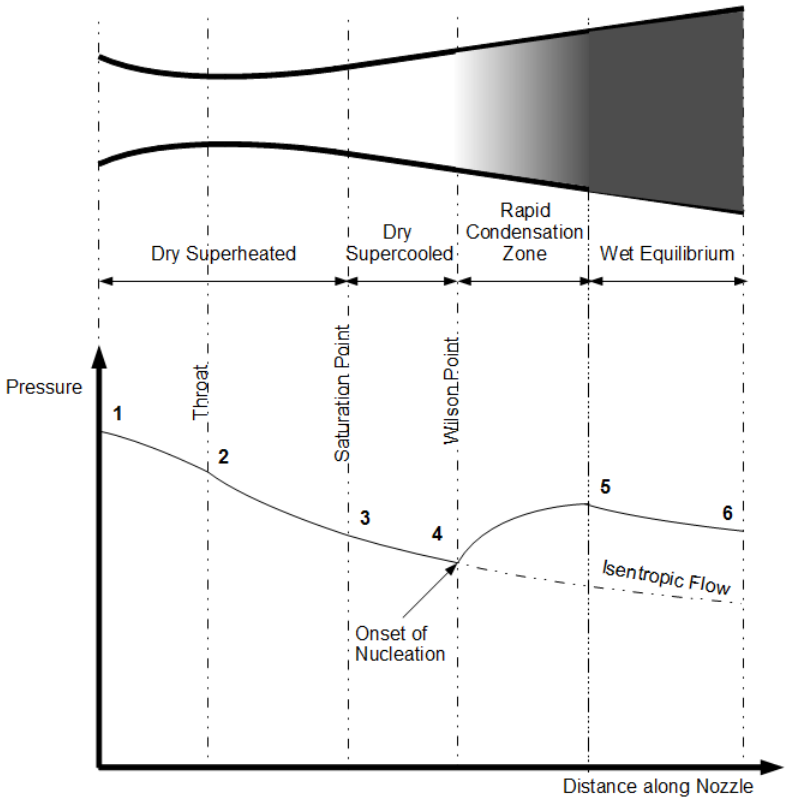

Figure 5.4.: Spontaneous condensation in a steam ejector (Adapted from [136])

The enthalpy drop during the expansion is less than if the flow were isentropic and the flow velocity out of the nozzle is less than the isentropically calculated velocity. The effect of supersaturation is that the steam discharge is approximately 5% greater than that calculated from the equilibrium data for steam at a given throat area.
Condensing flow is a special case of compressible fluid flow with friction and heat addition (due to condensation) with mass flow rate changes. The droplet formation and growth equations may be combined with one-dimensional gas dynamics equations to describe the flow. Notwithstanding these issues, ejector flow is often modelled assuming ideal gas behaviour.

5.3.3. CFD results

Figure 5.5 shows the relationship between the ejector nozzle, test section and flow diffuser. This configuration was modelled using CFD by a PhD candidate from the University of Southern Queensland.[1] The following conditions, typical of those encountered during these experiments, were used for the model:

- Generator stagnation pressure - 274 ± 2 kPa,
- Generator stagnation temperature - 416 ± 2 K,
- Test Section pressure - 6235 ± 20 Pa,

[1] Kavous Ariafar

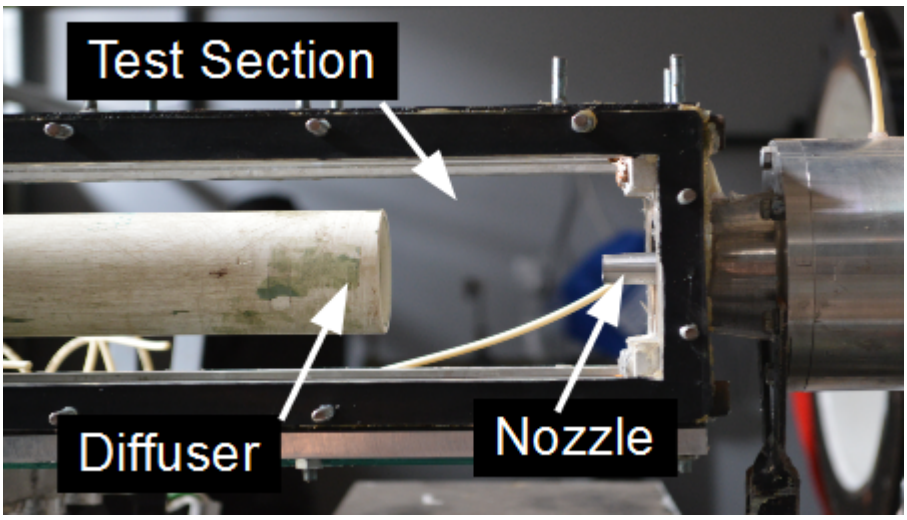

Figure 5.5.: Photograph of ejector test section showing the relationship between the nozzle and the diffuser

- Test section temperature - 335 ± 2 K, and
- Condenser pressure - 2480 ± 130 Pa.

Figures 5.6 to 5.8 show the results of the CFD calculations for the ejector conditions. The flow velocity at the centre of the nozzle exit was calculated to be 1.15 kms^{-1} reducing to 120 ms^{-1} at 7 mm from the centreline via the profile shown in figure 5.6. The computed static temperature from the flow centre to 3 mm was 288 K before rising to 336 K at the edge of the flow as shown in figure 5.7. Static pressure was $2.25 - 2.88$ kPa out to 3 mm before rising to 6.0 kPa at the edge of the flow as shown in figure 5.8. The flow was saturated from the centreline out to 3.5 mm and was unsaturated outside that radius. Thus, the ejector flow properties varied substantially across the flow. Since

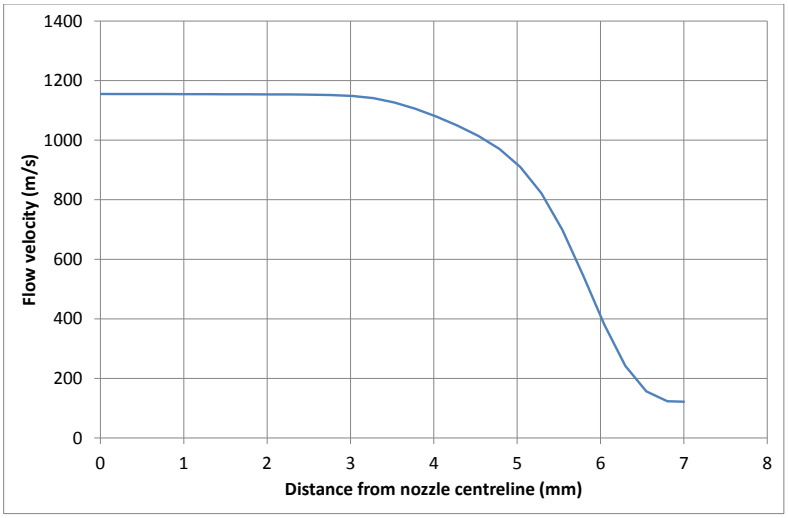

Figure 5.6.: CFD plot of velocity versus radial distance from nozzle centreline for the steam ejector at 15 mm downstream of the nozzle exit.

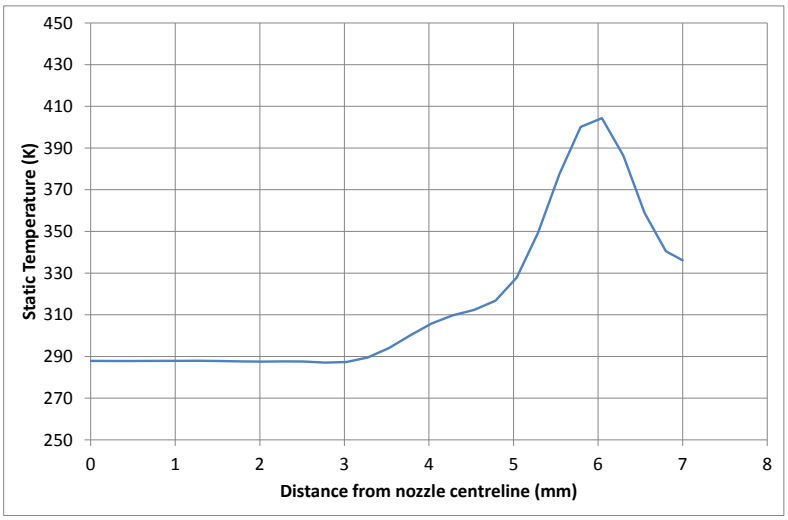

Figure 5.7.: CFD plot of static temperature versus radial distance from nozzle centreline for the steam ejector at 15 mm downstream of the nozzle exit.

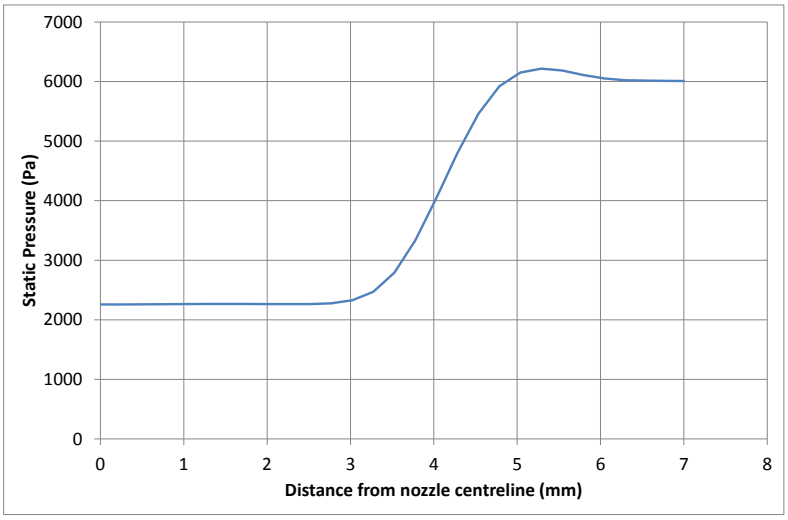

Figure 5.8.: CFD plot of static pressure versus radial distance from nozzle centreline for the steam ejector at 15 mm downstream of the nozzle exit.

TDLAS is a line of sight tool that integrates absorption along the beam path, it was expected to show the average, or ensemble, properties across the ejector flow.

5.4. Test method

Tests were performed in a graduated sequence beginning with atmospheric absorption and ending with tests using the operational steam ejector. The atmospheric absorption experiments aimed to verify the system performance after moving it from The University of Queensland to The University of Southern Queensland. In this section, the most important aspects of the experiments are disclosed together with a mixture of raw and processed data that is aimed to highlight the processing methodology to the reader. Figure shows the wavelength calibration curve for diode SN 1636 at a set TEC temperature of $19.5°$C. The current-wavelength calibration equation is:

$$\lambda = 33.606 I_{ld} + 1388.9 \tag{5.4}$$

where λ is in nm and I_{ld} is in amperes. A linear least-squares regression between the current and wavelength produced a correlation coefficient of $R^2 = 0.9968$ indicating the linearity of laser diode current versus wavelength at constant laser diode temperature. During the atmospheric absorption tests, the TDLAS system had a strong background reading from ambient lighting as evidence by spikes in the received power readings. This was reduced by covering the equipment with blackout curtains.

Figure 5.9 shows an absorption plot fitted to wavelength (blue line) and a spectrum derived from *HITRAN* using *HITRAN on the web* [60]. This plot shows broadening, especially for the experimentally observed feature at 1392.5335 nm. As this broadening reduced significantly when the sight tubes were purged with nitrogen, this broadening was believed to be due to absorption by atmospheric water vapour in the sight tubes. The *HITRAN* parameters were for a Voigt profile with a temperature of 313 K, a test section pressure of 10 kPa and atmospheric pressure of 94.3 kPa.

The polycarbonate absorbance was measured by placing either no, one or two sheets of 10 mm perspex in the light path and measuring the power received in each case. The test was performed six times to ensure repeatability. The measured absorbance was $7.0 \pm 0.2\%$ per sheet. The delivered steam and the test section temperatures were measured using K-type thermocouples. Steam delivery and test section pressures were measured using Wika Model A-10 pressure transducers and recorded using a Tektronix TDS-2024B oscilloscope. Reference [128] Appendix C contains details on the calibration of thermocouples and pressure transducers. Pressures and temperatures were recorded continuously during each test. Ambient pressure, temperature and humidity were manually recorded for each test.

5.4.1. No Flow Tests

Tests were conducted with the ejector test section evacuated but without steam flow through the ejector. The test section pressure was also applied above the condenser resulting in the test section atmosphere being saturated with water vapour. When the test section pressure reached the saturated

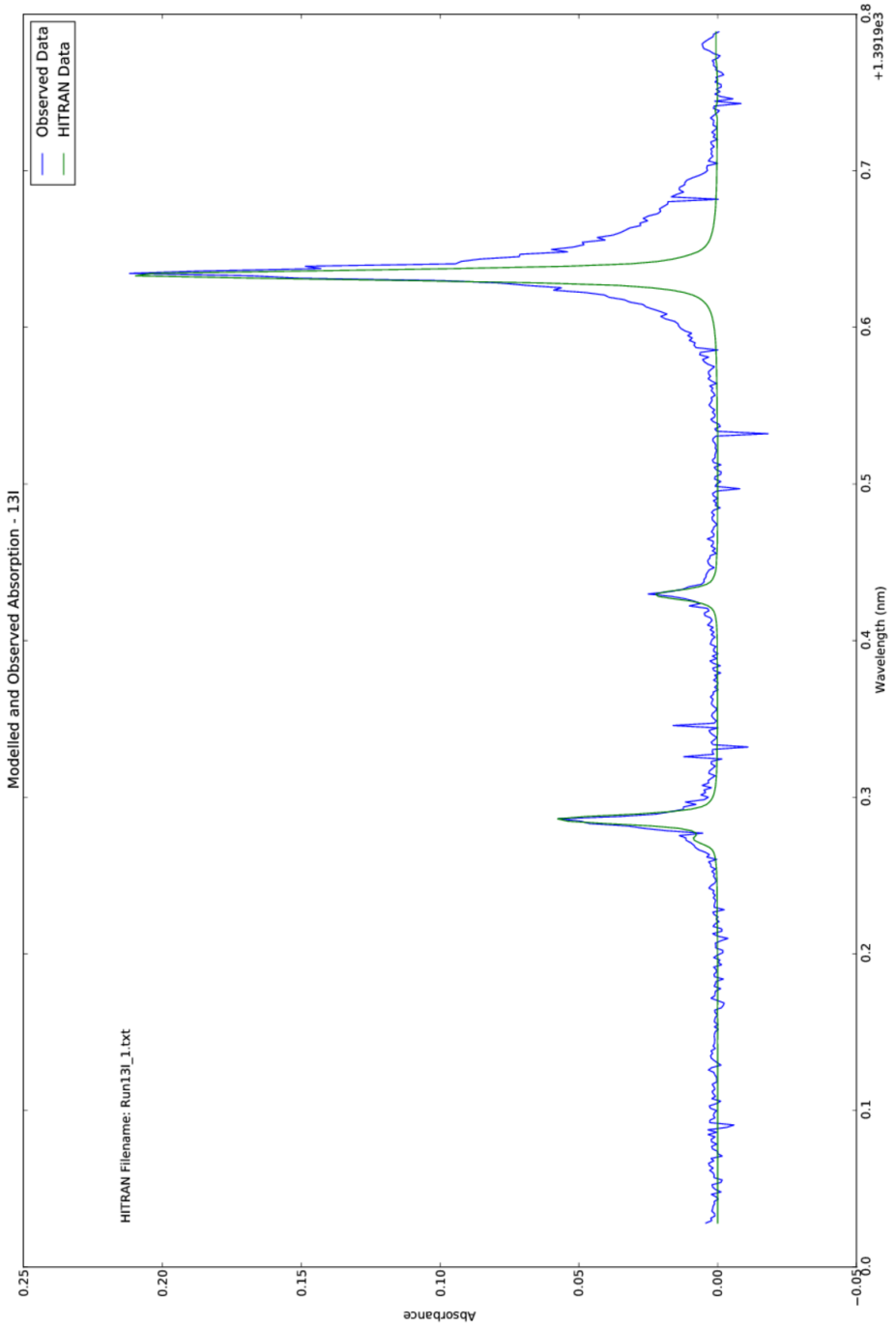

Figure 5.9.: Measured and simulated data for a no flow test without nitrogen purging. The broadening of the feature at 1392.5335 nm is due to atmospheric water absorption outside the test section.

Table 5.1.: Test section temperatures and pressures for no flow tests

Test	Temperature K	Pressure kPa
1	298 ± 1	6.8 ± 0.1
2	298 ± 1	5.0 ± 0.1
3	294 ± 1	4.5 ± 0.1
4	339 ± 1	6.5 ± 0.1

water vapour pressure appropriate to its temperature, the pressure could not be reduced further. Figure 5.10 shows a no flow test result where the laser diode current has been post-processed into wavelength and the received power has been converted to relative absorption. During this test, the test section temperature was 298 ± 1 K and the pressure was 6.77 ± 0.01 kPa as measured with the test section pressure transducer. Using the formula from Vehkamaki [135], the saturated vapour pressure of water at 298 K is 3120 Pa making the molar concentration of water vapour in those conditions 46.1%. Table 5.1 lists the test section conditions for the no flow tests. The steam generator was off for tests 1-4 allowing the test section temperature to be measured directly in those tests. The condenser was filled with water for tests 1 and 2 but was emptied before test 3; thus, the partial pressure of water vapour in the test section was significantly lower during test 3.

5.4.2. Steam flow tests

The test section was evacuated before a steady flow of water vapour was established through the nozzle. When the flow was dry[2], the window covers were raised and dry nitrogen was supplied to the sight tubes. During a typical test, laser diode current was increased from 115 mA to 140 mA in 400 steps. At each step, the laser diode current and temperature were recorded along with the power received by the power meter. Pressure and temperature data in the test section were recorded every 30 seconds using a National Instruments USB-6000 databox. Condensation has a significant effect on the laser path and the absorbed power from the laser. Condensation can cause intermittent scattering of the laser signal leading to changes in the received signal.

5.5. Analysis

The first analysis step involved conversion of the measured signals to optical frequency scales. The power received by the sensor is plotted against the laser diode bias current. This plot shows the four features used for later calibration and analysis. After eliminating outliers and the absorption features, a polynomial curve was fitted via a least-squares method to the power received curve to account for power variation with laser diode current. The power received was then converted to an absorption curve. Figure 5.11 shows a plot of absorbance versus wavelength for a test with adequate nitrogen

[2]Meaning that water droplets were not accumulating on the test section windows.

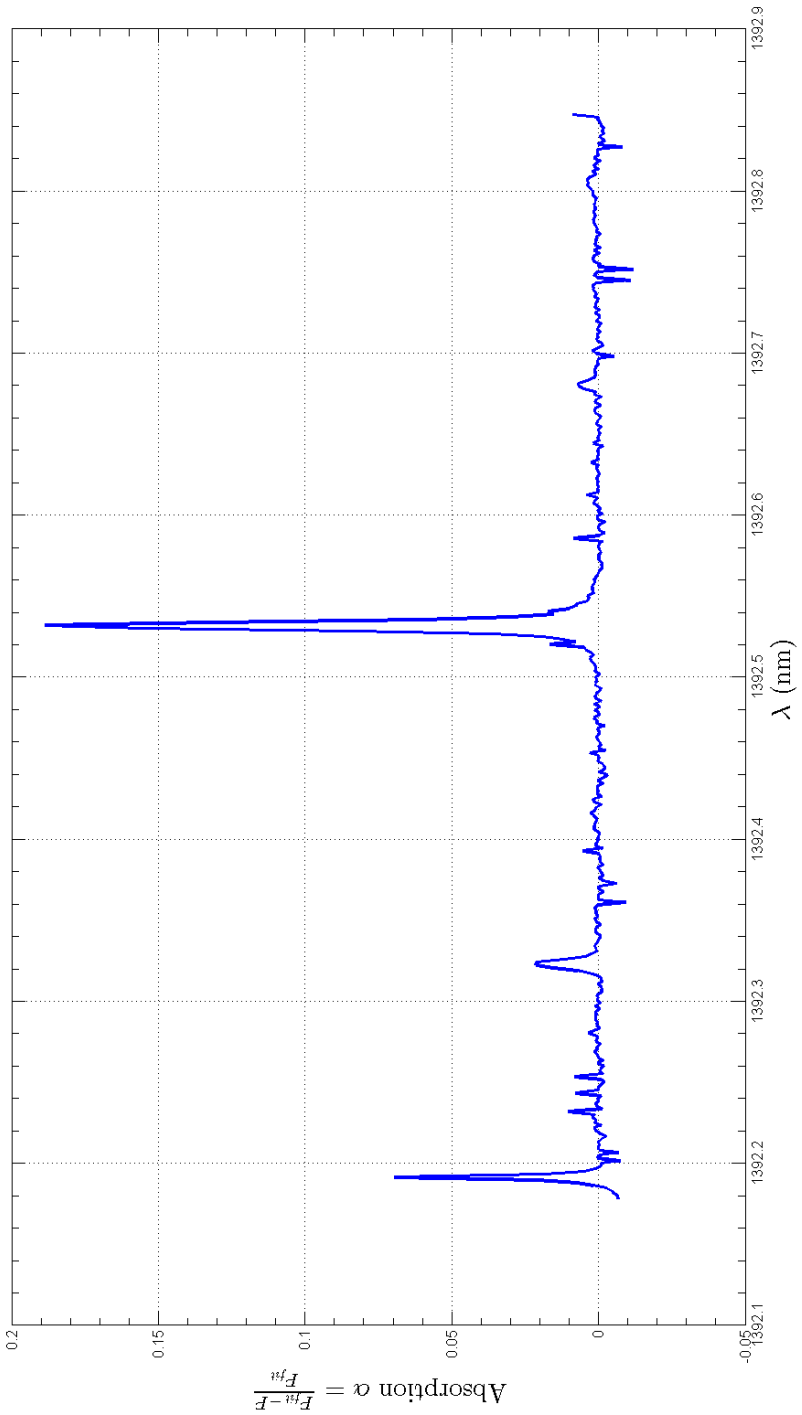

Figure 5.10.: Absorption versus wavelength for a typical no flow test. Test section temperature and pressure were 298 ± 1 K and 6.8 ± 0.1 kPa respectively.

purging. The *HITRAN* simulation parameters were for a Voigt profile with temperature of 294 K and pressure of 2.82 kPa. Four methods were used to analyse the data. Firstly, a ratio method was used

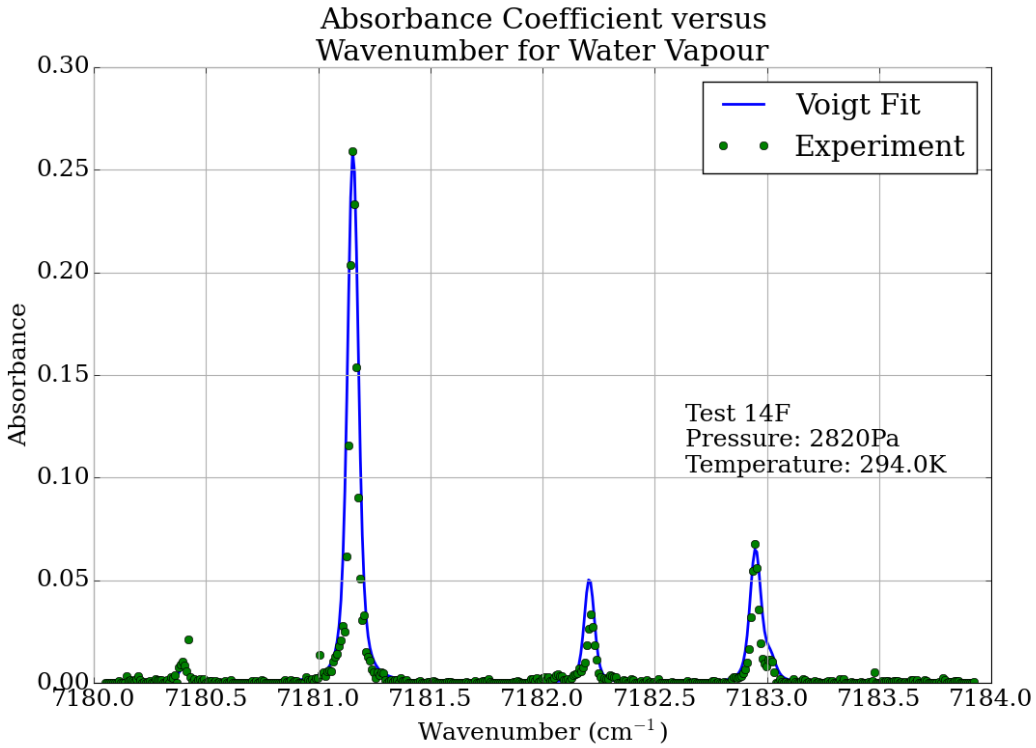

Figure 5.11.: Absorbance plot when the sight tubes are purged with nitrogen. There is minimal broadening due to atmospheric water absorption.

to derive flow temperature from the strength ratios of different features. The second method involved fitting the absorption data to a Boltzmann plot. Thirdly, *Hitran on the Web* was used to simulate the temperature and pressure plus water abundance in the flow. Finally, an iterative method was used to match the observed data with simulated data. Each method is discussed separately below.

5.5.1. Ratio method

In this method, the flow temperature was derived by taking the ratios of feature strengths then applying equation 3.39, reproduced here:

$$R_{12} = \frac{S\left(T_0, \nu^{(1)}\right)}{S\left(T_0, \nu^{(2)}\right)} \exp\left[-\left(\frac{\hbar c}{k}\right)\left(E_{low}^{(1)} - E_{low}^{(2)}\right)\left(\frac{1}{T} - \frac{1}{T_0}\right)\right] \tag{5.5}$$

Re-arranging this, we can obtain the temperature from a measured ratio of line strengths $R_{12_{meas}}$:

$$T = \left[\frac{1}{T_0} + -\left(\frac{k}{\hbar c}\right)\ln\left(\frac{R_{12_{meas}} S\left(T_0, \nu^{(2)}\right)}{S\left(T_0, \nu^{(1)}\right)}\right)\right]^{-1} \tag{5.6}$$

This technique is a form of the Boltzmann method limited to two lines. If this method was accurate, it would allow rapid calculation of flow properties and would have significant computational advantages

Table 5.2.: Features used for ratio measurements along with the lower state energy difference and the ratio of intensities at 298 K [57]

Ratio	Wavenumber 1 cm^{-1}	Wavenumber 2 cm^{-1}	$\|\Delta E_{low}\|$ cm^{-1}	$\frac{S\left(T_0,\nu^{(1)}\right)}{S\left(T_0,\nu^{(2)}\right)}$
5:1	7179.75201	7182.94962	1073	0.048033
5:2	7179.75201	7182.20911	1173	0.116958
5:3	7179.75201	7181.15578	1078	0.0119748
5:4	7179.75201	7180.39972	990	0.3213587
4:1	7180.39972	7182.94962	83.6	0.149468
4:2	7180.39972	7182.20911	183.5	0.36395
4:3	7180.39972	7181.15578	89.1	0.037263
3:1	7181.15578	7182.94962	79.4	4.01116
3:2	7181.15578	7182.20911	135.8	9.767
2:1	7182.20911	7182.94962	99.6	0.410686

over more computationally intensive techniques. This would be particularly advantageous in scramjet control.

Whilst there were theoretically 12 ratios that could be used to derive temperature, not all ratios were useful. For example, the lower energies (E_{low}) for the features at 7181.15578 cm^{-1} and 7182.92962 cm^{-1} were 137 cm^{-1} and 142 cm^{-1} respectively. Thus, the ratio between these two signals is relatively invariant with temperature across the range of test temperatures.

Table 5.2 lists the feature wavenumbers and energies for each ratio that was used in the analysis together with ratio of intensities at the reference temperature. Errors are not given at this stage since the values have all been sourced from *HITRAN*. Figure 5.12 shows how four intensity ratios of the features listed in table 5.2 theoretically vary with temperature at a pressure of 2 kPa. The best temperature discrimination is achieved by comparing the features at 7179.752 cm^{-1} and 7180.400 cm^{-1}. Unfortunately, both of these features are very weak at the test temperatures making any temperature measurement have a large error. Feature 3 at 7181.1558 cm^{-1} (1392.5335 nm) is the strongest line but has the lowest responsivity for temperature measurements when used in a ratio with other features. As this method proved to be the least accurate of those trialled, only one example will be used to illustrate typical results. The data from figure 5.11 were used as they were the best data obtained from these experiments. Only four features were detected in this example so the temperatures T_{est} for six ratios (4:1, 4:2, 4:3, 3:1, 3:2, 2:1) were calculated. Table 5.3 lists the measured intensity ratios and estimated temperatures calculated using these features. The errors listed are based on 2% relative error in each intensity calculation which was an estimate of the difficulty in measuring the peak absorption of each feature. Whilst this selection is somewhat arbitrary, it provides guidance on the impact of intensity measurement on the temperature calculation. Admittedly, the relative error in measuring the intensity of a strong feature such as the one at 7181.15578 cm^{-1} is significantly less than that for a weak feature (say, 7179.75201 cm^{-1}) so the calculated error when using the stronger

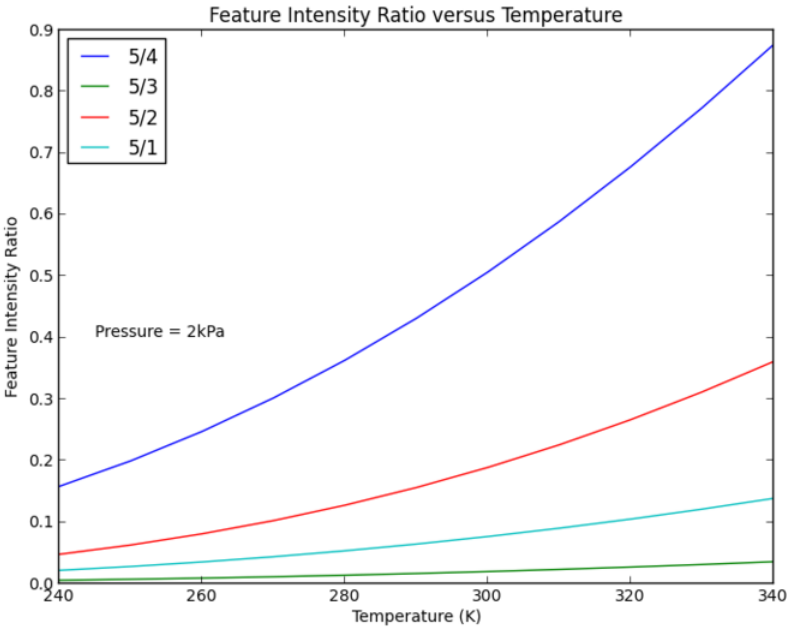

Figure 5.12.: Feature intensity ratio variation with temperature.

Table 5.3.: Estimated temperatures calculated using the ratio method on feature pairs listed in table 5.2

	$R_{12_{meas}}$	T_{est} (K)
4:1	6.7 ± 0.2	296 ± 14
4:2	3.3 ± 0.2	259 ± 5
4:3	26.9 ± 0.8	296 ± 14
3:1	0.25 ± 0.01	305 ± 45
3:2	0.124 ± 0.003	231 ± 40
2:1	2.0 ± 0.1	234 ± 23

feature is pessimistic. The relative error in the intensity ratio may be calculated using:

$$\begin{aligned} R_{12_{meas}} &= \frac{I_1}{I_2} \\ \frac{\partial R_{12_{meas}}}{R_{12_{meas}}} &= \sqrt{\left(\frac{\partial I_1}{I_1}\right)^2 + \left(\frac{\partial I_2}{I_2}\right)^2} \end{aligned} \tag{5.7}$$

The estimated temperatures ranged from 231 K to 305 K depending on the feature pair used for the calculation. The temperature errors range from 5 K to 45 K depending on the ratio. The calculated temperature varies depending on the ratio used; thus, this method is ineffective. The wide range of temperatures and errors are due to the following factors:

- Measurement noise levels were approximately $5-10\%$ of the feature height for smaller features. Whilst a relative error of 2% was used for the calculations as discussed above, this actual error would produce even less precise temperatures.

Table 5.4.: Properties of water features used for Boltzmann plots (Source: [57])

Wavenumber (cm^{-1})	Wavelength (nm)	E_{low} (cm^{-1})	Cross section (s^{-1})	Degeneracy
7179.75201	1392.8058	1216.195	12.83	45
7180.39972	1392.6801	225.8384	0.5419	21
7181.15578	1392.5335	136.7617	13.27	15
7182.20911	1392.32927	42.3717	1.432	9
7182.94962	1392.1857	142.2785	10.20	5

- The integrated intensity calculations were very sensitive to the selection of data points. This effect was greatest for very small or very large intensity ratios since a small error in the intensity of the smaller feature significantly changed the ratio. The estimated temperature changed by up to 200 K when one data point was omitted for the 3:2 ratio.

As a result of this analysis, coupled with unsuccessful attempts to measure temperature using absorption peak height ratios, the ratio method was not used further because there were better approaches.

5.5.2. Boltzmann plot

A Boltzmann plot may be used to determine the path-averaged static temperature by measuring multiple absorption features. The frequency-integrated absorption is normalized by the cross-section and degeneracy factor for each transition and then plotted versus the initial state energy divided by k_B. At the temperatures and transition frequencies studied here, the stimulated emission terms can be ignored (that is, $e^{-h\nu_{10}/kBT} \approx 0$). This results in the following relationship [16]:

$$\ln\left[\frac{A}{S_0}e^{-E_{low}/k_BT_0}\right] = -\frac{E_{low}}{k_BT} + \ln\left[\frac{Q\left(T_0\right)}{Q\left(T\right)}N_TL\right] \tag{5.8}$$

where $Q\left(T\right)$ is the partition function for the absorbing species, E_{low} is the initial state energy, N_T is the number density of the absorbing species and L is the path length. Table 5.4 lists the *HITRAN* data for the features used in the Boltzmann plots.

5.5.2.1. No flow test

To illustrate application of this technique to a no flow test, figure 5.13 is a Boltzmann plot for the absorption data in figure 5.10. The error bars were determined by assuming a relative intensity error of 2% as for other tests in this experiment. The actual errors for the two central data points are probably much lower (say below 1%) but the 2% value was used to assist in comparing the methods against each other. The calculated temperature using the Boltzmann plot was 346 ± 10 K. The temperature derived via the ratio method using the four optimal ratios was in the range $333 - 368$ K. The temperature measured using a thermocouple in the test section was 339 K; thus, there was reasonable correlation between the TDLAS measured temperature and the thermocouple-measured temperature for this no

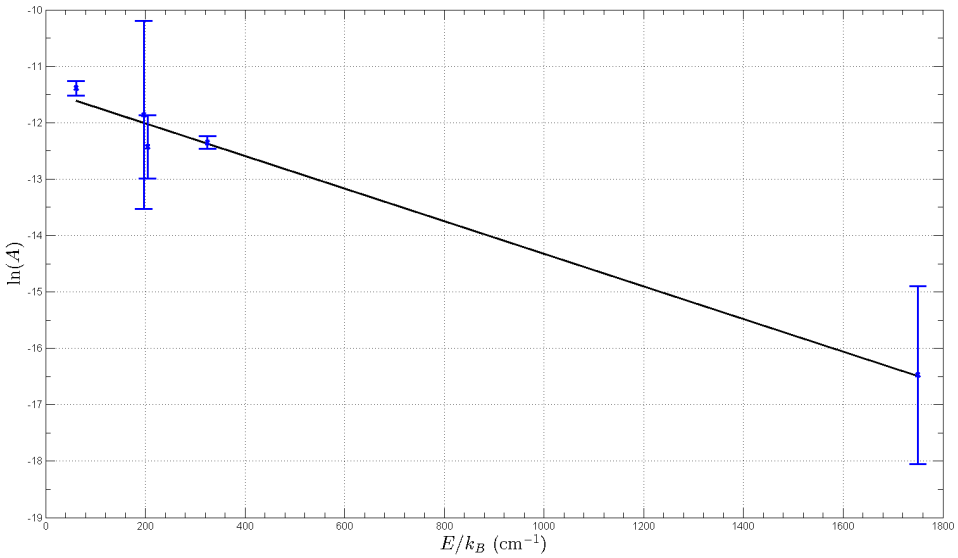

Figure 5.13.: Boltzmann plot for absorption data in figure 5.10. Blue crosses are experimental results whilst black line is a linear fit to the data.

flow test even with the large relative intensity error. Thus, the Boltzmann plot technique is accurate even though it is simple to apply.

5.5.2.2. Flow tests

Figure 5.14 shows a Boltzmann plot of the absorption data in figure 5.11. Four experimental points are marked by blue crosses with error bars whilst the black line is a least squares linear fit to the data. Again, the relative intensity error for each feature as assumed to be 2% for the sake of comparison. The actual errors for the two central data points in figure 5.14 are likely to be far less than those shown. The fit between experimental data and the linear fit was excellent for this example. The calculated temperature for this plot was 243 ± 10 K which again depended on the data points used to determine the integrated intensity; however, the dependence was reduced from that for the ratio method because all four intensities were used for the fit. The calculated temperature fell within the range determined using the ratio method (231 K to 305 K). The temperature modelled via CFD for these conditions ranged from 288 K to 336 K across the stream flow. The reason for the difference between the measured and modelled temperatures is not known but is likely to be due to a fault in the CFD model considering that the flow was two-phase. As may be seen from equation 5.8, the calculated temperature was inversely proportional to the natural logarithms of the integrated intensities. This made the temperature relatively insensitive to errors in the measured intensities. The graphical nature of this method highlighted any data points that were outliers.

Overall, the Boltzmann method was accurate and simple to apply provided the outlier data points did not adversely affect the integrated intensity calculation. The graphical nature of the technique provided a good understanding of the impact of errors. The method did not provide pressure information as it relied solely on the integrated absorbance of each feature.

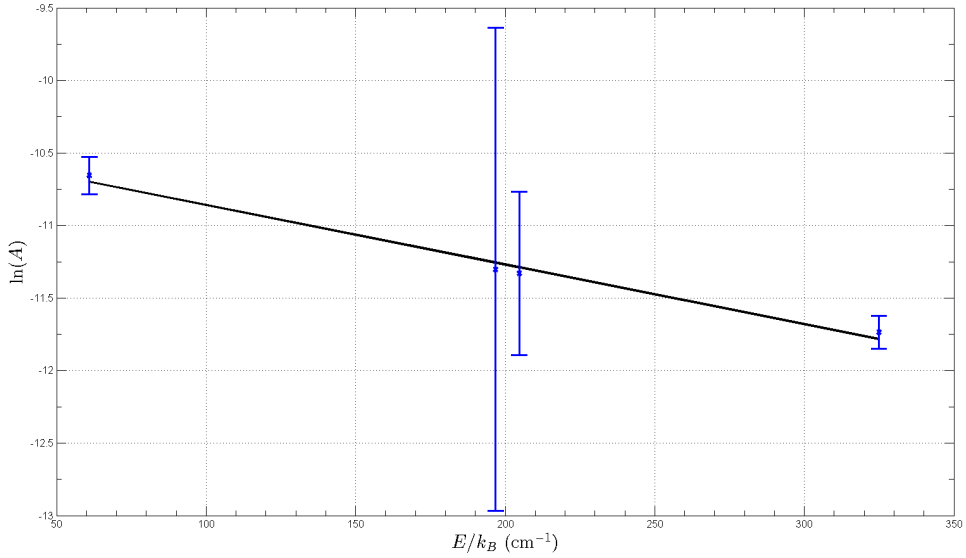

Figure 5.14.: Boltzmann plot for absorption data in figure 5.16. Blue crosses are experimental results whilst black line is a linear fit to the data. The error bars were determined by assuming a relative intensity error of 2%.

5.5.3. Hitran on the web

Next, *Hitran on the Web* [60] was used to simulate each test. The simulation parameters of temperature, pressure and abundance were varied until the relative root mean squared (RMS) error between the observed and simulated absorbances for each feature was minimised. This method depended on finding the optimal combination of pressure, temperature and abundance in order to accurately fit the spectral data. It improved upon the ratio method because the strengths of each feature were used rather than only two as was done in the ratio method. It also improved on the Boltzmann method because it enabled pressure measurements to be made.

5.5.3.1. No flow test

To illustrate the method, it is applied to no flow tests since the test section pressure and static temperature were measured conventionally for these tests. Table 5.5 lists the measured absorbances for each feature in Test 1 of table 5.1. Absorption spectra were calculated using *HITRAN on the Web* for an optical path of 10 mm. A Gaussian shape was selected with a wavenumber step of 0.01 cm^{-1} between 7179.5 cm^{-1} and 7183.5 cm^{-1}. The pressure for each simulation was 0.07 atm. The temperature was varied from 270 K to 330 K. The water vapour abundance was initially set to 45.5% reflecting the partial pressure of saturated water vapour (3.17 kPa) at a temperature of 298 K and an atmospheric pressure of 6.8 kPa. After calculating a spectrum, the absorbances for the features listed in table 5.5 were extracted. The calculated absorbances were compared with the measured ones listed in table 5.5 and the sum of RMS errors was calculated. Table 5.6 lists the RMS errors for various temperatures and abundances. The RMS error decreased as temperature increased at constant water vapour concentration. At 280 K, the RMS error increased significantly as the abundance decreased.

Table 5.5.: Measured absorbance for each feature in Test 1 with test section temperature of 298 K and pressure 6.8 kPa

Wavenumber cm^{-1}	Absorbance %
7179.75201	0.8 ± 0.1
7180.39972	1.1 ± 0.1
7181.15578	22.0 ± 0.1
7182.20911	1.1 ± 0.1
7182.94962	2.3 ± 0.1

Table 5.6.: Hitran fit data for Test 1 of table 5.1

Temperature K	Abundance %	RMS Error %
270	45.5	148
280	45.5	140
280	40.0	124
280	30.0	144
280	20.0	200
290	45.5	135
300	45.5	130
310	45.5	125
320	45.5	120
330	45.5	115
330	40.0	107
330	30.0	89
330	20.0	115

Table 5.7.: Directly measured temperatures and pressures for vacuum tests together with the *HITRAN*-fit temperature, pressure and water vapour concentrations

	Directly measured values		*HITRAN*-fit values		
Test	Temperature K	Pressure kPa	Temperature K	Pressure kPa	Concentration %
1	298 ± 1	6.8 ± 0.1	330 ± 5	7 ± 1	30 ± 2
2	298 ± 1	5.0 ± 0.1	305 ± 5	5 ± 1	30 ± 2
3	294 ± 1	4.5 ± 0.1	295 ± 5	4 ± 1	11 ± 2
4	339 ± 1	6.5 ± 0.1	333 ± 5	7.6 ± 1	28 ± 2

Table 5.8.: Measured absorbance for each feature in the steam test

Wavenumber cm^{-1}	Absorbance %
7180.39972	1.0 ± 0.1
7181.15578	26 ± 1
7182.20911	3.3 ± 0.1
7182.94962	6.8 ± 0.1

The minimum RMS error of 89% was at 330 K and 30% water vapour concentration. This error was excessive indicating that, perhaps, the Gaussian fit was not best; however, this was not immediately evident from the data. The process would have to be repeated for Lorentzian and Voigt profiles to determine the best profile. Table 5.7 presents the directly measured temperatures and pressures for the vacuum tests together with the TDLAS-derived temperature, pressure and water vapour concentrations. This method was found to give superior results to the peak height ratio method but was still inadequate because it was very time intensive and did not guarantee that a globally optimal combination of parameters had been found. It also did not give any indication of how well the calculated line shape matched the measured line shape.

5.5.3.2. Flow Tests

As another illustration of this method, consider a test where the steam generator was operating. During this test, transducers recorded the steam generator total pressure at 144.0 ± 0.2 kPa, condenser pressure was 6.5 ± 0.5 kPa and test section static pressure was 2480 ± 65 Pa. The test section static pressure sensor was located approximately 5 mm downstream from the TDLAS measurement and was in the centre of the flow. The test section temperature was not directly measured. Table 5.8 lists the measured absorbances for the steam test. Table 5.9 contains partial data used to optimise the *HITRAN* simulations for the steam test. The path length is included as an additional variable for this test. The quality of the fit is expressed in the table as a percentage RMS Error. To calculate this, the difference between the calculated and measured absorbance at each test point is normalised by the maximum measured absorbance. The percentage RMS error is then calculated from these normalised

Table 5.9.: *HITRAN*-fit data for steam test

Temperature K	Pressure kPa	Abundance %	Path length mm	RMS Error %
240	5.0	30	10	49
240	5.0	20	10	14.7
240	5.0	20	12	15
240	5.0	20	11.5	8.3
250	5.0	20	11.5	12.1
250	5.0	20	12	6.1
245	5.0	20	12	9.3
245	5.0	20	10	31.4
245	5.5	20	12	12.1
245	6.0	20	12	7.9
250	6.0	20	12	6.1
255	6.0	20	12	12.6
255	6.0	21	12	6.4

test point errors. This measure was found to be a very good indicator of the quality of fit between the modelled and measured absorbance.

The RMS errors are lower for this test than for any of the vacuum tests. The simulations were initialised using anticipated conditions derived from the CFD. The initial path length was set to 10 mm in recognition of the data in figures 5.8 to 5.6. The starting temperature was 240 K, the pressure was 5.0 kPa and the water vapour concentration was 30%. The RMS error decreased from 49% to 14.7% when water vapour concentration reduced to 20% from 30%. Increasing the path length to 12 mm and the temperature to 250 K reduced the RMS error to 6.1%. Further minor changes to parameters identified an optimal *valley* of conditions at $250 - 255$ K, $5.0 - 6.0$kPa, $20 - 21\%$ concentration and 12 mm path length. Combining the pressure with the water concentration gives the partial pressure of water vapour in the test section as $1.0 - 1.26$ kPa. Two other steam tests were simulated via this method. In the second test, the minimum RMS error was 26.9% at 295 K, 4.0 kPa and 11% concentration for a 12 mm path length. The RMS error increased to $31 - 32\%$ if the temperature was changed by 5 K or the pressure was changed by 0.5 kPa. The error increased to over 40% if the water vapour concentration was changed by $\pm 1\%$. Thus, the measured properties were 295 ± 5 K, 6.0 ± 0.5 kPa and an abundance of $21 \pm 0.5\%$ for a path length of 12 ± 0.5 mm. The water vapour partial pressure was 1.26 ± 0.01 kPa.

The third steam test was conducted after the generator had operated for more than one hour. During this time, the test section temperature increased significantly as evidenced when touching the test section wall. The test section static pressure was $6.0 - 9.0$ kPa when measured using a pressure probe. The actual test section temperature and water vapour concentration were unknown. A total of 38 *HITRAN* simulations were undertaken for this condition. Temperature was varied from 270 K to 340 K. The simulated pressure range was $6.0 - 9.0$ kPa and the water concentration range was $25 - 45\%$.

The optimal condition was found to be 333 ± 5 K, 7.5 ± 0.5 kPa and $28 \pm 0.5\%$ concentration which resulted in an RMS error of 22.6%. The water vapour partial pressure was 2.1 ± 0.1 kPa.This condition was approached from three separate directions; namely, temperature, pressure and concentration. All directions resulted in the same optimal condition.
When at the optimal condition, changing temperature by ± 2 K increased the RMS error by $\approx 0.2\%$ whilst a ± 0.5 kPa change in pressure resulted in an $\approx \pm 3\%$ increase in error. A $\pm 1\%$ change in water vapour concentration increased the RMS error by $\approx 1\%$. Thus, the optimal condition was accurately detectable albeit after considerable effort.
In summary, this method provided estimates of flow temperature, pressure and water concentration for both flow and no flow tests. The calculated temperature and pressure for no flow tests agreed well with values measured using thermocouples and pressure probes. The calculated pressures for flow tests agreed well with those measured using pressure probes. Negatively, the technique required a significant level of user interaction to generate each spectrum, download the data and match the downloaded data with the measurements. Even though the process was automated as much as possible, it was still laborious. Given the potential accuracy of this method, a more methodical and automated approach was sought to reduce the time and ensure that a wide range of conditions were simulated to find the global optimum.

5.5.4. Iterative fit method

A python program was written to iterate through various pressures and temperatures whilst calculating absorbance plots at each condition using feature data from *HITRAN* 2012 and fitting Voigt line shape profiles. The residuals between the modelled and measured absorbance data were calculated and the sum of the root-mean square of the residuals was derived. A Levenburg-Marquardt method [46] was applied to perform a non-linear least-squares minimisation of the residuals. For a typical run, there were 117 features in the *HITRAN* table and 4500 points were calculated for each feature. When combined with temperature, pressure and concentration options, the computational time required increased rapidly. To reduce computation time, a minimum feature intensity level was selectable by the user. By selecting a minimum intensity level for a feature (say 1×10^{-24}) the number of features modelled was reduced significantly. Also, the Gaussian line shape was independent of pressure. Thus, it was calculated once only for each temperature, further reducing the computational time.
The program accumulated the absorbances and calculated the residual between the measured and simulated data. For each combination of pressure and temperature, the residual was plotted. Figure 5.15 is a typical plot. At the optimal combination, the simulated and measured data were plotted together to visually confirm the fit.

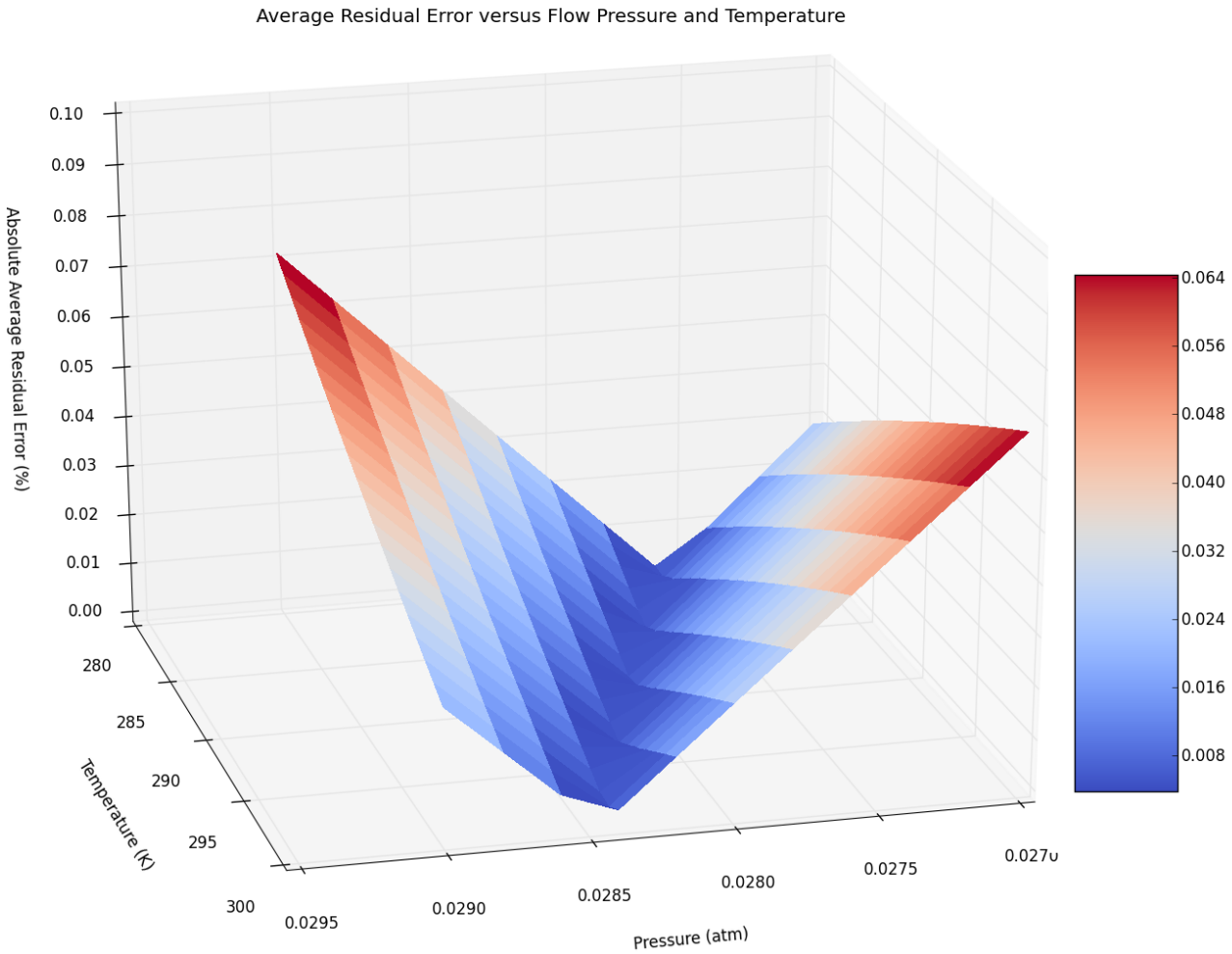

Figure 5.15.: Typical residual error between measured and simulated data plotted against flow pressure and temperature. The coloured bar shows the residual error from 0.008 (blue) to 0.064 (red).

Figure 5.16 shows the result from the second steam test discussed in section 5.5.3.2. The TDLAS measured temperature and partial pressure of water vapour were 294 ± 5 K and 2.82 ± 0.05 kPa respectively compared with 295 ± 5 K and 2.7 ± 0.1 kPa found using the *Hitran on the Web* method with a Voigt profile. Figure 5.17 shows the result from the third steam test discussed in section 5.5.3.2.

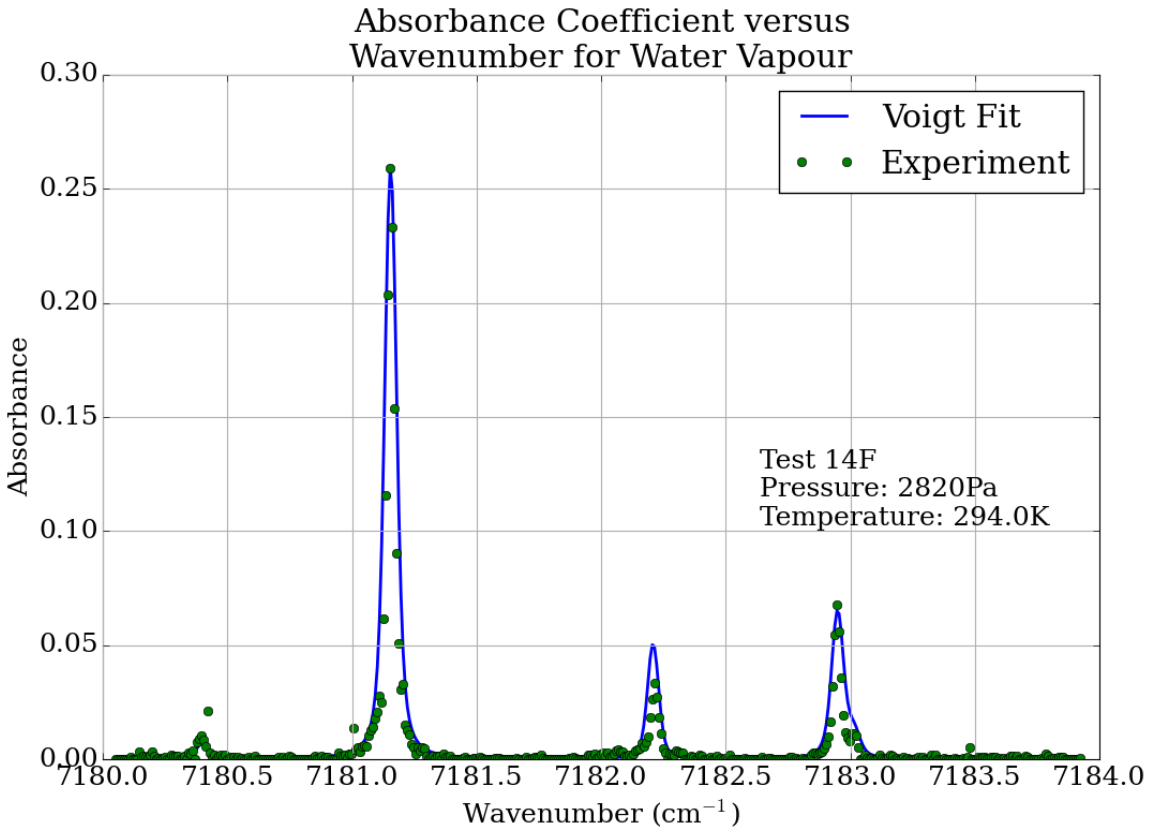

Figure 5.16.: Absorbance coefficient versus wavenumber for water vapour flow from an ejector at 2.82 ± 0.05 kPa pressure and 294 ± 5 K static temperature.

The measured temperature and water vapour partial pressure were 320 ± 5 K and 3.60 ± 0.05 kPa respectively using this method compared to 333 ± 5 K and 2.1 ± 0.1 kPa found using the *Hitran on the Web* method. Again, pressure difference is believed to be due to use of a Voigt profile for this method versus a Gaussian profile for the *Hitran on the Web* method.

Figure 5.18 shows the residual errors against temperature and pressure. Note that the optimal condition found using this method was different from that using the *HITRAN*-fit method. The absolute average residual error was $\approx 4\%$ using this method compared with 26.6% previously. This highlights that the *HITRAN*-fit method did not find the globally optimal solution. This method was very effective at quickly and accurately identifying the flow parameters. Absolute average residual errors of less than 0.1% were achievable together with pressure relative error of $\pm 2\%$ and temperature errors of ± 5 K. The primary accuracy advantage of this technique over the previous two methods was that it used each test point in the error minimisation routine rather than using two or four points. Also, Voigt profiles were fitted for each test. Thus, the effects of changing temperature, pressure and concentration could be examined. Plotting the residual errors on a three-dimensional surface plot provided insight into the relative sensitivity of the result to changes in the various parameters. Setting a lower

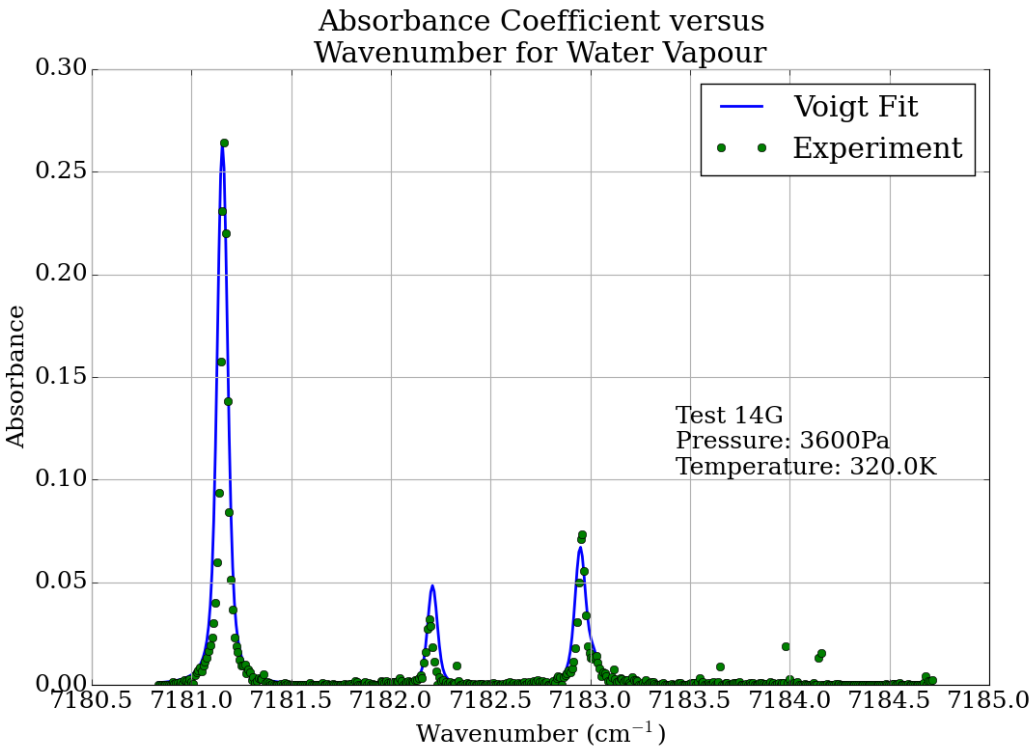

Figure 5.17.: Absorbance coefficient versus wavenumber for water vapour flow from an ejector at 3.60 ± 0.05 kPa pressure and 320 ± 5 K static temperature.

limit on feature strength was found to speed the computations without adversely affecting the result.[3]

[3]Thanks to Steven Lewis for suggesting this.

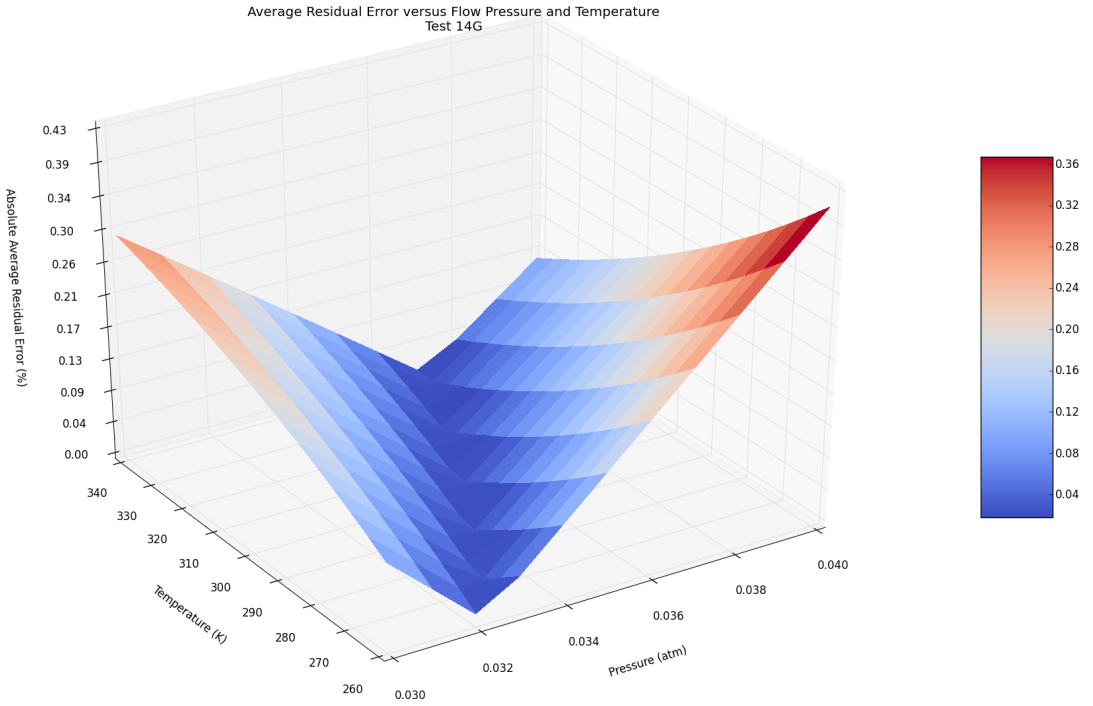

Figure 5.18.: Residual error between measured and simulated data plotted against flow pressure and temperature for a steam ejector operating at 3.60 ± 0.05 kPa pressure and 320 ± 5 K static temperature. The coloured bar shows the residual error from 0.04 (blue) to 0.36 (red).

5.6. Summary

Tables 5.10 and 5.11 respectively compare the no flow test section temperatures and pressure calculated using different techniques. Table 5.12 lists the temperature and pressure errors for the no flow

Table 5.10.: Comparison of temperature results for no flow tests

Test	Thermocouple K	Ratio K	Boltzmann K	*HITRAN*-fit K	Iterative K
1-3	298 ± 1	296 ± 14	296 ± 10	310 ± 18	294 ± 5
4	339 ± 1	350 ± 15	346 ± 10	333 ± 5	320 ± 5

Table 5.11.: Comparison of pressure results for no flow tests

Test	Transducer kPa	*HITRAN*-fit kPa	Iterative kPa
1	6.8 ± 0.1	7 ± 1	6.8 ± 0.1
2	5.0 ± 0.1	5 ± 1	5.0 ± 0.1
3	4.5 ± 0.1	4 ± 1	4.5 ± 0.1
4	6.5 ± 0.1	7.6 ± 1	6.5 ± 0.1

tests. The ratio method was, by far, the least accurate technique with respect to temperature and did not measure pressure or concentration. The Boltzmann plot temperature error was ± 10 K but this technique still did not measure the pressure or water vapour concentration. The techniques that used all points had temperature errors of ± 5 K. The iterative method was the most accurate in calculating pressure because it was able to identify the conditions that globally optimised the residual error.

Table 5.12.: Temperature and pressure errors for each method - no flow tests

Method	Temperature Error K	Pressure Error kPa	Concentration %
Ratio	± 50	Not measured	Not measured
Boltzmann Plot	± 10	Not measured	Not measured
HITRAN-fit	± 5	± 1	± 2
Iterative	± 5	± 0.1	± 1

For the tests with steam flowing, the iterative fit method was, by far, the most successful of those trialled. The ratio method was not used for the flow tests. Boltzmann plots could be used to estimate the temperature but did not provide pressure information. They were accurate and simple to apply provided any outlier points did not adversely affect the integrated intensity calculations.
Using *HITRAN on the Web*, was time consuming and required significant judgement in its application. It was able, however, to estimate temperature, pressure, water vapour abundance and path length. Using an RMS uncertainty condition allowed this method to be used to estimate temperature to ± 2 K.

The calculated pressures for flow tests agree well with those measured using pressure transducers in the test section.

The iterative fit method provided the best results as measured using an absolute residual uncertainty condition that was based on the temperature and pressure and the difference between calculated and measured spectral fits for each data point. Absolute average residual uncertainties of less than 0.1% were achievable together with pressure relative uncertainty of $\pm 2\%$ and temperature uncertainties of ± 5 K. Plotting the residual uncertainties ona three-dimensional surface plot provided insight into the relative sensitivity of the result to changes in parameters.

Direct absorption TDLAS was used to measure temperature, pressure and abundance in the mixing region of a steam ejector. The TDLAS measurements of pressure and temperature matched the observed values well when the matching technique used all features in conjunction with a *HITRAN* simulation coupled with a Levenburg-Marquardt non-linear least-squares minimisation of the residual between a Voigt fit of the CFD data and the measured data. These experiments show that direct absorption TDLAS can accurately measure properties in a steam ejector in both flow and no flow conditions. The test time required for these measurement was considered to be excessive for practical application. Using wavelength modulated spectroscopy with multiple lasers would overcome the time issue albeit for additional experimental complexity.

6. Scramjet Experiments

Hypersonic air-breathing vehicles are able to cruise and manoeuvre into and out of the atmosphere or to provide very rapid transport between remote Earth destinations [5]. Ramjets are useful at speeds up to Mach 5 but, above that, heating induced by the transition from supersonic to subsonic flow limits ramjet effectiveness. Supersonic combustion ramjets (scramjets) may be used above Mach 5 to provide high specific impulse propulsion for hypersonic vehicles. Scramjets need less internal cooling than ramjets because the airflow does not heat excessively. The relatively cool airflow gains heat through combustion. Scramjets may be fuelled by hydrogen or hydrocarbons.
The University of Queensland hypersonic test facilities have been used since the mid-1980s to investigate scramjets and planetary entry plasma flows. A free-piston reflected shock tunnel (T4) has been used extensively to characterise and measure scramjet combustion with the aid of thin film heat transfer gauges, pressure transducers, high-speed photography, and planar laser interferometry (PLIF) amongst other techniques. Reflected shock tunnels have relatively long test times of the order of 10 ms but the test gas can dissociate when the flow stagnates behind the reflected shock due to the high temperatures reached there. This can cause dissociation of the test gas flow leading to potentially flawed test results since some combustion initiation reactions are bypassed.
Free-piston super-orbital expansion tubes (such as the X2 and X3 facilities at the University of Queensland) were developed, amongst other reasons, to overcome the flow dissociation issue associated with reflected shock tunnels. The test gas in an expansion tunnel accelerates continuously as it travels to the test section. Thus, it does not stagnate and does not dissociate prior to reaching the test section [137]. The steady flow duration for an expansion tube is of the order of $0.1 - 1$ ms; much less than for a reflected shock tunnel.

6.1. System setup and design

The overall goal of this research was to develop and apply a TDLAS system that can perform measurements in expansion tunnels. These measurements, the first ever performed in such facilities at the University of Queensland, were expected to be challenging due to the characteristics of the flow facility including a short test time of approximately 1 ms, rapidly changing flow conditions during the test time, restrictions on the experimental layout, and operational and maintenance limitations with the expansion tunnel. Our understanding of these conditions could be significantly improved if TDLAS systems were able to probe the flow temperature and pressure as well as the concentration of short-lived species such as OH, NO or atomic oxygen and nitrogen.
Ideally, the flow temperature and water vapour concentration could be directly measured in the nozzle

of a scramjet. These measurements could be used to control fuel injection and optimise the scramjet operation to maximise thrust and minimise sources of drag. The harsh conditions in a scramjet nozzle currently prevent direct measurement of these parameters. Instead, indirect measurements of scramjet wall temperatures, heat transfer and static pressure are used to infer flow temperature and water vapour concentration from CFD simulations.

TDLAS offers a potential means to non-intrusively and yet directly measure temperature, water vapour concentration and pressure in the exhaust of a scramjet during an expansion tunnel experiment. Temperature can be derived using signal ratio techniques whilst water vapour concentration and pressure can be derived from the absorption and feature spectral shape. A TDLAS system was developed to probe water vapour in the exhaust of a hydrogen fuelled scramjet during expansion tunnel experiments.

Currently, thin film heat gauges and pressure transducers are used to measure scramjet wall temperature and duct pressures. The presence of combustion is then deduced from pressure and temperature changes. This technique is limited as it requires good knowledge of the scramjet internal flow; it relies on having accurate sensors with fast response rates, and it measures properties at the scramjet wall where the boundary layer and heat transfer to the wall can influence measurements. Also, the sensors are expensive and may be damaged in the demanding environment of the expansion tunnel.

During expansion tunnel tests, a scramjet model wall temperature will likely be close to room temperature [138]. Hence, the wall enthalpy ratio will be less than that seen in flight which is approximately 0.2. However, both skin friction and heat transfer become virtually independent of the wall enthalpy ratio at values less then 0.3 [138]. Anderson [139] states that wall reactivity is not simulated if the model wall temperature does not represent the flight wall temperature.

McGilvray [138] has stated that the start-time of a shielded total pressure probe in an expansion tunnel flow is in the order of 15 μs and the probe can introduce acoustic noise to signal readings. In longer test time facilities which have a similar flow environment, such as T4, thermal stress induced forces on the sensor can lead to false readings [138].

Using TDLAS to detect combustion was aimed at providing an advanced non-intrusive, direct detection approach that could be transferred to in-flight measurements. Ideally, flow temperature and water vapour concentration could be measured accurately using TDLAS.

The goal of this campaign was to detect combustion in the exhaust when gaseous hydrogen fuel was injected at the inlet of a scramjet. An expansion tunnel (described in appendix C) provided the operating conditions to simulate flight at a vehicle flying at 3.5 kms^{-1} at an altitude of 30 km with a dynamic pressure q_0 of 48.4 kPa. A steady test time of 1 ms was attained at the inlet of the scramjet (described in appendix D). Gaseous hydrogen was injected at the scramjet inlet via five holes inclined to the flow at $45°$. A Ludwieg tube was pressurised with hydrogen prior to the shot and the fuel was then injected into the scramjet as the expansion tunnel piston launched at the start of a shot.

The expansion tunnel was last operated eight months before the start of this campaign. During that time, the tunnel was significantly modified with changes that affected the flow conditions and pressure transducer signals recorded during shots. Of the 18 shots undertaken for this campaign, the first ten primarily aimed to verify that the tunnel operating conditions were acceptable after the modifications.

These shots began in July 2015 and were required to collect data for a paper to be presented at an international conference in August 2015. As a result, they were undertaken as a high priority.
The TDLAS experiments were of secondary priority and as such were constrained to have minimal impact on the verification process. The author was also given short notice of the experimental opportunity and was not able to undertake detailed analysis prior to the experiments. The three weeks between being notified of the opportunity and the first experiment were spend in modifying the scramjet, testing and calibrating pressure transducers, setting up the fuel system, modifying the data recording system, developing trigger mechanisms, designing and setting up the TDLAS system, calibrating the TDLAS system, writing control software and designing the nitrogen purging system.
Ideally, CFD simulations of the scramjet and fuel system would have been undertaken prior to the TDLAS experiments to model the conditions at the TDLAS test section. Unfortunately, the short notice precluded this and meant that any analysis would be undertaken post-test and that the experiments were more of a proof of concept for thelocally designed system. This impacted on the TDLAS optical system design as discussed in detail in appendix E.
The TDLAS system was designed to measure temperature using two water vapour absorption features near 1392 nm ($7181 - 7185$ cm^{-1}). The laser signals were sinusoidally modulated at 1 MHz with the aim that each modulation cycle encompassed the entire feature. Each laser was launched from outside of the dump tank through free space towards a small hole in the wall of the scramjet exhaust. After passing through the scramjet, the beams were received by photo detectors outside of the dump tank, amplified and recorded using a high-speed digital oscilloscope card. The data recording system used three time bases to record the expansion tunnel, fuel and TDLAS system data respectively. The fuel data recording time was of the order of 200 ms whilst the expansion tunnel and TDLAS recording times were of the order of 20 ms and 2 ms respectively. Ten expansion tunnel signals, 27 scramjet pressure signals, four fuel system signals and up to eight TDLAS signals were recorded simultaneously. The complexity of the data management methodology placed considerable strain on the recording system.
Four sets of experiments were conducted during this campaign:

- laboratory tests to verify the performance of the TDLAS system,
- scramjet tests using air as a test gas without fuel injection,
- scramjet tests using nitrogen as a test gas with fuel injection, and
- scramjet tests using air as a test gas without fuel injection.

Various issues were encountered during this campaign related to experimental design, hardware failures and software. As a result, the temperature and water vapour concentration in the scramjet exhaust were unable to be reliably calculated; however, the experiments showed that TDLAS has potential to make such measurements provided future researchers modify the experimental technique. It was considered that details of the campaign should be included for posterity and to assist researchers avoid some of the pitfalls encountered.

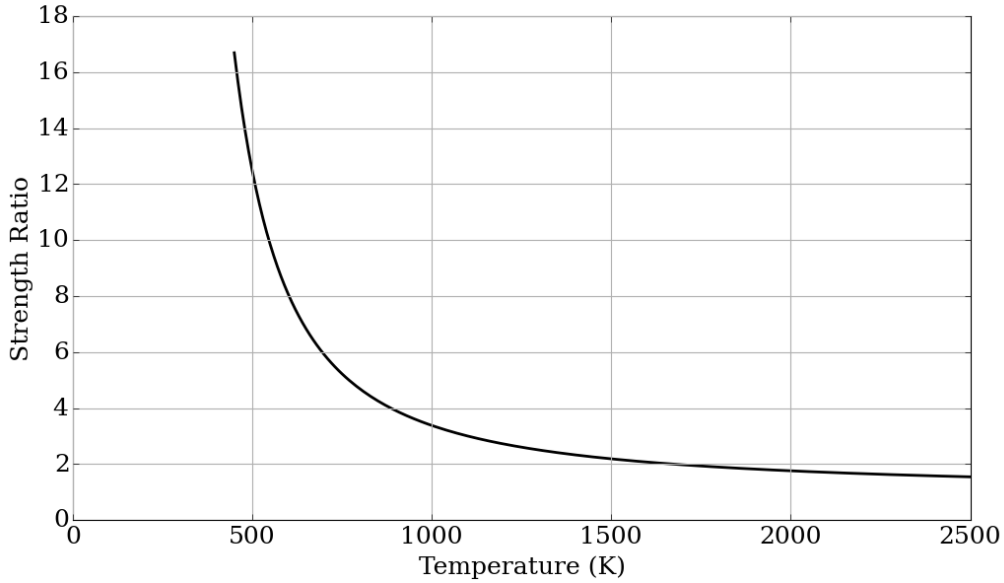

Figure 6.1.: Variation of strength ratio with temperature for features at $7181.15578\,\mathrm{cm}^{-1}$ and $7185.5966\,\mathrm{cm}^{-1}$

6.2. Simulations and models

The TDLAS measurements of temperature and water vapour concentration were not able to be compared with measurements made using other types of sensor such as thermocouples since the sensors would be destroyed by the flow. Instead, the anticipated conditions at the TDLAS test point were simulated via analytical models of the expansion tunnel, scramjet and TDLAS system.

6.2.1. Expansion tunnel and scramjet models

Analytical models of the expansion tunnel and scramjet were used to approximate the conditions at the TDLAS test section. These models were able to approximate temperature, pressure and water vapour concentration for a range of fuel injection pressures and test gases. The expansion tunnel and scramjet models are described in detail in appendices C and D respectively.

6.2.2. Temperature Calculation

The relative strength of two water vapour features changes with temperature as described in equation 3.39. The relative sensitivity of this ratio to temperature is as stated by equation **??**. Figure 6.1 shows the variation of R with temperature for the two target features. Below 1000 K, the feature at $7181.15578\,\mathrm{cm}^{-1}$ is stronger than that at $7185.5966\,\mathrm{cm}^{-1}$ making the ratio greater than unity at these temperatures. Figure 6.2 shows how the ratio sensitivity changes with temperature.

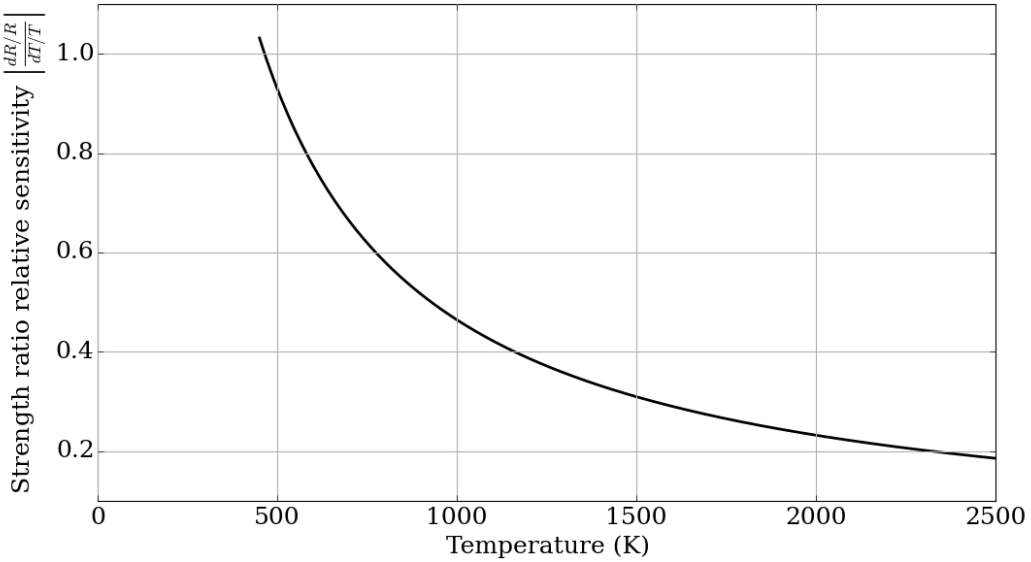

Figure 6.2.: Sensitivity of strength ratio to temperature for features at $7181.15578\,\mathrm{cm}^{-1}$ and $7185.5966\,\mathrm{cm}^{-1}$

6.2.3. TDLAS Simulation

A model of the TDLAS absorption path was developed to determine the likely impact of laboratory humidity and scramjet conditions on the measurements. The ideal scramjet spectra (obtained when there is no external absorption) are considered first to set a baseline. Then, laboratory humidity is increased so that the impact on the spectra can be seen. Next, modulation is applied to the laser diode current The path from the laser diodes to the photo-diodes can be divided into three sections (ignoring

Table 6.1.: TDLAS path sections together with typical properties for channel 1 during a shot with air as a test gas and no fuel injection

Section	**Environment**	**Distance** (m)	**Pressure** (kPa)	**Temperature** (K)
A	Laboratory	1.508	103.7	293
B	Dump Tank	1.400	0.080	270
C	Scramjet	0.100	3.1	400

the BK7 glass windows) as listed in table 6.1. If the properties in section i are P_i (pressure), x_i (water vapour concentration), l_i (path length) and $S^{(j)}\left(T_i\right)$ (line strength), the absorbance of a single feature along the path is:

$$A^{(j)} = \sum_{i=A,B,C} P_i x_i l_i S^{(j)}\left(T_i\right) \tag{6.1}$$

6.2.3.1. Ideal scramjet spectra

If the absorption by the laboratory air and dump tank are both set to zero, the ideal spectra for various scramjet conditions can be modelled. The effects of changing scramjet temperature, pressure and water vapour concentration are shown in this section. Absorption is plotted using a logarithmic scale to highlight differences due to conditions. The laser channel wavenumbers are highlighted in each figure by dashed lines. This analysis is presented to assist in understanding how changes in scramjet parameters change the absorbance and shape of spectral lines.

Temperature variation. Figure 6.3 shows the variation in absorption in the scramjet as temperature changes at constant pressure (3.1 kPa) and water vapour concentration (10%) typical of experiments using air as a test gas without fuel injection. The maximum absorption for the laser channel at 7181.15578 cm^{-1} occurs at lower temperatures and the absorption decreases as temperature increases. While the absorption at the second laser channel (7185.599 cm^{-1}) also decreases as temperature increases, the fall is less due to the increased lower state energy for that line. Thus, the temperature may be deduced from the strength ratio of the two lines.
Figure 6.4 shows the variation in absorption in the scramjet as temperature changes at constant pressure (50 kPa) and water vapour concentration (10%) typical of experiments using air as a test gas with fuel injection. At a pressure of 50 kPa typical of that in the exhaust of a scramjet that has combustion

present, the absorption is one hundred times greater than at 3.1 kPa for the same concentration and temperature conditions. The HWHM of each line is also increased from the lower pressure condition.

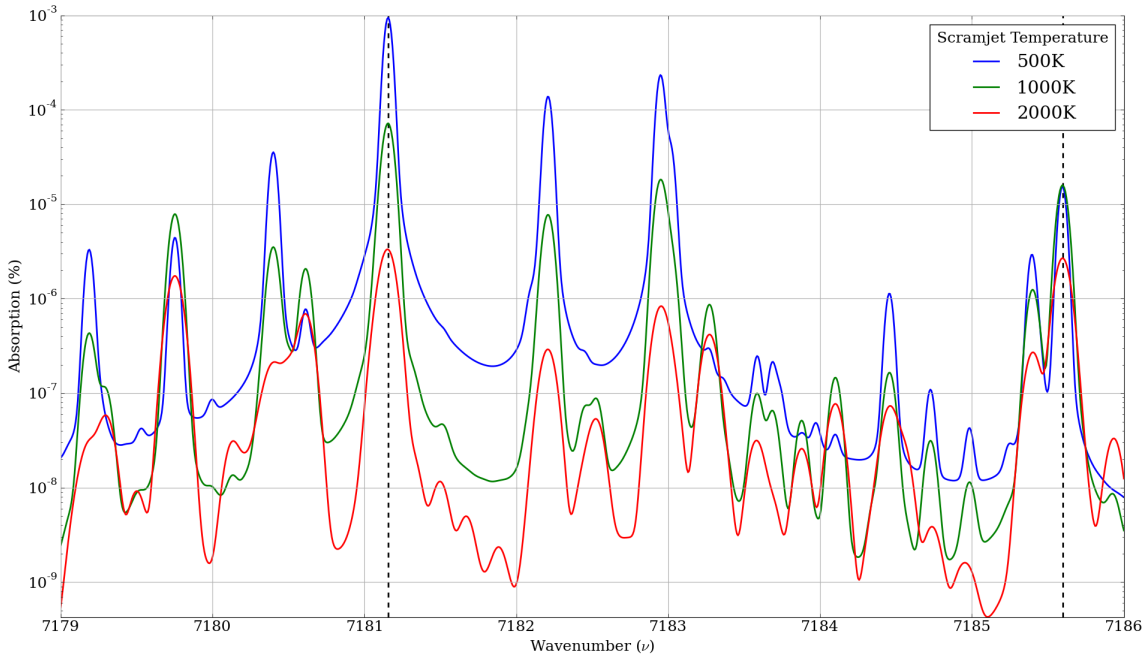

Figure 6.3.: Scramjet absorption variation with temperature at constant pressure (3.1 kPa) and water vapour concentration (10%) typical of experiments using air as a test gas without fuel injection.

Pressure variation. Figures 6.5 and 6.6 show the effect of pressure variation at room and high temperature respectively at constant water vapour concentration (10%). Scramjet pressure has a stronger influence than temperature on spectra. As pressure increases at constant temperature and water vapour concentration, features broaden and strengthen. At laboratory temperature (298 K) and 50 kPa, channel 1 absorption is greater than 0.1% but channel 2 absorption is four hundred times less than channel 1. At a scramjet temperature of 2000 K, the two laser channel features have approximately the same absorption irrespective of the pressure in the scramjet, for constant water vapour concentration. As expected, the features are much narrower at high temperature than low.

Water vapour concentration. As combustion occurs in the scramjet combustor, the water vapour concentration in the exhaust increases. Figure 6.7 shows the impact of various water vapour concentrations on the spectra at constant temperature (2000 K) and pressure (50 kPa). The absorption and feature width increase with water vapour concentration but the influence is less than that of both temperature and pressure. This lack of variation would make calculation of water vapour concentration difficult using only TDLAS.

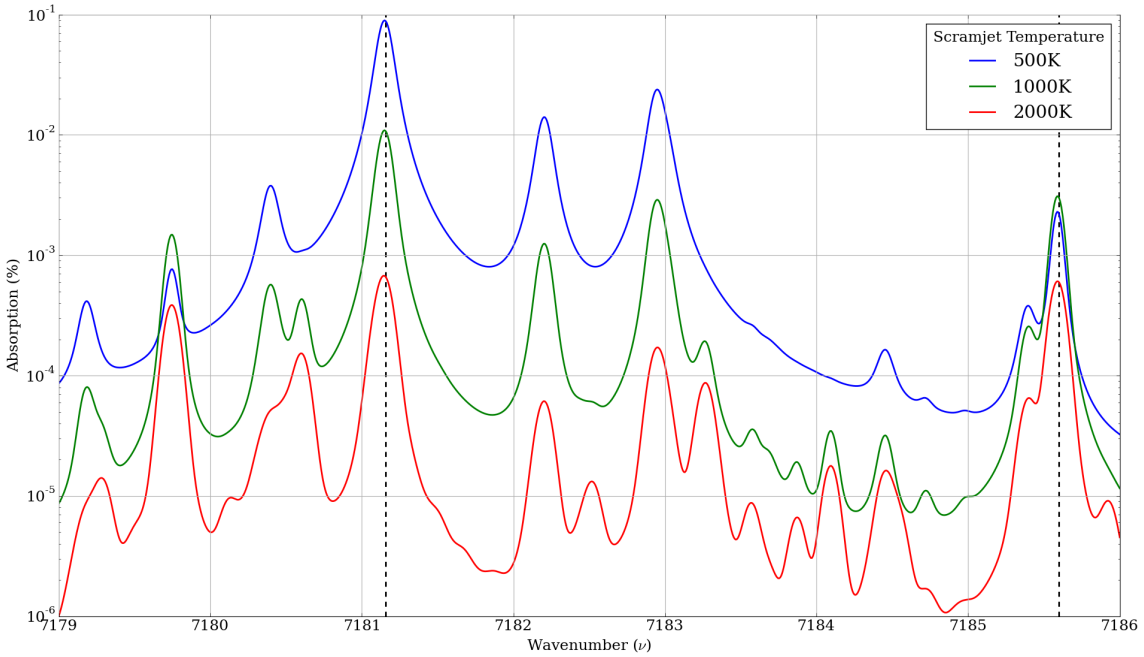

Figure 6.4.: Scramjet absorption variation with temperature at constant pressure (50 kPa) and water vapour concentration (10%) typical of experiments using air as a test gas.

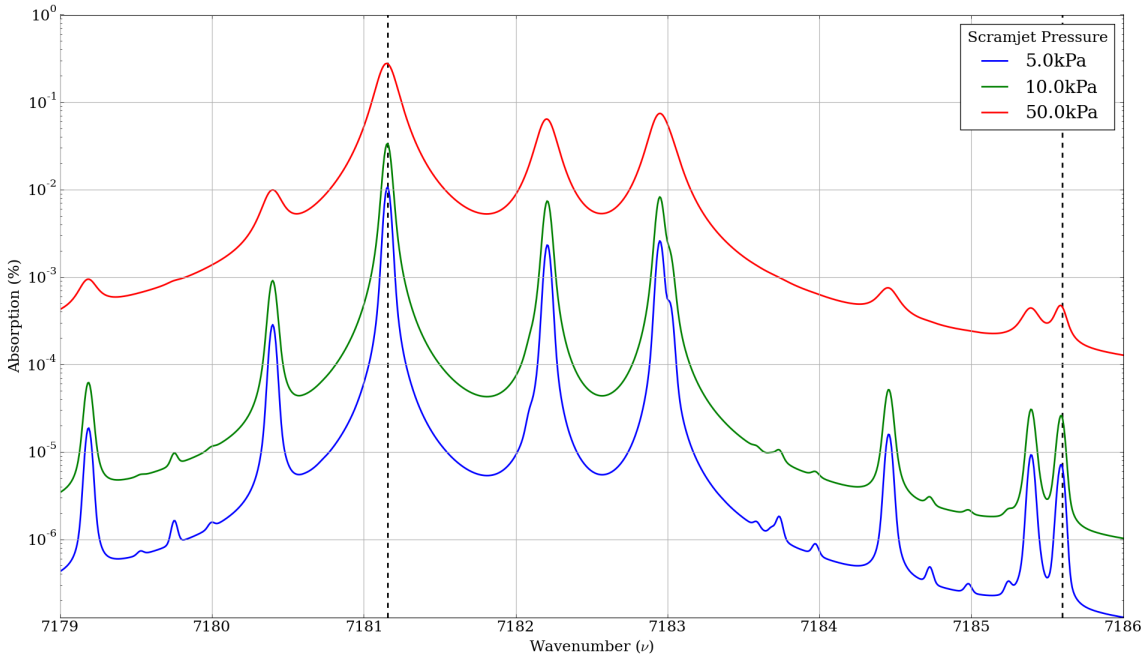

Figure 6.5.: Scramjet absorption variation with pressure at constant temperature (298 K) and water vapour concentration (10%).

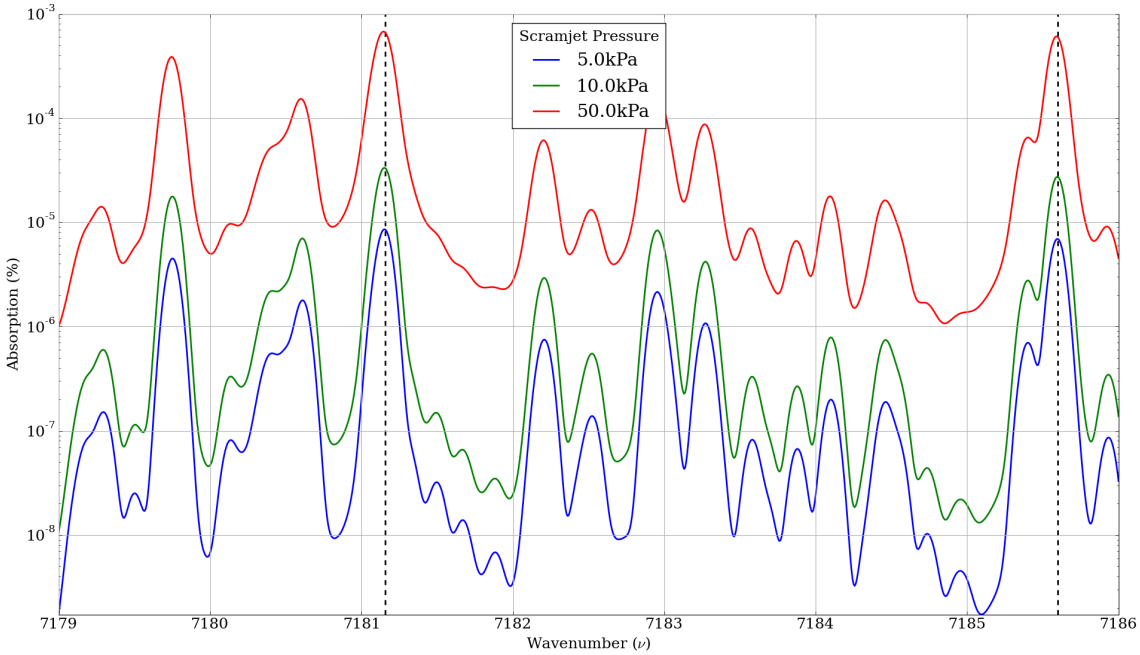

Figure 6.6.: Scramjet absorption variation with pressure at constant temperature (2000 K) and water vapour concentration (10%).

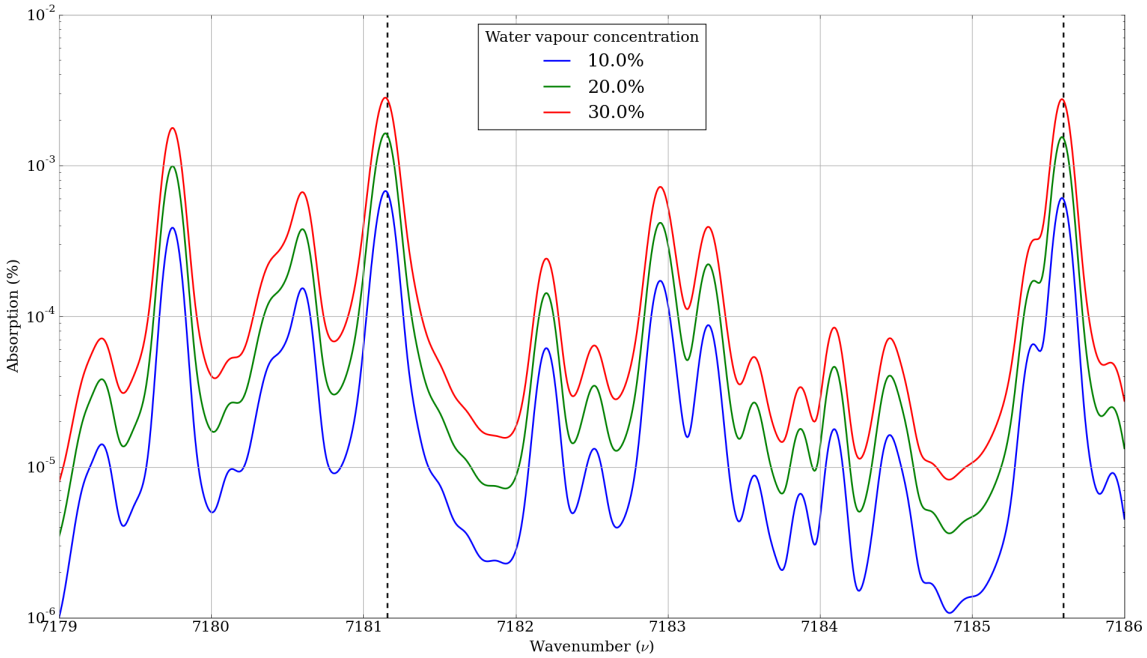

Figure 6.7.: Scramjet absorption variation with water vapour concentration at constant temperature (2000 K) and pressure (50 kPa).

6.2.3.2. Laboratory humidity variation

When determining the impact of laboratory humidity variation, assume that the scramjet is operating at the optimal TDLAS detection conditions; namely, high temperature (2000 K), high pressure (50 kPa) and water vapour concentration (30%). Also assume that the laboratory temperature and pressure are constant at 298 K and 101.3 kPa respectively. Finally, assume that the dump tank temperature and pressure are 298 K and 80 Pa respectively indicating that the dump tank is evacuated ready for a shot. Humidity in the laboratory has a very significant effect on the spectra and, consequently, on any TDLAS measurements where the path traverses through the laboratory environment. The major impacts are due to the pressure and path length through the laboratory, As may be seen in figure 6.8, laboratory humidity totally overwhelms the scramjet spectra at 20% relative humidity. The scramjet TDLAS signals are not discernible from the background even though optimal scramjet conditions were modelled. The absorption due to the second channel is relatively constant as humidity increases whereas the channel 1 absorption and HWHM both increase together with humidity. This characteristic may assist in determining whether humidity affected the observations. The relative humidity in the laboratory varied from 36% to 77% for experiments across the campaign. While the path was partially purged using a locally designed system, humidity may have influenced the readings since the purging system was developed and implemented on an ad-hoc basis and was not specifically designed and manufactured for these experiments.

6.3. Results

Given that these experiments did not successfully measure temperature and water vapour in a scramjet exhaust, the results that were obtained are presented to enable readers to gain an understanding of the

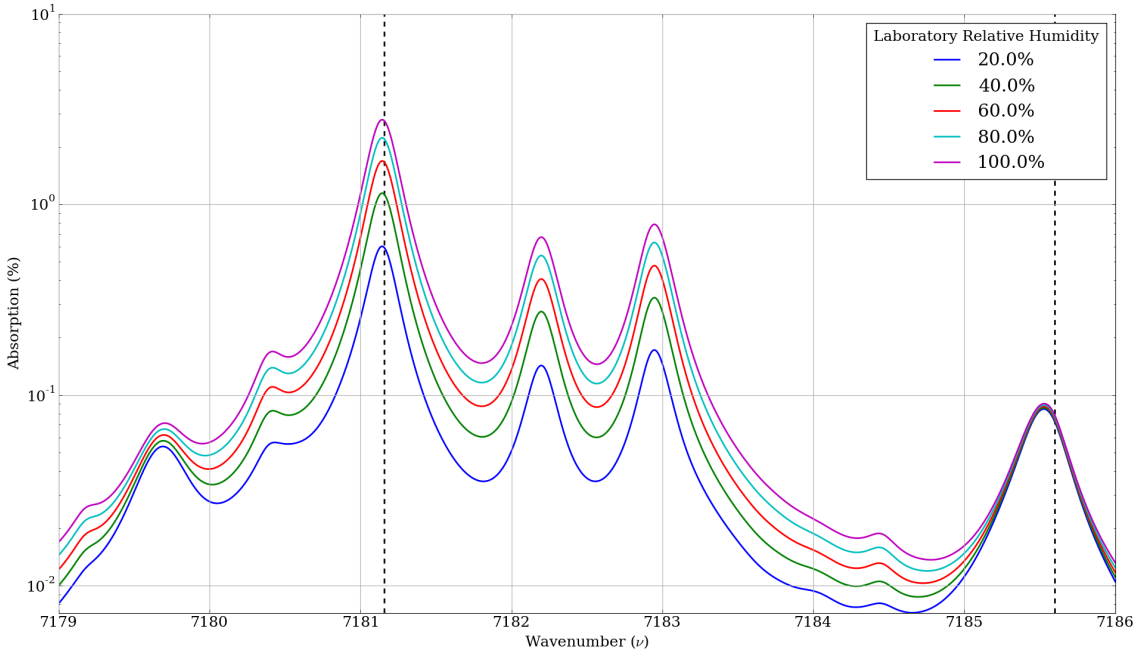

Figure 6.8.: Absorption variation with laboratory relative humidity.

extent of measurements achieved.

6.3.1. Laboratory test results

The laboratory tests verifying the TDLAS system performance are discussed in detail in appendix B and are summarised here. Laboratory tests were conducted to tune the TDLAS lasers to the centrelines of the relevant water vapour features; align the optics; determine the effect of changing modulation amplitude; and, to confirm the effect of purging the laser path with dry nitrogen. Both direct absorption and wavelength modulation spectroscopy were undertaken during the laboratory tests. They revealed the strong influence of humidity on absorption of the lasers leading to a requirement to purge the laser path with nitrogen. These tests were performed in two groups. The first group of tests were used to align optics and set the laser diode parameters for the two target water vapour features. During these trials, the laser paths were at laboratory pressure temperature and humidity to ensure that the water vapour features were strong. The second set of trials was undertaken with the evacuated dump tank in the path and with the nitrogen purging system operating.
Observations from the laboratory tests were:

- Whilst the function generator indicated that it was generating a sinusoidal waveform at 1 MHz, the received signal frequencies were over 2 MHz with spectral distributions of approximately 300 kHz HWHM.

- The recorded signals were discretised in voltage. The peak-to-peak voltage of the digital-to-analogue converter was set too high for the amplified photo detector signals. When coupled with a 12-bit converter, steps could be seen in the recorded signals.

- The function generator output impedance of $50\ \Omega$ was coupled to the laser diode mounts which also had impedances of $50\ \Omega$. Thus, when the generator output amplitude was 1 V, it was believed that a similar voltage was being fed into the laser diode mounts. However, the generator output was also fed into the data recording system which had an input impedance of 1 MΩ. The high impedance of the data recorder meant that the laser diodes were modulated by $10-15$ mV instead of 1 V as desired.

- The reduced modulation voltage meant that the lasers were modulated across 10% of each feature instead of the entire feature as desired.

- The laser diodes displayed temperature hysteresis with the output power at any laser diode current differing when the current was decreasing compared to when it was increasing. This resulted in a range of transmittances for any given wavelength.

- An etalon was not available to accurately measure laser frequency changes; thus, excessive reliance was placed on models and simulations without independent verification.

- The laboratory tests were conducted at room temperature only and tests were not undertaken at elevated temperatures and reduced pressures. Thus, the expected TDLAS response at these conditions was not verified.

- The nitrogen purging system which was devised *on the fly* for these experiments, was only partially effective. Thus, humidity may have affected most of the results.
- The concept of using large amplitude sinusoidal modulation of the laser signals appeared to be effective but, after detailed signal analysis, did not easily produce the desired results.

Figure 6.9 shows an extracted signal from an atmospheric test where the diode was sinusoidally modulated at 1.0 MHz and 400 mV peak-to-peak and sampled at 60 Msps. Appendix B has details of the signal extraction process. This figure shows transmittance data (transformed to be relative to wavenumber) for one laser diode for 150 μs of the test. The figure also shows the calculated transmittance for the feature based on the pressure, temperature, humidity, path length and laser modulation amplitude for the test. As this figure shows a number of salient features, it is worth considering in detail. The test temperature, pressure and relative humidity were 23°C, 102.5 kPa and 51% respectively. The water vapour concentration was calculated to be 1.3%. The transmittance has been rescaled so that it is centred on the mean transmittance. There is considerable scatter in the data at each wavenumber due to laser power variation (to be discussed further below). The striations in the data are due to digitisation issues with the analogue to digital converter in the data recording system. This plot is typical of atmospheric tests where the humidity was relatively high. Figure 6.10

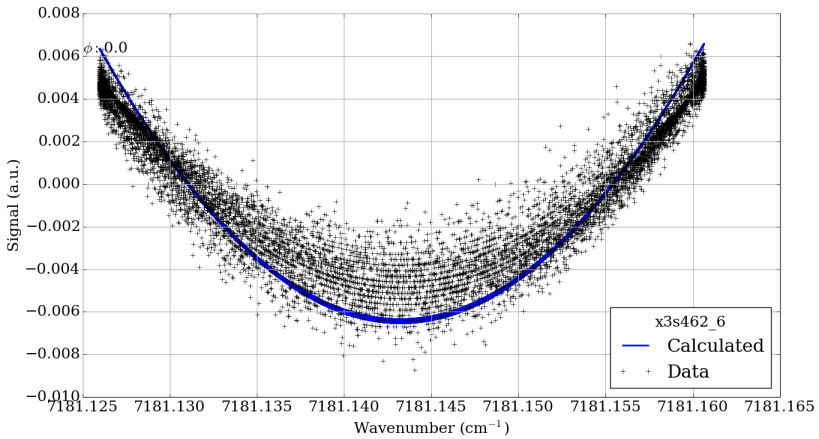

Figure 6.9.: Calculated and measured data for channel 1 of a laboratory test at 51% relative humidity.

shows the frequency distribution for the test and channel above. The peak frequency is 2.288 MHz with a second maximum at 3.3 MHz. The feature at 28 MHz is an aliased signal due to the peak frequency. The feature at 7 MHz is a harmonic of the main and second peaks while the two narrow features at 12 MHz and 20 MHz are higher order harmonics of the other signals. The frequency spread around the two major peaks indicates signal noise and power variation as mentioned for the previous figure. Figure 6.11 displays the extracted TDLAS data for channel 1 of an atmospheric test where the relative humidity was 15%, corresponding to a water vapour concentration of 0.5%. Again, the figure contains calculated plot of transmittance based on the environmental parameters for the test (25.2 °C and 101.27 kPa). The reduced humidity causes this plot to have a very different form from that for the medium humidity condition. Lower humidity corresponds to reduced absorption by the feature and, thus, less data scatter at any wavenumber. The widely separated data tracks are

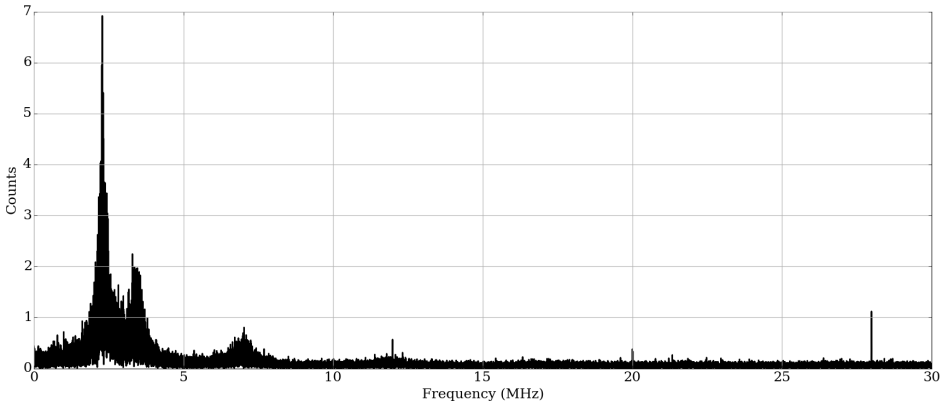

Figure 6.10.: Frequency spectrum for channel 1 of a laboratory test at 51% relative humidity.

due to hysteresis in the laser diode power output as the current modulates. The diode temperature peaks at maximum current and nadirs at minimum current. This was verified by tracing the signal in terms of laser diode current. details of the investigation are in appendix F. The TEC is not able to maintain the exact laser diode temperature since its control frequency (approximately 10 Hz) is very low compared with the modulation frequency. This feature is highlighted by using a large amplitude sinusoidal modulation waveform. The laser diode power hysteresis effect is also visible for channel

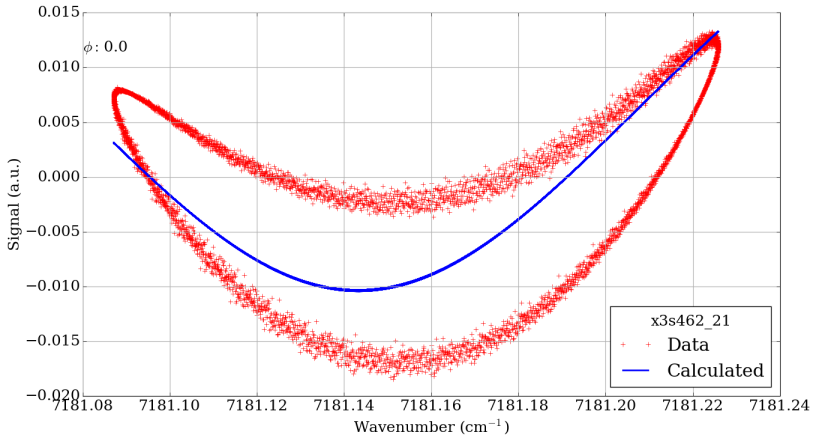

Figure 6.11.: Calculated and measured data for channel 1 of a laboratory test at 15% relative humidity.

2 of the same experiment as shown in figure 6.12. The scatter is reduced below that for channel 1 because of the lower absorption by the second feature. These results show that the system was observing water vapour absorption with varying relative humidity in atmospheric tests. They highlight the importance of eliminating extraneous water vapour from the laser path outside of the desired test section. They also show the strong effect that laser power hysteresis has on measurements at high modulation frequencies. If successful TDLAS experiments are to undertaken in the MHz modulation range, this hysteresis will have to be either eliminated of compensated for during analysis.

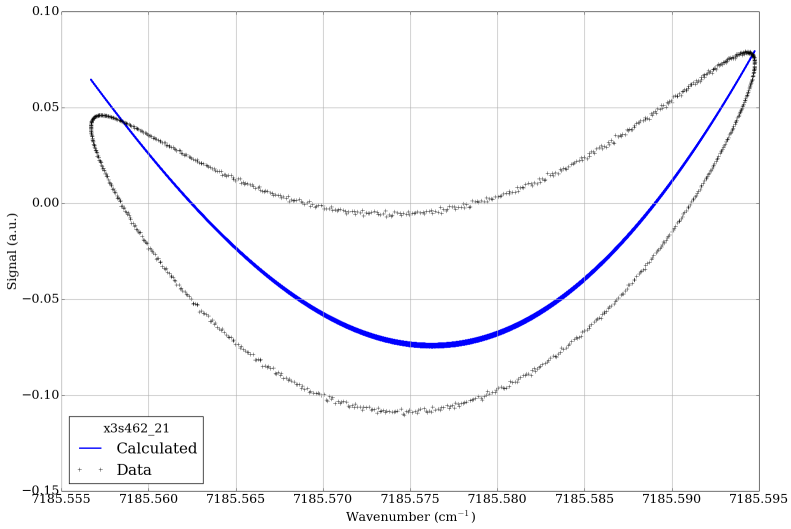

Figure 6.12.: Calculated and measured data for channel 2 of a laboratory test at 15% relative humidity.

6.3.2. Scramjet observations

Before considering the TDLAS signals, let's review the pressure trace at the exit from the combustor during two typical shots. Figure 6.13 displays typical combustor exit pressures for two shots using air as a test gas with no fuel injection. There are four time regimes shown: pre-test, flow establishment, test and post-test times. Pre-test is the regime before any shock waves arrive at the pressure sensor. The pressure initially rises as the flow establishes and acceleration tunnel air passes through the combustor. During test time the combustor exit pressure gradually rises. Post-test is indicated by significant pressure variations due to test gas that has been processed multiple times by shock waves. As may be seen from the plot, the pressure is very repeatable for shots with air test gas without fuel injection. Figure 6.14 shows the combustor exit pressure for a fuel into nitrogen shot. The pressure initially rises as the flow establishes and acceleration tunnel air passes through the combustor. After peaking, the static pressure falls and the test time begins at approximately 20.5 ms after the primary diaphragm ruptured. During the test time, combustor exit pressure is relatively constant apart from when unsteady shock waves pass the transducer. Test time lasts for about 1.4 ms, after which test gas that has been processed by multiple shock waves passes the sensor. The pressure trace for a fuel into air shot displays an increasing test time pressure due to combustion.

6.3.2.1. TDLAS plots

Following on from the laboratory experiments where it was found that the modulation amplitude was much less than planned, the TDLAS observations for the scramjet experiments are presented qualitatively rather than quantitatively. Figure 6.15 compares the TDLAS photo detector ratio signals for two shots with air as a test gas where one shot had fuel injection but the other did not.[1] Both traces display changes in the signals as the flow establishes. This may be due to amplifier latency

[1] Only the signal ratio was recorded for the first ten experiments. Both channels were recorded for later experiments.

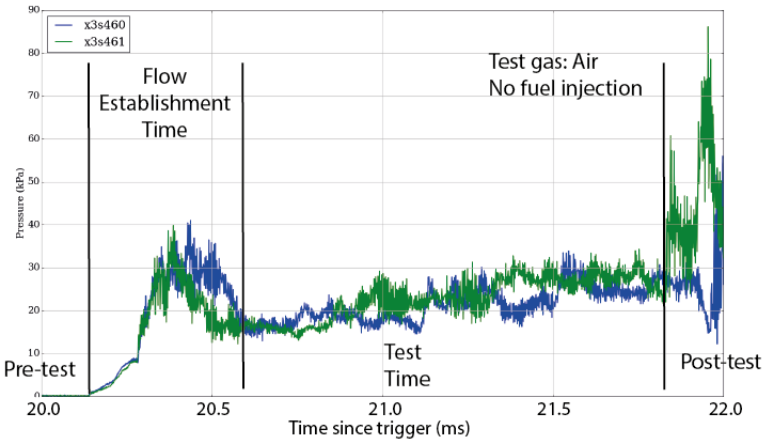

Figure 6.13.: Combustor exit pressure for air test gas shots without fuel injection.

as the luminosity rises with arrival of the acceleration tunnel gas or due to absorption changes or a combination of both effects. Figure 6.16 shows the FFT for channel 2 $(7185.599\ \mathrm{cm}^{-1})$ for a shot with fuel injection into air test gas. There is a large peak due to the modulation at 999.8 kHz with a second peak at 2.000 MHz. There is low-level, wide spectrum noise around these two peaks. The TDLAS system was able to detect combustion products in the scramjet exhaust. With improvements to the design and operation of the system, it should be capable of measuring temperature and other scramjet parameters.

6.4. Issues limiting results

As may be expected for experiments involving complex interactions, rapid changes in test conditions, high-speed data acquisition and short test times, each experiment was a learning experience. With each tunnel turn-around requiring four hours of work, these lessons were expensive in terms of time and personnel and, as a consequence, are documented here to assist future researchers.

6.4.1. TDLAS

Approximately three weeks were spent setting up the TDLAS system for these experiments. Also, amplifiers were designed and manufactured plus control software was developed. The short test time imposed considerable constraints on the TDLAS system including a requirement to modulate the lasers at 1 MHz. Ideally, optical fibres would have been used to transfer the laser signals to the test section; however, this was not done because significant modifications to the scramjet model would have been needed.

The laser recording was initially sampled at 24 Msps with 2000 pre-trigger samples and 100,000 samples with the trigger level set at 0.1 V rising signal from TR01 (the first PCB sensor on the

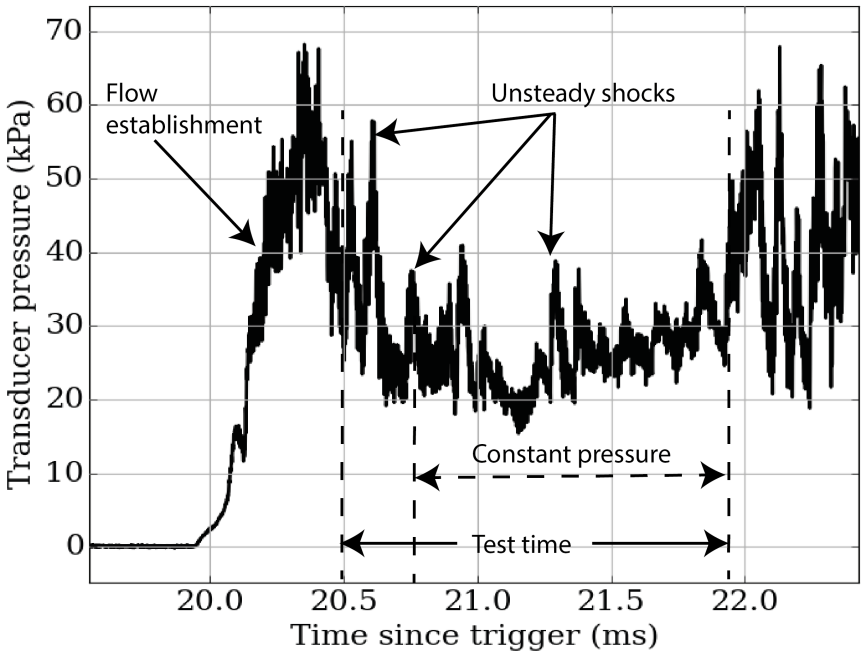

Figure 6.14.: Combustor exit pressure for a fuel into nitrogen shot.

scramjet inlet). The aim was to trigger recording as the flow established in the scramjet then record 4 ms of flow through the scramjet. This trigger method worked for one shot but failed on the second because the system did not trigger until the contaminated flow after the test time arrived. The sample rate was increased, the number of pre-trigger samples was changed and the trigger source and level were changed methodically until data were reliably recorded. The final configuration was a sampling rate of 60 Msps, 400,000 total samples and 250,000 pre-trigger samples being triggered by a 0.1 V rising signal from TR01. The laser alignments with the test section and to the photodetectors had to be verified before each shot. If the scramjet was opened, the entire laser path had to be verified.
For the first nine shots, the individual laser channels were not recorded; only the signal ratio was measured. This was done in the belief that it would provide enough information for analysis. The issue was that, if a channel had problems, the cause of the problem could not be isolated. Both laser channels were recorded for all later shots. The fuel system PCB initially recorded intermittently even though the PCB was checked after each shot. The intermittency was caused by flow within the instrumentation area of the scramjet due to damage near the leading edge. After the damage was repaired, the PCB worked correctly.

6.4.2. Scramjet

The scramjet test model moved during initial tests due to recoil of the expansion tube during piston launch. Given that the test section hole diameter was 10 mm, this movement invalidated the test. The scramjet was secured in the dump tank for subsequent experiments. The scramjet forward structure had been damaged during previous experiments allowing flow to enter the instrumentation section of the model. This caused PCB wires to break and move. Also, shrapnel from the primary diaphragm impinged on the scramjet leading edges. Any damage to the scramjet should be repaired immediately

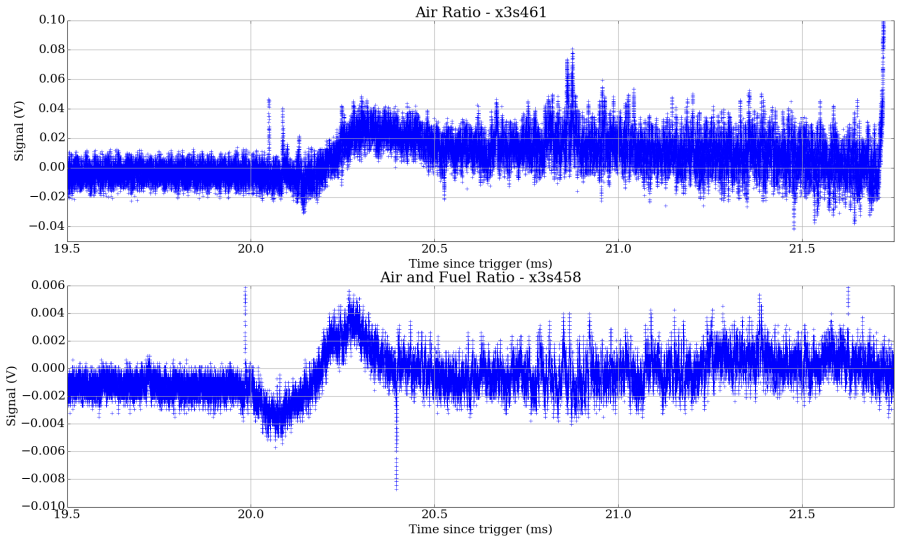

Figure 6.15.: Comparison of TDLAS signal ratios for shots x3s458 and x3s461. Both shots had air as test gas. Shot x3s461 did not have fuel injection whereas shot x3s458 did have fuel injection.

to prevent secondary damage from occurring. The leading edges should be filed and sharpened between each shot to ensure that flow conditions are repeatable. The fuel system pressure transducer was affected by the inflow, invalidated some of the earlier pressure measurements.

6.4.3. Data recording system

Two Kulite pressure sensors were used to measure the pressure at the laser test section. Both worked correctly between shots but one continually failed during shots. No spare Kulites were available due to experimental requirements on T4. At the end of the campaign, the suspect Kulite was found to have a very small portion of exposed wiring that failed under dynamic loads. The data acquisition system failed on shot x3s468 so no data was recorded for that shot. The data acquisition system failed catastrophically after shot x3s471 terminating the campaign.

6.5. Suggestions for improvement

Future researchers could improve upon these experiments by:

- characterizing the TDLAS performance using heated water vapour in a controlled environment,
- using fibre optics to launch and detect the TDLAS signals within the dump tank rather than external to the dump tank,
- if the TDLAS path is external to the dump tank, designing a specific nitrogen purging system to reduce absorption be atmospheric water vapour.
- independently measuring the flow temperature in the scramjet test section for comparison with the TDLAS measurements,

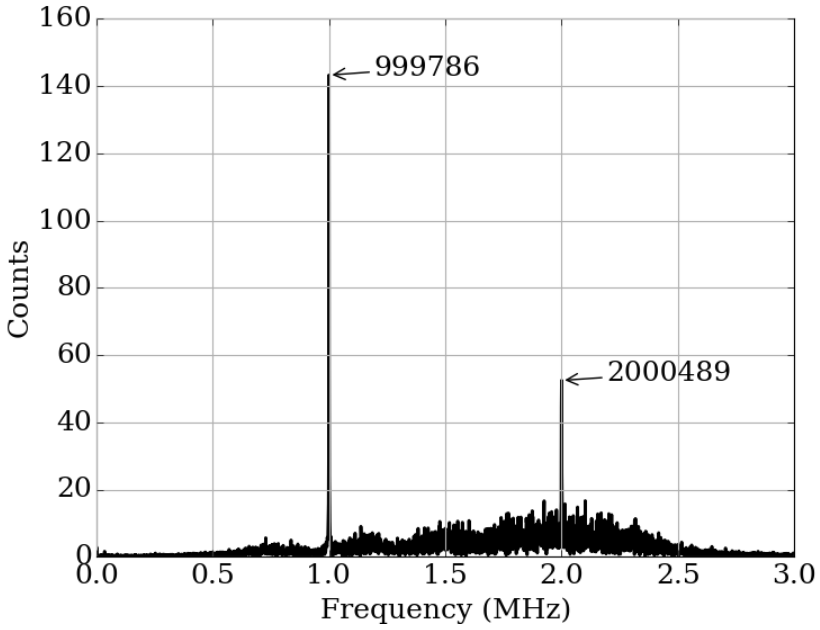

Figure 6.16.: FFT of the TDLAS signal at 7185.599 cm^{-1} for a fuel into air shot.

- using high-speed video to record the visual conditions at the test section during a test.
- using a digital waveform generator to modulate the lasers,
- using a scramjet with a wider profile to increase the absorption path length, and
- incorporating TDLAS calculations into scramjet CFD models to alleviate the use of analytical models.

The simulations discussed earlier in this chapter indicate that the TDLAS campaign had potential to successfully measure the combustion chamber parameters. Temperature and pressure are both readily measurable using TDLAS. Water vapour concentration can be derived but an additional independent sensor such as static pressure or wall temperature may be needed for this measurement.

6.6. Summary

These experiments were very challenging to design, perform and analyse due to the rapidly changing test conditions, short test time and complex experimental procedures required. Nevertheless, TDLAS was able to qualitatively detect combustion and lack of combustion in a scramjet exhaust during expansion tube experiments.

These experiments have clearly shown that TDLAS has the potential to be able to measure water vapour concentration and flow temperature in the exhaust of a scramjet. Suggestions for future research directions are listed to help progress this measurement technique towards a practical implementation. Future researchers should ensure that CFD incorporating TDLAS is undertaken prior to any experiments in order to have quantitative data against which the TDLAS observations can be compared.

7. Atomic Oxygen Measurements

The shock wave ahead of a body travelling at hypersonic speed through the upper atmosphere dissociates air molecules into atoms and ions via radiative transfer. The concentration of atomic oxygen in the boundary layer strongly influences the heat transfer into the body [145]. Knowing the concentration and number density of oxygen atoms ahead of hypersonic vehicles would improve heat transfer estimates and allow designers to optimise heat shield thickness.
Atomic oxygen is readily produced in shock tube flows [138] but is believed to be present on low concentrations in expansion tube flows. Having a method of remotely measuring the concentration of atomic oxygen in both flow types would be advantageous to researchers and vehicle designers. TDLAS may be useful to measure the properties of atomic oxygen in a super-orbital facility such as the X2 or X3 expansion tube. This capability is currently not available at the University of Queensland. Before applying TDLAS to atomic oxygen measurement, we need to determine the feasibility of using TDLAS for oxygen measurements in a steady-state, laboratory environment where experiments can be easily performed and adjustments made to optimise the techniques.
Atomic oxygen may also be produced in a laboratory environment using an Evenson cavity [146]. This may provide a relatively stable environment in which to develop TDLAS techniques and determine the feasibility of using TDLAS to measure the population density of high lying levels of atomic oxygen before applying the methods to the more challenging conditions of an expansion tunnel or shock tube.
This chapter discusses experiments aimed at measuring atomic oxygen concentration in a microwave generated plasma using TDLAS to probe the oxygen triplet at 844.6 nm. Detecting absorption by atomic oxygen in a plasma may be difficult given that the atoms are highly excited and emit radiation that could overwhelm the laser absorption. Although the plasma temperature was anticipated to be of the order of $1500 - 2500$ K, any spectral features were expected to be narrow due to the plasma pressure being between 80 Pa and 300 Pa. The primary contributors to spectral line width were likely to be Doppler and van der Waals broadening.
Section 7.7 discusses the requirements of a TDLAS system to probe atomic oxygen in an expansion tunnel for experiments on planetary entry flows or hydrogen fuelled scramjets.

7.1. Motivation

The study of atomic oxygen concentrations within the Earth's mesosphere and lower thermosphere is among the principle interests of atmospheric scientists. Atomic oxygen contributes to the creation of ozone, global climate change and to the expansion and contraction of the atmosphere [147]. The

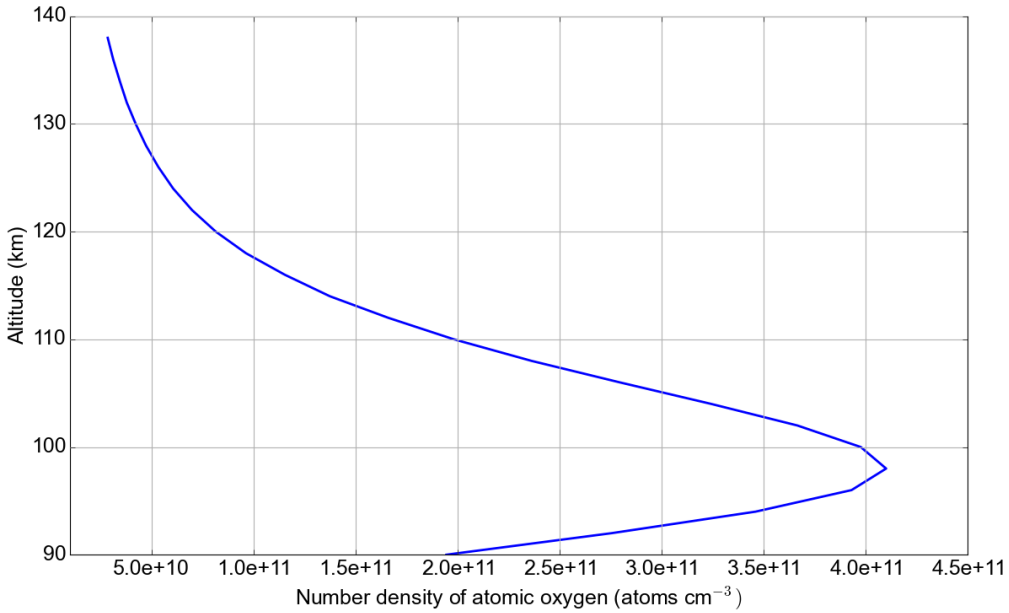

Figure 7.1.: Number density of atomic oxygen in the atmosphere at altitudes from 90 km to 138 km [147]

number density of atomic oxygen is significant in the upper atmosphere as shown in Figure 7.1. During atmospheric entry, molecules behind the bow shock dissociate into atoms which, in turn, may ionise. These highly reactive atoms and ions strongly affect heat transfer into the heat shield of a spacecraft via catalytic reactions [148]. Reducing the mass fraction of spacecraft assigned to heat shields is an area of significant past and current research. Thus, it is important to accurately characterise the flow ahead of heat shields during atmospheric entry conditions.

The hypersonic free-piston shock tunnels and expansion tubes at UQ have test times that are of the order of one millisecond. They simulate atmospheric entry but have the limitation that they do not generate persistently high temperatures in the test section. As such, they are of limited use in testing ablation of heat shields unless the test piece is pre-heated as described by Zander [149]; however, dissociation occurs downstream of shock waves generated in expansion tubes. There is research interest in measuring the atomic oxygen and nitrogen concentrations in these flows as this knowledge may lower the uncertainties associated with heat shield design. Emission spectroscopic techniques have been used in the past to measure population densities of high lying levels of atomic species behind the shock wave in expansion tunnel flows. TDLAS techniques may supplement emission spectroscopy in these measurements provided they could be shown to work in similar flow conditions beforehand.

Arc jets facilities have been extensively used for reusable TPS testing. The nature of plasma precludes researchers from being able to accurately measure ion concentrations within the flow so test conditions are usually defined using either the expected heat-flux level or the anticipated surface temperature for a material [150]. The Institute for Spacecraft systems (IRS) at The University of Stuttgart uses plasma wind tunnel facilities to qualify heat shield materials for spacecraft, develop planetary entry measurement techniques and validate numerical codes. The IRS tunnels use plasma torches to

generate high temperature, enthalpy and pressure flows with test times of up to 10 minutes.
TDLAS has the potential to improve particle concentration measurements in plasma flows. Previously, Martin et al [150] used a tunable diode laser sensor for in-situ monitoring of temperature in the arc heater of the NASA Ames 60 MW Interaction Heating Facility. The external cavity laser was tuned to 777.2 nm and laser absorption was used to monitor the population of electronically excited oxygen atoms in an air plasma flow. IRS has a New Focus Model 6300 Velocity Tunable Diode Laser controller with a New Focus Model 6316 external-cavity tunable diode laser. The laser head provides a stable, tuned laser output at wavelengths between 834 nm and 854 nm with the laser diode at an operating temperature of $20°$C and a recommended current of 60 mA [151].
Microwave discharges can be used as excitation sources for gaseous electronic studies, for light sources and for the production of free radicals [146]. An Evenson cavity is an air-cooled, quarter-wave coaxial cavity with adjustable coupling and stub tuning that is operated at 2.45 GHz [152] to ionise a gas without undue heating. A low loss dielectric tube made of quartz or ceramic contains the background gas. The microwave discharge system had previously been used as a source of atomic oxygen to calibrate sensors for spacecraft [153]. Evenson cavities are ideal for proof of concept experiments for novel technologies or applications because they can be used on a bench top. A limitation of the microwave discharge is that the plasma is less than 1 cm thick [154] and is spatially confined, limiting access for test equipment.
In these experiments, an Evenson cavity drawing up to 300 W of power was used to generate a plasma in both low pressure air and oxygen and TDLAS was then used to probe the oxygen triplet at 844.6 nm. The techniques developed in these experiments can be applied to expansion tunnel flows.

7.2. Theory

Temperature is usually derived from TDLAS measurements of the ratios of two features that have considerably different lower energy states. In these experiments, an atomic oxygen triplet at 844.6 nm was the target for TDLAS. This triplet was chosen because a tunable diode laser that operated at wavelengths between 834 nm and 854 nm was available at IRS. As shown in table 7.2, the three lines have the same $^3S^o$ lower state energy which effectively eliminates the ratio method of temperature determination.

Air Equilibrium Composition. At room temperature and pressure, air consists of 71% N_2, 28% O_2 and 1% other gases. As temperature increases, the composition of air changes due to dissociation initially then due to ionisation of the products of dissociation. There is no significant dissociation at temperatures below 2000 K at a sea level atmospheric pressure of 101 kPa [2]. Scramjets operate at combustion pressures of about 50 kPa [2].
Oxygen molecules (O_2) are almost completely dissociated by 3000 K whilst nitrogen (N_2) dissociates above 5000 K [107]. Figure 7.2 shows the air equilibrium composition for temperatures up to $30,000$ K. As may be seen in figure 7.2, oxygen atoms begin to ionise at approximately 7000 K. At $17,000$ K, O^+ accounts for 10% by species mole fraction of the equilibrium composition of air.

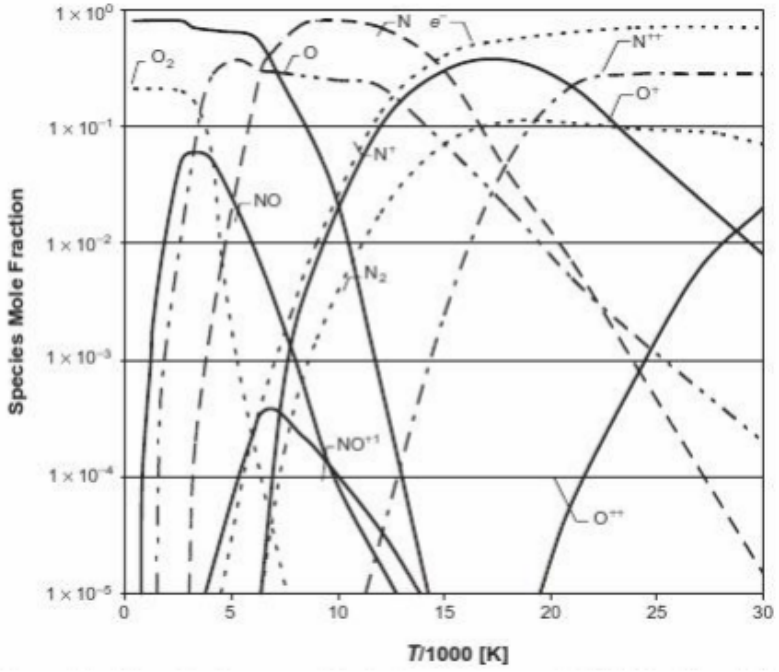

Figure 7.2.: Air equilibrium composition for temperatures up to $30,000$ K [2].

Above $19,000$ K, oxygen ions further ionise to O^{++}.
Flows in scramjet inlets, diffusers and combustors have temperature ranges from the wall temperature (say 300 K) to the combustion temperature (approximately 3000 K at the highest). Thus, there are three thermal regions of interest when considering detecting the oxygen composition in scramjet flows:

1. Region I - $T < 2000$ K. In this region, oxygen molecules predominate the composition.
2. Region II - 2000 K $\leq T < 3000$ K. In this temperature range, both oxygen molecules and atoms are present in the flow with the balance being a function of the temperature.
3. Region III - $T \geq 3000$ K. Here, oxygen atoms predominate.

A TDLAS system to determine the oxygen content in a scramjet should ideally detect oxygen molecules (for region I temperatures) and oxygen atoms (for regions II and III). As the most interesting chemistry is likely to occur in region II, that region should be used as the basis for the system design.

The partial pressure of atomic oxygen relative to molecular oxygen in a weakly ionised plasma increases with temperature in accordance with Dalton's law of partial pressures [150]. After atomic oxygen is formed, a portion of the atoms will be in the meta-stable $^3S^o$ state. The $^3S^o$ lower state of the oxygen transition is metastable in that it is not coupled to the ground state via one-photon selection rules. An atom in a metastable state must collide with another particle to transition to a lower level [28]. In a plasma, the population of this state increases to measurable levels and the transition can have strong absorption intensity.

Since TDLAS relies on absorption of the laser radiation by the medium, measuring the absorption by a plasma may give an indication of the number density of the meta-stable state which, in turn, can give the partial pressure. The spectral features are subjected to Doppler and van der Waals broadening. The former depends on the excitation temperature while the latter depends on the properties of absorber and perturber particles in the gas. The effects of both broadening mechanisms may be convolved to give a Voigt line shape.
Thus, the line shape, transmittance and pressure of a test condition may be used to derive the number density, partial pressure and temperature of the oxygen atoms in the plasma.
This section begins by discussing the relationship between the partial pressures of molecular and atomic oxygen at different temperatures. This will establish a relationship between temperature, pressure and mole fraction of atomic oxygen. Next, the Boltzmann distribution for population of electronic levels in a plasma is stated. The Boltzmann distribution formula requires calculation of the partition function so a simple method to calculate this for atomic oxygen is stated.
After discussing plasma properties, the focus moves to spectroscopic features and data relevant to TDLAS. The spectral properties of neutral oxygen for the triplet at 844.6 nm are given together with the formula for line strength of an atomic transition. The Beer-Lambert law is stated before formulae are given for Doppler, van der Waals broadening and the Voigt profile.

7.2.1. Atomic oxygen plasma properties

Number density. Assuming that a plasma is weakly ionised, the total number density of oxygen is calculated from the ideal gas law and Dalton's law of partial pressures as [150]:

$$n_O = \frac{P x_O}{kT} \tag{7.1}$$

where P is the total pressure and x_O is the mole fraction of atomic oxygen. Figure 7.3, derived using data from reference [155], shows the ratio of partial pressures of atomic and molecular oxygen vary with temperature in a pure oxygen gas at pressures typical of these experiments. Figure 7.1 shows the variation in atomic oxygen number density with temperature in a pure oxygen gas at pressures typical of these experiments.

Boltzmann distribution. When a plasma is in thermal equilibrium, the relative populations of all electronic levels follow a Boltzmann distribution described by a common temperature [28]. If the plasma is also in chemical equilibrium, the gas is described by a unique temperature (T). For such a plasma, the lower state number density (n_l) of an electronic transition is related to the total number density of atomic oxygen (n_O) by:

$$\frac{n_l}{n_O} = \frac{g_l}{Q_O} \exp\left(-\frac{E_{low}}{kT}\right) \tag{7.2}$$

where g_l is the degeneracy of the lower state, k is Boltzmann's constant and Q_O is the atomic oxygen partition function.

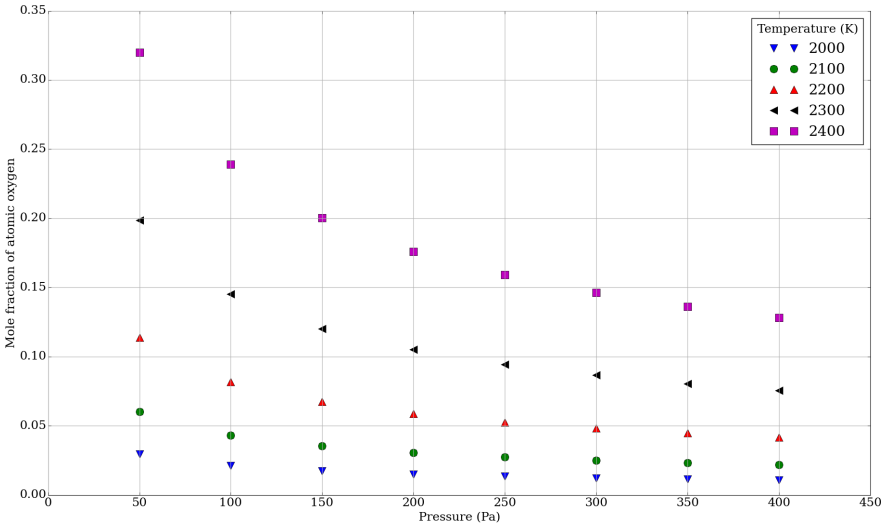

Figure 7.3.: Mole fraction of atomic oxygen at various pressures and temperatures [155]

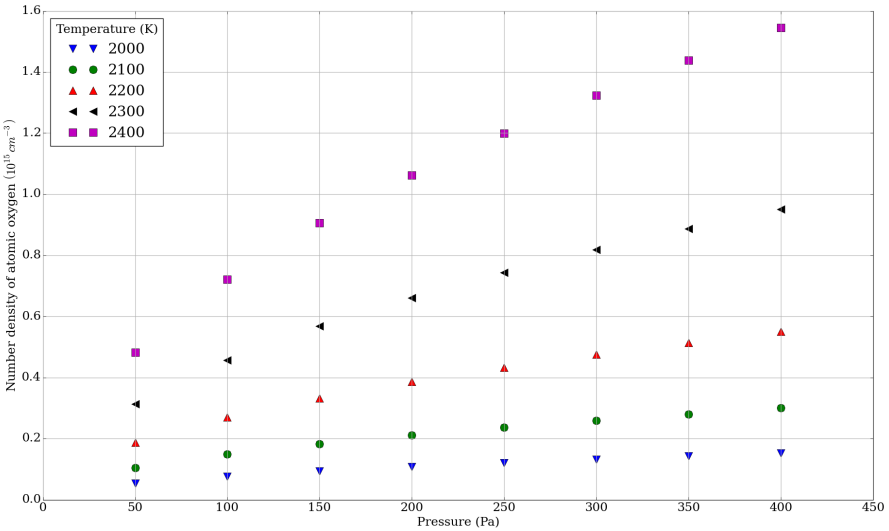

Figure 7.4.: Number density of atomic oxygen at various pressures and temperatures [155]

Table 7.1.: Levels and group data as a function of ionisation cut-off energy for oxygen atoms [110]

Δ_s cm^{-1}	Number of Levels	G	ϵ eV
250	94	22,940	13.4656
500	83	22,660	13.4643
750	79	22,564	13.4639
1000	68	7844	13.3727

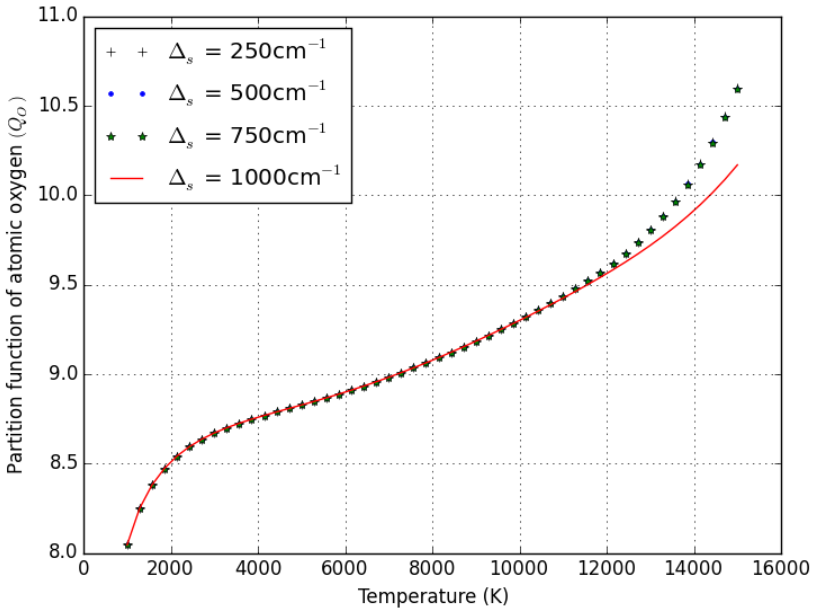

Figure 7.5.: Atomic oxygen partition function versus temperature for various ionisation cut-off energies [150]

Partition function. Colonna et al [110] developed a simplified method to calculate partition functions and thermodynamic properties of atomic species whereby the states are grouped in a few virtual levels. All of the atomic levels are grouped into a few lumped levels with average energy ϵ and global statistical weight G, dependent only on the energy cut-off criterion Δ_s selected to lower the ionisation potential used to truncate the partition function [150].

The statistical weights and energies are calculated by summing over the states belonging to each group. Table 7.1 reproduces the level and group data from reference [150]. Figure 7.5 is a plot of the partition function versus temperature for different ionisation cut-off energies. Below $10,000$ K, the partition function is independent of ionisation cut-off energy. The three level partition function for oxygen Q_O is [110]:

$$\begin{aligned} Q_O &= 9\exp\left(-\frac{9.67077\times10^{-3}}{T}\right)+ \\ &\quad 6\exp\left(-\frac{2.33774}{T}\right)+G\exp\left(-\frac{\epsilon}{T}\right) \end{aligned} \tag{7.3}$$

where G is the group statistical weight, ϵ is the group energy and the temperature T is expressed in eV. In these experiments, the temperature was anticipated to be in the range $2000 - 5000$ K making Q_O nearly independent of the ionisation cutoff energy [150]. Following the guidance of Martin et al, an ionisation cut-off energy of $250\,\mathrm{cm}^{-1}$ was used for this study making $G = 22,940$ and $\epsilon = 13.4656$ eV.

Calculation flowchart. Figure 7.6 shows how these equations are applied to obtain the number density of the lower state of atomic oxygen at a given temperature and pressure. CEA in the diagram stands for the NASA computer program *Chemical Equilibirum with Applications*[155, 156]. The flowchart is entered at the top where estimates of oxygen plasma temperature T and pressure P are input to CEA which produces mole fraction values for atomic oxygen x_O, molecular oxygen and ozone at those conditions. Only the atomic oxygen mole fraction is used further in these calculations. The temperature estimate is also used in conjunction with Colonna's three level partition function for oxygen (equation 7.3) to determine the partition function Q_O at that temperature. Dalton's law (equation 7.1) is then applied using P, T and x_O to calculate the number density of atomic oxygen n_O at those conditions. Having Q_O, n_O and T, Boltzmann's law (equation 7.2) is used together with data from table 7.2 to calculate the number density of the lower state of each feature at temperature T.

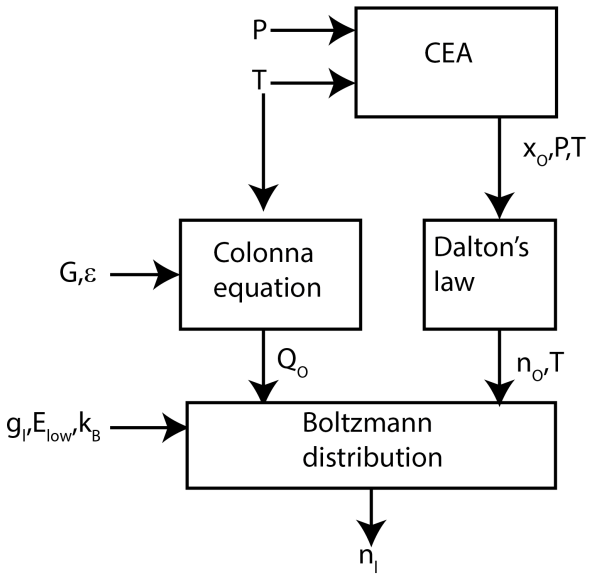

Figure 7.6.: Flowchart of calculations used to obtain the number density of the lower state of atomic oxygen n_l

Spectral properties. Table 7.2 lists the properties of neutral oxygen for the triplet at 844.6 nm including the Einstein coefficient (A_{ul}), lower and upper state energies (E_l and E_u), transition terms and rotational quantum numbers (J) [64].

Table 7.2.: Properties of neutral oxygen at 844.6 nm [64]

Relative Intensity	λ nm	A_{ul} 10^8 s^{-1}	E_l cm^{-1}	E_u cm^{-1}	Terms	J
250	844.625	0.322	76794.978	88631.303	$^3S^o \rightarrow ^3P$	$1 \rightarrow 0$
300	844.636	0.322	76794.978	88631.146	$^3S^o \rightarrow ^3P$	$1 \rightarrow 2$
300	844.676	0.322	76794.978	88630.587	$^3S^o \rightarrow ^3P$	$1 \rightarrow 1$

Spectral transmittance. The spectral transmittance τ_λ of a laser beam that propagates through a linearly absorbing medium with constant properties is:

$$\begin{aligned} \tau_\lambda &= \exp\left(-\alpha_\lambda\right) \\ &= \exp\left(-S_{lu} n_l \chi_\lambda l\right) \end{aligned} \tag{7.4}$$

where α_λ is the spectral absorbance, n_l is the lower state number density, χ_λ is the lineshape function and l is the optical path length.

Line strength. Martin et al [150] state that the line strength of an atomic transition S_{lu} in cm molecule^{-1} with a line centre wavelength λ_0 is:

$$S_{lu} = \frac{\lambda_0^2}{8\pi c} A_{ul} \frac{g_u}{g_l} \left[1 - \exp\left(-\frac{hc}{\lambda_0 k_B T_{ex}}\right)\right] \tag{7.5}$$

where h is Planck's constant, c is the speed of light, A_{ul} is the Einstein A coefficient, g_l is the lower state degeneracy, g_u is the upper state degeneracy and T_{ex} is the excitation temperature that describes the ratio of populations in the lower and upper states of the transition.
Martin et al [150] discusses the various spectral feature broadening mechanisms for a plasma in an arc jet facility. The current experiments were conducted at low pressure ($80 - 200$ Pa) whereas Martin used pressures of $2 - 9$ atm. In this work, only Doppler and van der Waals broadening are considered as they dominate at temperatures below approximately 6000 K while Stark broadening is also significant at higher temperatures.

Doppler broadening. Doppler broadening induces a Gaussian line shape function with a full-width at half-maximum (FWHM) $\Delta\lambda_D$ related to translational temperature [28]:

$$\Delta\lambda_D = \lambda_0 \sqrt{\frac{8 k_B T_{ex} \ln 2}{m_O c^2}} \tag{7.6}$$

where λ_0 is the feature centre wavelength and m_O is the atomic mass of oxygen. Readers should refer to Martin et al [150] for details on van der Waals and Stark broadening which both have Lorentzian line shape functions.

Table 7.3.: Van der Waals perturber constants for an atomic oxygen absorber

Perturber	m^*_{ap} $\times 10^{-26}$ kg	E_p $\times 10^{-18}$ J
O	1.33	1.52
N	1.24	1.65
O_2	1.77	0.99
N_2	1.69	2.02
NO	1.73	0.88
Ar	1.90	1.86

van der Waals broadening. The van der Waals FWHM is given by [150]:[1]

$$\Delta\lambda_{vdW} \approxeq 0.98\frac{\lambda_O^2}{c}\left[\frac{44.5\times 9\pi\hbar^5}{16m_e^3}\right]^{0.4}\left[\frac{8k_BT_{ex}}{\pi}\right]^{0.6}\frac{P}{k_BT_{ex}}\sum_p\left[\frac{x_p}{E_p^{0.8}\left(m^*_{ap}\right)^{0.6}}\right] \tag{7.7}$$

where subscripts a and p represent the absorber and collider respectively, E_p is the perturber resonance-level excitation energy, m_e is the electron mass, m^*_{ap} is the reduced mass of the absorber and perturber and x_p is the mole fraction of perturber p. Table 7.3 lists the van der Waals perturber constants for an atomic oxygen absorber [150]. Figure 7.7 shows how the Doppler and van der Waals FWHMs vary with temperature at constant pressure for parameters used in these experiments. A Voigt line shape may be used to model the convolution of the Gaussian and Lorentzian line shapes. Using the algorithm developed by Humlíček [45], the integrated area under the Voigt curve may be calculated for the experimental conditions. The Voigt a parameter for this case is:

$$a = \frac{\sqrt{\ln 2}\Delta\lambda_{vdW}}{\Delta\lambda_D} \tag{7.8}$$

Voigt profile calculation. Figure 7.8 shows the calculation flowchart used to obtain the Voigt line shape χ_λ for a test condition. The Doppler and van der Waals FWHMs ($\Delta\lambda_D$ and $\Delta\lambda_{vdW}$ respectively) for each feature are calculated before using Humlíčeks algorithm to determine the line shape χ_i.

Spectral transmittance calculation. Figure 7.9 shows the methodology used to calculate the spectral transmittance for each feature. Using the properties in table 7.2 together with temperature T, the line strength S_{lu} may be calculated using Martin's equation (equation 7.5). The line shape is then used with the lower state number density n_l, path length l and line strength S_{lu} to obtain the spectral transmittance τ_λ using the Beer-Lambert relationship. The total transmittance is calculated by summing the spectral contribution due to each feature at a wavelength λ. The measured minimum transmittance may be used together with the plasma pressure to derive the atomic oxygen number

[1] Formula (14) in reference [150] is incorrect. The corrected formula is stated here.

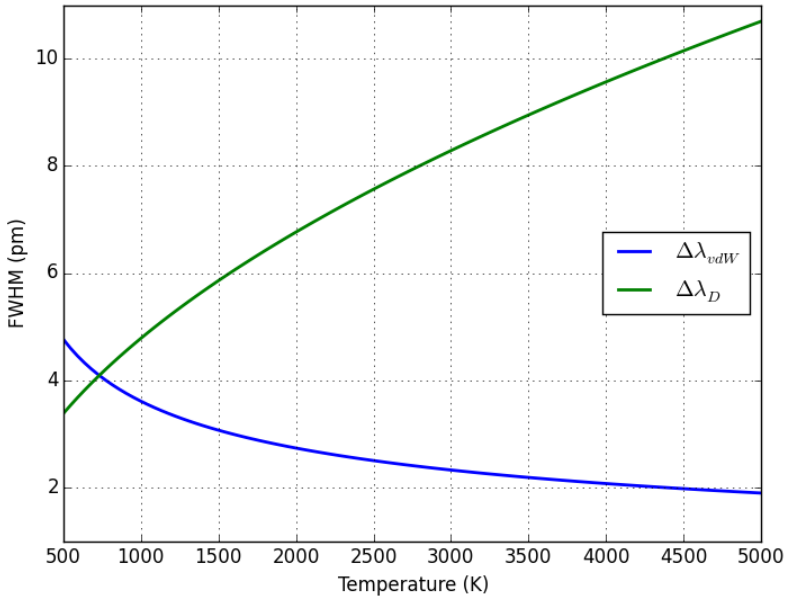

Figure 7.7.: Doppler and van der Waals FWHMs for atomic oxygen at 200 Pa

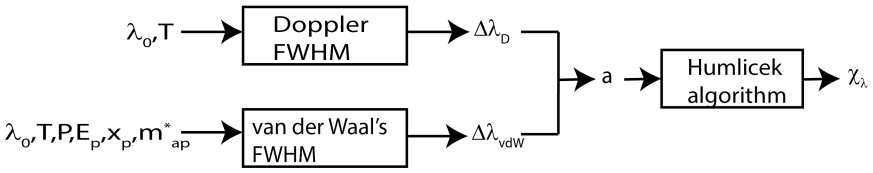

Figure 7.8.: Flowchart of the calculations for the Voigt profile lineshape

density and excitation temperature via these flowcharts and computer models.

7.3. Experiment Setup

As mentioned earlier, these experiments were undertaken during a four week visit to the University of Stuttgart. The first task was to become familiar with the operation of the laser diode system and oscilloscope. As series of experiments were undertaken to characterise the laser system and compare the measured performance with those specified in the manufacturer's datasheets. Experiments were conducted to measure the wavelength, output power, low frequency and high frequency modulation response as well as identifying any mode hops or other untoward behaviour in the system.
Next the Evenson cavity was operated without the laser system but with a photodetector to observe the background signal. Trials with air in the cavity were conducted at various pressures and forward and reverse powers whilst qualitative observations were made of the plasma. After becoming familiar with the cavities operation, the author developed an arrangement to direct the laser output through the cavity to the photodetector. The laser was operated across its wavelength range to detect oxygen when the cavity was filled with air. These experiments were not successful and it was questioned whether

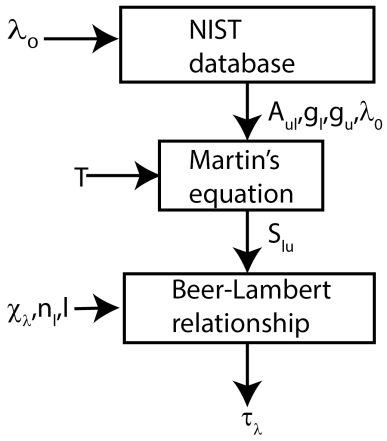

Figure 7.9.: Flowchart of the calculations for the spectral transmittance τ_λ

any atomic oxygen was being generated in the cavity.
An eschelle spectrometer was used to identify that atomic oxygen was present in the cavity albeit in very small amounts. With this knowledge, pure gaseous oxygen was then used in following experiments to ensure that the oxygen concentration was high enough to be detected. The TDLAS experiments were then successful.

7.4. Equipment Arrangement

Figure 7.10 is a schematic diagram of the experimental layout. Gaseous oxygen was supplied to an evacuated quartz tube that was coupled to a microwave generator. When an RF signal was applied to the tube and the operating conditions were set correctly, a plasma was generated in the tube. The plasma consisted of free electrons, atomic and molecular oxygen. A tunable diode laser system illuminated the plasma with modulated laser power at the atomic oxygen triplet near 844 nm. Two photo-diodes were used to measure the absorbance of the laser by the gas. An oscilloscope recorded the photodiode, laser controller and function generator signals.

Evenson tube. RF power was generated by a Sairem Model GMP Evenson microwave generator producing up to 300 W of power at 2.45 GHz. Microwave energy was fed through a flexible coaxial cable to a coaxial-to-waveguide transition which was connected to a microwave window via a manual impedance tuner and a sliding short circuit. A 50 mm diameter $\times$ 595 mm quartz glass optical cell was fitted in the microwave window. The optical cell was new before the experiments. A vacuum pump evacuated the tube prior to it being filled with gaseous oxygen to the test pressure. Figure 7.11 shows the principle components of the microwave generator.

7.4.1. Laser controller and head description

A New Focus Model 6300 Velocity Tunable Diode Laser controller was used in conjunction with a New Focus Model 6316 external-cavity tunable diode laser. The laser head used a Littman-Metcalf

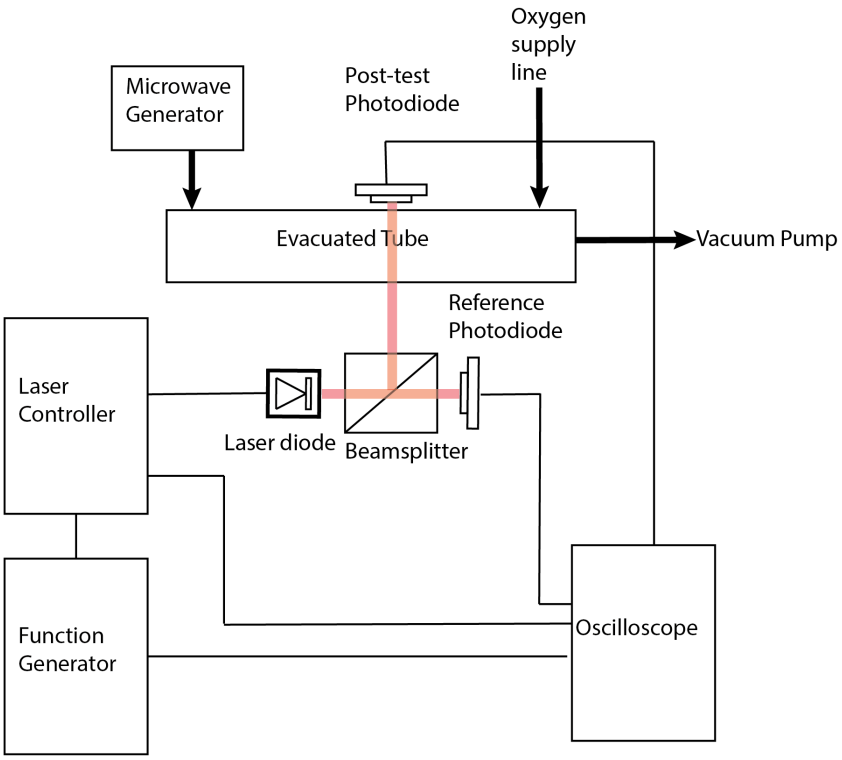

Figure 7.10.: Schematic diagram of test arrangement.

[157] configuration to provide a stable, tuned laser output at wavelengths between 834 nm and 854 nm with the laser diode at an operating temperature of 20°C and a recommended current of 60 mA [151].

Littman-Metcalf mechanism. Figure 7.12 is a schematic diagram of the Littman-Metcalf mechanism in the laser diode head. The laser diode is mounted on a fixed surface that contains the temperature and current controllers. One face of the diode (designated 'HR' in the schematic) is coated with a highly reflective coating whilst the opposite face ('AR') has an anti-reflective coating to prevent feedback from affecting the diode operation. The laser output is collimated by a lens before striking a diffraction grating at near grazing incidence. The beam is diffracted towards the turning mirror which reflects the light for the reverse path. The output beam is formed from the portion of the laser light that is reflected from the grating rather than being diffracted [151]. The highly reflective side of the laser diode, diffraction grating and turning mirror form a resonant cavity that tunes to one wavelength with a passband that is only a few gigahertz wide. Different wavelengths diffract off the grating at different angles. The lasing wavelength is the only one that is diffracted perpendicular to the tuning mirror. The wavelength is changed by changing the angle of the tuning mirror. The laser wavelength is changed over a wide range by changing the turning mirror angle using a DC motor or over a narrow range using a piezo-transducer ('PZT') mounted on the rear of the mirror. An angle sensor provides feedback on the mirror angle and a power monitor measures the laser output power. The narrow grating spectral filter forces the laser to operate in a single longitudinal mode.

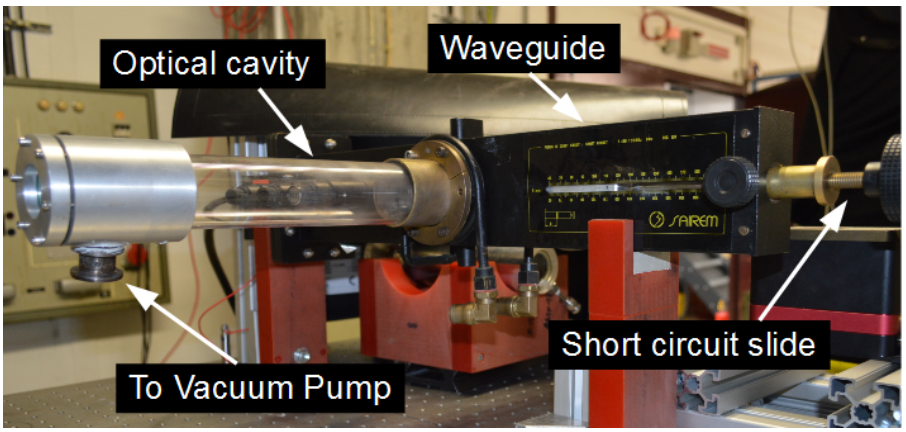

Figure 7.11.: Microwave generator components

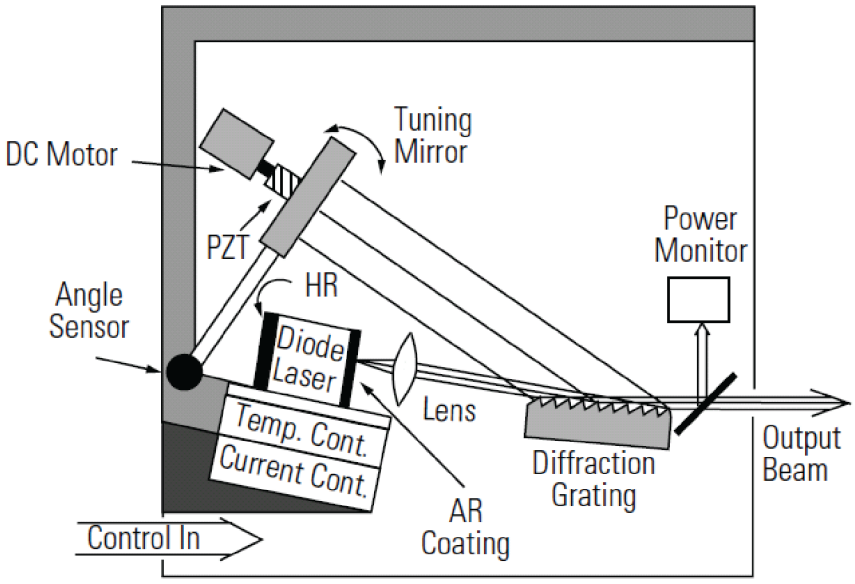

Figure 7.12.: New Focus laser diode head Littman-Metcalf mechanism [151]. See text for details.

Low frequency modulation. The laser could be modulated at low frequencies from DC to 2 kHz (at the 3dB rolloff point) by applying a sinusoidal signal to the frequency modulation input on the laser controller. This signal controlled the PZT voltage such that an increased voltage at the input decreased laser wavelength. In this mode, the laser frequency modulation range was ± 30 GHz [151].[2]

High frequency modulation. The laser head input was AC-coupled with frequency roll-offs at 50 kHz and 100 MHz. The current could be modulated at up to 1 MHz by supplying ± 10 V to the current modulation input on the laser controller or up to 100 MHz by supplying 1 V_{p-p} (peak-to-peak) to a connection on the laser head.

[2] A wavelength of 844.636 nm corresponds to 11839.42 cm^{-1}; thus, when a ± 30 GHz modulation is applied, the frequency varies between 11838.42 cm^{-1} and 11840.42 cm^{-1} and the wavelength varies between 844.564 nm and 844.636 nm.

7.4.2. Optical path

Figure 7.13 shows the physical relationship between the plasma generator and the optical components. The equipment layout ensured that the laser signal passed through the core of the plasma. During a test, the function generator fed an RF sine wave signal into the laser controller which, in turn, modulated the laser diode. The laser diode output was split into two components using a Thorlabs

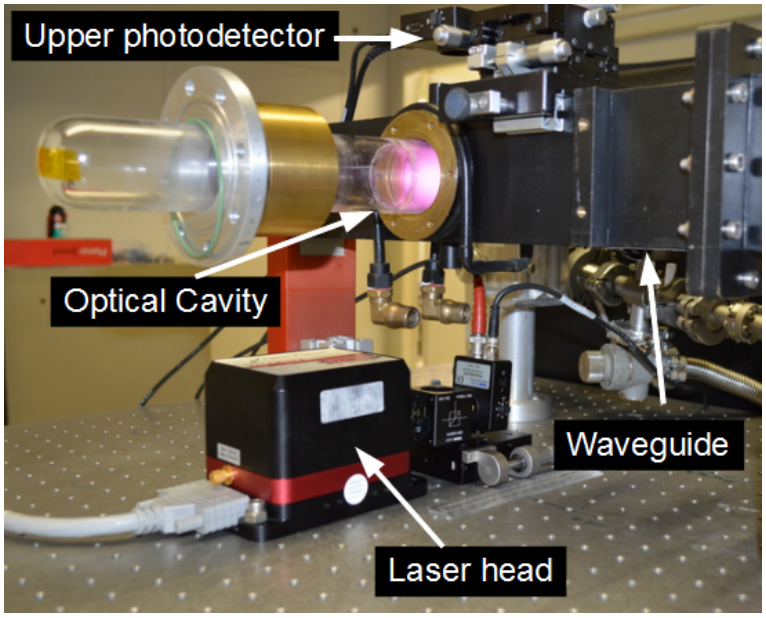

Figure 7.13.: Microwave test layout - side view

CM1-BS014 beam splitter. A photo-detector (Thorlabs PDA36-EC) measured a reference signal that had not traversed the plasma to alleviate laser power variation issues. Figure 7.14 shows the layout of the laser head, beam splitter and reference photo-detector. The laser head butted against the beam splitter which was, in turn, directly connected to the reference photo-detector. The beam splitter was tilted at approximately 5° to the horizontal so that the laser beam passed through the optical cavity at an angle to avoid interference etalons. The upper photo-detector was mounted on an arm that was

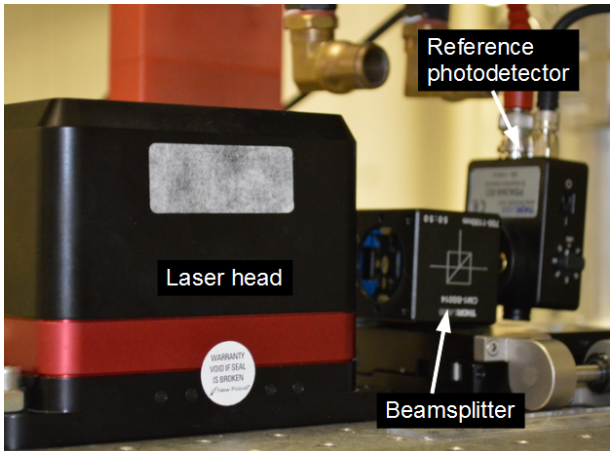

Figure 7.14.: Laser head, beamsplitter and reference photodetector

fixed to a mounting table as shown in figure 7.15. This configuration allowed the photo-detector to be precisely oriented to maximise the received signal strength. The ratio between the two photo-detector signals was used to measure absorption by the plasma.

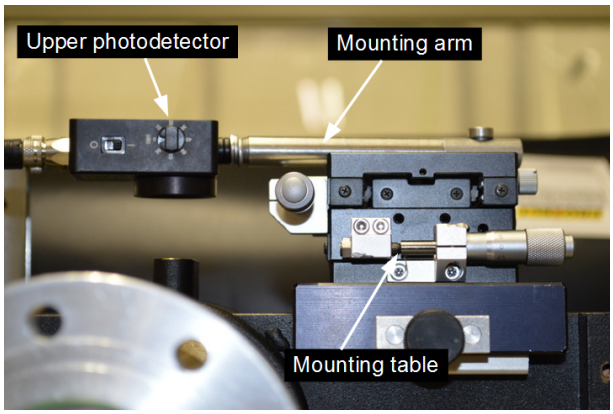

Figure 7.15.: Upper photodetector setup

Function generator and oscilloscope. A Rigol Model DG5072 function/arbitrary waveform generator modulated the frequency and laser diode current. A LeCroy WaveSurfer Model 24Xs-A oscilloscope recorded the laser controller and photo-diode signals.

Background signal. The photo-detectors (Thorlabs PDA36-EC) initially produced a constant output of 10 V even though the gain was set to 0 dB. The ambient lighting in the laboratory provided a strong signal to the detector. During bench tests of the laser, an aperture was placed immediately before the detector to limit the ambient light input. When the laser was off, the detector output was 0 V. With the laser on, the detector output was approximately 6 V indicating that the aperture was effective in limiting the ambient light input to the photodiode. During tests involving the Evenson cavity, a blackout curtain was used to eliminate background light from the TDLAS system.

7.5. Laser system characterisation

The laser was characterised during bench tests to determine the relationship between temperature, voltage, wavelength and modulation amplitude to verify the manufacturer's data. This was important in order to ensure that fine features could be detected. If the laser had mode hops or jumps in wavelength, it could easily miss a feature. Under certain operating conditions, the laser displayed mode hops and unstable performance. These mode hops were overcome by reducing the laser current modulation amplitude and by minimising the mechanical modulations of the laser head. Strong etalon effects due to interference from the surfaces of the optical cavity were detected initially. These were avoided by angling the laser beam so that it was not normal to the cavity.

Manufacturer datasheets. Figures 7.16 to 7.18 are the manufacturer's datasheets for the laser system. Figure 7.16 shows the calibration of output power versus laser diode current from the acceptance

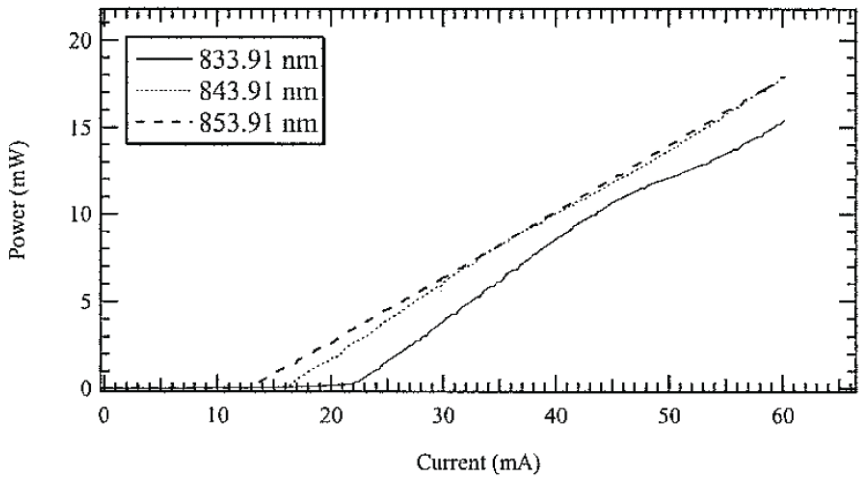

Figure 7.16.: Laser diode power versus current calibration at an operating temperature of 20.4°C [151].

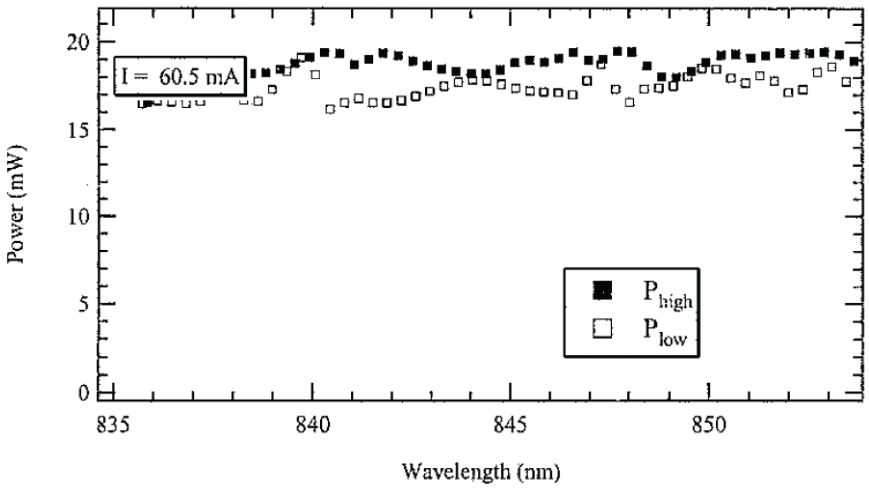

Figure 7.17.: Laser diode lower and upper output power P_{low} and P_{high} variation with wavelength at a laser diode current of 60.5 mA [151].

test datasheet for the diode used in these experiments. Figure 7.17 shows the laser diode lower and upper output power (P_{low} and P_{high} respectively) variation with wavelength at a laser diode current of 60.5 mA and an operating temperature of 20°C. Figure 7.18 shows how laser diode wavenumber varies with piezo-transducer (PZT) voltage expressed as a percent of full-scale at a laser diode current of 60.5mA

7.6. Atomic Oxygen Measurements

Presence of atomic oxygen. An eschelle spectrometer (Aryelle 150 with QImaging Rolera Camera and 400 μm multi-mode optic fibre) was used to verify that atomic oxygen was present in the plasma. The microwave parameters were changed whilst monitoring the eschelle spectrometer output until atomic oxygen emission at 844.6 nm was detected. There was no excited atomic oxygen if the forward

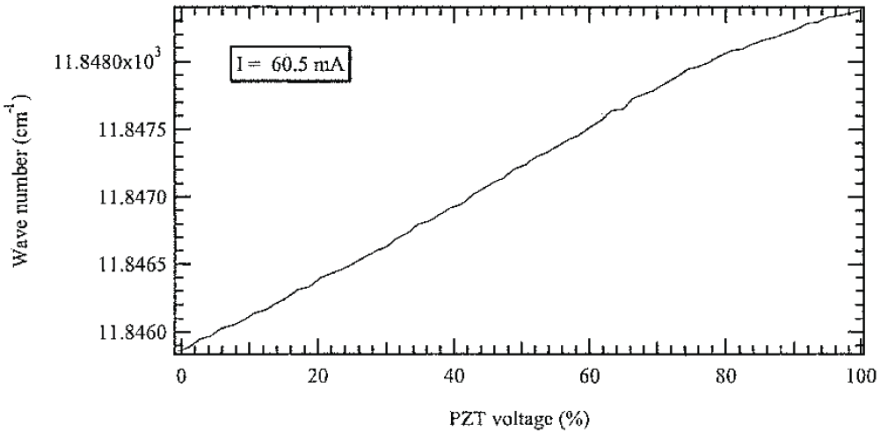

Figure 7.18.: Laser diode wavenumber variation with piezo-transducer (PZT) voltage expressed as a percent of full-scale at a laser diode current of 60.5mA [151]

microwave power was set to below 200 ± 20 W. This setting together with a pure oxygen atmosphere was used for later measurements. The optical cell was evacuated to 10^{-2} Pa and purged with pure oxygen twice. After a third evacuation, the optical cell was filled with oxygen to between 80 Pa and 300 Pa before the microwave generator was turned on. The microwave power into the generator was maximized using the sliding short circuit while the power reflected into the generator was kept below 60 ± 10 W using the impedance tuners. Typically, transmitted powers of up to 250 W were obtained. When ionisation occurred, the plasma glowed pink due to emission from excited nitrogen molecules. With the plasma present, the cell pressure increased by approximately 10%. For instance, the cell pressure was set to 82 ± 2 Pa without a plasma present and increased to 88 ± 2 Pa when the plasma illuminated. The plasma was localised near the surface of the optical cell with a thickness visually estimated to be 10 ± 3 mm.

7.6.1. Initial conditions

The number density of molecular oxygen (n_{O_2}) in the optical cell without the microwave discharge operating may be calculated using the real gas equation. Assume that the test gas is pure molecular oxygen at 298 K and 200 Pa when the microwave discharge is not operating. The mole fraction of molecular oxygen (x_{O_2}) in this case is 1.0 and the number density of molecular oxygen is:

$$\begin{aligned} n_{O_2} &= \frac{P x_{O_2}}{kT} \\ &= 1.449 \times 10^{16} \text{ molecules cm}^{-3} \end{aligned} \tag{7.9}$$

The mole fraction of atomic oxygen at these conditions is negligible as calculated using *Chemical Equilibrium with Applications* (CEA) [155].

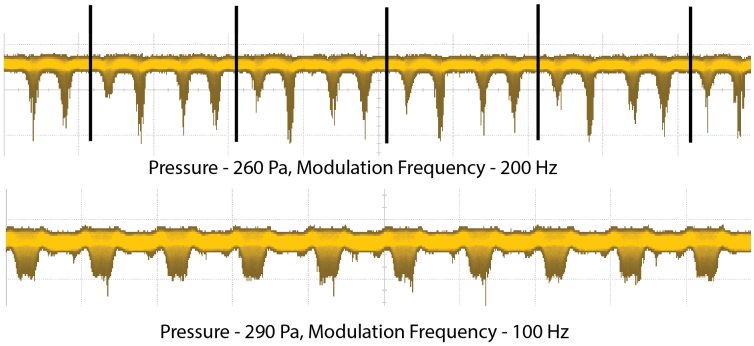

Figure 7.19.: Typical oscilloscope traces for two tests

7.6.2. Oscilloscope traces

Figure 7.19 shows typical oscilloscope traces of the intensity ratio between the post-test section photodetector and the reference photo-detector. Each trace contains five seconds of data recorded at 0.5 million samples per second with a horizontal scale of 10 ms/division and a vertical scale of 26.3 mV/division. The traces are *filled* with points due to the spontaneous emission of radiation from excited atoms and from electrons recombining with ions. The Einstein A coefficient for each feature was 322×10^8 Hz making the lifetime of atoms excited by absorption small compared to the modulation frequency.

The upper trace test section pressure was 260 ± 10 Pa with a laser modulation frequency of 200 ± 1 Hz and a microwave forward power of 270 ± 10 W. The test section pressure for the lower trace was 290 ± 10 Pa and the modulation frequency was 100 ± 1 Hz whilst the microwave forward power was 300 ± 10 W. The feature widths and heights in the upper trace are 1.7 ± 0.6 ms and 24 ± 21 mV respectively with the uncertainty measured at three standard deviations. Vertical bars have been added to the trace to highlight a periodic nature with a frequency of 50 Hz. The cause of the periodic behaviour is not known but it may relate to the AC power frequency in the laboratory. The broadband base noise is believed to result from rotational relaxation of molecular oxygen vibronic states [154]. The feature widths and heights in the lower trace are 3.0 ± 0.4 ms and 12.4 ± 1.8 mV respectively with the uncertainty measured at three standard deviations.

The lower trace features are more consistent and are wider (in the time domain) than those in the upper trace. The laser centre wavelength was set to 844.71 nm for each test when measured using the wavelength output from the laser controller and the oscilloscope. The modulation voltage for both tests was 700 mV_{pp}, equivalent to the wavelength changing by ± 0.67 nm. Thus, the laser transitioned all three features in each test. Aside from modulation frequency, the laser settings are unlikely to have caused the feature differences.

The features in the 200 Hz trace may be narrower because the laser dwell time on each feature is reduced compared to the 100 Hz test. This hypothesis may be tested by reducing the modulation amplitude as the frequency increases which should result in broader spectral features at higher modulation frequencies. Care should be taken to ensure that the laser transits each feature as the modulation amplitude reduces.

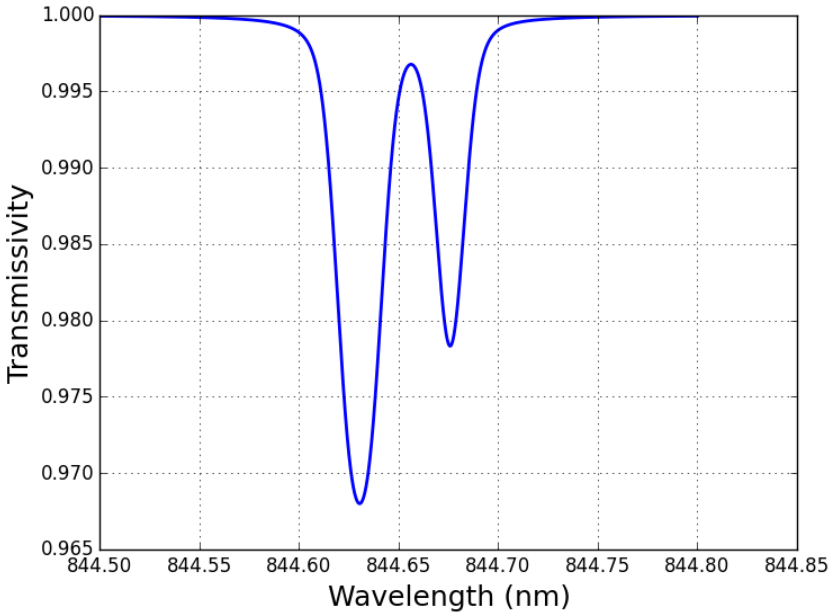

Figure 7.20.: Transmissivity through 10 mm of atomic oxygen at 2200 K and 200 Pa.

7.6.3. Transmissivity with discharge present

When the microwave discharge begins radiating, assume that the vibrational temperature increases to 2200 K. This temperature was chosen as it is within Region II discussed above and it represents a relatively low level of ionisation. It is indicative of the anticipated temperature. At this temperature and 200 Pa, *Chemical Equilibrium with Applications* (CEA)[155] predicts that the atomic oxygen mole fraction is 5.702×10^{-2}. The atomic oxygen number density n_O is 3.754×10^{14} molecules cm^{-3}. From Colonna's formula in equation 7.3, the internal partition function for atomic oxygen Q_O at 2200 K is 8.5524.

The strength of the feature at 844.636 nm, calculated using equation 7.5, is 8.1267×10^{-15} cm molecule^{-1} when $T_{ex} = 2200$ K for $g_l = 3$, $g_u = 8$ and $A_{ul} = 32.2$ MHz. The Doppler FWHM of the feature, calculated using equation 7.6, was 7.1 pm. The van der Waals FWHM was 2.6 pm when calculated using equation 7.7. The Voigt a parameter was 0.3109. Figure 7.20 shows the resultant transmissivity through a path length of 10 mm. The minimum transmissivity is 96.8%. The measured minimum transmissivity for this example was 96.83% and the associated number density was 3.964×10^{14} molecules cm^{-3}. The relative uncertainty in transmissivity is:

$$\frac{\delta\tau}{\tau} = 0.03\% \tag{7.10}$$

The relative uncertainty in the number density is:

$$\frac{\delta n_O}{n_O} = 5.29\% \tag{7.11}$$

The assumed temperature was lower than the actual temperature. Increasing the temperature increases the mole fraction of atomic oxygen which, in turn, increases the number density. The esti-

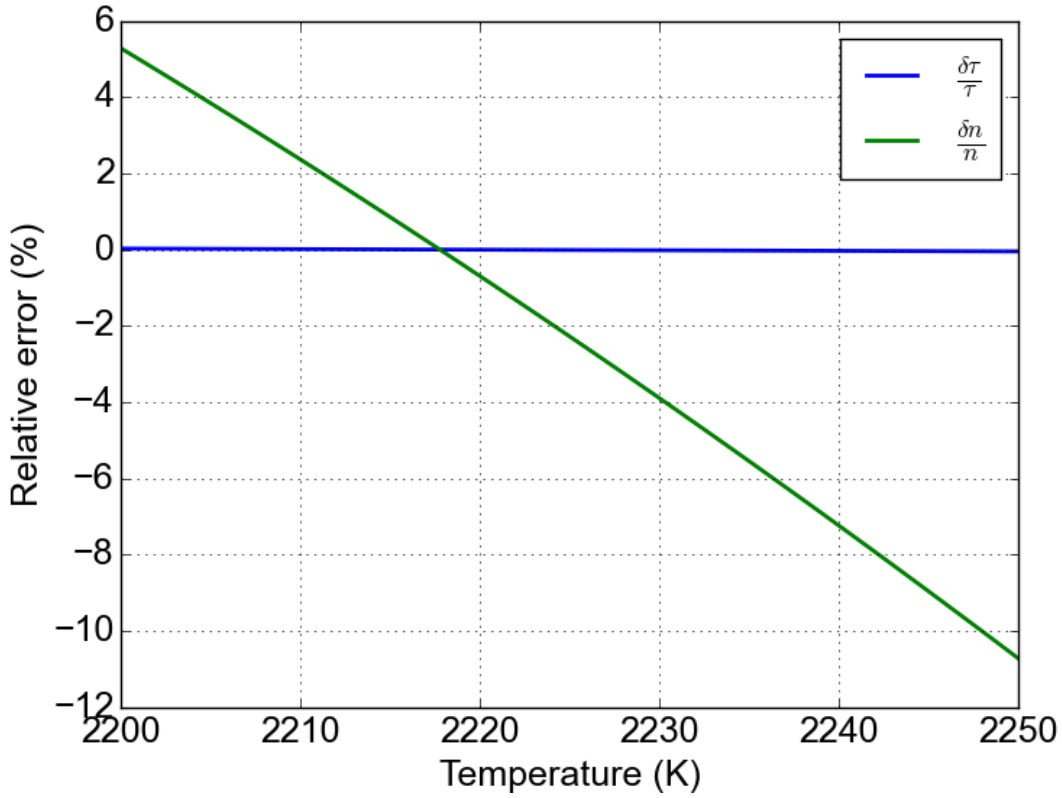

Figure 7.21.: Relative uncertainties in transmissivity and number density versus temperature

mated test section temperature was adjusted until the measured atomic oxygen number density was equal to the theoretically calculated number density, and the measured and calculated intensity ratios were approximately equal. Figure 7.21 shows how the relative uncertainties in transmissivity and number density vary with assumed temperature for this example. The relative uncertainty in transmissivity crosses the abscissa at 2221 K whilst that in number density crosses at 2217 K when the minimum intensity ratio for the photodetectors is 98.6%. The measured pressure and an estimated temperature were used to calculate the atomic oxygen number density n_O, internal partition function Q_O, and lower state number density n_l. The strength of each feature S_{lu} at 844.636 nm was calculated together with the Doppler FWHM and van der Waals FWHM. The Voigt profile line shape χ_λ was then calculated for each feature. The spectral transmittance τ_λ was found for each feature by multiplying this with the lower state number density n_l, line strength S_{lu} and path length l. The total transmissivity was determined by summing the three contributions at each wavelength. The calculated minimum transmissivity was then compared with the measured minimum and the temperature estimate was changed until the difference between the calculated and measured minimum transmissivity was minimised.

7.6.4. Temperature calculation

As an example, at a test pressure of 200 Pa, the measured minimum transmissivity was 96.8%. The calculated optimal temperature was 2218.2 K, the minimum transmissivity was 96.8%. The Doppler

and van der Waals FWHMs were 7.12 pm and 2.64 pm respectively. The number density of atomic oxygen n_O was 3.97×10^{14} molecules cm^{-3} and the atomic oxygen concentration x_O was 6.08%.

7.6.5. Measured transmissivity

Table 7.4 lists the minimum measured transmissivity for test cell pressures from 190 Pa to 290 Pa. These values were derived from the oscilloscope recordings of the reference and signal photo-detector voltages. The pressure gauge reading uncertainty was ± 2 Pa. The transmissivity uncertainty was estimated from the oscilloscope trace for the ratio measurement. This process was repeated for other

Table 7.4.: Measured test section pressure and minimum transmissivity

Pressure Pa	τ_{min} %
190 ± 2	96.94 ± 0.01
200 ± 2	96.83 ± 0.01
210 ± 2	96.70 ± 0.01
220 ± 2	96.57 ± 0.01
230 ± 2	96.45 ± 0.01
240 ± 2	96.33 ± 0.01
250 ± 2	96.23 ± 0.01
260 ± 2	96.12 ± 0.02
270 ± 2	96.00 ± 0.01
280 ± 2	95.89 ± 0.01
290 ± 2	95.89 ± 0.01

test conditions with the results shown in table 7.5. To achieve the accuracies listed in the table, CEA was used to obtain a map of x_O at intervals of 10 K between 2180 K and 2250 K and intervals of 20 Pa between 170 Pa and 310 Pa. Although the calculated temperatures were not independently verified, they are of the same order as translational temperatures measured in plasma tunnels at IRS.

TDLAS has proven useful for measuring plasma temperatures in full-scale plasma tunnels. Provided the atomic oxygen concentration or the path length is sufficient, TDLAS may also measure the concentration and temperature in the flow upstream of a test piece in an expansion tunnel. Issues that need to be considered when making the measurement are accurately determining plasma thickness and ensuring that the atmosphere is pure oxygen. Noting that the molecular oxygen concentration in air is approximately 20%, the laser absorption in air at similar conditions to those used in these tests would be less than 1%. During early experiments in this campaign, air was used and atomic oxygen was not detected.

Table 7.5.: Measured test section pressure and calculated temperature, number density and mole fraction of atomic oxygen

Pressure Pa	Temperature K	n_O $\times 10^{14}$ molecules cm^{-3}	x_O %
190	2206 ± 2	3.82 ± 0.01	6.11 ± 0.01
200	2216 ± 2	3.97 ± 0.01	6.03 ± 0.01
210	2218 ± 2	4.13 ± 0.01	5.99 ± 0.01
220	2218 ± 2	4.29 ± 0.01	5.94 ± 0.01
230	2218 ± 2	4.45 ± 0.01	5.90 ± 0.01
240	2218 ± 2	4.61 ± 0.01	5.87 ± 0.01
250	2233 ± 2	4.73 ± 0.01	5.77 ± 0.01
260	2233 ± 2	4.87 ± 0.01	5.74 ± 0.01
270	2232 ± 2	5.02 ± 0.01	5.70 ± 0.01
280	2232 ± 2	5.17 ± 0.01	5.66 ± 0.01
290	2218 ± 2	5.17 ± 0.01	5.45 ± 0.01

7.7. TDLAS system for expansion tunnels

This section examines TDLAS equipment required to detect atomic oxygen in expansion tunnel experiments of planetary entry flows and scramjet flows fuelled by hydrogen and air.

Planetary Entry Conditions. Figure 7.22 [3] shows a corrected spectrum of the Earth atmospheric entry of the Hayabusa capsule before the point of maximum heating. The spectrum has been corrected for spectral radiance of the capsule and the sensitivities of the camera, spectrometer and diffraction grating. Prominent features include molecular oxygen absorptions at 687.2 nm, 689.3 nm, 760.5 nm and 763.2 nm plus atomic oxygen emissions at 777.2 nm, 777.4 nm, 777.5 nm, 844.62 nm, 844.63 nm and 844.67 nm. The atomic features are superimposed on a blackbody curve corresponding to a temperature of 3200 K. After these corrections, the spectral radiances of the nitrogen and oxygen lines in the $800 - 900$ nm region are of the same order of magnitude as the oxygen feature at 777 nm. According to the NIST atomic spectroscopy database[64], the 777 nm and 844 nm oxygen lines have approximately the same intensity.

Expansion tunnel spectrum. Figure 7.23 shows a spectrum from an experiment in the X-2 expansion tube. The spectral features are annotated and show contributions due to aluminium I (Al I), carbon II (C II), hydrogen α (H α), nitrogen I (N I) and nitrogen II (N II), oxygen I (O I), and sulphur I (S I). The relevant conditions for this shot were that the flow speed was 8.4 kms^{-1} and the test gas was air at 10 kPa. The spectrum was observed in the stagnated flow immediately upstream (behind the bow shock) of a flat plate perpendicular to the flow. The hydrogen, oxygen and nitrogen lines derive from the test gas whilst the aluminium lines derive from the secondary diaphragm.[3] This brief

[3]The carbon emission may derive from carbon dioxide in the test gas or from out-gassing of the test model. The sulphur emission may derive from out-gassing of the model leading edge. The model in this shot was made from 304 stainless

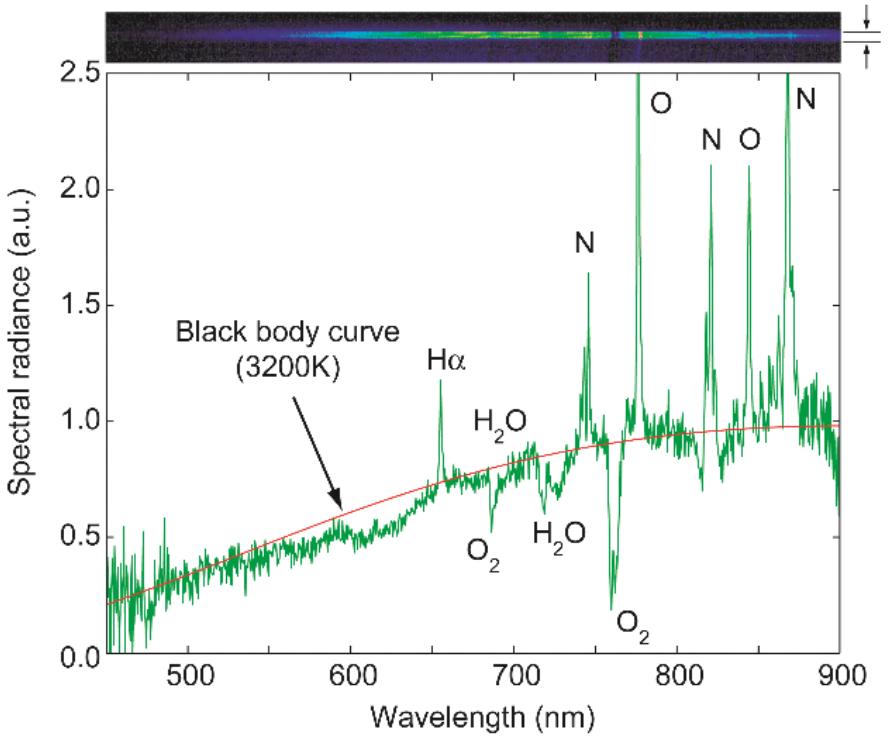

Figure 7.22.: Corrected Hayabusa spectrum [3]. The image at the top of the figure is a false clour representation of the raw image spectral intensity variation with wavelength.

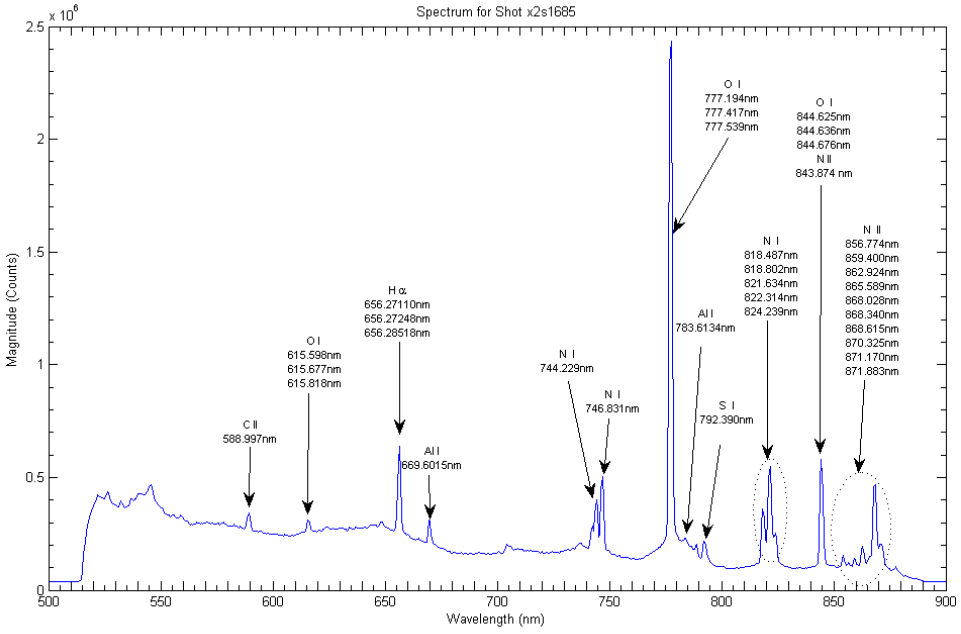

Figure 7.23.: Raw spectrum from a planetary entry flow experiment in the X2 expansion tunnel.

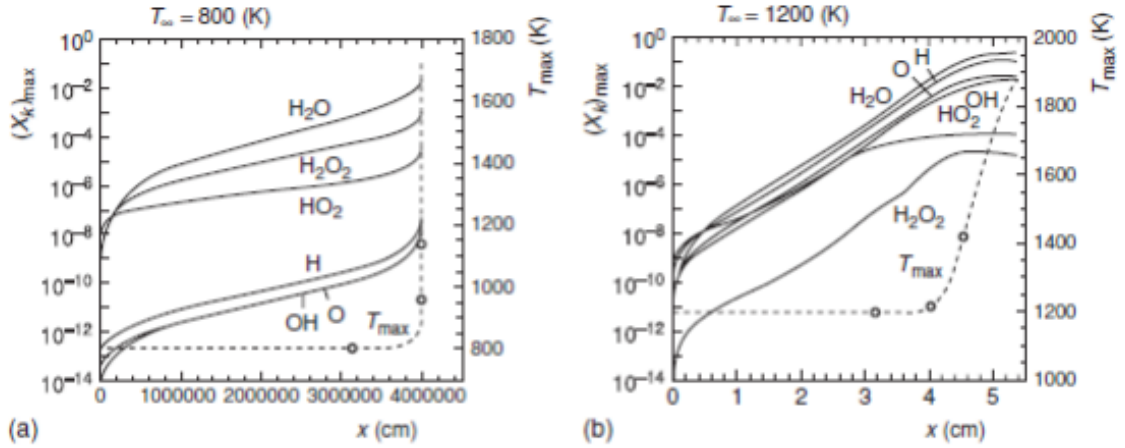

Figure 7.24.: Axial distribution of species maximum mole fraction and maximum temperature in a scramjet combustor [2].

analysis has shown that both the 777 nm and 844 nm emissions of atomic oxygen may be suitable for use in tunable diode laser absorption spectroscopy (TDLAS) testing in expansion tubes. The features are prominent and well-defined in both planetary entry and expansion tunnel flows using an Earth atmospheric test gas.

7.7.1. Scramjet Conditions

The scramjet parameters depend on the fuel and operating/test conditions. This analysis assumes that hydrogen is used to fuel the scramjet and air is used as the working fluid. The chemical and thermal conditions vary axially in a scramjet. Segal [2] Figure 6.16 (reproduced as Figure 7.24) shows the axial distribution of species maximum mole fraction $(X_k)_{max}$ and maximum temperature T_{max} originating from a splitter plate for hydrogen-air chemistry.

As shown in Figure 7.24(a), a low initial temperature ($T_\infty = 800$ K) has a predominance of HO_2 production over chain-branching reactions producing O, H and OH. At higher temperatures (such as $T_\infty = 1200$ K), Figure 7.24(b) shows how the situation is reversed and O, H and OH production predominates over HO_2. Note also that the H_2O products in both cases reach temperatures over approximately 1600 K, whilst the temperatures of the other products and intermediaries vary from around 1200 K at the lower stagnation temperature to approximately 1900 K at the higher one. Thus, the concentration and temperature of O, H or OH species may give us an idea of the stagnation temperature and reaction conditions in the scramjet combustor.

Figure 7.25 shows the calculated hydrogen diffusion time along with the ignition time for a premixed, stoichiometric hydrogen-oxygen system plus the calculated ignition times for premixed hydrogen-oxygen depending on the amount of electronically excited oxygen molecules (O_2) in the mixture. In

steel comprising iron (Fe), $17.5 - 20\%$ chromium (Cr), $8 - 11\%$ nickel (Ni), $< 2\%$ manganese (Mn), $< 1\%$ silicon (Si), $< 0.08\%$ carbon (C), $< 0.045\%$ phosphorus (P), $< 0.03\%$ sulphur (S). Whilst the sulphur content of the stainless steel is very low, it has a boiling point of 444.6^0 C causing it to out-gas sooner than other constituents of the steel. Note also that the spectral emissions between approximately 520 nm and 550 nm may correspond with emissions from Fe and Cr that have out-gassed from the stainless steel.

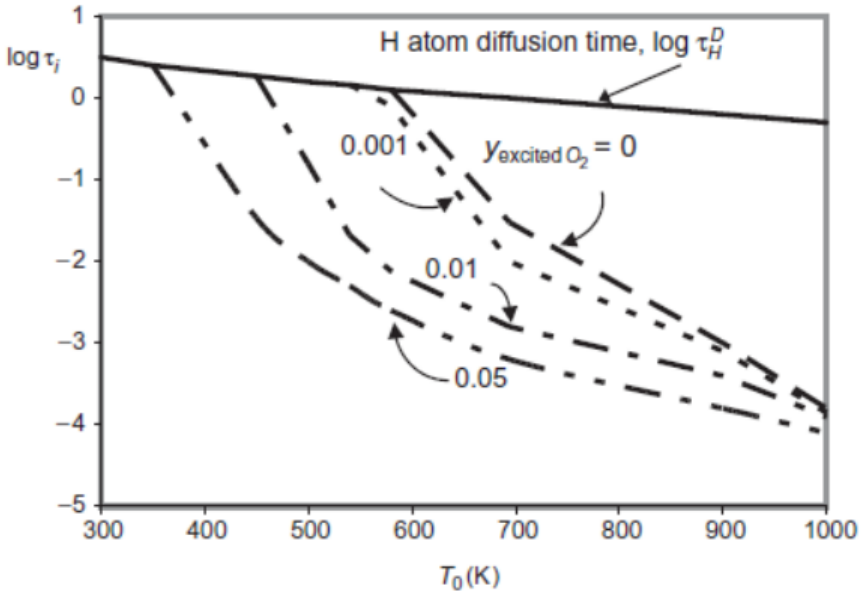

Figure 7.25.: Effect of adding electronically excited oxygen molecules on ignition of a premixed hydrogen-oxygen system [2].

this figure, the unbroken line is the hydrogen atom diffusion time. The ignition time curve (rightmost dashed line) intersects the diffusion time curve at $T = 580$ K. The intersection temperature decreases as electronically excited oxygen molecules are added to the flow. The phenomenon occurs at proportions of electronically excited O_2 to total O_2 of 0.1% and the intersection temperature decreases continuously as the proportion of excited O_2 increases.[2] Segal states that the ignition time and length of the combustion zone may be reduced by introducing excited oxygen molecules to the scramjet flow through either passing the flow through a strong shock wave that is anchored to the inlet or by introducing an electric discharge to the inlet flow. This may be due to the oxygen molecules being closer to their dissociation energy after excitation. Combustion would be initiated earlier in this case since the dissociation reaction is the initiating reaction in the combustion process [2, 137].

7.7.2. Test Conditions

Figure 7.26 shows the relationships between total enthalpy, pressure, temperature and Mach number for a typical hypersonic vehicle. The rightmost solid curve in the figure shows how total enthalpy changes with Mach number along the vehicle flight path. Flow compression by the inlet shifts the parameters to the left as illustrated by the large arrow. The shaded region is then the region at the entrance to the combustor.

As stated in chapter 6, the X3 expansion tunnel produces operating conditions to simulate flight at a vehicle flying at 3.5 kms^{-1} at an altitude of 30 km with a dynamic pressure q_0 of 48.4 kPa. A steady test time of 1 ms can be attained at the inlet of the scramjet. For the scramjet in chapter 6, gaseous hydrogen is injected at the scramjet inlet via five holes inclined to the flow at $45°$. A Ludwieg tube is pressurised with hydrogen prior to test and the fuel is injected into the scramjet as the expansion tunnel piston launched at the start of a shot. Chapter 6 extensively discusses experiments aimed at

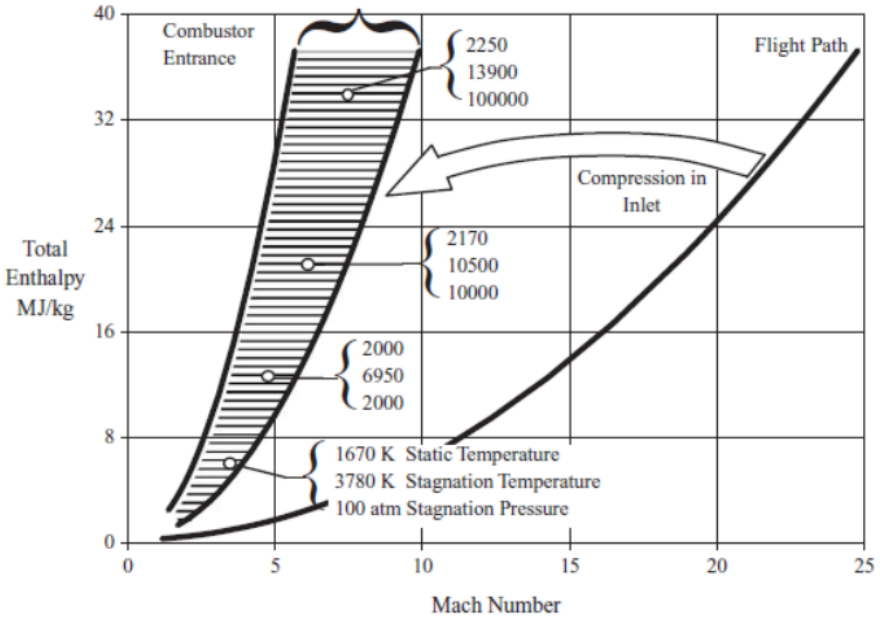

Figure 7.26.: Total enthalpy, pressure and temperature requirements for a combustion chamber simulation [2].

detecting water vapour in the exhaust of a scramjet in the X3 expansion tunnel. This discussion is additional to the information in chapter 6 and its related appendices.

7.7.3. Atomic Oxygen Spectrum

Atomic oxygen may be present in either of two forms: neutral oxygen atoms (O I) or singly ionised oxygen atoms (O II). The ionisation temperature for oxygen is well above that expected in a scramjet so atomic oxygen is likely to be present in the neutral O I form. The properties of atomic oxygen are listed in Table 7.7. The ground state of neutral oxygen atoms (O I) is $1s^2 2s^2 2p^4\, ^3P_2$ with an ionisation

Table 7.6.: Properties of atomic oxygen isotopes.

Isotope	Molecular Weight	Relative Abundance	Spin	Magnetic Moment
^{16}O	15.994915	99.76%	0	-1.89379
^{17}O	16.999311	0.048%	$\frac{5}{2}$	
^{18}O	17.999160	0.20%	0	

energy of 13.61805 eV. Singly ionised oxygen (O II) has a ground state of $1s^2 2s^2 2p^3\, ^4S^0_{\frac{3}{2}}$ and an ionisation energy of 35.1211 eV [158]. Table 7.8 lists the persistent lines of oxygen atoms in the near infra-red region of the spectrum as detailed on the NIST *Handbook of Basic Atomic Spectroscopic Data* website[64]. In this table, the transition probability (A_{ki}) is given in 10^8 s^{-1} and the energy levels are in cm^{-1}. From Table 7.8 three bands of lines are within our area of interest. These are around $777.194 - 777.539$ nm, $844.625 - 844.676$ nm, 926.601 nm and $1316.389 - 1316.485$ nm. The transition probabilities for the lines at 1316 nm are very low meaning that these lines are not

Table 7.7.: Persistent lines of oxygen neutral atoms.

Intensity	Wavenumber (cm^{-1})	Wavelength (nm)	A_{ki} ($\times 10^8$) (s^{-1})	$E_i - E_k$ (cm^{-1})	Terms	J
300	12 866.8	777.194	0.369	73 768.200	$^5S^0$	2
				86 631.454	^5P	3
250	12 863.1	777.417	0.369	73 768.200	$^5S^0$	2
				86 627.778	^5P	2
250	12 861.1	777.539	0.369	73 768.200	$^5S^0$	2
				86 625.757	^5P	1
250	11 839.6	844.625	0.322	76 794.978	$^3S^0$	1
				88 631.303	^3P	0
300	11 839.4	844.636	0.322	76 794.978	$^3S^0$	1
				88 631.146	^3P	2
300	11 838.9	844.676	0.322	76 794.978	$^3S^0$	1
				88 630.587	^3P	1
200	10 792.1	926.601	0.445	86 631.454	^5P	3
				97 420.630	$^5D_0$	4
250	7596.5	1316.389	0.0714	88 630.587	^3P	1
				96 225.049	$^3S^0$	1
250	7596.0	1316.485	0.119	88 631.146	^3P	2
				96 225.049	$^3S^0$	1

strong. Whilst the line at 926.6 nm has a high transition probability of 0.445×10^8 s^{-1}, it is a single line and it relies on an earlier transition to the ^5P state. This transition is the result of the three lines at 777 nm; thus, the band at 777 nm is much more intense than the line at 926 nm. The strongest lines are centred on 777.4 nm and 844.64 nm. The 844 nm lines are due to a transition $^3S^0 \leftarrow^3 P$. In their ground state, oxygen neutral atoms have two electrons in the ^3P orbital. The 777 nm lines rely on a transition from the ^5P orbital. This is not a ground state so the oxygen neutral atoms are less likely to occupy this state than the ^3P state.

Ideally, both bands (777nm and 844.64 nm) should be used to detect oxygen atoms in expansion tube and scramjet flows. The advantage of observing both bands is that the flow temperature may be derived by comparing the relative intensities of the two bands using the line ratio method.

Kwon et al [159] reported using an SDL5420-C laser diode emitting at 843 nm at room temperature to investigate the lines in atomic oxygen $(3\,^3S_1 \rightarrow 3\,^3P_{0,1,2})$ and measure the velocity distribution of the lower level $(3\,^3S_1)$. The SDL5420-C laser diode is a 150 mW CW laser with no photodiode or TEC in a C-type package. Table 7.9 lists the laser characteristics for the SDL5420-C laser diode [160]. Kwon's team used radio-frequency discharge to populate the oxygen atoms in excited states by collisions with metastable argon buffer gas.

Katsch et al [161] observed the atomic oxygen lines at 777 nm and 844 nm via laser induced fluorescence spectroscopy with two photon excitation using a Ni:YAG laser. The oxygen was mixed with 2% argon and the gas was excited via radio frequency discharge in the plasma. Knake et al [162] used xenon calibrated two photon laser induced fluorescence spectroscopy via a Nd:YAG-pumped dye laser to investigate atomic oxygen densities in the discharge core of a cold jet-like plasma. Knake examined fluorescence light at a wavelength of 844 nm. Atomic oxygen densities of the order of 10^{15} cm^{-3} were detected. Cartry et al [163] determined the loss rate of atomic oxygen from the surface of silica under microwave plasma conditions at around 133 Pa. They used optical fibres to sample the atomic oxygen lines at 777 nm and 844 nm. The laser diode system used in the Stuttgart experiments was considered for expansion tunnel trials. Based on the earlier work, that laser's modulation bandwidth was inadequate for the short test time of expansion tunnel experiments. Various suppliers were approached for price and availability of suitable laser diodes. All responses were either too expensive for this study or were high risk with no guarantee of suitable performance. As a result, it is recommended that a future researcher focus solely on developing an atomic oxygen TDLAS system for expansion tunnel tests. A similar analysis can be undertaken for other species of interest such as nitrous oxide or hydroxyl radicals. These are of interest as they are the rate-limiting pre-cursors for combustion in scramjets.

7.8. Summary

Experiments were performed to measure the temperature and atomic oxygen concentration in an Evenson cavity using TDLAS to probe the triplet at 844.6 nm. The calculated atomic oxygen mole fraction was between 5.4% and 6.1% when the cavity was filled with pure oxygen to pressures between 190 Pa and 290 Pa and the microwave generator power was $270 - 300$ W. The experiments

Table 7.8.: Laser characteristics for SDL5420-C Laser Diode

Laser Characteristic	Symbol	Minimum	Typical	Maximum	Unit
CW output power	P_0	-	-	150	mW
Centre wavelength	λ_c	-	4	-	
Spectral width	$\Delta\lambda$	-	3	5	nm
Slope efficiency	$\eta_D = P_0/(I_{op} - I_{th})$	0.75	0.85	-	mW mA^{-1}
Conversion efficiency	$\eta = P_0/(I_{op}V_{op})$	-	30	-	%
FWHM Beam divergence					
Parallel to Junction	$\theta_{\parallel}$	-	9	-	^{0}
Perpendicular to junction	$\theta_{\perp}$	-	30	-	^{0}
Threshold current	I_{th}	-	35	45	mA
Forward current	I_f	-	210	230	mA
Series resistance	R_s	-	4.0	6.0	Ω
Thermal resistance	R_{th}	-	60	-	^{0}C W^{-1}
Recommended case temperautre	T_c	-20	-	30	^{0}C

showed that this method can be used successfully provided the test setup and conditions are appropriate. Further experiments are required to extend the application to different pressures, excitation temperatures and configurations.

A brief analysis was also presented of a TDLAS system that could detect atomic oxygen in reflected shock tunnel or expansion tunnel experiments. Whilst the system was not implemented for this study, the information presented may assist future researchers to develop an atomic oxygen TDLAS system for free-piston tunnels.

8. Conclusion

Tunable diode laser absorption spectroscopic methods have been applied to two high speed gas flows and a rarefied gas in an Evenson tube. Direct methods were used to measure conditions in the test section of a steam ejector. The atomic oxygen concentration was measured in a plasma generated by an Evenson cavity. Water vapour concentration and temperature in the nozzle of a scramjet installed in the test section of an expansion tube were investigated. Each of these applications entailed unique test methods and data analysis techniques.

Steam ejector tests. The steam ejector test section was modified to reduce spurious readings due to water condensation and atmospheric water absorption. Direct absorption techniques were used to plot high fidelity spectra with up to 20 test points per feature. Three data analysis methods were compared: a temperature ratio method, an internet simulation and a locally-developed optimisation program. The optimisation program was the most accurate method and had an added benefit of illustrating the relative impact of temperature and pressure on the accuracy of profile fitting.

Water vapour tests. The scramjet experiments required data to be recorded using multiple time bases to accommodate the three time-frames for the expansion tube, fuel injection and TDLAS systems. Electronic components were designed and used to combine waveforms and amplify photodetector outputs. Mathematical models were developed to simulate the expansion tube, scramjet and TDLAS system. Given the short test time (approximately 1 ms), an innovative large amplitude method was used to modulate the lasers. A nitrogen purging system was developed to reduce atmospheric absorption. A unique optical layout was used to ensure that the TDLAS measurements were repeatable between expansion tube runs. Digital signal processing techniques were used to replace a lock-in amplifier for extracting the TDLAS signal from the recorded data. The experiments were of limited success due to various design and experimental issues. They did, however, demonstrate the feasibility of using TDLAS to make observations and measurements in scramjets. The scramjet experiments were, by far, the most difficult to perform and analyse due to:

- the work required to turn the X3 expansion tube around between shots,
- rapid changes in flow conditions, temperature and pressure in the test section.
- PCB and Kulite transducer failures in the scramjet model,
- data recording and timing requirements,
- external absorption by water vapour,

- difficulty in determining the exact modulation frequency for the lasers,
- the National Instruments databox experiencing hardware failure,
- lack of intensity calibration of the TDLAS system at high temperature.

Nevertheless, these experiments showed that TDLAS of water vapour has potential to be successfully applied to scramjet combustion. Future researchers could improve upon these experiments by:

- characterizing the TDLAS performance using heated water vapour in a controlled environment,
- using fibre optics to launch and detect the TDLAS signals within the dump tank rather than external to the dump tank,
- if the TDLAS path is external to the dump tank, designing a specific nitrogen purging system to reduce absorption be atmospheric water vapour.
- independently measuring the flow temperature in the scramjet test section for comparison with the TDLAS measurements,
- using high-speed video to record the visual conditions at the test section during a test.
- using a digital waveform generator to modulate the lasers,
- using a scramjet with a wider profile to increase the absorption path length, and
- incorporating TDLAS calculations into scramjet CFD models to alleviate the use of analytical models.

Atomic oxygen tests. A VCSEL laser diode in a Littman Litrow mechanism was used for the plasma measurements. The laser and associated mechanism were characterised before any plasma measurements were attempted. The laser system configuration was modified to eliminate interference and uncertainties due to etalons, background radiation and mechanical movement. Pure gaseous oxygen was used as a test gas to maximise the effect of the test gas on the laser system. After measuring the minimum transmissivity of the test gas at the oxygen triplet wavelength, a series of calculations were performed to derive the atomic oxygen concentration and excitation temperature in the plasma. The derived temperatures were approximately 2200 K and the atomic oxygen concentrations were in the range $5.4-6.1\%$. A brief analysis was also presented of a TDLAS system that could detect atomic oxygen in expansion tunnel experiments. Whilst the system was not implemented for this study, the information presented may assist future researchers to develop an atomic oxygen TDLAS system for expansion tunnels. Such a system would have application to gas-surface interactions and, specifically, to catalycity.

8.1. Thesis outcomes

Not all lines are research are immediately successful. As Georges Lathrop reported after interviewing Thomas Edison in 1889:

> Not long ago I asked Mr. Edison which of his inventions had caused him the greatest amount of study, and required the most elaborate experiments.
>
> He replied promptly: Ṫhe electric light. For, although I was never myself discouraged, or inclined to be hopeless of success, I cannot say the same for all of my associates. And yet, through all those years of experimentation and research, I never once made a discovery. All my work was deductive, and the results I achieved were those of invention, pure and simple. I would construct a theory and work on its lines until I found it was untenable. Then it would be discarded at once and another theory evolved. This was the only possible way for me to work out the problem, for the conditions under which the incandescant electric light exists are peculiar and unsatisfactory for close investigation. ... I speak without exaggeration when I say that I have constructed *three thousand* different theories in connection with the electric light, each one of them reasonable and apparently likely to be true. Yet only in two cases did my experiments prove the truth of my theory. [164]

The aim of this research was to develop and test a TDLAS system that could perform measurements in expansion tunnels at The University of Queensland. Expansion tunnels have similar peculiarities to the incandescent electric light discussed by Mr Edison. Both involve vacuums and high temperatures. Both are difficult to investigate by sight alone. In the case of expansion tunnels, the interactions are unsteady, transient and involved high enthalpies and flow velocities. Whilst the incandescent electric light was the cutting edge of technology in Edison's time; safe, regular and affordable hypersonic flight is at the cutting edge of technology today. To achieve this, we must construct theories, work on them until they are untenable, discard them and evolve newer theories. The outcomes of this thesis were:

- A modular TDLAS system was designed and implemented to detect multiple chemical species simultaneously via a combination of direct and wavelength modulated spectroscopy.
- The temperature, pressure and water vapour concentration at the exit of a steam ejector were measured via direct absorption spectroscopy with uncertainties of ± 5 K, ± 100 Pa and ± 1 % respectively.
- The locally designed TDLAS system was used to detect water vapour in the exhaust of a scramjet model installed in the X3 expansion tunnel at the University of Queensland. Combustion products were detected in the scramjet exhaust. With improvements to the design and operation of the system, it should be capable of measuring temperature and other scramjet parameters. Recommended improvements were suggested to achieve this aim.
- The requirements of a TDLAS system to detect atomic oxygen in expansion tunnel experiments were investigated. Recommendations for such a system were made.

- Atomic oxygen temperature, concentration and number density in a plasma generated in an Evenson cavity were measured using TDLAS. The spectral triplet at 844.6 nm was observed for this measurements showing that narrowly spaced lines can be used for TDLAS.
- Programs were developed using open source software to control multiple TDLAS instruments, perform direct absorption spectroscopy, extract and model spectroscopic parameters, analyse spectroscopic measurements and calibrate diode laser wavelength and output power parameters.

8.2. Integration into current research field

This research provides a basis on which a working TDLAS system can be developed for the expansion tunnels at the University of Queensland. This system could probe multiple chemical species simultaneously along the same line of sight with a $1-2$ mm beam diameter immediately downstream of a models' bow shock. Currently, emission spectroscopy is used as the state of the art for these measurements. The emission spectroscopic methods integrate the signal over time and provide limited discrimination of transient observations during experiments. The TDLAS system that was developed has the potential to achieve time-steps of the order of 1 μs which would be extremely useful in the X2 and X3 tunnels as it would allow researchers to correlate the spectroscopic observations with high-speed video taken during experiments. Also, the system could target specific species such as atomic oxygen or nitrogen, CN, molecular oxygen or hydrogen in the free stream or inside a scramjet.
Another field that could be examined using the system is the concentration of species at the exit of an expansion tunnel nozzle compared with that at the exit of a reflected shock tunnel. This may provide more information about the impact of free radicals that have been generated by stagnated flows. An improved knowledge of the amount and distribution of these radicals would validate assumptions made about the nozzle exit flows for expansion tunnels and reflected shock tunnels.

8.3. Summary

TDLAS was applied to three environments typical of hypersonic or rarefied gas research. The temperature and water concentration in a steam ejector flow were measured using direct detection. The excitation temperature and atomic oxygen concentration in a rarefied gas plasma were measured. Each campaign required innovative solutions to experimental problems but, in the end, TDLAS was successfully applied on a proof-of-concept basis in each environment. The TDLAS measurement technique can be used to characterise the flows in expansion facilities, assist with performance analysis of hypersonic combustion, and investigate gas-surface interactions for TPS in high-enthalpy facilities. This research has shown that, with innovative ideas and solutions, TDLAS has a firm future in hypersonic and rarefied gas applications.

Bibliography

[1] A.D. Griffiths. *Development and Demonstration of a Diode Laser Sensor for a Scramjet Combustor*. PhD thesis, Australian National University, Setpember 2005.

[2] Segal C. *Scramjet Engine: Processes and Characteristics*. Cambridge University Press, Cambridge, 2009.

[3] Eichmann TB, Khan R, McIntyre TJ, Jacobs CM, Porat H, Buttsworth DR, and Upcroft B. Radiometric temperature analysis of the Hayabusa spacecraft re-entry. In *28th International Symposium on Shock Waves*, Manchester, UK, 2011.

[4] John J. Bertin. *Hypersonic Aerothermodynamics*. AIAA, 1994.

[5] E.T. Curran and S.N.B. Murthy, editors. *Scramjet Propulsion*, volume 189 of *Progress in Astronautics and Aeronautics*. American Institute of Aeronautics and Astronautics, Inc., Reston, Virginia, 2000.

[6] D. Gildfind. *Development of High Total Pressure Scramjet Flow Conditions using the X2 Expansion Tube*. PhD thesis, University of Queensland, 2012.

[7] G. Herdrich, M. Auweter-Kurtz, H. Böhrk, M. Fertig, and S. Löhle. Test facilities for high enthalpy planetary entry simulation. In K. Fletcher, editor, *Thermal Protection Systems and Hot Structures*, number ESA SP-631 in Proceedings of the 5th European workshop held 17-19 May 2006 at ESTEC, Noordwijk, The Netherlands. European Space Agency, 2006.

[8] E. D. Hinkley and P. L. Kelley. Detection of air pollutants with tunable diode lasers. *Science*, 171(3972):pp. 635–639, 1971.

[9] Reid J, Shewchun J, Garside BK, and Ballik EA. High sensitivity pollution detection employing tunable diode lasers. *Applied Optics*, 17(2):300–307, Jan 1978.

[10] J. Reid and D. Labrie. Second-harmonic detection with tunable diode lasers - comparison of experiment and theory. *Applied Physics B: Lasers and Optics*, 26:203–210, 1981.

[11] D.T. Cassidy and J. Reid. Harmonic detection with tunable diode lasers - two-tone modulation. *Applied Physics B: Lasers and Optics*, 29:279–285, 1982.

[12] S.T. Sanders, J. Wang, J.B. Jeffries, and R.K. Hanson. Diode-laser absorption sensor for line-of-sight gas temperature distributions. *Applied Optics*, 40(24):4404–4415, 2001.

[13] A.D. Griffiths and A.F.P. Houwing. Diode laser absorption spectroscopy of water vapor in a scramjet combustor. *Applied Optics*, 44(31):6653–6659, Nov 2005.

[14] M.S. Brown, S. Williams, C.D. Lindstrom, and D.L. Barone. Progress in applying tunable diode laser absorption spectroscopy to scramjet isolators and combustors. Technical Report AFRL-RZ-WP-TP-2010-2146, Air Force Research Laboratory, United States, May 2010.

[15] S. O'Byrne and S. Wittig. Measurement of hypersonic inlet flow using diode laser absorption spectroscopy. In *Proceedings of the 8th Australian Space Science Conference Canberra 29 September - October 1 2008*, pages 68–75, 2009.

[16] C.D. Lindstrom, K.R. Jackson, S. Williams, R. Givens, W.F. Bailey, C.J. Tam, and W.F. Terry. Shock-train structure resolved with absorption spectroscopy. Part 1: System design and validation. *AIAA Journal*, 47(10):2368–2378, 2009.

[17] C. D. Lindstrom, D. Davis, S. Williams, and C.J. Tam. Shock-train structure resolved with absorption spectroscopy. Part 2: Analysis and CFD comparison. *AIAA Journal*, 47(10):2379–2390, 2009.

[18] M. Gruber, C. Carter, M. Ryan, G.B. Rieker, J.B. Jeffries, R.K. Hanson, J. Liu, and T. Mathur. Laser-based measurements of OH, temperature, and water vapor concentration in a hydrocarbon-fueled scramjet. *44th AIAA/ASME/SAE/ASEE Joint Propulsion Conference and Exhibit*, 2008.

[19] Ian A. Schultz, Christopher S. Goldenstein, Christopher L. Strand, Jay B. Jeffries, Ronald K. Hanson, and Christopher P. Goyne. Hypersonic scramjet testing via diode laser absorption in a reflected shock tunnel. *Journal of Propulsion and Power*, 30(6):1586–1594, October 2014.

[20] Raphäel Vallon, Jacques Soutadé, Jean-Luc Vérant, Jason Meyers, Sébastien Paris, and Ajmal Mohamed. A compact tunable diode laser absorption spectrometer to monitor CO_2 at 2.7μ m wavelength in hypersonic flows. *Sensors*, 10(6):6081–6091, 2010.

[21] A Zybin, C Schnürer-Patschan, M.A Bolshov, and K Niemax. Elemental analysis by diode laser spectroscopy. *TrAC Trends in Analytical Chemistry*, 17(8-9):513 – 520, 1998.

[22] E. D. Hinkley. High-resolution infrared spectroscopy with a tunable diode laser. *Applied Physics Letters*, 16(9):351–354, 1970.

[23] Ronald K. Hanson. Shock tube spectroscopy: advanced instrumentation with a tunable diode laser. *Applied Optics*, 16(6):1479–1481, Jun 1977.

[24] R. K. Hanson, P. A. Kuntz, and C. H. Kruger. High-resolution spectroscopy of combustion gases using a tunable IR diode laser. *Applied Optics*, 16(8):2045–2048, Aug 1977.

[25] K. Niemax, A Zybin, C. Schnürer-Patschan, and H. Groll. Semiconductor diode lasers in atomic spectrometry. *Analytical Chemistry News and Features*, pages 351–356, June 1996.

[26] Peter Werle. A review of recent advances in semiconductor laser based gas monitors. *Spectrochimica Acta Part A: Molecular and Biomolecular Spectroscopy*, 54(2):197 – 236, 1998.

[27] Jane Hodgkinson and Ralph P Tatam. Optical gas sensing: a review. *Measurement Science and Technology*, 24(1):012004, 2013.

[28] A.P. Thorne, U. Litzén, and S. Johansson. *Spectrophysics - Principles and Applications*. Springer-Verlag, Berlin, 1999.

[29] J.H. Ferziger and H.G. Kaper. *Mathematical theory of transport processes in gases*. North-Holland Publishing Company, 1972.

[30] N.V. Vitanov, B.W. Shore, L. Yatsenko, K. B ohmer, T. Halfmann, T. Rickes, and K. Bergman. Power broadening revisit: theory and experiment. *Optics Communications*, 199:117–126, November 2001.

[31] M.L. Citron, H.R. Gray, C.W. Gabel, and C.R. Stround Jr. Experimental study of power broadening in a two-level atom. *Physical Review A*, 16(4):1507–1512, October 1977.

[32] H.M. Foley. The pressure broadening of spectral lines. *Phys. Rev.*, 69(11 and 12):616–628, June 1946.

[33] P. W. Anderson. Pressure broadening in the microwave and infra-red regions. *Phys. Rev.*, 76:647–661, Sep 1949.

[34] R. H. Dicke. The effect of collisions upon the doppler width of spectral lines. *Phys. Rev.*, 89:472–473, Jan 1953.

[35] R. G. Breene. Line shape. *Rev. Mod. Phys.*, 29:94–143, Jan 1957.

[36] J. Buldyreva, N. Lavrentieva, and V. Strarikov. *Collisional Line Broadening and Shifting of Atmospheric Gases*. Imperial College Press, London, 2010.

[37] Stanley Bloom and Henry Margenau. Quantum theory of spectral line broadening. *Phys. Rev.*, 90:791–794, Jun 1953.

[38] Philip L. Varghese and Ronald K. Hanson. Collisional narrowing effects on spectral line shapes measured at high resolution. *Applied Optics*, 23(14):2376–2385, Jul 1984.

[39] Louis Galatry. Simultaneous effect of doppler and foreign gas broadening on spectral lines. *Phys. Rev.*, 122:1218–1223, May 1961.

[40] C.J. Tsao and B. Curnutte. Line-widths of pressure-broadened spectral lines. *Journal of Quantitative Spectroscopy and Radiative Transfer*, 2(1):41 – 91, 1962.

[41] Rolf Arndt. Analytical line shapes for Lorentzian signals broadened by modulation. *Journal of Applied Physics*, 36(8):2522–2524, 1965.

[42] Ellis E. Whiting, James O. Arnold, and Gilbert C. Lyle. Calculation of molecular band spectra assuming a Gaussian line profile. *Journal of Quantitative Spectroscopy and Radiative Transfer*, 7(5):725 – 739, 1967.

[43] E.E. Whiting. An empirical approximation to the Voigt profile. *Journal of Quantitative Spectroscopy and Radiative Transfer*, 8(6):1379–1384, 1968. cited By (since 1996) 141.

[44] J. Humlícek. An efficient method for evaluation of the complex probability function: The Voigt function and its derivatives. *Journal of Quantitative Spectroscopy and Radiative Transfer*, 21(4):309 – 313, 1979.

[45] J. Humlícek. Optimized computation of the Voigt and complex probability functions. *Journal of Quantitative Spectroscopy and Radiative Transfer*, 27(4):437 – 444, 1982.

[46] W.H. Press, B.P. Flannery, S.A. Teukolsky, and W.T. Vetterling. *Numerical Recipes: the art of scientific computing*. Cambridge University Press, Cambridge UK, 1987.

[47] Xiang Ouyang and Philip L. Varghese. Reliable and efficient program for fitting Galatry and Voigt profiles to spectral data on multiple lines. *Applied Optics*, 28(8):1538–1545, Apr 1989.

[48] R.D. May and C.R. Webster. Data processing and calibration for tunable diode laser harmonic absorption spectrometers. *Journal of Quantitative Spectroscopy and Radiative Transfer*, 49(4):335–347, 1993.

[49] Jonas Westberg, Junyang Wang, and Ove Axner. Fast and non-approximate methodology for calculation of wavelength-modulated Voigt lineshape functions suitable for real-time curve fitting. *Journal of Quantitative Spectroscopy & Radiative Transfer*, 113(16):2049–2057, November 2012.

[50] Jingsong Li, Uwe Parchatka, and Horst Fischer. Applications of wavelet transform to quantum cascade laser spectrometer for atmospheric trace gas measurements. *Applied Physics B - Lasers and Optics*, 108(4):951–963, SEP 2012.

[51] Julian Skrotzki, JanChristoph Habig, and Volker Ebert. Integrative fitting of absorption line profiles with high accuracy, robustness, and speed. *Applied Physics B*, pages 1–14, 2013.

[52] Xin Zhou, Xiang Liu, Jay B Jeffries, and R K Hanson. Development of a sensor for temperature and water concentration in combustion gases using a single tunable diode laser. *Measurement Science and Technology*, 14(8):1459, 2003.

[53] J.T.C. Liu, J.B Jeffries, and R.K. Hanson. Measurements of spectral parameters of water-vapour transitions near 1388 and 1345 nm for accurate simulation of high-pressure absorption spectra. *Measurement Science and Technology*, 18(5):1185–1194, 2007.

[54] J.T.C. Liu, G.B. Rieker, J.B. Jeffries, M.R. Gruber, C.D. Carter, T. Mathur, and R.K. Hanson. Near-infrared diode laser absorption diagnostic for temperature and water vapor in a scramjet combustor. *Applied Optics*, 44(31):6701–6711, Nov 2005.

[55] G.B. Rieker, H. Li, X. Liu, J.B. Jeffries, R.K. Hanson, M.G. Allen, S.D. Wehe, P.A. Mulhall, and H.S. Kindle. A diode laser sensor for rapid, sensitive measurements of gas temperature and water vapour concentration at high temperatures and pressures. *Measurement Science and Technology*, 18(5):1195–1204, 2007.

[56] C.S. Goldenstein, J.B. Jeffries, and R.K. Hanson. Diode laser measurements of linestrength and temperature-dependent lineshape parameters of H_2O-, CO_2-, and N_2- perturbed H_2O transitions near 2474 and 2482 nm. *Journal of Quantitative Spectroscopy and Radiative Transfer*, 130(0):100 – 111, 2013. HITRAN2012 special issue.

[57] L.S. Rothman, I.E. Gordon, Y. Babikov, A. Barbe, D. Chris Benner, P.F. Bernath, M. Birk, L. Bizzocchi, V. Boudon, L.R. Brown, A. Campargue, K. Chance, E.A. Cohen, L.H. Coudert, V.M. Devi, B.J. Drouin, A. Fayt, J.-M. Flaud, R.R. Gamache, J.J. Harrison, J.-M. Hartmann, C. Hill, J.T. Hodges, D. Jacquemart, A. Jolly, J. Lamouroux, R.J. Le Roy, G. Li, D.A. Long, O.M. Lyulin, C.J. Mackie, S.T. Massie, S. Mikhailenko, H.S.P. Müller, O.V. Naumenko, A.V. Nikitin, J. Orphal, V. Perevalov, A. Perrin, E.R. Polovtseva, C. Richard, M.A.H. Smith, E. Starikova, K. Sung, S. Tashkun, J. Tennyson, G.C. Toon, Vl.G. Tyuterev, and G. Wagner. The HITRAN 2012 molecular spectroscopic database. *Journal of Quantitative Spectroscopy and Radiative Transfer*, 130:4–50, November 2013.

[58] C.O. Laux. Radiation and nonequilibrium collisional-radiative models. In D. Fletcher, Charbonnier J.-M., Sarma G.S.R., and Magin T., editors, *Physico-Chemical Modeling of High enthalpy and Plasma Flows*, von Karman Institute Lecture Series 2002-07, Belgium, 2002. Rhode-Saint-Genese.

[59] L.S. Rothman, I.E. Gordon, R.J. Barber, H. Dothe, R.R. Gamache, A. Goldman, V.I. Perevalov, S.A. Tashkun, and J. Tennyson. HITEMP, the high-temperature molecular spectroscopic database. *Journal of Quantitative Spectroscopy and Radiative Transfer*, 111(15):2139 – 2150, 2010. XVIth Symposium on High Resolution Molecular Spectroscopy.

[60] S.N. Mikhailenko, Yu.L. Babikov, and V.F. Golovko. Information-calculating system Spectroscopy of Atmospheric Gases. The structure and main functions. *Atmospheric and Oceanic Optics*, 18(9):685–695, 2005.

[61] Laurence S. Rothman. The evolution and impact of the HITRAN molecular spectroscopic database. *Journal of Quantitative Spectroscopy and Radiative Transfer*, 111(11):1565 – 1567, 2010. 50 Years of JQSRT.

[62] C. Claveau, A. Henry, D. Hurtmans, and A. Valentin. Narrowing and broadening parameters of H_2O lines perturbed by He, Ne, Ar, Kr and nitrogen in the spectral range 1850-2140 cm^{-1}. *Journal of Quantitative Spectroscopy and Radiative Transfer*, 68(3):273 – 298, 2001.

[63] Aamir Farooq, Jay B Jeffries, and Ronald K Hanson. In situ combustion measurements of H_2O and temperature near 2.5 μm using tunable diode laser absorption. *Measurement Science and Technology*, 19(7):075604, 2008.

[64] NIST. Handbook of basic atomic spectroscopic data, 2012.

[65] G. Durry, V. Zéninari, B. Parvitte, T. Le Barbuarbu, F. Lefevre, J. Ovarlez, and R.R. Gamache. Pressure-broadening coefficients and line strengths of H_2O near 1.39 μm: application to the in situ sensing of the middle atmosphere with balloonborne diode lasers. *Journal of Quantitative Spectroscopy and Radiative Transfer*, 94(34):387 – 403, 2005.

[66] Robert A. Toth. Extensive measurements of $H_2^{16}O$ line frequencies and strengths: 5750 to 7965 cm^{-1}. *Applied Optics*, 33(21):4851–4867, Jul 1994.

[67] V. Nagali, S.I. Chou, D.S. Baer, and R.K. Hanson. Diode-laser measurements of temperature-dependent half-widths of H_2O transitions in the 1.4 μm region. *Journal of Quantitative Spectroscopy and Radiative Transfer*, 57(6):795 – 809, 1997.

[68] Muriel Lepere, Annie Henry, Alain Valentin, and Claude Camy-Peyret. Diode-laser spectroscopy: Line profiles of H_2O in the region of 1.39 μm. *Journal of Molecular Spectroscopy*, 208(1):25 – 31, 2001.

[69] L. S. Rothman, C. P. Rinsland, A. Goldman, S. T. Massie, D. P. Edwards, J-M. Flaud, A. Perrin, C. Camy-Peyret, V. Dana, J. y. Mandin, J. Schroeder, A. Mccann, R. R. Gamache, R. B. Wattson, K. Yoshino, K.V. Chance, K. W. Jucks, L. R. Brown, V. Nemtchinov, and P. Varanasi. The HITRAN molecular spectroscopic database and Hawks (HITRAN Atmospheric Workstation): 1996 Edition. *Journal of Quantitative Spectroscopy and Radiative Transfer*, 60(5):665 – 710, 1998.

[70] Corinne Delaye, Jean-Michel Hartmann, and Jean Taine. Calculated tabulations of H_2O line broadening by H_2O , N_2, O_2, and CO_2 at high temperature. *Applied Optics*, 28(23):5080–5087, Dec 1989.

[71] V. Nagali, J.T. Herbon, D.C. Horning, D.F. Davidson, and R.K. Hanson. Shock-tube study of high-pressure H_2O spectroscopy. *Applied Optics*, 38(33):6942–6950, 1999.

[72] L. S. Rothman, A. Barbe, D. Chris Benner, L. R. Brown, C. Camy-Peyret, M. R. Carleer, K. Chance, C. Clerbaux, V. Dana, V. M. Devi, A. Fayt, J. M. Flaud, R. R. Gamache, A. Goldman, D. Jacquemart, K. W. Jucks, W. J. Lafferty, J. Y. Mandin, S. T. Massie, V. Nemtchinov, D. A. Newnham, A. Perrin, C. P. Rinsland, J. Schroeder, K. M. Smith, M. A. H. Smith, K. Tang, R. A. Toth, J. Vander Auwera, P. Varanasi, and K. Yoshino. The HITRAN molecular spectroscopic database: Edition of 2000 including updates through 2001. *Journal of Quantitative Spectroscopy and Radiative Transfer*, 82(1-4):5 – 44, 2003.

[73] Xiang Liu, Xin Zhou, Jay B. Jeffries, and Ronald K. Hanson. Experimental study of H_2O spectroscopic parameters in the near-IR (6940-7440 cm^{-1}) for gas sensing applications at elevated temperature. *Journal of Quantitative Spectroscopy and Radiative Transfer*, 103(3):565 – 577, 2007.

[74] L.S. Rothman, D. Jacquemart, A. Barbe, D. Chris Benner, M. Birk, L.R. Brown, M.R. Carleer, C. Chackerian, Jr., K. Chance, L.H. Coudert, V. Dana, V.M. Devi, J.-M. Flaud, R.R. Gamache, A. Goldman, J.-M. Hartmann, K.W. Jucks, A.G. Maki, J.-Y. Mandin, S.T. Massie, J. Orphal, A. Perrin, C.P. Rinsland, M.A.H. Smith, J. Tennyson, R.N. Tolchenov, R.A. Toth, J. Vander Auwera, P. Varanasi, and G. Wagner. The HITRAN 2004 molecular spectroscopic database. *Journal of Quantitative Spectroscopy and Radiative Transfer*, 96(2):139 – 204, 2005.

[75] Reginald Fessenden. Electric signaling apparatus, 1905.

[76] M.C. Teich. Infrared heterodyne detection. *Proceedings of the IEEE*, 56(1):37–46, Jan 1968.

[77] Philip C.D. Hobbs. *Building Electro-optical Systems - Making It All Work*. John Wiley and Sons, Inc, 2000.

[78] Joel A. Silver. Frequency-modulation spectroscopy for trace species detection: theory and comparison among experimental methods. *Applied Optics*, 31(6):707–717, Feb 1992.

[79] P. Kluczynski, J. Gustafsson, A.M. Lindberg, and O. Axner. Wavelength modulation absorption spectrometry - An extensive scrutiny of the generation of signals. *Spectrochimica Acta Part B: Atomic Spectroscopy*, 56(8):1277 – 1354, 2001.

[80] Hejie Li, Gregory B. Rieker, Xiang Liu, Jay B. Jeffries, and Ronald K. Hanson. Extension of wavelength-modulation spectroscopy to large modulation depth for diode laser absorption measurements in high-pressure gases. *Applied Optics*, 45(5):1052–1061, Feb 2006.

[81] G.B. Rieker, J.B. Jeffries, and R.K. Hanson. Calibration-free wavelength-modulation spectroscopy for measurements of gas temperature and concentration in harsh environments. *Applied Optics*, 48(29):5546 – 5560, 2009.

[82] G.B. Rieker, J.B. Jeffries, R.K. Hanson, T. Mathur, M.R. Gruber, and C.D. Carter. Diode laser-based detection of combustor instabilities with application to a scramjet engine. In *Proceedings of the Combustion Institute*, volume 32, pages 831 – 838, Montreal, QC, Canada, 2009.

[83] Brian F. Ventrudo and Daniel T. Cassidy. Operating characteristics of a tunable diode laser absorption spectrometer using short-external-cavity and DFB laser diodes. *Applied Optics*, 29(33):5007–5013, Nov 1990.

[84] S.F. Hanna, R. Barron-Jimenez, T.N. Anderson, R.P. Lucht, J.A. Caton, and T. Walther. Diode-laser-based ultraviolet absorption sensor for nitric oxide. *Applied Physics B*, 75:113–117, 2002.

[85] Thomas N. Anderson, Robert P. Lucht, Rodolfo Barron-Jimenez, Sherif F. Hanna, Jerald A. Caton, Thomas Walther, Sukesh Roy, Michael S. Brown, James R. Gord, Ian Critchley, and Luis Flamand. Combustion exhaust measurements of nitric oxide with an ultraviolet diode-laser-based absorption sensor. *Applied Optics*, 44(8):1491–1502, Mar 2005.

[86] T.N. Anderson, R.P. Lucht, T.R. Meyer, T. Mathur, K.D. Grinstead, J.R. Gord, M.R. Gruber, and C.D. Carter. Measurements of NO and OH concentrations in vitiated air using diode laser-based ultraviolet absorption sensors. In *45th AIAA Aerospace Sciences Meeting and Exhibit, 8-11 January 2007*, pages 14p–, Reno, Nevada, 2007. AIAA. AIAA 2007-467.

[87] Mark G Allen. Diode laser absorption sensors for gas-dynamic and combustion flows. *Measurement Science and Technology*, 9(4):545, 1998.

[88] J.T.C. Liu. *Near-Infrared diode Laser Absorption Diagnostics for Temperature and Species in Engines*. PhD thesis, Stanford University, High Temperature Gasdynamics Laboratory, Department of Mechanical Engineering, October 2004. TSD Report 154.

[89] T. Cai, G. Wang, H. Jia, and X. Gao. Temperature and water concentration measurements in combustion gases using a DFB diode laser at 1.4 microns. *Laser Physics*, 18(10):1133, 2008.

[90] M.P. Arroyo and R.K. Hanson. Absorption measurements of water vapor concentration, temperature, and line-shape parameters using a tunable InGaAsP diode laser. *Applied Optics*, 32(30):6104–6116, Oct 1993.

[91] L.S. Rothman, R.R. Gamache, R.H. Tipping, C.P. Rinsland, M.A.H. Smith, D.Chris Benner, V.Malathy Devi, J.-M. Flaud, C. Camy-Peyret, A. Perrin, A. Goldman, S.T. Massie, L.R. Brown, and R.A. Toth. The HITRAN molecular database: Editions of 1991 and 1992. *Journal of Quantitative Spectroscopy and Radiative Transfer*, 48(5-6):469 – 507, 1992.

[92] M. A. Bolshov, Y. A. Kuritsyn, V. V. Liger, V. R. Mironenko, S. B. Leonov, and D. A. Yarantsev. Measurements of the temperature and water vapor concentration in a hot zone by tunable diode laser absorption spectrometry. *Applied Physics B: Lasers and Optics*, 100(2, SI):397–407, August 2010.

[93] L. Chang, J. Jeffries, and R. Hanson. Mass flux sensing via tunable diode laser absorption of water vapor. *AIAA Journal*, 48(11):2687, 2010.

[94] Louis C. Philippe and Ronald K. Hanson. Laser diode wavelength-modulation spectroscopy for simultaneous measurement of temperature, pressure, and velocity in shock-heated oxygen flows. *Applied Optics*, 32(30):6090–6103, Oct 1993.

[95] M.S. Brown, D.L. Barone, W.F. Terry, T. Barhorst, and S. Williams. Accuracy, precision and scatter in TDLAS measurements. In *48th AIAA Aerospace Sciences Meeting*, number AIAA 2010-302 in 48th AIAA Aerospace Sciences Meeting Including the New Horizons Forum and Aerospace Exposition, 4 - 7 January 2010, Orlando, Florida, 2010.

[96] C.D. Carter, M.R. Gruber, G.B. Rieker, J.B. Jeffries, and R K. Hanson. Diode laser-based detection of combustor instabilities with application to a scramjet engine. *Proceedings of the Combustion Institute*, 32:831–838, 2010.

[97] A. Sappey, L. Sutherland, D. Owenby, P. VanHoudt, J. Hannam, Q. Zhao, P. McCormick, P. Masterson, M. Estes, S. Williams, and T. Barhorst. Flight-ready TDLAS combustion sensor for hypersonics. *16th AIAA/DLR/DGLR International Space Planes and Hypersonic Systems and Technologies Conference*, 2009.

[98] Andrew D. Sappey, Lee Sutherland, David Owenby, Paul VanHoudt, Jerry Hannam, Qingchun Zhoa, Patrick J. McCormick, Bernard P. Masterson, and Michael Estes. Flight-ready TDLAS combustion sensor for the HIFiRE 2 hypersonic research program. Technical Report AEDC-TR-10-T-6, Arnold Engineering Development Center, September 2009.

[99] Kevin R. Jackson, Mark R. Gruber, and Salvatore Buccellato. Mach 6-8+ hydrocarbon-fueled scramjet flight experiment: The HIFiRE Flight 2 project. *Journal of Propulsion and Power*, 31(1):36–53, July 2014.

[100] Datta V. Gaitonde. Progress in shock wave/boundary layer interactions. *Progress in Aerospace Sciences*, 72:80–99, 2015.

[101] Ian A. Schultz, Christopher S. Goldenstein, Jay B. Jeffries, Ronald K. Hanson, Robert D. Rockwell, and Christopher P. Goyne. Spatially resolved water measurements in a scramjet combustor using diode laser absorption. *Journal of Propulsion and Power*, 30(6):1551–1558, April 2014.

[102] Ian A. Schultz, Christopher S. Goldenstein, R. Mitchell Spearrin, Jay B. Jeffries, Ronald K. Hanson, Robert D. Rockwell, and Christopher P. Goyne. Multispecies mid-infrared absorption measurements in a hydrocarbon-fueled scramjet combustor. *Journal of Propulsion and Power*, 30(6):1595–1604, September 2014.

[103] Fei Li, XiLong Yu, Hongbin Gu, Zhi Li, Yan Zhao, Lin Ma, Lihong Chen, and Xinyu Chang. Simultaneous measurements of multiple flow parameters for scramjet characterization using tunable diode-laser sensors. *Applied Optics*, 50(36):6697–6707, December 2011.

[104] Albert Einstein. Strahlungs-emission und -absorption nach der quantentheorie. *Verhandlungen der Deutschen Physikalischen Gesellschaft*, 18:318–323, 1917.

[105] Robert C. Hilborn. Einstein coefficients, cross sections, f values, dipole moments, and all that. *American Journal of Physics*, 50(11):982–986, 1982.

[106] Y. Babou, Ph. Riviére, M.-Y. Perrin, and A. Soufiani. High-temperature and nonequilibrium partition function and thermodynamic data of diatomic molecules. *International Journal of Thermophysics*, 30:416–438, 2009.

[107] C.F. Hansen and S.P. Heims. A review of the thermodynamic, transport and chemical reaction rate properties of high-temperature air. Technical Note 4359, National Advisory Committee for Aeronautics, Ames Aeronautical Laboratory, Moffett Field, California, July 1958.

[108] J. Fischer, R. R. Gamache, A. Goldman, L. S. Rothman, and A. Perrin. Total internal partition sums for molecular species in the 2000 edition of the hitran database. *Journal of Quantitative Spectroscopy and Radiative Transfer*, 82(1-4):401 – 412, 2003. The HITRAN Molecular Spectroscopic Database: Edition of 2000 Including Updates of 2001.

[109] A. Goldman, R. R. Gamache, A. Perrin, J. M. Flaud, C. P. Rinsland, and L. S. Rothman. Hitran partition functions and weighted transition-moments squared. *Journal of Quantitative Spectroscopy and Radiative Transfer*, 66(5):455 – 486, 2000.

[110] Gianpiero Colonna and Mario Capitelli. A few level approach for the electronic partition function of atomic systems. *Spectrochimica Acta Part B: Atomic Spectroscopy*, 64(9):863 – 873, 2009.

[111] Marcus Vidler and Jonathan Tennyson. Accurate partition function and thermodynamic data for water. *The Journal of Chemical Physics*, 113(21):9766–9771, 2000.

[112] J Shao, L. Lathdavong, P. Kluczynski, S. Lundqvist, and S. Axner. Methodology for temperature measurements in water vapor using wavelength-modulation tunable diode laser absorption spectrometry in the telecom C-band. *Applied Physics B*, 2009.

[113] Various. Spectroscopy of atmospheric gases, May 2012.

[114] J.J. Olivero and R.L. Longbothum. Empirical fits to the Voigt line width: A brief review. *Journal of Quantitative Spectroscopy and Radiative Transfer*, 17(2):233–236, 1977.

[115] R.J. Wells. Rapid approximation to the Voigt/Faddeeva function and its derivatives. *Journal of Quantitative Spectroscopy and Radiative Transfer*, 62(1):29 – 48, 1999.

[116] Jonas Westberg, Junyang Wang, and Ove Axner. Methodology for fast curve fitting to modulated Voigt dispersion lineshape functions. *Journal of Quantitative Spectroscopy and Radiative Transfer*, 133:244–250, January 2014.

[117] M.C. Amann. *Tunable Laser Diodes*. Artech House, Norwood, MA USA, 1998.

[118] P.C.D. Hobbs. Ultrasensitive laser measurements without tears. *Applied Optics*, 36(4):903–920, Feb 1997.

[119] Thorlabs. *Operation Manual - Thorlabs Instrumentation - Mainframe PRO8000, PRO8000-4 and PRO800*. Newton, New Jersey, version 3.1 edition, September 2010.

[120] Laser components GmbH. *Specdilas D series DFB lasers for Spectroscopy*. Olching, Germany, June 2000.

[121] Laser components GmbH. *Data sheet for DFB-laser diode 1636-2629b*. Olching, Germany.

[122] Laser components GmbH. *Data sheet for DFB-laser diode 1243-2629b*. Olching, Germany.

[123] Laser components GmbH. *Data sheet for DFB-laser diode 1743-2629b*. Olching, Germany.

[124] Thorlabs. *Mounted 0.55 NA aspheric lens f=4.51 mm, DW=780nm, C coated*. Newton, New Jersey, Revision B edition, February 2014.

[125] Thorlabs. *Product Specification Sheet - FGA21 Photodiode*. Newton, New Jersey, Revision B edition, January 2010.

[126] Thorlabs. *Product Specification Sheet -*. Newton, New Jersey, revision A edition, October 2008.

[127] Thorlabs. *Operation Manual - Thorlabs Instrumentation - Optical Power and Energy Meter PM100D*, version 17654-D02 Rev E edition, November 2009.

[128] Ghassan Fadil Lattif Al-Doori. *Investigation of Refrigeration System Steam Ejector Performance Through Experiments and Computational Simulations*. PhD thesis, University of Southern Queensland, Toowoomba, 2013.

[129] Giuseppe Grazzini, Adriano Milazzo, and Samuele Piazzini. Prediction of condensation in steam ejector for a refrigeration system. *International Journal of Refrigeration*, 34(7):1641 – 1648, 2011.

[130] J.H. Keenan J.K. Salisbury, J. Kaye. *Kent's Mechanical Engineers' Handbook*. John Wiley and Sons Inc, New York, twelfth edition, 1950.

[131] F. Bakhtar and M. Piran. Thermodynamic properties of supercooled steam. *International Journal of Heat and Fluid Flow*, 1(2):53–62, 1979.

[132] F. Bakhtar and R.A. Webb. Tabular method of estimating nucleating steam flows. *International Journal of Heat and Fluid Flow*, 4(4):217 – 227, 1983.

[133] Zheng Li, Arnaud Borner, Ali Rahnamoun, Deborah A. Levin, and Adri van Duin. BGK and MD simulations of H_2O supersonic condensed jets. In *AIAA Aviation*. American Institute of Aeronautics and Astronautics, June 2014.

[134] Philip G. Hill. Condensation of water vapour during supersonic expansion in nozzles. *Journal of Fluid Mechanics*, 25(03):593–620, 1966.

[135] H. Vehkamaki. *Classical nucleation theory in multicomponent systems*. Springer-Verlag, 2006.

[136] N. A. Malek Hasini H., M.Z. Yusoff. *Mechanical Engineering*. InTech, 2012.

[137] Judy Odam. *Scramjet Experiments using Radical Farming*. phdthesis, 2004.

[138] Matthew McGilvray. *Scramjet testing at high enthalpies in expansion tube facilities*. PhD thesis, The University of Queensland, St Lucia, 2008.

[139] G.Y. Anderson. *Hypersonic Combustion - Status and Directions*. Kluwer Academic Publishers, 1994.

[140] R.G. Morgan and D.E. Gildfind. X3 reflected shock tunnel for extended flow duration. In *2014 Asia-Pacific International Symposium on Aerospace Technology*, volume 99 of *APISAT2014*. Science Direct, 2014.

[141] Jorge Sancho. *Scramjet Testing at High Total Pressure*. PhD thesis, University of Queensland, St Lucia, 2014.

[142] P.A. Jacobs. Shock tube modelling with L1d. Technical report, 1998.

[143] R.G. Morgan, T.J. McIntyre, P.A. Jacobs, M.N. Buttsworth, D.R.and Macrossan, R.J. Gollan, B.R. Capra, A.M. Brandis, D. Potter, T.B. Eichmann, C.M. Jacobs, M. McGilvray, D. Van Diem, and M.P. Scott. Impulse facility simulation of hypervelocity radiating flows. *European Space Agency, (Special Publication)*, 629 SP, 2006.

[144] P.A. Jacobs, I. Gollan, R.J.and Jahn, and D.F. Potter. *The Eilmer3 Code: User Guide and Example Book*. The University of Queensland, St Lucia, Queensland, 2015.

[145] N.M. Reddy. The use of self-calibrating probes to measure free-stream atom concentration in a hypersonic flow. Contractor Report CR-78, NASA, University of Toronto, Toronto, Canada, May 1967.

[146] F. C. Fehsenfeld, K. M. Evenson, and H. P. Broida. Microwave discharge cavities operating at 2450 MHz. *Review of Scientific Instruments*, 36(3):294–298, 1965.

[147] J. Allen and T. Hauser. Improved atomic oxygen quantification within the Earth's upper atmosphere through numerical corrections. *Journal of Spacecraft and Rockets*, 45(5):965–974, September-October 2008.

[148] G. Duffa. *Ablative Thermal Protection Systems Modeling*. AIAA, 2012.

[149] F. Zander, R. G. Morgan, U. Sheikh, D. R. Buttsworth, and P. R. Teakle. Hot-wall reentry testing in hypersonic impulse facilities. *AIAA Journal*, 51(2):476–484, November 2012.

[150] M.N. Martin, L.S. Chang, J.B. Jeffries, R.K. Hanson, A. Nawaz, J.S. Taunk, D.M. Driver, and G. Raiche. Monitoring temperature in high enthalpy arc-heated plasma flows using tunable diode laser absorption spectroscopy. In *44th AIAA Plasmadynamics and Lasers Conference.*, San Diego, CA, June 2013.

[151] New Focus. *Model 6300 User's Manual - The Velocity Tunable Diode Laser*. New Focus, Weβling, Germany, 2002.

[152] Bruce McCarroll. An improved microwave discharge cavity for 2450 MHz. *Review of Scientific Instruments*, 41(2):279–280, 1970.

[153] M. Eberhart, S. Löhle, A. Steinbeck, T. Binder, and S. Fasoulas. Measurement of atomic oxygen in the middle atmosphere using solid electrolyte sensors and catalytic probes. *Atmospheric Measurement Techniques*, 8(9):33701–3714, September 2015.

[154] R. Hippler, S. Pfau, M. Schmidt, and K.H. Schoenbach, editors. *Low temperature plasma physics*. Wiley-VCH, Berlin, 2001.

[155] S. Gordon and B.J. McBride. Computer program for calculation of complex chemical equilibrium compositions and applications. Technical Report Reference Publication 1311, NASA, Cleveland, Ohio, 1994.

[156] B.J. McBride and S. Zehe, M.J.and Gordon. NASA Glenn coefficients for calculating thermodynamic properties of individual species. Technical Publication 211556, NASA, Glenn Research Center, Cleveland, Ohio, September 2002.

[157] Michael G. Littman and Harold J. Metcalf. Spectrally narrow pulsed dye laser without beam expander. *Applied Optics*, 17(14):2224–2227, Jul 1978.

[158] J. Emsley. The elements. In *Oxford Chemistry Guides*. Oxford University Press, New York, NY, 1995.

[159] Namic Kwon, Young-Hwan Yun, and Wonho Jhe. Optogalvanic study of the atomic-oxygen laser lines at 844.5 nm. *Phys. Rev. A*, 52:R895–R897, Aug 1995.

[160] JDS Uniphase. *Product Bulletin - SDL-5400 Series, 50 to 200 mW, 810/830/852 nm Single-mode Laser Diodes*. Japan, 2012.

[161] H. M. Katsch, A. Tewes, E. Quandt, A. Goehlich, T. Kawetzki, and H. F. Dobele. Detection of atomic oxygen: Improvement of actinometry and comparison with laser spectroscopy. *Journal of Applied Physics*, 88(11):6232–6238, 2000.

[162] N Knake, D Schr oder, J Winter, and V Schulz von der Gathen. Investigations on the generation of atomic oxygen inside a capacitively coupled atmospheric pressure plasma jet. *Journal of Physics: Conference Series*, 227(1):012020, 2010.

[163] Gilles Cartry, Xavier Duten, and Antoine Rousseau. Atomic oxygen surface loss probability on silica in microwave plasmas studied by a pulsed induced fluorescence technique. *Plasma Sources Science and Technology*, 15(3):479, 2006.

[164] George Parsons Lathrop. Talks with edison. *Harper's magazine*, 80:425–435, December 1889.

[165] John H. Scofield. Frequency-domain description of a lock-in amplifier. *American Journal of Physics*, 62(2):129–133, 1994.

[166] J. Gummer and Hawksworth S. Spontaneous ignition of hydrogen. Technical Report Research Report RR615, Health and Safety Laboratory, Buxton UK, 2008.

[167] C.J. Jachimowski. An analytical study of the hydrogen-air reaction mechanism with application to scramjet combustion. NASA Technical Report 2791, NASA, Langley Research Center, Hamption, Virginia, 1988.

[168] V. Wheatley. MECH 4450 - Aerospace Propulsion Lecture Notes. Technical Report Lecture 9: Scramjets, The University of Queensland, St Lucia, 2013.

[169] L.S. Rothman, I.E. Gordon, A. Barbe, D.C. Benner, P.F. Bernath, M. Birk, V. Boudon, L.R. Brown, A. Campargue, J-P. Champion, K. Chance, L.H. Coudert, V. Dana, V.M. Devi, S. Fally, J-M. Flaud, R.R. Gamache, A. Goldman, D. Jacquemart, I. Kleiner, N. Lacome, W.J. Lafferty, J-Y. Mandin, S.T. Massie, S.N. Mikhailenko, C.E. Miller, N. Moazzen-Ahmadi, O.V. Naumenko, A.V. Nikitin, J. Orphal, V.I. Perevalov, A. Perrin, A. Predoi-Cross, C.P. Rinsl, M. Rotger, Mm Simecková, M.A.H. Smith, K. Sung, S.A. Tashkun, J. Tennyson, R.A. Toth, A.C. Vandaele, and J. Vander Auwera. The HITRAN 2008 molecular spectroscopic database. *Journal of Quantitative Spectroscopy and Radiative Transfer*, 110(9-10):533 – 572, 2009.

[170] Standford Research Systems, Inc. *Model DS340 Synthesized function generator*. Sunnyvale, California, revision 1.7 edition, January 1999.

[171] Analog Devices. *160 dB Range (100 pA - 100 mA) Logarithmic converter AD8304*. Norwood, MA, USA, revision a edition, 2002.

[172] Texas Instruments. *LM358, LM258, LM158, LM2904 Dual operational amplifiers*. Dallas, Texas, revision u edition, January 2017.

[173] National Instruments. *60 MS/s, 60 MHz, 12-Bit, 8-channel digitizers NI PCI-5105, NI PXI-5105*. Austin, Texas, November 2014.

[174] M.G. Zabetakis. Flammability characteristics of combustible gases and vapors. Technical Report Bulletin 627, US Department of the Interior, Bureau of Mines, 1965.

A. Lock-in amplifiers

Lock-in amplifiers are extensively used in WMS-2f TDLAS. These phase sensitive detectors can extract signals from noisy data. Their theory is discussed in the appendix with the aim of developing a software form of a lock-in amplifier. A lock-in amplifiers consists of five stages as shown in figure A.1: a signal amplifier, a voltage controlled oscillator (VCO), a phase sensitive detector (PSD), a low-pass filter, and a DC amplifier [165]. This treatment is a traditional version that uses real numbers and cosine functions. A sinusoidal signal $V_o \cos(\omega_0 t + \delta)$ (where δ is the phase angle) is fed into the signal channel input and is amplified by the AC amplifier stage. This stage includes a bandpass filter centred at f_0 to eliminate significant extraneous signals. The AC amplifier gain G_{ac} is determined by the sensitivity setting of the lock-in and its output is:

$$V_{ac}(t) = G_{ac} V_0 \cos(\omega_0 t + \delta) \tag{A.1}$$

The VCO output is at frequency ω_0 and has a phase angle ϕ:

$$V_{VCO}(t) = E_0 \cos(\omega_0 t + \phi) \tag{A.2}$$

The PSD output is:

$$\begin{aligned} V_{PSD}(t) &= G_{ac} V_0 E_0 \cos(\omega_0 t + \delta) \cos(\omega_0 t + \phi) \\ &= \frac{G_{ac} V_0 E_0}{2} [1 + \cos(2\omega_0 t + \delta + \phi)] \end{aligned} \tag{A.3}$$

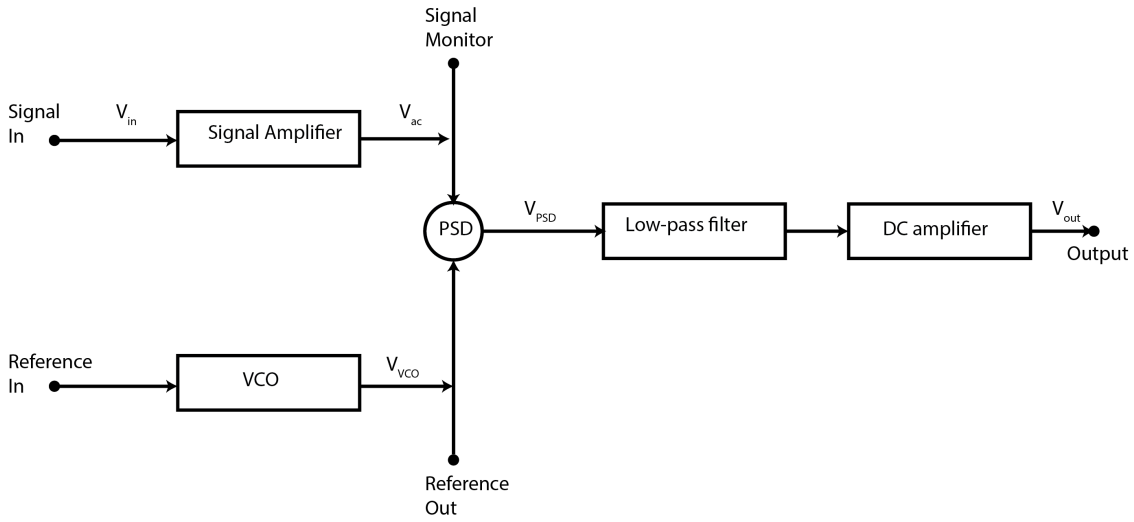

Figure A.1.: Block diagram of a lock-in amplifier.

For most applications, the DC component is used; however, WMS-2f uses the second harmonic component. The phase of an electronic lock-in is adjustable to maximise the output voltage. The final output DC voltage is directly proportional to the signal amplitude V_0 and is:

$$V_{out} = \frac{G_{dc} G_{ac} V_0 E_0}{2} \tag{A.4}$$

where G_{dc} is the voltage gain of the DC amplifier.
A low pass filter has been used to eliminate the $2\omega_0$ component. This filter also integrates the signal and reduces the gaussian noise in the DC amplifier. Scofield [165] highlights that many commercial lock-in amplifiers use a square wave as the VCO output instead of a sinusoid. The VCO output for a square wave is:

$$V_{VCO}(t) = \sum_{n=0}^{\infty} \frac{4E_0}{2n+1} \sin\left[(2n+1)\,\omega_0 t + \phi_n\right] \tag{A.5}$$

In this case, the ac amplifier must include a bandpass filter centred on the frequency of interest and attenuating other frequencies.

B. In-situ testing

Prior to using the TDLAS system in the expansion tube, in-situ testing was undertaken using laboratory conditions. Flame and heated test cell measurements were not undertaken because of time constraints associated with other experiments in X3 coupled with occupational health and safety concerns in using an open flame in the expansion tube laboratory. This is an area for future researchers to investigate. Examining the raw laser and pressure data, laser signal ratios and derived temperatures all provide valuable insight into the physics and dynamics of the test section conditions.

In-situ tests were conducted after verification that the expansion tunnel was operating correctly and after conducting ten shots with air as a test gas. During those shots, the ratio of the two photo detectors, as output from the ratio amplifier, was measured. The two individual photo detector signals were not recorded because it was thought that the ratio would contain sufficient information to extract the flow parameters. The TDLAS measurements were not consistent across these ten shots and the cause of the inconsistency could not be found. The experimental layout was changed to record each photo detector signal on separate channels. At the same time, in-situ tests were undertaken to check that each channel was producing signals.

The tests were initially undertaken with a path length of 3.608 m between each laser diode and its detector. The path was at laboratory conditions (typically 102 ± 1 kPa, 296 ± 2 K and $40 \pm 10\%$ relative humidity). Direct absorption measurements were taken to confirm the wavelength and power characteristics of each laser. Then, one laser was set at 7181.15578 cm^{-1} whilst the other was set to 7185.599 cm^{-1}. Each laser was modulated simultaneously using the output from an SRS DS340 function generator set to produce a 1 MHz sinusoidal signal at a peak-to-peak amplitude of 1 V. Two equal length locally-manufactured cables connected the BNC output of the function generator to the SMA inputs of the laser diode mounts. The cable impedance was $50\ \Omega$ matching the impedances of the function generator and laser mounts. Using two equal length cables aimed to remove any phase differences between the signals reaching the mounts. BNC Tee-junctions were used to extract the signals from the sole output of the function generator.

In order to measure the modulation characteristics, a third BNC Tee-junction was connected to the function generator output and terminated at the National Instruments PXI-5105 digital oscilloscope card after travelling through a 10 m $50\ \Omega$ impedance coaxial cable. The data recordings were triggered using the fuel system trigger.

Figure B.1 shows the recorded frequency generator signal for a typical in-situ test. The upper figure shows the entire signal of 240,000 samples recorded in approximately 4 ms. The centre figure is an expanded view of 10,000 samples during the test time from 1.65 ms to 1.49 ms prior to trigger. The lower figure shows a further expansion of the 1000 data points near 1.565 ms prior to trigger. The measured modulation voltage (11 mV) was approximately 1% of the expected value (1 V). Also,

the waveform was not sinusoidal even though a 1 V sinusoidal signal was selected on the frequency generator. As seen in the figure, the function generator signal typically was falling during the in-situ tests. The cause of this fall was not found but it was seen on every in-situ test. During the

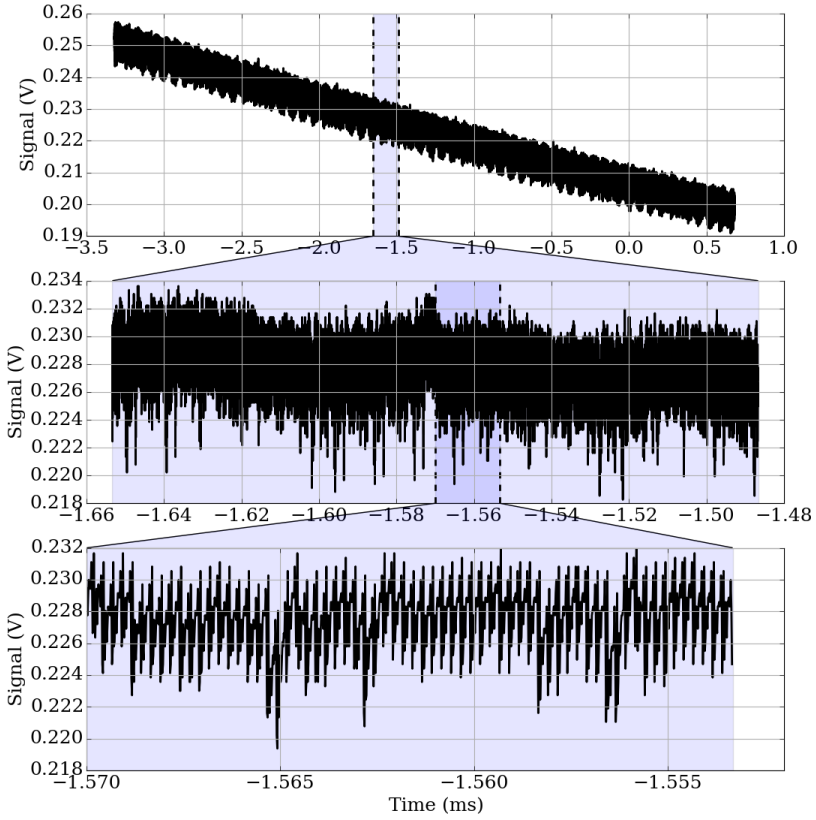

Figure B.1.: Modulation signal for shot x3s462 pretest 6. The upper figure shows the entire signal of 240,000 samples recorded in approximately 4 ms. The centre figure is an expanded view of 10,000 samples during the test time from 1.65 ms to 1.49 ms prior to trigger. The lower figure shows a further expansion of the 1000 data points near 1.565 ms prior to trigger.

experiments, the small measured modulation amplitude was thought to be an aberration caused by the 1 MΩ impedance of the NI PXI-5105 digital oscilloscope. The two laser diode mounts had 50 Ω impedances matching the 50 Ω output impedance of the function generator. Therefore, it was assumed that the modulation amplitude for each laser diode mount was 1 V. After analysing the data, this assumption was found to be incorrect. The modulation signal distortion may have been due to reflected signals from the high impedance interface.

Figure B.2 shows the raw data for Channel 1 (7181.15578 cm^{-1}) during an in-situ test. Laboratory conditions for the pre-test were 102.5 ± 0.2 kPa, 295 ± 1 K and $50 \pm 5\%$ relative humidity. The dump tank was not in the TDLAS path and fuel was not injected. The path length was 3.06 ± 0.01 m and the lasers were modulated at 1 MHZ with $V_{pp} = 1.0$ V. The observed signals in figure B.2 are in the range ± 4 mV. Striations due to the limited data recording resolution are clearly visible in the extracted signal. The input voltage full scale range (FSR) for the National Instruments PXI-5105 card was selectable from $0.05, 0.2, 1, 6$ or 30 V with an input impedance of 1 MΩ and 12-bits resolution.

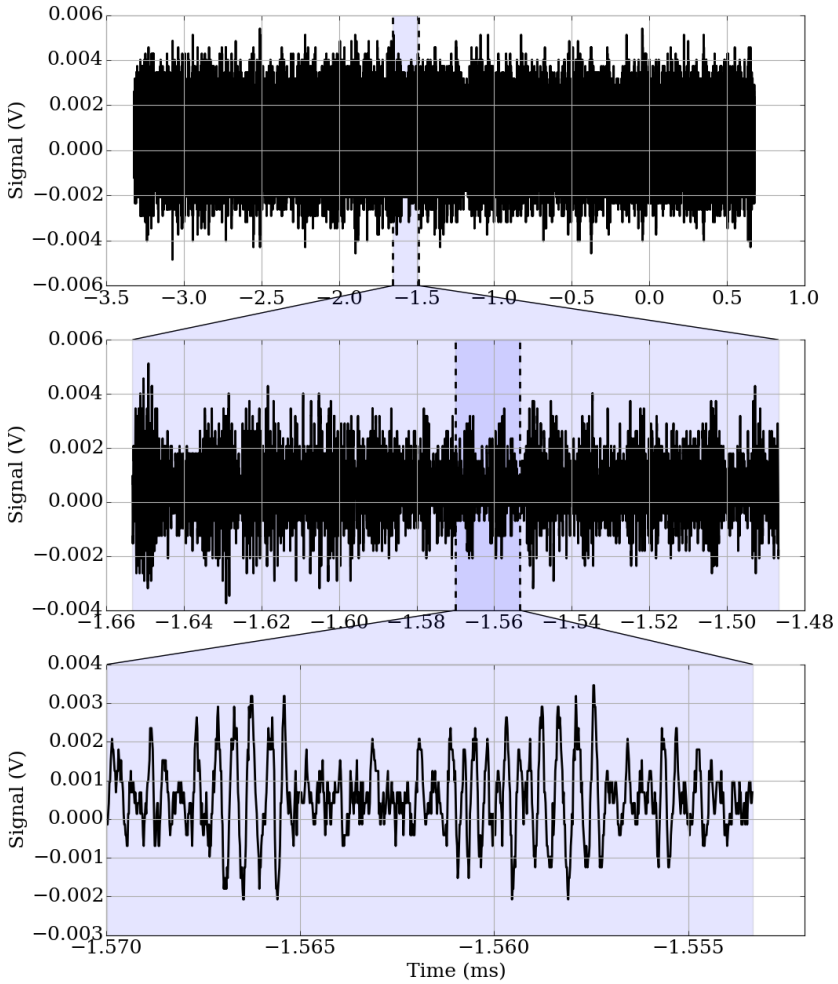

Figure B.2.: Shot x3s462 Pretest 6 channel 1 laser signal. The upper figure shows the entire signal of 240,000 samples recorded in approximately 4 ms. The centre figure is an expanded view of 10,000 samples during the test time from 1.65 ms to 1.49 ms prior to trigger. The lower figure shows a further expansion of the 1000 data points near 1.565 ms prior to trigger.

For these experiments, the full-scale range was set to 1 V making the resolution 244 μV. After the experiments were complete, this resolution was found to be inadequate because of the small signal voltage. It would have been better to set the FSR to either 50 mV or 200 mV to improve the signal resolution.

Figure B.3 shows the spectral plot for the observed signal for channel 1 during the pretest. The peak frequency is 2.271 MHz. Comparing with the spectral plot for channel 2 in figure B.4, the peak frequency in the latter is 2.256 MHz which is 25 kHz below channel 1's frequency. The reasons for these observed frequencies and the difference between them are not known. The spectral distribution for channel 2 is more spread than that of channel 1. This may be due to the small relative absorbance of the feature at 7185.559 cm^{-1} compared to that of the other feature at room temperature. An important feature of each in-situ test spectrum is the frequency distribution around the modulation

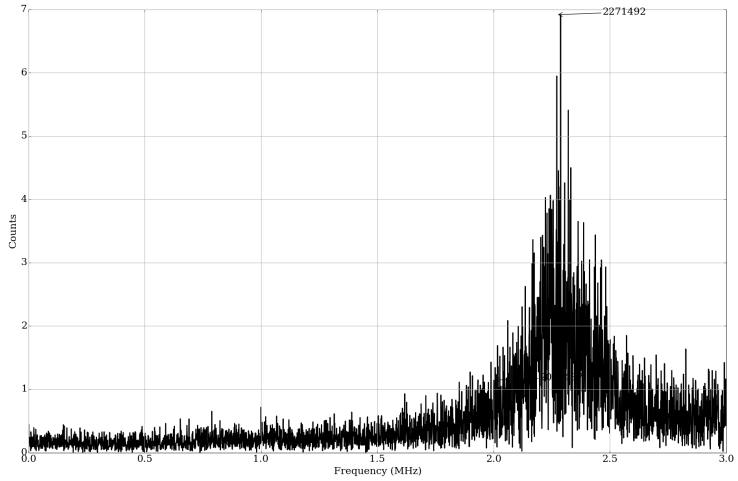

Figure B.3.: Frequency spectrum for shot x3s462 pretest 6 channel 1 signal.

peak. Considering that the lasers were modulated with pure sinusoidal waveforms, one would expect that the received signal would be mono-tonal or slightly spread. Instead, the HWHM of the spectral distribution is approximately 300 kHz in figure B.3. Figure B.5 is the signal extracted using a lock-in

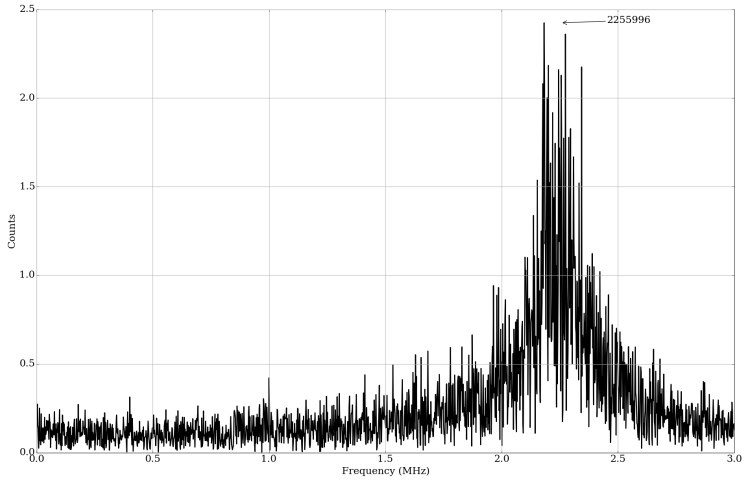

Figure B.4.: Frequency spectrum for shot x3s462 pretest 6 channel 2 signal.

amplifier with a frequency of $2,271,492$ Hz for channel 1 in this test. A Voigt transmission profile was developed for the test characteristics (295 K, 102.5 kPa, 51% relative humidity and 3.608 m path length). The laser diode centre current, modulation voltage and relative phase were adjusted until the modelled line shape aligned with the observed one. The final model values were:

- Laser diode centre current: 110.335 mA,
- Modulation voltage: 11 mV, and
- Relative phase: 0.0π radians.

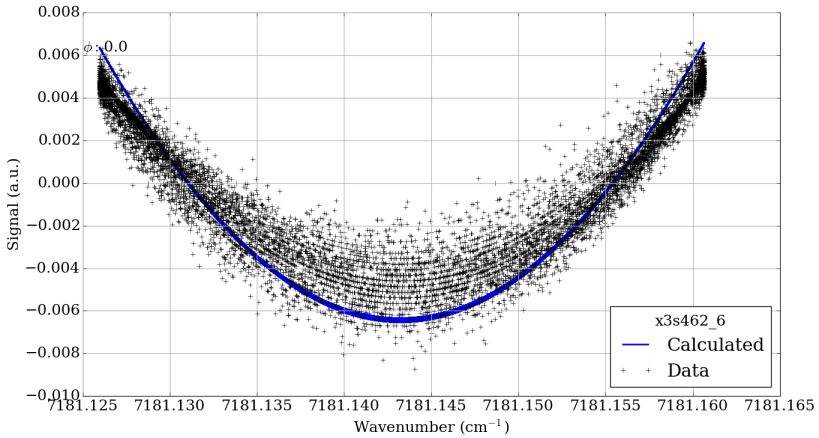

Figure B.5.: Calculated and measured data or shot x3s462 pretest 6 channel 1 signal. The data represent 10,000 measurements during the test time from 1.65 ms to 1.49 ms prior to trigger.

The transmission model was scaled so that mean was aligned with 0.0 V and the maxima aligned with the maximum measured values. The calculated Voigt profile aligns well with the measured data; however, the width of the model data is less than that of the measured data. The wide distribution of measured values is probably due to distortion of the modulation signal. Figure B.6 shows similar data for the other laser diode for the same test. The model values were:

- Laser diode centre current: 79.865 mA,
- Modulation voltage: 11 mV, and
- Relative phase: 0.0π radians.

Again, the measured and theoretical data align well but the large variation in measured data at each wavenumber coupled with the inadequate modulation voltage precludes extracting accurate temperature and pressure results from the data. If this technique is to be used, the issues with modulation voltage need to be resolved. Unfortunately, this problem was not found during the experimental campaign. All tests were undertaken with the frequency generator connected to both low and impedance terminations. Examination of all recorded modulation signals revealed that the voltage range was approximately $10 - 15$ mV during each shot.

B.1. Impact of reduced modulation amplitude on results

The reduced modulation voltage problem impacted on all results since a premise of the experimental technique was that the TDLAS signals encompassed each feature enabling the HWHM, feature strength and area to be deduced. Because the modulation amplitude range was of the order of 0.04 cm^{-1} instead of the desired $0.4 - 1.5$ cm^{-1}, none of the planned methods were able to produce accurate temperature, water vapour concentration or pressure results. Figures B.7 and B.8 illustrate the problem for the two features used in this campaign.

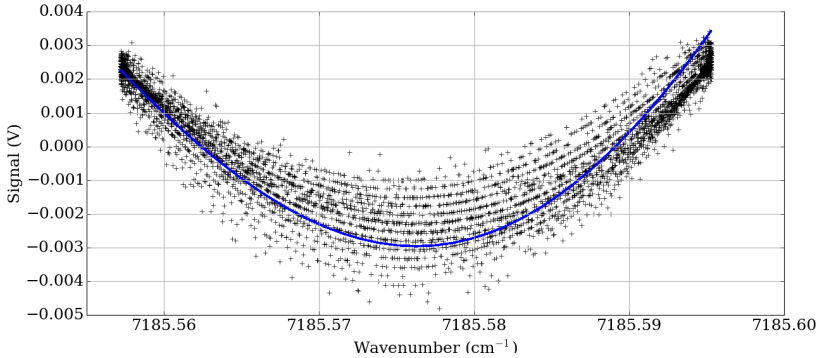

Figure B.6.: Calculated and measured data or shot x3s462 pretest 6 channel 2 signal. The data represent 10,000 measurements during the test time from 1.65 ms to 1.49 ms prior to trigger.

Figure B.7 shows the effect of reduced modulation range on the absorbance plot for the feature at 7181.15578 cm^{-1} and figure B.8 shows a similar effect for the second target feature at 7185.599 cm^{-1}. The scramjet test section parameters for these simulations were 2000 K, 50.0 kPa with a water vapour concentration of 10%. The centre plot of each figure shows the approximate modulation range initially planned for the experiments whilst the lower plot shows the approximate actual modulation ranges. Instead of traversing the entire features, only the centre 10% of each feature was traversed. These small samples of the spectral features were insufficient for deriving flow parameters as initially planned.

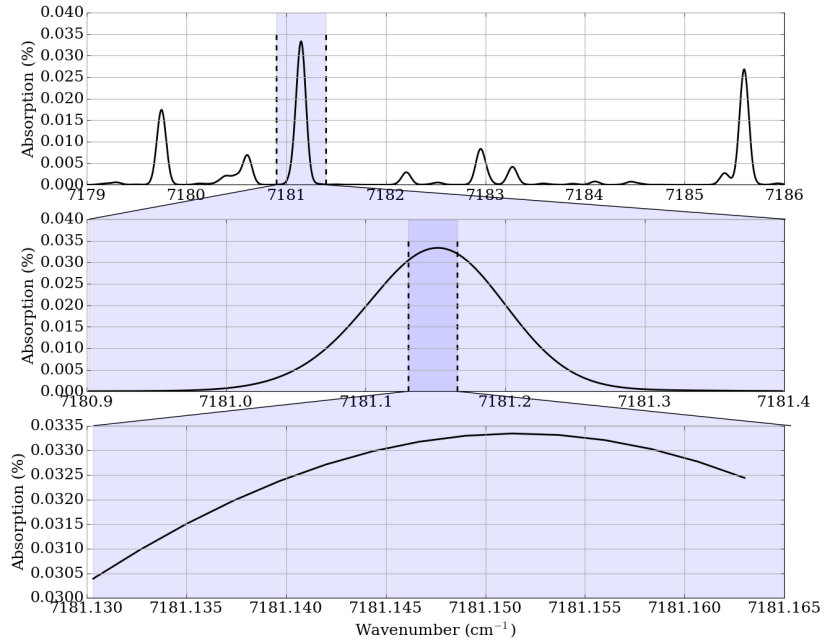

Figure B.7.: Exploded view of feature at 7181.15578 cm^{-1} showing desired modulation range in centre plot and actual range (approximate) in lower plot.

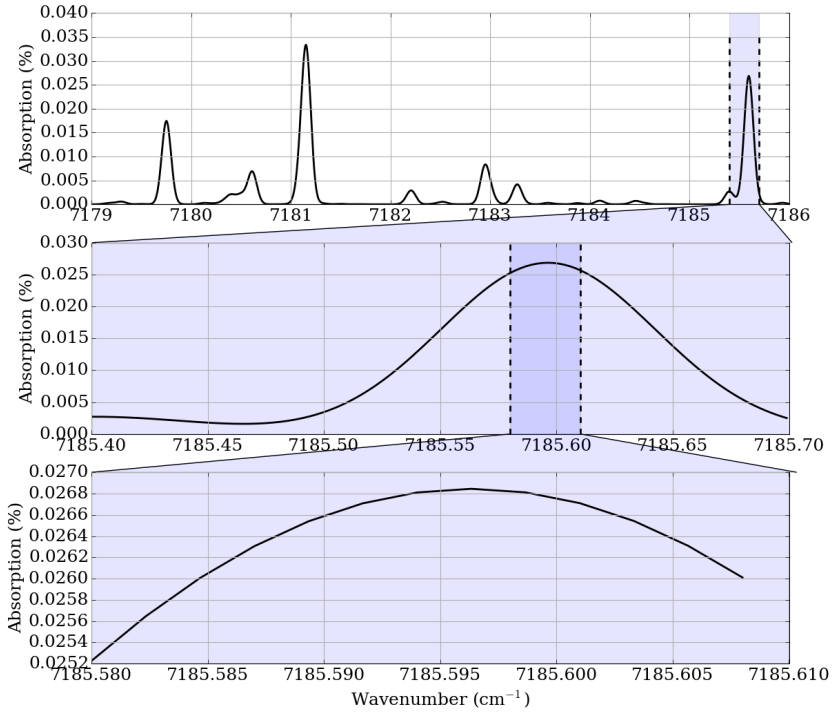

Figure B.8.: Exploded view of feature at 7185.599 cm^{-1} showing desired modulation range in centre plot and actual range (approximate) in lower plot.

C. Expansion Tunnel

The X3 super-orbital expansion tunnel at the University of Queensland can produce Mach 10-15 flows typical of a space trajectory corridor. Figure C.1 is a schematic diagram of the expansion tube. Prior to a shot, an air reservoir at the upstream end of the tube is filled with compressed air to a pressure of approximately 3.8 MPa absolute. When the reservoir is opened, a piston within the compression tube (CT) is accelerated downstream compressing a 30 kPa $40:60$ Argon/Helium driver gas mixture that is contained by a mild steel primary diaphragm. A driven tube downstream of the primary diaphragm holds helium gas at approximately 70 kPa absolute that is contained by a mylar secondary diaphragm. The primary diaphragm ruptures at a pressure of approximately 17.5 MPa. After diaphragm rupture,

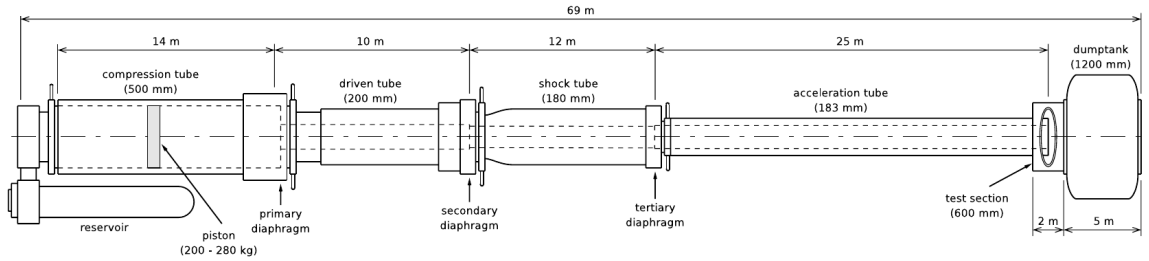

Figure C.1.: Schematic diagram of X3 expansion tube. Source: [6]

the compression gas flows through the hole. The compression gas pressure is much greater than the driven gas pressure causing the flow through the primary diaphragm to be choked. The mass flow depends only on the compression gas stagnation conditions. A shock wave travels down the driven tube ahead of the interface between the compression and driven gases compressing the gas ahead of the interface until the secondary diaphragm ruptures.

A shock tube (ST) downstream of the secondary diaphragm holds the test gas which is contained by a mylar tertiary diaphragm. For these experiments, the test gas was either laboratory air or gaseous nitrogen at 39 kPa. The test gas is, in turn, processed by a shock wave and compressed until the tertiary diaphragm ruptures. The acceleration tube (AT) downstream of the tertiary diaphragm is evacuated to a pressure (typically less than 120 Pa for these experiments). The test gas accelerates down the acceleration tube then expands as it travels through the nozzle. A model scramjet is held in the dump tank downstream of the nozzle while the test gas flows through the scramjet.

The expansion tunnel operating conditions aimed to simulate a vehicle flying at $3.5\,\mathrm{kms}^{-1}$ at an altitude of 30 km with a dynamic pressure q_0 of 48.4 kPa. Table C.1 lists the expansion tube operating parameters.

Table C.1.: Expansion tunnel parameters

Parameter	Target Value
Sancho [141] Shot	x3s403
Primary Diaphragm Thickness	2 mm
Secondary Diaphragm Thickness	25 μm
Tertiary Diaphragm Thickness	25 μm
Reservoir Pressure	3.8 MPa
Compression Tube Pressure	30 kPa
Compression Tube Mixture	0.4:0.6 Ar:He
Driver Pressure	90 kPa
Driver Gas	He
Shock Tube Pressure	39 kPa
Shock Tube Gas	Air/Nitrogen
Acceleration Tube Pressure	120 Pa
Acceleration Tube Gas	Air

C.1. Driven tube

Figure C.2 shows typical pressure traces from PCB transducers in the driven tube during shot x3s451. The primary diaphragm ruptured at a static pressure of 17.5 MPa as measured using the compression tube (CT) PCB transducer. The driven tube was filled with 70 kPa of helium gas prior to the shot. Sensor ST3 is 2.57 m upstream of the secondary diaphragm. The shock speed was calculated at 3.046 kms^{-1} based on the time between pressure rises at the two sensors. The pressure at sensor ST1 increases as the compression tube gas enters the driven tube. We can calculate the properties in front of and behind the shock using well known shock tube formulae.
If W_s is the shock speed and a_1 is the speed of sound in the driver gas, the shock Mach number M_s is given by:[1]

$$M_s = \frac{W_s}{a_1} \tag{C.1}$$

The shock wave static pressure ratio $\frac{p_2}{p_1}$ is:

$$\frac{p_2}{p_1} = 1 + \frac{2\gamma}{\gamma + 1}\left(M_s^2 - 1\right) \tag{C.2}$$

where γ is the ratio of specific heats for the fill gas (1.4 for air and 1.6667 for helium and argon).
The induced mass flow velocity U_p behind the shock is:

$$U_p = \frac{a_1}{\gamma}\left(\frac{p_2}{p_1} - 1\right)\left(\frac{2\gamma}{\gamma + 1}\right)^{0.5}\left(\frac{p_2}{p_1} + \frac{\gamma - 1}{\gamma + 1}\right)^{-0.5} \tag{C.3}$$

[1]The subscript 's' represents the shock, '1' is ahead of the shock, 2' is behind the shock and '4' represents the conditions in the gas upstream of the diaphragm.

Table C.2.: Comparison of post-shock properties in the driven gas calculated using ideal gas formulae and CEA. Conditions were $P_1 = 70.0$ kPa of helium, $T_1 = 298$ K and $W_s = 3046$ ms^{-1}

Property	CEA Value	Ideal Value
P_2 (kPa)	769.31	776.51
T_2 (K)	1092.13	1093.66
ρ (kgm^{-3})	0.33911	0.34184
Enthalpy (MJkg^{-1})	4.1233	4.1320
C_p (kJkg^{-1}K^{-1})	5.1932	5.1932
γ	1.6667	1.6667
a_2 (ms^{-1})	1944.5	1945.8
p_2/p_1	10.990	11.093
T_2/T_1	3.665	3.670
ρ_2/ρ_1	2.9988	3.0226
V_2 (ms^{-1})	2030.3	2038

The diaphragm pressure ratio $\frac{p_4}{p_1}$ is:

$$\frac{p_4}{p_1} = \frac{p_2}{p_1}\left[1 - \frac{(\gamma-1)(a_1/a_4)(p_2/p_1-1)}{\sqrt{2\gamma\left[2\gamma+(\gamma+1)(p_2/p_1-1)\right]}}\right]^{\frac{-2\gamma}{\gamma-1}} \tag{C.4}$$

If the initial enthalpy in the driven gas is h_1 and the initial and final specific heats at constant pressure are C_{p_1} and C_{p_2}, the final enthalpy is:

$$h_2 = h_1 + \frac{(C_{p_1} + C_{p_2})(T_2 - T_1)}{2} \tag{C.5}$$

Assuming that the temperature of the fill gas was 23°C and that ideal gas conditions apply, h_1 is zero for helium at 298 K. The sound speed in the driven tube was 1010.5 ms^{-1}, the shock pressure ratio was 11.093, the shock temperature ratio was 3.670 and the induced mass flow velocity was 2.038 kms^{-1}. CEA was used to confirm the ideal calculations and check whether dissociation had any effect on the post-shock gas composition. Table C.2 compares the post-shock properties in the driven tube gas using both methods. Given that helium was used as the driven gas, dissociation was not observed. The CEA values are used for downstream calculations. Any reflected shock is weak due to the low burst pressure of the mylar diaphragm. The reflected shock arrival time at sensor ST3 was calculated to be approximately 1.53 ms after secondary diaphragm rupture in this case. The calculated pressure behind the shock was 776.5 kPa using ideal theory and 769.3 kPa using CEA whereas the measured pressure is approximately 880 kPa prior to secondary diaphragm rupture falling linearly with time after rupture to 670 kPa at the arrival time for any reflected shock wave.

To summarise, the driven tube conditions agree reasonably with theory considering that the secondary diaphragm ruptures. A reflected shock is not observed. The initial pressure behind the shock is higher than calculated theoretically but decreases to below the theoretical value after the secondary

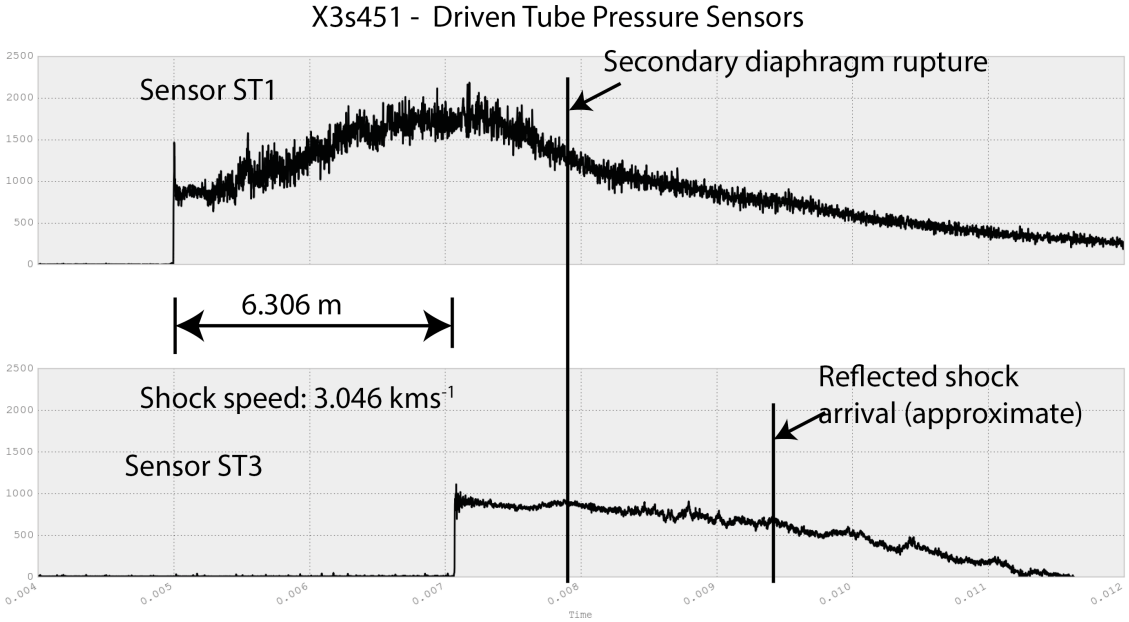

Figure C.2.: Pressure traces from sensors ST1 and ST3 for shot x3s451.

diaphragm ruptures. The CEA calculated values were used for downstream calculations.

C.2. Shock tube

The shock tube was filled with either air or nitrogen to 39 kPa prior to each shot. Figure C.3 contains the pressure traces from PCB sensors ST6 and ST7 for shot x3s451. Sensor ST7 was approximately 1.70 m upstream from the tertiary diaphragm. The shock speed was 1.836 kms^{-1} for shot x3s451. At a fill gas temperature of 23°C, h_1 is -4.4845 kJkg^{-1} and C_{p_1} is 1.0047 kJkg^{-1}K^{-1} [156]. Assuming ideal gas conditions, the sound speed in the shock tube was 345 ms^{-1}, the shock pressure ratio was 32.883, the shock temperature ratio was 6.447 and the induced mass flow velocity was 1.476 kms^{-1}. CEA was used to confirm the ideal calculations and check whether dissociation had any effect on the post-shock gas composition. Table C.3 compares the post-shock properties in the test gas using both methods. There was minimal dissociation in the flow with the atomic oxygen mole fraction being 8.0512×10^{-6}. The CEA values are used for downstream calculations. The tertiary diaphragm ruptured 0.926 ms after the shock passed sensor ST7. The theoretical reflected shock arrival time at sensor ST7 was approximately 2.60 ms after tertiary diaphragm rupture. The calculated pressure behind the shock was 1.282 MPa whereas the measured pressure was between 1.48 MPa and 1.23 MPa prior to secondary diaphragm rupture then fell with time to 930 kPa at the arrival time for any reflected shock wave.

The shock tube conditions agree reasonably with theory. A reflected shock was not observed. The initial pressure behind the shock agreed with the theoretical value and decreased after the tertiary diaphragm ruptured.

Table C.3.: Comparison of post-shock properties in the test gas calculated using ideal gas formulae and CEA. Conditions were $P_1 = 39.0$ kPa of air, $T_1 = 298$ K and $W_s = 1836$ ms^{-1}

Property	CEA Value	Ideal Value
P_2 (MPa)	1.3094	1.2824
T_2 (K)	1734.44	1921.2
ρ (kgm^{-3})	2.6301	2.3255
Enthalpy (MJkg^{-1})	1.63032	1.63073
C_p (kJkg^{-1}K^{-1})	1.2701	1.00464
γ	1.2920	1.400
a_2 (ms^{-1})	802.0	878.7
p_2/p_1	33.576	32.883
T_2/T_1	5.820	6.447
ρ_2/ρ_1	5.7688	5.1005
V_2 (ms^{-1})	1517.74	1476

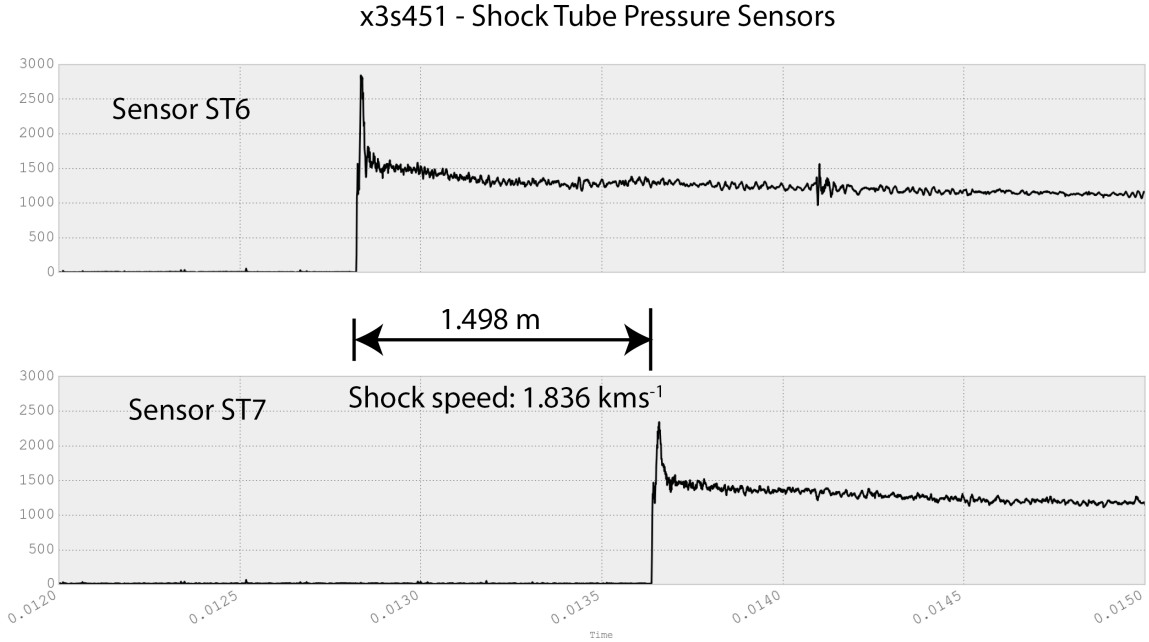

Figure C.3.: Pressure traces from sensors ST6 and ST7 for shot x3s451.

Table C.4.: CEA calculated and ideal gas post-shock properties for a shock wave processing air with $P_1 = 120$ Pa, $T_1 = 298$ K and $W_s = 3485$ ms^{-1}.

Property	CEA Value	Ideal Value
P_2 (kPa)	15.481	14.27
T_2 (K)	3370	6456
ρ (kgm^{-3})	1.4255×10^{-2}	7.700×10^{-3}
h_2 (MJkg^{-1})	6.00932	6.187
C_p (kJkg^{-1}K^{-1})	4.5419	1.0047
γ	1.1621	1.400
a_2 (ms^{-1})	1123.4	1610.7
p_2/p_1	129.009	118.9
T_2/T_1	11.308	20.786
ρ_2/ρ_1	10.1613	5.7200
V_2 (ms^{-1})	3142.03	2876

C.3. Acceleration tube

The acceleration tube was evacuated to approximately 120 Pa of air at $23°$C. At these conditions, the enthalpy h_1 was -4.4845 kJkg^{-1} and $C_{p_1} = 1.0047$ kJkg^{-1}K^{-1} [156]. Sensors AT7 and AT8 were used to measure the shock speed and static pressure immediately before the expansion nozzle. Sensor AT8 was approximately 0.7 m upstream of the start of the nozzle expansion. The shock speed between sensors AT7 and AT8 was measured at 3.485 kms^{-1} for shot x3s453.[2] Assuming ideal gas properties and no dissociation, the theoretical shock Mach number was 10.10, the shock pressure ratio was 118.9, the shock temperature ratio was 20.786 and the mass inflow speed was 2.876 kms^{-1}. The post shock temperature was 6456 K based on no dissociation.

The ideal gas post-shock values for static temperature, density, specific heat at constant pressure, sound speed and inflow velocity were significantly different from the values calculated using CEA. Thus, ideal gas relationship were not used to calculate acceleration gas properties post-shock even though the ideal gas static pressure was of the same order of magnitude as the CEA value. CEA-calculated static temperature was 3370 K and static pressure was 15.481 kPa. The static pressure agrees with the measured post-shock value of 15.5 kPa. The pressure increase above the ideal value is due to the presence of atomic oxygen and NO in the flow. The test gas expands as it travels down the acceleration tube until its static pressure matches that of the post-shock accelerator gas (15.481 kPa in this case). Table C.5 contains analytical results for the test gas conditions at the start and end of the acceleration tube. As may be seen from figure C.4, the measured pressure was approximately 15.0 kPa which compares well with the theoretical value. The test gas does not immediately follow the acceleration tube shock; instead, processed acceleration tube gas precedes the test gas. The processed test gas slug is 120 mm long based on pressure ratios. It arrives at AT8 42 μs after the shock as shown in figure C.4. The test gas is highlighted in the figure.

[2] Driven and shock tube conditions were the same for shots x3s451 and x3s453

Table C.5.: Test gas properties at the start and end of acceleration tube

Property	Inlet Value	Exit Value
Static Pressure	1.3094 MPa	15.481 kPa
Static Temperature	1734.44 K	455.8 K
Density	2.6301 $\left(\text{kgm}^{-3}\right)$	0.11831 $\left(\text{kgm}^{-3}\right)$
γ	1.2920	1.3908
Sound speed	802.0 ms^{-1}	426.6 ms^{-1}
Mach Number	1.8924	7.3656
C_p	1.2701 $\text{kJkg}^{-1}\text{K}^{-1}$	1.0216 $\text{kJkg}^{-1}\text{K}^{-1}$
Total Pressure	8.447 MPa	8.447 MPa
Total Temperature	2678.1 K	2678.1 K
P/P_t	0.15502	0.0018328
T/T_t	0.64764	0.17021
Velocity	1517.7ms^{-1}	3142.0ms^{-1}

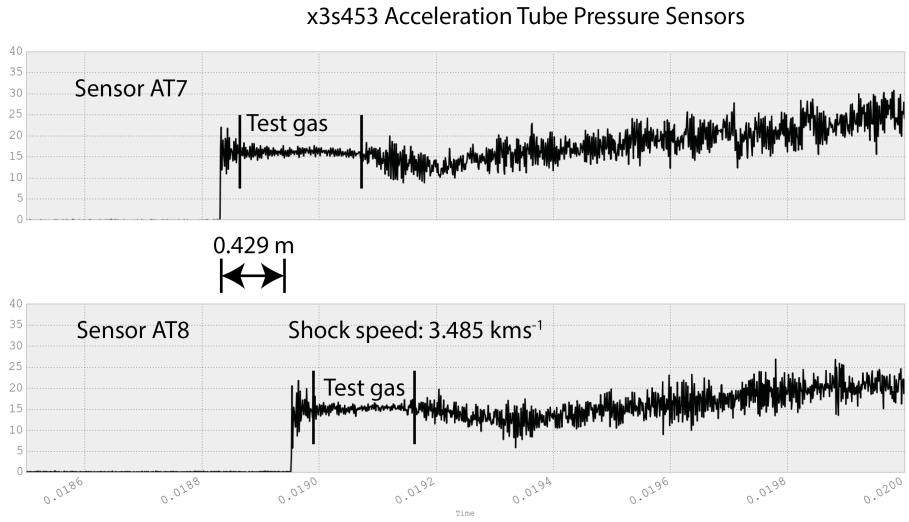

Figure C.4.: Pressure traces from sensors AT7 and AT8 for shot x3s453. The test gas slug is delineated for each sensor.

C.4. Nozzle

The nozzle area ratio for X3 was 5.806358.[3] Table C.6 lists the calculated conditions for the test gas at the nozzle inlet and exit. Note that these values do not account for Mirels effects, flow separation and boundary layer development.

Table C.6.: Calculated nozzle inlet and exit properties for the test gas

Property	Inlet Value	Exit Value
Mach Number	7.3656	10.98
Static Pressure	15.481 kPa	1.186 kPa
Static Temperature	455.8 K	211.2 K
γ	1.3908	1.4012
C_p	1.0216 kJkg^{-1}K^{-1}	1.0025 kJkg^{-1}K^{-1}
Sound speed	426.6 ms^{-1}	291.47 ms^{-1}
Total Pressure	8.447 MPa	8.4447 MPa
Total Temperature	2678.1 K	2678.1 K
A/A*	141.8434	823.594
P/P_t	1.8328×10^{-3}	1.4049×10^{-4}
T/T_t	0.17021	0.07887
Velocity	3142.0 ms^{-1}	3200.3 ms^{-1}
Density	0.11831 kgm^{-3}	0.01957 kgm^{-3}

[3] Initial diameter - 182.6 mm and final diameter - 440 mm

D. Scramjet

A scramjet consists of an inlet, isolator, combustor and nozzle. Oblique shock waves slow the inlet airflow from the free stream Mach number to approximately Mach 3 before entry to the isolator. Fuel may be injected at the inlet or isolator depending on the scramjet design. The isolator and combustor use reflected oblique shock waves to provide hot zones and initiate supersonic combustion. As the flow is supersonic, pressure rises do not progress upstream. Turbulent mixing of the un-burnt reactants with the burnt products enhances combustion. The nozzle is used to accelerate the exhaust flow providing thrust to the engine. Figure D.2 shows the test scramjet inlet from upstream. Table D.1 lists the free stream target values for these experiments. The scramjet model used in this campaign was

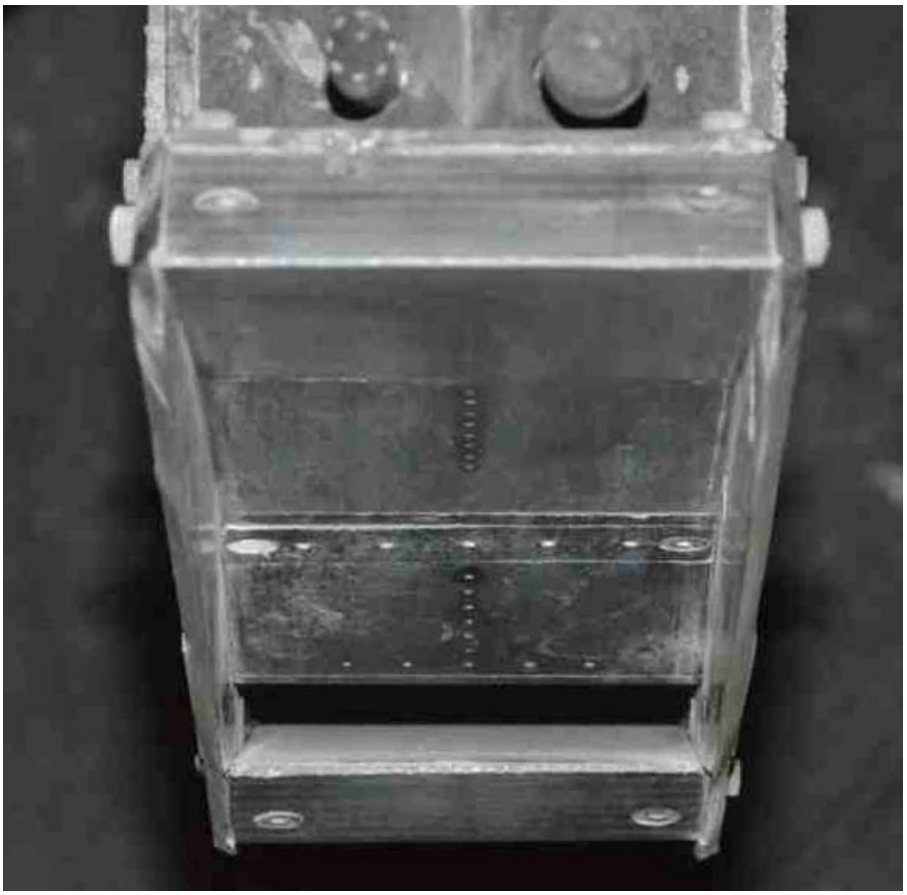

Figure D.1.: Scramjet inlet as seen from upstream

based on designs previously tested in T4, X2 and X3. It is designed for a free-stream flow at Mach 10 and uses inlet injection of gaseous hydrogen as its fuel. The scramjet flow path has a rectangular cross-section consisting of the three ramp inlet, a straight duct combustor, a linear nozzle and a cowl surface [141]. Figure D.2 is a schematic diagram of the X3 scramjet model showing its principal

Table D.1.: Free stream target values for X3 test condition. (Adapted from Sancho [141])

Parameter	symbol	Value
Pressure	p_0	896 Pa
Temperature	T_0	262 K
Density	ρ_0	0.012 kgm^{-3}
Velocity	U_0	3.5 kms^{-1}
Mach Number	M_0	10.0
Enthalpy	H_0	6.13 MJkg^{-1}

dimensions and angles. The model is made from mild steel and has replaceable leading edges for

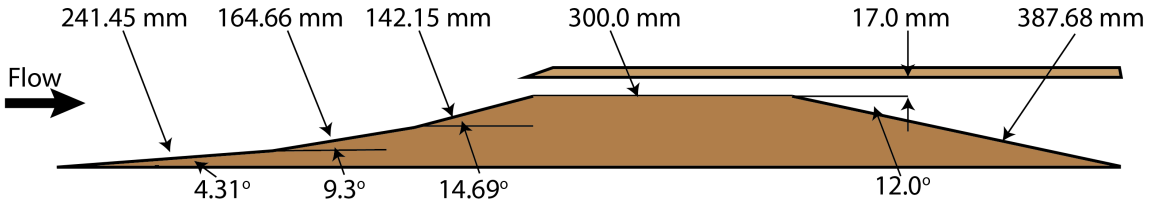

Figure D.2.: Schematic diagram of X3 scramjet model showing principal dimensions. Flow is from left to right. Model width is 100 mm.

the first ramp and the cowl. Twenty-seven PCB dynamic pressure sensors and two Kulite pressure sensors measured the scramjet flow path pressures.

An 8 mm hole was drilled through each side wall of the nozzle to allow TDLAS beams to traverse the nozzle flow. The hole centres were 70 mm downstream from the combustor exit. This corresponded to taking measurements in the scramjet nozzle where the nozzle height was 28.9 mm and its cross-sectional area was 1.70 times the combustor cross-sectional area. This position and diameter were selected based on the following criteria:

- The hole was downstream of the expansion fan at the start of the nozzle so the flow would be well established there.
- The hole diameter was four times the laser beam diameters so the lasers could be angled there the holes and cross at the combustor centreline.
- The hole diameter was less than 30% of the nozzle height so the hole would have a small impact on nozzle flow.
- The lasers could be directed through the dump tank windows on both sides. The dumptank window position was fixed and provided limited access to the scramjet nozzle. With the hole in this position, the lasers cleared the window edge by 10 mm.

Consideration was given to inserting BK7 glass plugs into the holes to eliminate flow disturbance. This was not done because previously such plugs had often failed during shots. Also, the glass would carbonise during each shots but could not be cleaned without replacing the glass.

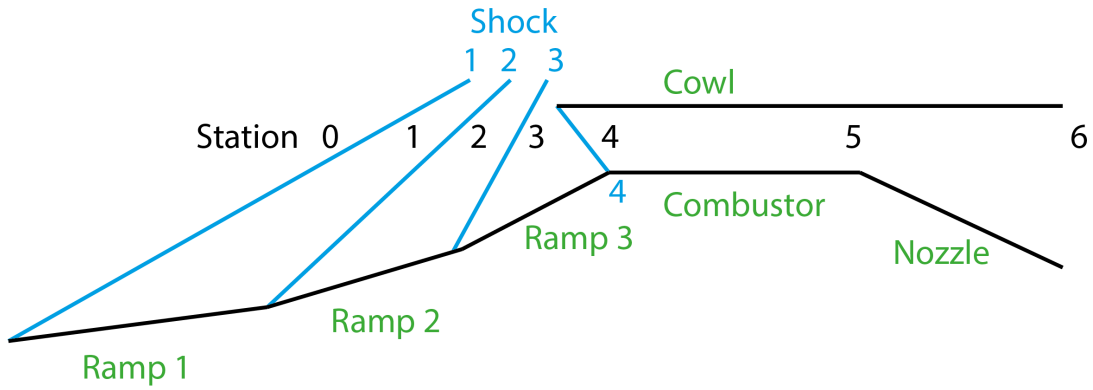

Figure D.3.: Scramjet schematic diagram showing naming convention for ramps, stations and shocks. Shock numbers are shown in blue whilst station numbers are shown in black.

Parameter	Value
M_0	10.98
T_0	211.2 K
P_0	1.186 kPa
α	0°

Table D.2.: Scramjet mathematical model free stream parameters

D.1. Scramjet analytical model

Whilst Sancho used CFD to model the scramjet, this work aimed to apply TDLAS to scramjet measurements so CFD was not undertaken. Instead, a mathematical model was developed based on Rankine-Hugoniot equations, Rayleigh flow in the combustor and thermodynamic relations. Figure D.3 shows the naming convention used in the mathematical model for scramjet components, stations and shocks. Table D.2 lists the free stream parameters used for the mathematical model of the scramjet. These are the test gas parameters as listed in table C.6. The dynamic pressure q_0 for this condition is 48.4 kPa when calculated using:

$$q_0 = \frac{1}{2} p_0 \gamma M_0^2 \tag{D.1}$$

The fuel injection point was on the second inlet ramp 125 mm upstream of third ramp. The mass flow of hydrogen through the injectors was calculated using the data and formula given in Table 5.4 of reference [141]. The mass flow $\dot{m}_f$ was:

$$\dot{m}_f \approx 0.58 C_d A P_f \sqrt{\frac{\gamma_f}{R_f T_f}} \tag{D.2}$$

where C_d is the injector discharge coefficient, A is the injector area, P_f is the fuel stagnation pressure, γ_f is the ratio of specific heats for gaseous hydrogen, R_f is the gas constant for hydrogen, and T_f is the fuel stagnation temperature. Data in reference [156] was used to model the specific heat and ratio

Table D.3.: Fuel parameters used for scramjet mathematical model

Parameter	Value
T_f	298 K
A	15.7 mm^2
C_d	0.5
H_{PR}	120 MJkg^{-1}
R_f	4124 JK^{-1}kg^{-1}
$\frac{m_f}{m_{air\ Stoich}}$	0.0291
P_f	$0.5 - 1.5$ MPa
ϕ	$0.5 - 1.0$

Table D.4.: Inlet ramp and cowl angles with associated shock angles

Component	Ramp Angle	Shock Angle
1^{st} ramp	$4.31°$	$12.76°$
2^{nd} ramp	$9.30°$	$19.26°$
3^{rd} ramp	$14.69°$	$26.09°$
Cowl	$0°$	$23.64°$

of specific heats for hydrogen gas.

Table D.3 lists the parameters used to model the gaseous hydrogen fuel. The temperature in the laboratory was approximately 298 K for all tests. The hydrogen stagnation pressure was set to specific values between 0.5 MPa and 1.5 MPa to align with the tests in reference [141]. All other parameters in table D.3 were selected to align with those in reference [141]. Oblique shock relations were used to calculate the flow conditions on each ramp of the inlet. At the inlet exit, a cowl shock turns the flow to enter the combustor. Table D.4 lists the inlet ramp and cowl angles with associated calculated shock angles at the free stream conditions listed in table D.2. Table D.5 lists the flow properties at each station of the inlet. The flow Mach number decreases from a free stream value of approximately 11.0 to 6.6 at station 3. The flow enthalpy at the inlet is approximately 5.3 MJkg^{-1} whilst the flow speed falls from 3.2 kms^{-1} to 3.07 kms^{-1} prior to the cowl shock. Static temperature and pressure prior to the cowl shock are ≈ 550 K and 24.4 kPa respectively whilst the flow density is 155 gm^{-3} there. Table D.6 lists the flow properties at station 4 assuming no combustion until that point. This assumption is reasonable considering that the spontaneous ignition temperature for gaseous hydrogen in air is above $500°$C [166].[1]

The flow Mach number at station 4 is 4.29 whilst the static temperature and pressure increase to 1130 K and 164 kPa respectively. To compare these parameters with a previous study, Jachimowski [167] stated that a scramjet has typical initial combustor conditions of Mach 8, static temperature 670 K, static pressure 0.5 atm and flow speed 2.09 kms^{-1}. Jachimowski's conditions are enveloped

[1] Although reference [166] cites an experiment where auto-ignition occurred when high pressure hydrogen was admitted to a shock tube filled with air if the shock wave Mach number exceeded 2.8 at a temperature of 575 K.

Table D.5.: Calculated parameters at each inlet station

Parameter	Station			
	0	1	2	3
M_i	10.98	9.21	7.75	6.59
T_i (K)	211.2	295.0	408.1	547.2
P_i (kPa)	1.186	3.402	9.504	24.407
γ_i	1.4012	1.4001	1.3946	1.3817
T_{T_i} (K)	5319	5304	5238	5086
P_{T_i} (MPa)	92.77	83.75	78.57	78.081
ρ_i (kgm^{-3})	0.0196	0.0402	0.0812	0.1554
a_i (ms^{-1})	291.4	344.3	404.1	465.8
U_i (ms^{-1})	3200	3172	3130	3071
H_i (MJkg^{-1})	5.333	5.3293	5.314	5.285

Table D.6.: Calculated parameters at scramjet station 4

Parameter	Value
M_4	4.289
T_4	1133.4 K
P_4	164.4 kPa
γ_4	1.3272
T_{T_4}	4544 K
P_{T_4}	45.96 MPa
ρ_4	0.5054 kgm^{-3}
a_4	657.0 ms^{-1}
U_4	2818 ms^{-1}
H_4	5.291 MJkg^{-1}

by those at stations 3 and 4 (after the cowl shock). Thus, the scramjet combustor initial conditions are assumed to be suitable for hydrogen ignition. This appendix provides details of the scramjet combustor mathematical model based on that presented in reference [168]. Figure D.4 is a schematic diagram of the combustor showing the boundary of the thermodynamic model. Air mass flux $\dot{m}_{air}$ and fuel mass flux $\dot{m}_f$ flow into the combustor at station 3. The fuel enthalpy is h_f. A friction force F_r acts at the wall over an area A_w whilst heat flux $\dot{q}$ flows to the wall. Combined mass flux $\dot{m}_{air}+\dot{m}_f$ flows out of the combustor at station 4. The distance along the combustor is non-dimensionalised as $X(x)$:

$$X(x) = \frac{x - x_3}{x_4 - x_3} \tag{D.3}$$

where x_3 and x_4 are combustor inlet and exit positions respectively and x is a position in the combus-

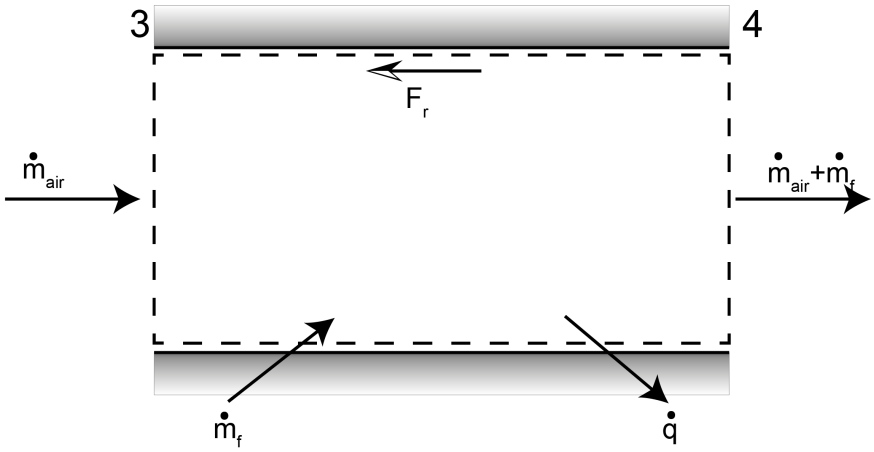

Figure D.4.: Schematic diagram of combustor showing boundary of thermodynamic model

tor. This model assumes:

- the combustion has constant cross-sectional area,
- there is no heat loss to the structure (that is, $\dot{q} = 0$),
- the gas is calorically perfect with constant R_b, c_{p_b} and γ_b.

The combustor inlet mass flux $G = \dot{m}_{air}$ is:

$$G = \rho_3 V_3 \tag{D.4}$$

The combustor inlet momentum flux K is:

$$K = \rho_3 V_3^2 + p_3 \tag{D.5}$$

The combustor inlet stagnation enthalpy h_3 is:

$$h_3 = c_{p_3} T_3 + \frac{1}{2} V_3^2 \tag{D.6}$$

The conditions at state $3b$[2] may be determined while conserving mass, momentum and energy fluxes.

$$\begin{aligned} G &= \rho_{3b} V_{3b} \\ K &= \rho_{3b} V_{3b}^2 + p_{3b} \\ h_t &= c_{p_{3b}} T_{3b} + \frac{1}{2} V_{3b}^2 \end{aligned} \tag{D.7}$$

The velocity in terms of state $3b$ is:

$$V_{3b} = \frac{\gamma_b}{\gamma_b + 1} \left[\frac{K}{G} + \sqrt{\left(\frac{K}{G}\right)^2 - \frac{2h_t\left(\gamma_b^2 - 1\right)}{\gamma_b^2}} \right] \tag{D.8}$$

[2] In terms of burner gas properties

This velocity is used with equations D.7 to obtain the combustor density and static temperature in terms of burner gas properties:

$$\rho_{3b} = G/V_{3b} \tag{D.9}$$

$$T_{3b} = \frac{h_t - V_{3b}^2}{2c_{p_3 b}} \tag{D.10}$$

An empirical correlation is used for combustion efficiency η:

$$\eta\left(x\right) = \eta_{max}\frac{\theta X\left(x\right)}{1+\left(\theta-1\right)X\left(x\right)} \tag{D.11}$$

where η_{max} is the maximum combustion efficiency and θ is a constant derived from curve fits. In this study, $\eta_{max} = 0.8$ and $\theta = 5$. The combustor wall friction is:

$$F_r = \frac{1}{2}C_f\gamma_b p_3 M_3^2 A_w \tag{D.12}$$

where C_f is the coefficient of friction and A_w is the combustor wall area. Friction reduces the combustor exit to entrance static pressure ratio as follows:

$$\frac{p_4}{p_3} = \frac{1+\gamma_b M_3^2\left(1-C_f A_w/2A_3\right)}{1+\gamma_b M_4^2} \tag{D.13}$$

In this study, $A_w/A_3 = 41.4191$ and C_f was assumed to be 0.002. The maximum allowable combustor temperature ratio to avoid inlet unstart $\tau_{b_{max}}$ is:

$$\tau_{b_{max}} = \frac{\left[1+\gamma_b M_3^2\left(1-C_f A_w/2A_3\right)\right]^2}{2\left(\gamma_b+1\right)M_3^2\left[1+\left(\gamma_b-1\right)M_3^2/2\right]} \tag{D.14}$$

Figure D.5 is a plot of $\tau_{b_{max}}$ versus combustor inlet Mach number M_3 for this configuration. At $M_3 = 4.89$ typical of these experiments, combustor inlet temperature T_3 was calculated to be 1133 Kand $\tau_{b_{max}} = 1.839$ making the maximum allowable combustor exit temperature $T_{4_{max}} = 2084$ K. The maximum allowable equivalence ratio ϕ_{max} to avoid inlet unstart is:

$$\phi_{max} = \frac{c_{p_b}T_3}{f_{ST}h_{PR}}\left(\tau_{b_{max}}-1\right) \tag{D.15}$$

where $c_{p_b} = 1510$ Kkg^{-1}K^{-1}, $f_{ST} = 0.0291$ and $h_{PR} = 120$ MJkg^{-1}. Figure D.6 is a plot of ϕ_{max} versus combustor inlet Mach number M_3 for this configuration. At $M_3 = 4.89$ typical of these experiments, $\phi_{max} = 0.411$. The enthalpy at each position along the combustor is given by:

$$h_b\left(x\right) = h_3 + \frac{\eta_b\theta_b x f h_{PR}\phi}{\left[1+\left(\theta_b-1\right)x\right]} \tag{D.16}$$

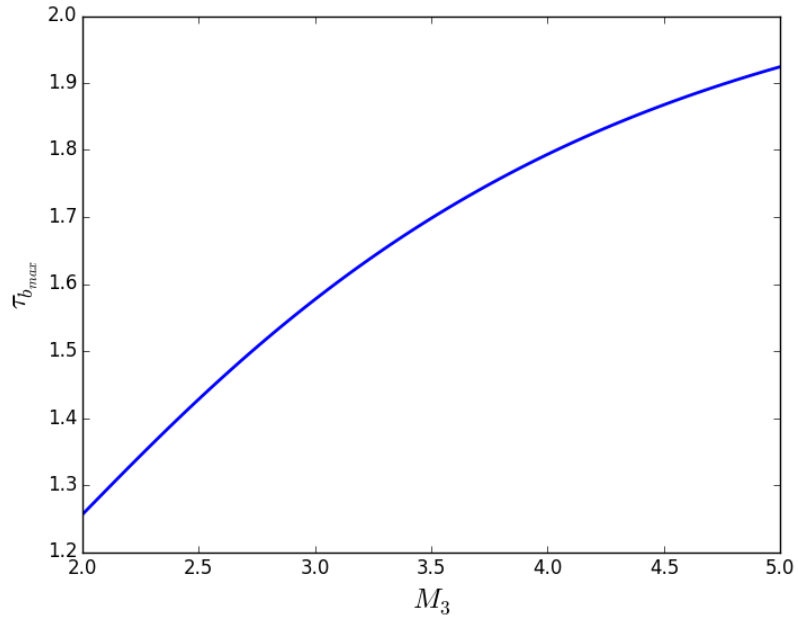

Figure D.5.: Maximum allowable combustor temperature ratio $\tau_{b_{max}}$ versus combustor inlet Mach number M_3 for $C_f = 0.002$, $\gamma_b = 1.238$ and $A_w/A_3 = 41.4191$.

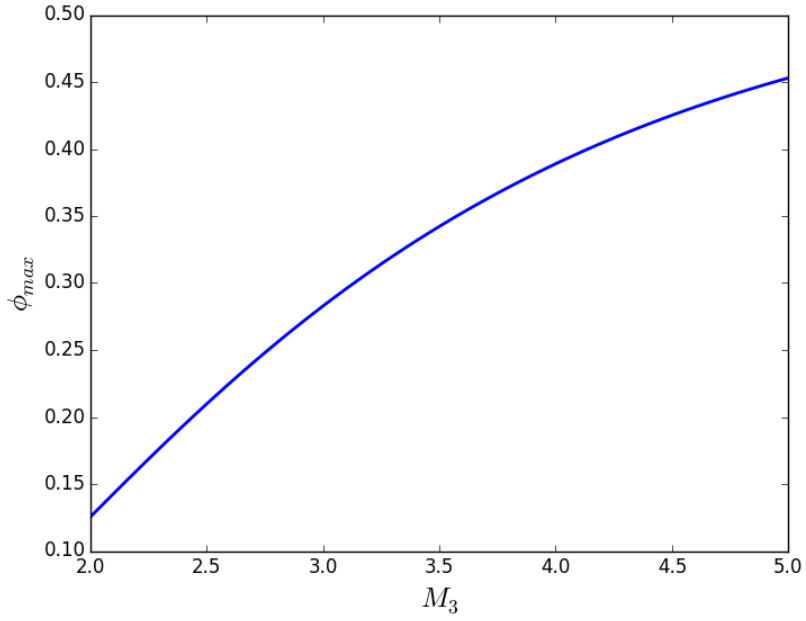

Figure D.6.: Maximum allowable equivalence ratio $\phi_{b_{max}}$ versus combustor inlet Mach number M_3 for $C_f = 0.002$, $\gamma_b = 1.238$, $A_w/A_3 = 41.4191$, $c_{p_b} = 1510$ Jkg^{-1}K^{-1}.

Table D.7.: Parameters used to model the combustor

Parameter	Value
R_b	290.3 Jkg^{-1}K^{-1}
γ_b	1.238
C_{p_b}	1.51 kJkg^{-1}K^{-1}
$\eta_{b_{max}}$	0.8
θ	5.0
C_f	0.2%

D.2. Parameters

The following parameters are used to define the combustion chamber:

- Gas constant (R_b),
- Ratio of specific heats (γ_b),
- Specific heat at constant pressure (c_{p_b}),
- Combustion efficiency (η_b),
- Combustion efficiency curve constant (θ_b),
- Skin friction coefficient (c_{f_b}),
- Ignition point (x_{ig}),
- Equivalence ratio (ϕ),
- Stoichiometric mass ratio (f), and
- Enthalpy of combustion, (h_{PR}).

Table D.7 lists the combustor parameters used in the mathematical model including the gas constant (R_c), ratio of specific heats (γ_c), specific heat at constant pressure (C_{p_c}), combustion efficiency (η_c), combustion efficiency curve constant (r), and skin friction coefficient (C_{f_c}). Tables D.8 and D.9 list the combustor and nozzle exit parameters for various equivalence ratios.

Table D.8.: Calculated combustor exit parameters for various fuel equivalence ratios

	Equivalence Ratio				
Parameter	0	0.25	0.50	0.75	1.0
M_5	4.631	3.593	2.989	2.575	2.261
T_5 (K)	986.3	1564	2146	2734	3328
P_5 (kPa)	147.9	240.0	338.0	442.9	556.4
γ_5	1.238	1.238	1.238	1.238	1.238
C_{p_5} $\left(\text{Jkg}^{-1}\text{K}^{-1}\right)$	1510	1510	1510	1510	1510
T_{T_5} (K)	3503	3966	4429	4891	5354
P_{T_5} (MPa)	108.1	30.39	14.63	9.127	6.600
ρ_5 $\left(\text{kgm}^{-3}\right)$	0.5165	0.5287	0.5424	0.5580	0.5758
a_5 (ms^{-1})	595	750	878	991	1094
U_5 (ms^{-1})	2757	2694	2625	2552	2473
H_5 $\left(\text{MJkg}^{-1}\right)$	5.291	5.989	6.688	7.386	8.084

Table D.9.: Calculated nozzle exit parameters for various fuel equivalence ratios

	Equivalence Ratio				
Parameter	0	0.25	0.50	0.75	1.0
M_6	5.720	4.354	3.606	3.112	2.750
T_6 (K)	716.0	1218	1739	2272	2818
P_6 (kPa)	17.74	30.41	43.86	58.10	73.21
T_{T_6} (K)	3503	3966	4428	4891	5354
P_{T_6} (MPa)	68.59	14.11	5.681	3.134	2.064
ρ_6 $\left(\text{kgm}^{-3}\right)$	0.0854	0.0860	0.0869	0.0881	0.0895
a_6 (ms^{-1})	507	662	790	904	1006
U_6 (ms^{-1})	2901	2880	2850	2812	2768
H_6 $\left(\text{MJkg}^{-1}\right)$	5.291	5.989	6.688	7.386	8.084

E. Optical System Design

As stated in chapter 2, TDLAS has been previously applied to hydrocarbon combustion, shock tubes and scramjets. Water vapour is present as a primary combustion product in scramjets. Its abundance, coupled with the strong line strengths for the vibrational bands in the near infra-red makes it suitable for absorption spectroscopy studies. The flow in a scramjet isolator or combustor is inhomogeneous and highly reactive due to the presence of fuel, air, supersonic flows and high temperatures. The absorbance is difficult to calculate because the line shape and strength vary with temperature, pressure and species concentrations. The experimental design was largely based on the work of Griffiths [1] with refinements imposed by local constraints. Griffiths' work was selected because it involved TDLAS of scramjets, it was well documented and it was conducted at another Australian university.

E.1. Optical path

Two laser channels were used so two mounts were required. The mounts had to be on the same side of the dump tank because the cables connecting them to the laser controller were 1 m long. The front panels of the mounts were square with sides of 88.9 mm. This was the minimum allowable distance between the laser diodes without using turning mirrors. Because of financial constraints, turning mirrors were not procured so the laser diode mounts were arranged to direct target the 8 mm diameter hole in the scramjet. Noting that the beams had to exit through the other 8 mm hole that was 100 mm away on the other side of the scramjet, the laser mounts had to be at least 1 m from the dump tank window or 1730 mm from the scramjet side.

Similarly, the photo-detectors were placed so that the laser beams would strike them after exit from the dump tank. Being smaller than the laser mounts, the detectors were placed between 438 mm and 501 mm from the dump tank window. The mounts and detectors were arranged so that the path length for each channel was equal at 1508 mm through free space, 1366 mm through the dump tank outside o the scramjet and 100 mm inside the scramjet.

The beams were aligned at atmospheric conditions using a laser viewing card held at the mount-side hole in the scramjet. When the beams were incident on that hole, the viewing card was used to confirm that the beam passed through the second hole. The mounts were moved vertically, and in two directions horizontally until the beams passed cleanly through the scramjet. After aligning the beams with the scramjet, the detectors were moved to maximise the signal from each laser.

The beam diameters were 1 mm along their length to ensure that the entire beam fell on the active area of the detector (2.0 mm diameter for Thorlabs FGA21 photodiodes). Beam alignment was verified before each shot by measuring the detector signals.

Any movement of the scramjet would obscure the laser beams. Therefore, the scramjet was physically secured in the dump tank to prevent any movement during a shot. This arrangement was verified using a high-speed camera during an early shot. There was a concern that the dump tank itself would move slightly during a shot due to the recoil of the expansion tube. Fortunately, high-speed video confirmed that the dump tank was steady during these shots.
Figure E.1 is a schematic diagram of the setup. Two laser mounts (Thorlabs model TCLDM9) were aligned so that the beams would cross at the centreline of the scramjet. This allowed clear discrimination of the beams whilst ensuring that they were spatially correlated. The angular alignment also reduced the impact of etalons from the dump tank. The path length within the scramjet was 100 mm.

E.2. Nitrogen purging

A purging system was made using cardboard boxes, 100 mm diameter PVC tubes, PVC wrap and brass piping. The laser mounts were contained within one half of the construction. The laser beams were sent down the PVC tubes which were mounted flush with the dump tank windows. Gaseous dry nitrogen was fed into this structure via brass pipes. The detectors were mounted in the construction on the opposite side of the dump tank.
As regular access was required to adjust the detector positions, a tent-like structure that covered the dump tank window and detectors was used. Gaseous dry nitrogen was fed into the tent near the detectors and a dehumidifier was used to reduce the relative humidity in the tent. Nevertheless, some

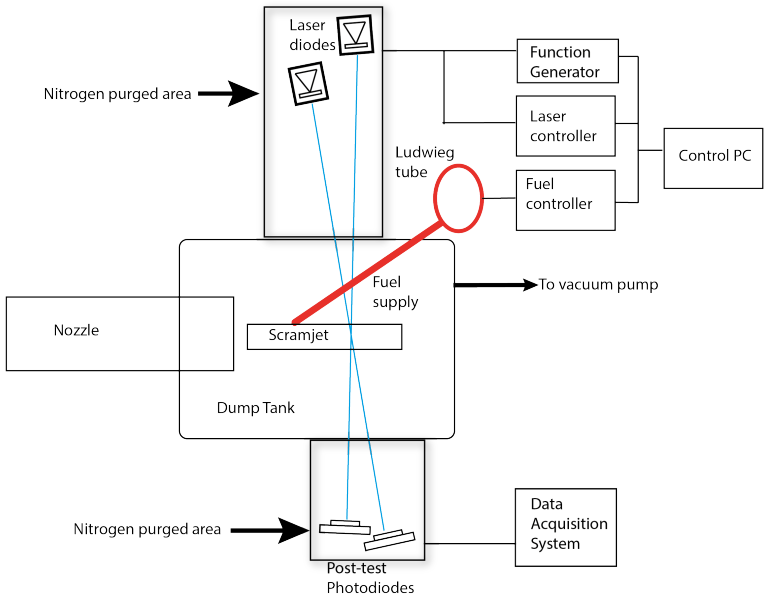

Figure E.1.: Schematic diagram of X3 scramjet TDLAS setup.

water vapour was present at all times (since the relative humidity in the tent was measured at 30-35%). This was verified using direct absorption TDLAS and a similar method to that presented in chapter 5. Any water vapour present in the path was intended to be compensate for during the later analysis.

E.3. Line selection

Griffiths [1] probed transitions at 7181.15578 cm^{-1} and 7179.7521 cm^{-1} in his experiments. Since his work was being used as the basis for these experiments, the laser diodes that were procured operated in this region. As shown in chapter 4, the wavelength range for the diodes was approximately $1391 - 1394$ nm ($7173.6 - 7189.1$ cm^{-1}) depending on the operating temperature. According to *HITRAN* 2012 [57], there are 600 water vapour lines in this range. The methodology of Zhou et al [52] (as modified by Griffiths) was used to select the target features for this study. The selection rules used for this study were:

- Lines must have sufficient strength over the intended temperature range.
- The line pairs should be distinct at atmospheric pressure.
- The line pairs should have similar strength to maximise signal to noise ratio and reduce overlap. Whereas Zhou et al imposed a limit of $0.2 \leq R_{ls} \leq 5$; the limit used for this study was $0.05 \leq R_{ls} \leq 20$ to account for the wide range of line strengths available.
- The line pairs should have sufficient relative sensitivity; that is, change in line ratio with temperature.
- The lines should be free from interference from neighbouring transitions.
- The line wavelengths should be located where the laser diode current is in the range $80-120$ mA so that the laser power is high and the power varies linearly with laser diode current.

Griffiths discussed at length the need to verify the line strength variation with temperature because of issues with *HITRAN* 2000 which was the version he used. He highlighted in a footnote that *HITRAN* 2004 had corrected some of these issues. During the initial stages of experiments for this study, similar issues were found with *HITRAN* 2008 [169]; namely, missing lines and incorrect line strengths. These inaccuracies led to major problems in calibrating the laser diodes against wavelength. The publication of *HITRAN* 2012 [57] included a significant improvement in feature details in the wavelength range of interest and allowed the laser diodes to be accurately calibrated against wavelength as discussed in chapter 4.

E.4. Candidate features

Given the large improvement in the *HITRAN* database over the years since Griffiths' work, the candidate feature line strengths were not independently verified for this study. Table E.1 lists the *HITRAN* properties of candidate water vapour features for these experiments [57]. The feature at

Table E.1.: Properties of candidate water features [57]

Wavenumber (cm^{-1})	Wavelength (nm)	Intensity (cmmol^{-1})	γ_a (cm^{-1})	γ_S (cm^{-1})	E_{low} (cm^{-1})	r
7179.75201	1392.8058	1.802×10^{-22}	0.0456	0.265	1216.1945	0.61
7180.39972	1392.6801	5.608×10^{-22}	0.098	0.500	225.8384	0.69
7181.15578	1392.5335	1.505×10^{-20}	0.1008	0.488	136.7617	0.71
7182.20911	1392.32927	1.541×10^{-21}	0.107	0.375	42.3717	0.76
7182.94962	1392.1857	3.752×10^{-21}	0.097	0.51	142.2785	0.71
7185.596571	1391.6729	1.995×10^{-22}	0.0342	0.371	1045.0583	0.62
7185.596909	1391.6728	5.984×10^{-22}	0.0421	0.195	1045.0577	0.62

7181.15578 cm^{-1} was selected for use because it was strong at atmospheric pressure had strong air- and self-broadening and had a lower state energy of 136.7617 cm^{-1} resulting in a strong temperature sensitivity of line strength. The three lines at 7180.39972 cm^{-1}, 7182.2091 cm^{-1} and 7182.94962 cm^{-1} were not probed because their lower state energies were close to that of the first selected feature. The feature at 7179.752 cm^{-1} which had been probed by Griffiths was not used because its line strength at atmospheric pressure and temperature was very low. This made it difficult to detect the feature during system setup. The doublet at 7185.596 cm^{-1} was selected as the second probe feature because its lower state energy was 1045.058 cm^{-1} given good temperature sensitivity, it was detectable at laboratory conditions and the two features may have been distinguishable at the low pressure expected in the dump tank prior to firing ($80 - 120$ Pa).

E.5. Selected feature properties

Table E.2 lists the *Hitran* 2012 data used for each feature observed in this campaign including wavenumber ν, wavelength λ, intensity at 298 K S, Einstein A coefficient A_0, air-broadened HWHM γ_{air}, self-broadened HWHM γ_{self}, lower state energy E_{low}, coefficient of temperature dependence of air-broadened HWHM r, air-broadened pressure shift of line transition $\delta\nu$, upper state statistical weight g_u and lower state statistical weight g_l.

E.6. Laser diode wavelength calibration

One channel of the laser diode controller controlled diode SN 1636 set to a centre wavelength of 1392.5335 nm. Figure 5.4 shows the wavelength calibration curve for diode SN 1636 at a set TEC temperature of 19.5°C. The current-wavelength calibration equation was:

$$\lambda = 33.606 I_{ld} + 1388.9 \tag{E.1}$$

Table E.2.: Hitran 2012 data for each feature. Source [57]

Parameter	**Feature 1a**	**Feature 1b**	**Feature 2**
ν (cm^{-1})	7185.596571	7185.596909	7181.15578
λ (nm)	1391.6729	1391.6728	1392.5335
S $\left(\text{cm molecule}^{-1}\right)$	1.995×10^{-22}	5.984×10^{-22}	1.505×10^{-20}
A_0 ($\times 10^6$ s^{-1})	16.8	16.8	13.27
γ_{air} (cm^{-1})	0.0342	0.0421	0.1008
γ_{self} (cm^{-1})	0.3710	0.1950	0.4880
E_{low} (cm^{-1})	1045.0583	1045.0577	136.7617
r	0.62	0.62	0.71
$\delta\nu$ ($\text{cm}^{-1}\text{atm}^{-1}$)	-0.016300	-0.013460	-0.012510
g_u	13	39	15
g_l	13	39	21

where λ is in nm and I_{ld} is in A. The laser diode current was 110.259 mA and the TEC temperature was set to 19.5°C. A second channel controlled diode SN 1243 set to a centre wavelength of 1391.6729 nm. Figure 4.19 shows the wavelength calibration curve for diode SN 1243 at a set TEC temperature of 19.5°C. The current-wavelength calibration equation was:

$$\lambda = 33.517 I_{ld} + 1389.0 \tag{E.2}$$

where λ is in nm and I_{ld} is in amperes. The laser diode current and TEC temperature were 79.865 mA and 19.5°C respectively.

E.7. Laser diode power calibration

Figures E.2 and E.3 show the power versus current calibrations for laser diodes SN 1243 and SN 1636 respectively at thermo-electric controller (TEC) temperature of 19.5°C. At this temperature, each laser diode was able to target a feature of interest at an acceptable power level. The third-order polynomial power fit equation for SN 1636 (P_{1636}) was:

$$\begin{aligned} P_{1636} &= -680.4778 i_{LD}^3 + 14.68466 i_{LD}^2 + 61.38655 i_{LD} \\ &\quad -0.93769 \qquad\qquad 0.015 \text{ A} \leq i_{LD} \leq 0.15 \text{ A} \end{aligned} \tag{E.3}$$

and that for SN 1243 (P_{1636}) was:

$$\begin{aligned} P_{1243} &= -1467.01336 i_{LD}^3 + 196.52514 i_{LD}^2 + 66.13125 i_{LD} \\ &\quad -1.054502 \qquad\qquad 0.015 \text{ A} \leq i_{LD} \leq 0.15 \text{ A} \end{aligned} \tag{E.4}$$

The output power was normalised with reference to the power at the centre current. Figure E.4 schematically shows the relationships between laser diode current, wavelength, wavenumber, output

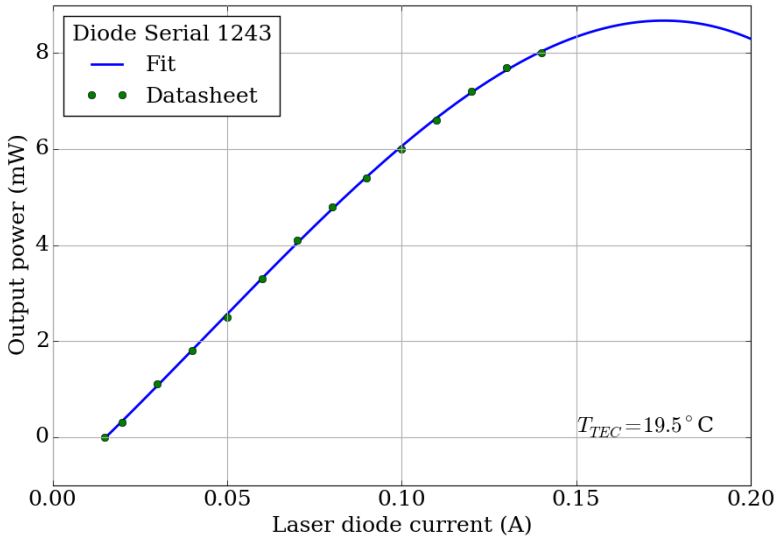

Figure E.2.: Power calibration plot for laser diode SN 1243 at a set TEC temperature of $19.5°$C

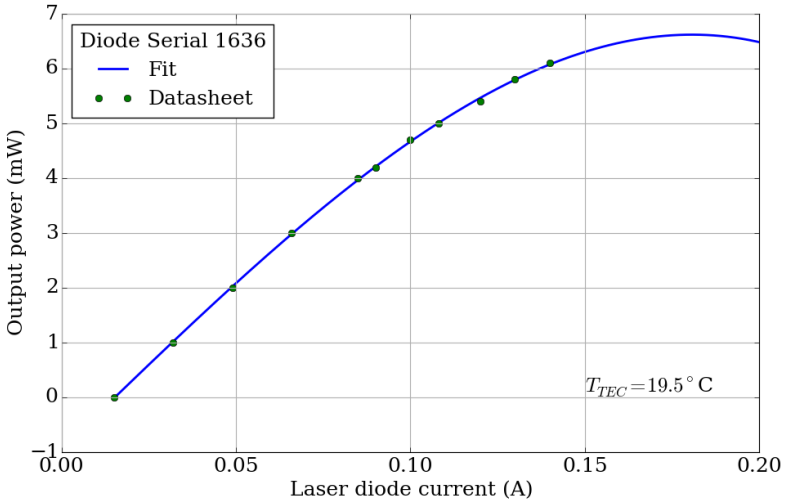

Figure E.3.: Power calibration plot for laser diode SN 1636 at a set TEC temperature of $19.5°$C

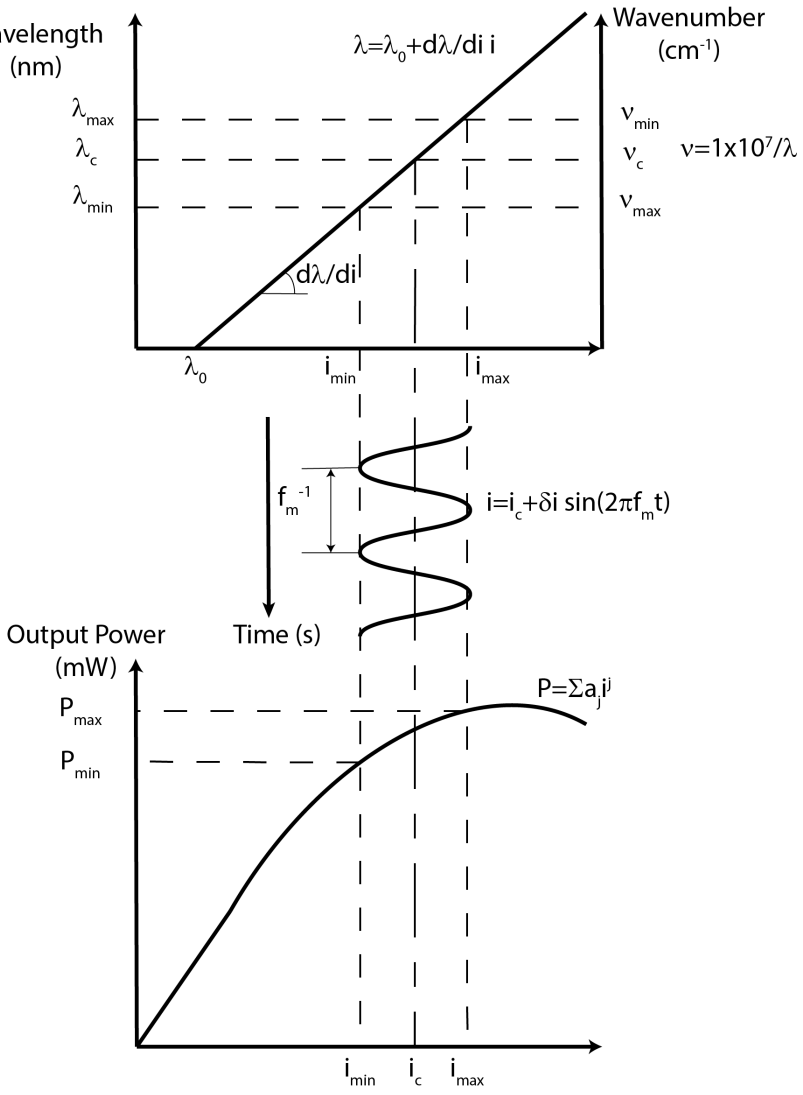

Figure E.4.: Relationships between laser diode parameters

power, time and modulation frequency. As shown in the top graph, wavelength is a linear function of laser diode current and is inversely related to wavenumber. The middle section of the figure depicts the time-based sinusoidal variation of laser diode current. The bottom graph shows the third-order polynomial relationship between output power and laser diode current. Table E.3 summarises the data for each laser diode.

E.8. Laser modulation

The laser diodes were initially planned to be modulated for $2f$-WMS with a sinusoidal modulation at 1 MHz superimposed on a saw-tooth waveform at 100 kHz. These frequencies were chosen to have 10 low amplitude sinusoidal cycles per sawtooth period with 100 sawtooth cycles in the anticipated test time of 1 ms. The intention was to average each ten $2f$-WMS readings to obtain good time discrimination.

The data recording system was able to sample at either 2 Msps, 12 Msps or 60 Msps. Sampling

Table E.3.: Laser diode parameters

Parameter	**Symbol**	**Slot 1**	**Slot 3**
Diode SN		1636	1243
TEC Temperature	T_{TEC}	19.5 °C	19.5 °C
Centre Current	i_{LD_c}	110.259 mA	79.865 mA
Centre Wavelength	λ_c	1392.5335 nm	1391.6729 nm
Centre Wavenumber	ν_c	7181.15578 cm^{-1}	7185.5966 cm^{-1}
Centre Power	P_c	5.0971 mW	4.7333 mW

at 2 Msps would introduce aliasing problems since the sampling rate was two times the modulation frequency. A sampling rate of 60 Msps was chosen to provide good waveform discrimination. As discussed in chapter 4, the laser diode mounts had bias-T radio frequency inputs that were specified to be modulated at frequencies above 100 kHz. During preparation for the experiments, a 100 kHz sawtooth waveform was fed into the bias-T input of a mount and the laser signal was measured using a photo-detector and oscilloscope. There was no modulation detected. After extensive troubleshooting, the modulation signal was found to be not reaching the laser diode. The mount manufacturer eventually advised that the bias-T inputs only worked above 500 kHz and that the response at 100 kHz was reduced by 20 dB.

The $2f$-WMS technique depended critically on having the sawtooth modulation at a sufficiently low frequency to allow multiple sinusoidal cycles during each sawtooth one. With the minimum modulation frequency at 500 kHz, only two sinusoidal cycles would be averaged. While higher sawtooth and sinusoidal frequencies could be used, there were no function generators available to this study that could produce a sawtooth waveform at 1 MHz or higher. Thus, the plan to use $2f$-WMS was abandoned.

Instead, both laser diodes were modulated with large amplitude sinusoidal waveforms. The theory provided in chapter 3 was based on $2f$-WMS with a specific proviso that large modulation amplitudes were not considered since they introduced second-order effects. Therefore, the theoretical basis for these experiments had to be recast. Time constraints meant that this was not done prior to the experiments. Instead, the data was gathered first and the method of analysis was developed afterwards.

A Stanford Research Systems DS340 synthesised function generator was used to generate waveforms for most of the WMS experiments [170]. Sine waveforms could be generated at frequencies up to 15.1 MHz respectively with 1 Hz resolution and ± 25 ppm accuracy. Peak-to-peak voltages from 50 mV to 10 V could be generated into 50Ω loads. The DS340 could be controlled remotely via a GPIB interface. Readers should refer to the DS340 manual [170] for a detailed description of the function generator. The lasers were simultaneously modulated using a sine wave at a frequency near 1.0 MHz and amplitude $0.5 - 2.0$ V peak-to-peak with the signals coupled to the laser mounts via a 50 Ω cable. The laser diode current modulation range was $\pm 5 - 20$ mA around the centre current.

E.9. Signal detection

Thorlabs FGA21 photo diodes were used to detect the laser beams during wavelength modulation spectroscopy measurements. Table 4.6 lists the relevant specifications for the photo diodes. The active area diameter of 2.0 mm was approximately twice as large as the laser beam diameter ensuring that the beam did not overfill the photodiode. The rise time of 66.0 ns was fast enough to accommodate rapid changes induced by the scramjet flow and modulation rate whilst the 5.3 MHz bandwidth was approximately five times the laser modulation frequency. A bias voltage of 0.6 V was placed between the cathode and the circuit ground to lower the photo diode capacitance. The responsivity of 0.9 AW^{-1} was constant at the test wavelengths and was suitable for these experiments.

E.10. Signal amplification

Hobbs [118] invented all-electronic noise cancellation circuits that largely eliminated excess laser intensity noise as a source of measurement error. Griffiths [1] used a log-ratio detector based on Hobbs' design. Figure E.5 is a circuit diagram of the log-ratio detector used by Griffiths. The reference signal strikes photo-detector PD1 whilst the post-test signal strikes PD2. Transistors Q1 and Q2 are a matched bipolar junction transistor (BJT) pair. Griffiths used this design because of its noise suppression and bandwidth. The output voltage of this circuit V_{out} is:

$$V_{out} = -G \ln \left(\frac{i_{ref}}{i_{sig}} - 1 \right) \tag{E.5}$$

where $G = kT/e$ is the circuit gain, i_{ref} and i_{sig} are the currents from the reference and signal photodiodes respectively. Griffiths states that the bandwidth of the feedback loop f_c is:

$$f_c = \frac{R_1 i_{sig}}{2\pi G C_f \left(R_1 + R_2\right)} \left[1 + \exp \left(\frac{V_{out}}{G} \right) \right] \tag{E.6}$$

For this log-ratio amplifier to operate correctly, the two BJTs had to be kept at the same temperature. Griffiths describes a temperature stabilisation circuit that he used. Readers should refer to reference [1] for more details. Griffiths' amplifier design was not suitable for this study because it had inadequate bandwidth for the modulation frequency and rapidly changing flow parameters expected in the expansion tunnel tests. Instead, a commercially available equivalent was sourced to simplify system manufacture whilst ensuring that calibrated results could be obtained.

The photo-diode signals were amplified by 160dB range logarithmic converters from Analog Devices (Model AD8304) [171]. The AD8304 converter is temperature compensated and has a maximum bandwidth of 10 MHz [171]. It has eight decades of range $(160$ dB$)$ with a law conformance of 0.1 dB from 1 nA to 1 mA. The converter had an output bandwidth of 10 MHz and a 15 Vms^{-1} slew rate. The high bandwidth and slew rate meant that these converters were suitable for modulation frequencies of 1 MHz or higher. The narrow law conformance and wide current range made these converters suitable for photo-detector applications. The current of a biased photo-diode (I_{PD}) is

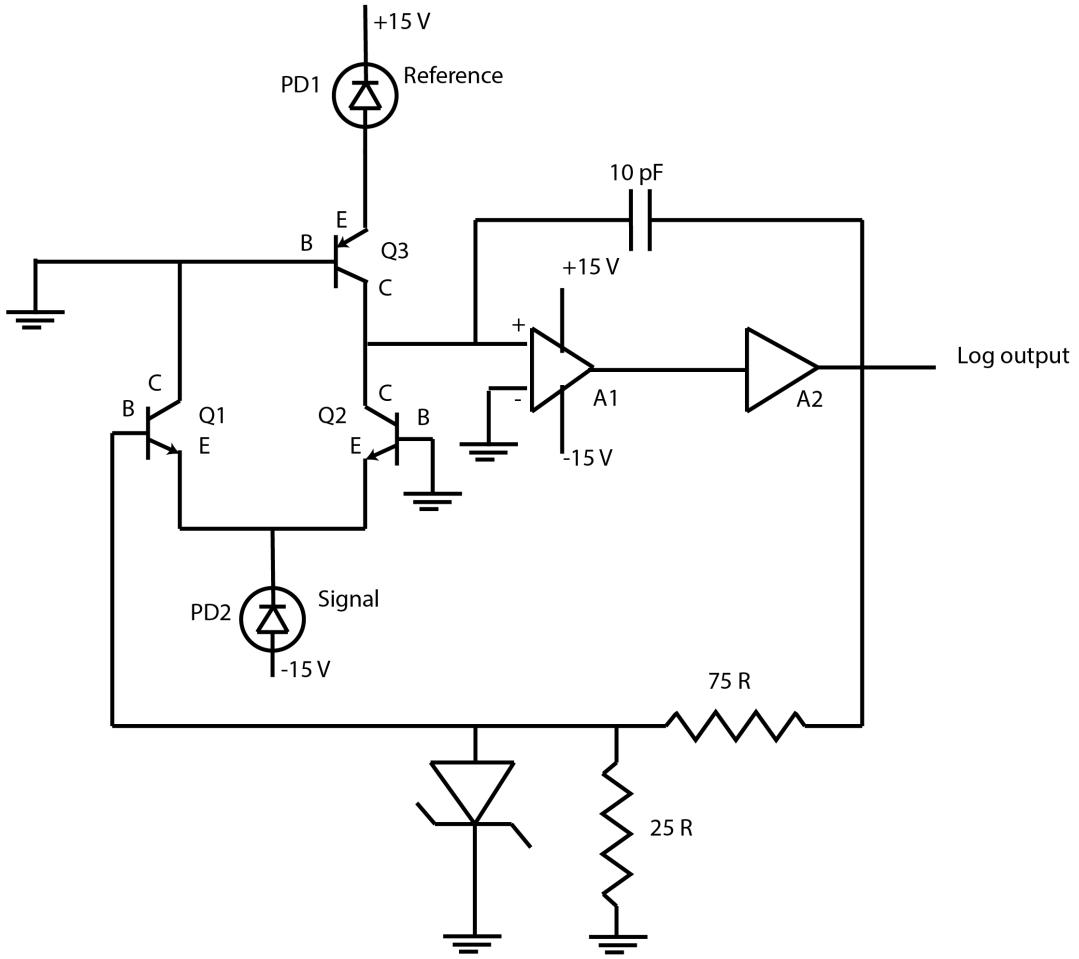

Figure E.5.: Circuit diagram of Griffith's log-ratio detector (less temperature stabilisation and power supply). Adapted from [1]

related to the optical power incident on it (P_{OPT}) by the responsivity (ρ):

$$I_{PD} = \rho P_{OPT} \tag{E.7}$$

As stated above, the Thorlabs FGA-21 photo-diode responsivity was 0.9 AW^{-1} at the wavelengths used for these experiments. The intermediate output voltage of the AD8304 (V_{LOG}) is related to the input current (I_{PD}) by [171]:

$$V_{LOG} = V_Y \log_{10}(I_{PD}/I_Z) \tag{E.8}$$

where V_Y is called the slope voltage and I_Z is called the intercept. For the AD8304, V_Y is 200 mV/decade $(10$ mV/dB$)$ and the I_Z is 100 pA which corresponds to an equivalent incident power of 110 pW for a responsivity of 0.9 AW^{-1}. Thus, the output voltage is related to the power received by the photo-diode by:

$$V_{LOG} = 0.2\text{V} \log_{10}(P_{OPT}/110\text{ pW}) \tag{E.9}$$

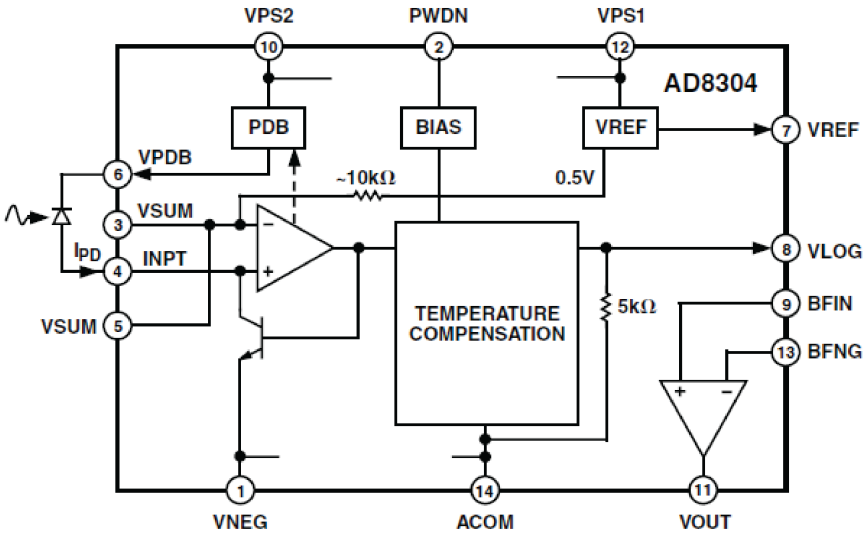

Figure E.6.: Functional block diagram of Analog Devices AD8304 logarithmic converter. Source: [171]

An optical power of 1 mW generates an output voltage of 496 mV. As the author had limited electronic design and manufacture skills, evaluation boards for the converters were purchased from Analog Devices. Figure E.7 is a schematic diagram of the evaluation board. The board was factory set for photo-conductive mode with a buffer gain of unity providing a slope of 10 mV/dB and an intercept of 100 pA. The photo-diode bias was applied from pin BIASER and the current was received at pin INPUT. The intermediate output was taken at pin LOG OUT and a buffer output was taken at BUFFER OUT. A voltage regulator as shown in figure E.8 was designed to provide 5 V of regulated

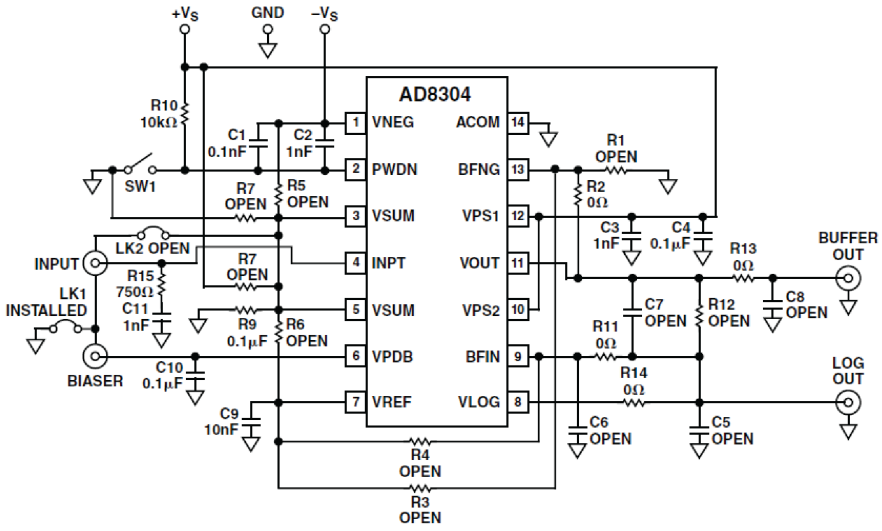

Figure E.7.: AD8304 evaluation board schematic [171]

supply to the components. A signal comparator as shown in figure E.9 was locally designed to compare the outputs from two AD8304 evaluation boards. One amplifier of a Texas Instruments LM358 dual operational amplifier is used to compare the two input signals. The LM358 has a unity gain

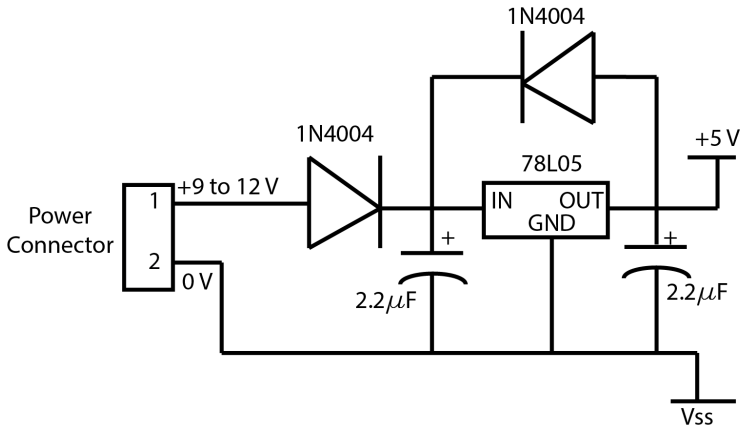

Figure E.8.: Schematic diagram of voltage regulator for ratio amplifier

bandwidth of 0.7 MHZ and a slew rate of 0.3 V/μs making it suitable for the modulation frequency in these experiments [172].The positive input terminal is kept 2.5 V above the negative one to ensure the output has the correct phase. One photo-diode was connected to board A whilst the other photo diode was connected to board B. The buffer outputs were applied as V_{in_A} and V_{in_B} whilst V_{out} is the ratio signal. A rail splitter as shown in figure E.10 was used to provide a 2.5 V mid voltage (V_{mid}) to

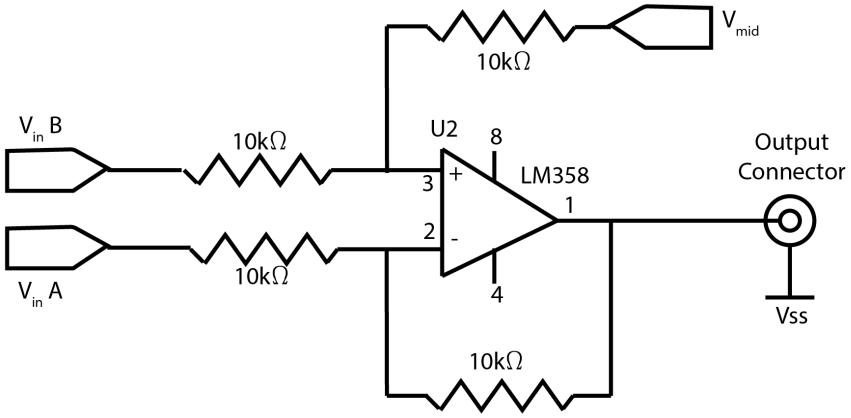

Figure E.9.: Schematic diagram of signal comparator

the positive input terminal. Using this design, the individual photo-detector signals could be recorded together with the ratio of the two signals.

E.11. Data recording

The recording time frames in these experiments extended from 1 μs to 100 ms. On the longer side, fuel injection (refer to appendix G for details) was triggered when the compression tube recoiled due to piston launch. The piston takes approximately 100 ms to travel along the compression tube. A delay of 95 ms was imposed after piston launch before fuel was injected into the scramjet.

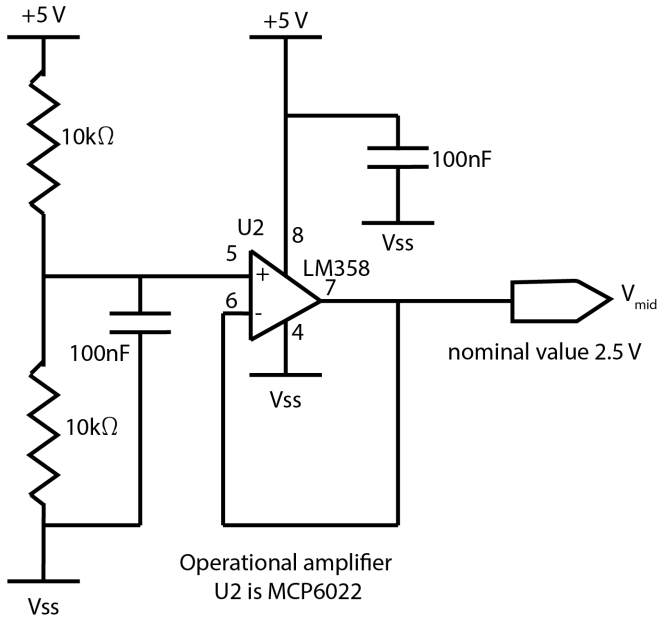

Figure E.10.: Schematic diagram of rail splitter

As the piston reached the primary diaphragm, the compression tube pressure rise triggered recording of the tunnel and scramjet pressure traces. The scramjet flow initiated approximately 20 ms after pressure rise at the compression tube PCB. The test time at the TDLAS test point was 1 ms whilst the modulation frequency was 1 MHz and the TDLAS sample rate was 60 Msps. This five-order of magnitude range of timing meant that detailed consideration had to be given to the data recording methodology. A National Instruments embedded system was used to record data using three time bases. The pre-existing LabVIEW program was modified extensively to include a third time base plus to incorporate a PXI-5105 digital oscilloscope which had not previously been used on X3.

The first time base sampled pressures in the expansion tunnel and scramjet recording 34 channels at 1 Msps. Recording was triggered by a rise on the pressure sensor at the primary diaphragm station and lasted for 35 ms. The flow arrived at the scramjet approximately 20 ms after start. The second time base was used for the fuel injection system. It was triggered by recoil of the tunnel when the piston launched and sampled at 10 ksps. One second of data for six channels was recorded with fuel injection occurring 95 ms after trigger. The third time base was used for the TDLAS system. A National Instruments PXI-5105 Digital Oscilloscope [173] sampled up to eight channels simultaneously with 12-bit resolution and 24 Msps or 60 Msps sampling rates. It had 512 MB of internal memory allowing it to record up to $400,000$ samples per channel. Recording was triggered by a rise in pressure at the leading edge of the scramjet. Since this data had not previously been used to trigger recordings, it is now discussed in detail.

After examining data from previous researchers, it was found that the scramjet leading edge pressure rose when gas in the acceleration tube began to flow through the scramjet as shown in figure E.11. During pre-test time, the scramjet pressure was the same as the dump tank pressure ($80-120$ Pa). The initial pressure rise reached approximately 13 kPa during the flow establishment time before reducing to the test pressure of $3-5$ kPa. During test, the scramjet inlet static pressure is relatively constant.

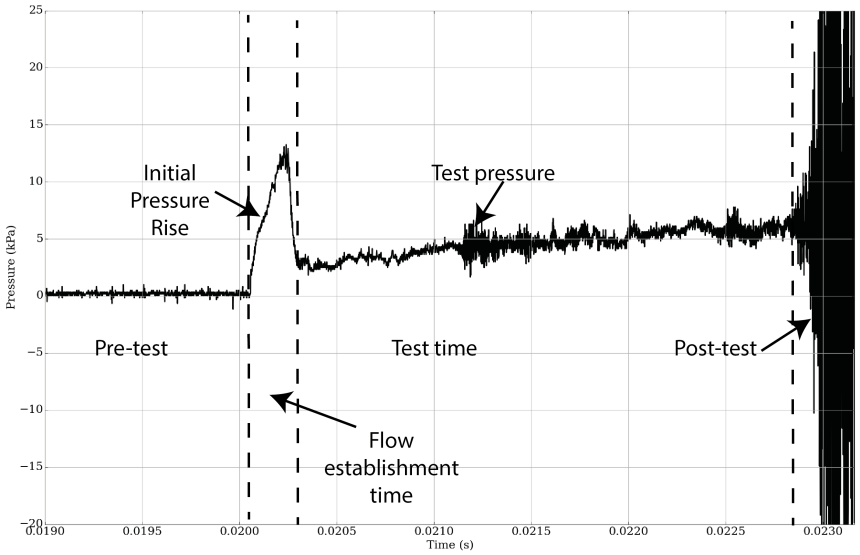

Figure E.11.: Scramjet leading edge pressure trace

Table E.4.: Databox measurement parameters

Parameter	Expansion Tube	Fuel System	TDLAS
Sampling Frequency	1 MHz	10 kHz	60 MHz
Number of Samples	$40,000$	$10,000$	$240,000$
Pretrigger Samples	5000	1000	$200,000$
Trigger Level	500 kPa	0.1 V	0.1 V
Trigger Source	ST1	RB0	TR01
Trigger Type	Rising	Falling	Rising

The test time ends when strong pressure fluctuations occur due to shock-processed test gas impinge on the scramjet. The flow took between 177 ± 6 μs and 236 ± 17 μs to traverse from the scramjet leading edge to the TDLAS test section depending on the exact fuel and test gas mixture. This pressure rise indicated that the driver gas had reached the scramjet; thus, the test samples were prior to the pressure rise. The TDLAS recording time was 3.33 ms prior to, and 0.67 ms after triggering. A issue that arose due to using three different time bases and trigger sources was timing coordination across the three sampling frequencies. The scramjet leading edge pressure (Transducer TR01) was measured in each time base to provide this coordination. Table E.4 lists typical measurement parameters for the NI Databox.

E.12. Signal extraction

Significant effort was required to develop a process to extract spectroscopic information from the received laser signals. This was due to the short test time, rapidly changing test conditions and the method used to modulate the lasers. The signal extraction technique is described here using shot x3s469 as an example. This shot involved fuel being injected into air test gas. Figure E.12 shows the

raw photo detector signal for channel 1.

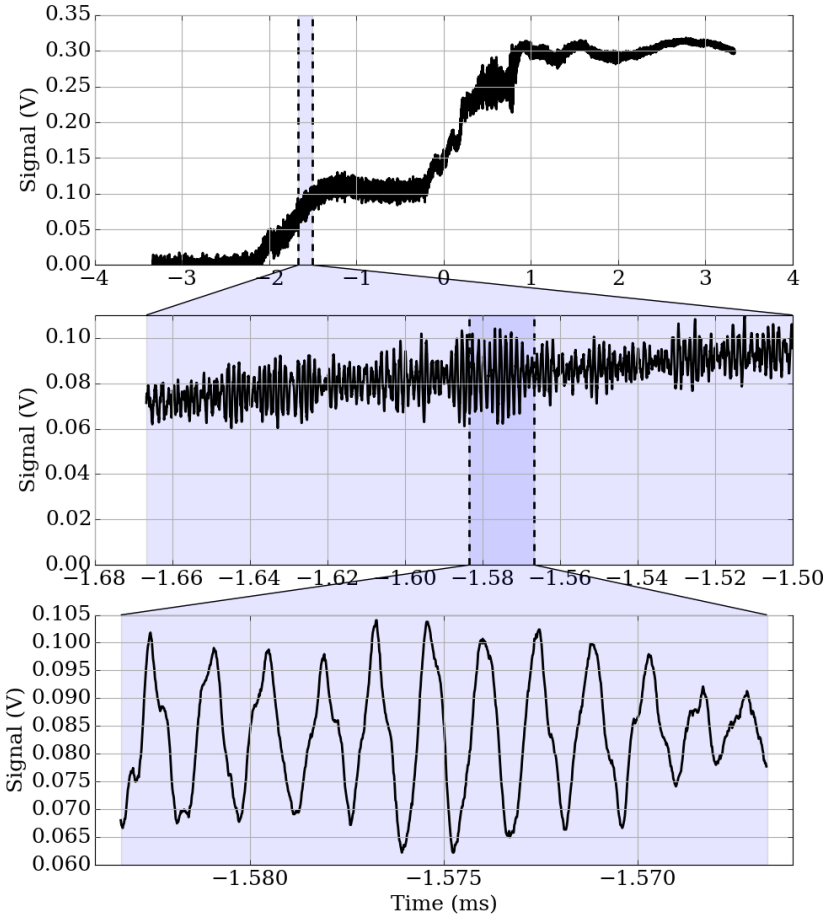

Figure E.12.: Shot x3s469 channel 1 laser signal. The upper figure shows the entire signal of 400,000 samples recorded in approximately 7 ms. The centre figure is an expanded view of 10,000 samples during the test time from 1.65 ms to 1.5 ms prior to trigger. The lower figure shows a further expansion of the 1000 data points near 1.575 ms prior to trigger.

E.12.1. Frequency extraction

A high fidelity (N=65536) Fast Fourier Transform (FFT) was applied to each photo-detector signal to extract the modulation frequency. This was done because the indicated modulation frequency on the signal generator was not always correct. Figure E.13 shows the spectral plot for channel 2 of shot x3s469. There are two primary frequencies at 999789 Hz and 2000489 Hz. The lasers were being modulated at 1 MHz making the lower observed frequency due to the function generator modulation of the laser power. The higher observed frequency was present in almost all observed signals. It is believed to be due to coupling between the function generator signal, the thermo-electric cooler and the spectroscopic feature. The sinusoidal laser current modulation was centred near the feature centreline; thus, the feature maximum was traversed twice in each modulation cycle. As the

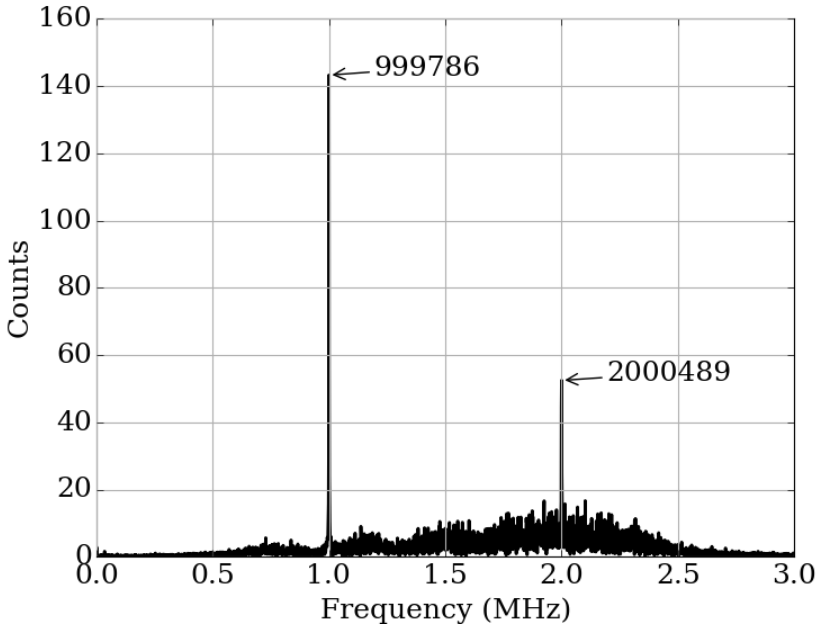

Figure E.13.: Frequency spectrum for shot x3s469 channel 2 signal

laser diode was modulated, the output power changed. The thermo-electric cooler was designed to maintain the diode at a constant temperature. An Analog Devices AD590 thermistor was used to measure the TEC temperature. The device datasheet stated that the thermistor time constant when used with aluminium plate was 0.1 s. The thermistor is powered by direct current which is converter from 50 Hz AC power by a rectifier in the Thorlabs PRO8000 laser controller. Coupling between the rectifier and thermistor time constant are suspected of inducing a 500 Hz shift in the observed signal.

E.12.1.1. Lock-in amplifier

A software lock-in amplifier was locally developed to extract the TDLAS signal from the received signals. Appendix A briefly discusses lock-in amplifiers. The advantages of using a software lock-in amplifier included accurately setting the frequency, simply varying the lock-in phase to maximise the output signal, and the ability to vary the packet size of signals. A selected sample of the photo-detector signal was then processed using a software lock-in amplifier at twice the measured frequency and at a phase delay that optimised the amplifier output. Typically, 10-20 modulation cycles (corresponding to $10 - 20$ μs packet length) were used for each optimisation. For instance, figure E.14 shows how the maximum lock-in amplifier output amplitude varied with phase angle for shot x3s469 channel 1 between -2.0 ms and -1.67 ms prior to trigger. The phase angle that maximised the lock-in amplifier output in this case was 1.22π.

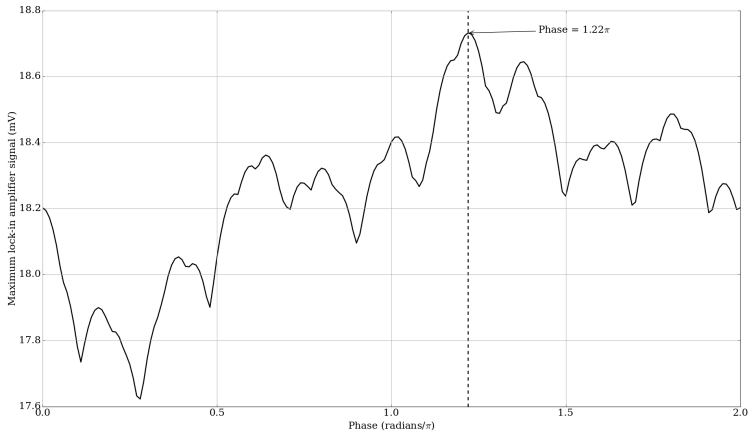

Figure E.14.: Lock-in amplifier maximum signal output variation with phase angle for shot x3s469 between times of 2.0 ms and 1.67 ms prior to trigger

F. Scramjet tests

In this appendix, three different experimental conditions are discussed: air as a test gas without fuel injection, nitrogen as a test gas with fuel injection, and air as a test gas with fuel injection.

F.1. Air as a test gas without fuel injection

The first set of experiments used laboratory air as a test gas without any fuel injection. These experiments were primarily designed to verify the tunnel modifications whilst establishing the correct operating conditions of the TDLAS system. The water vapour content in the test gas was due to humidity in the laboratory. The laboratory temperature varied between $19°\text{C}$ and $24°\text{C}$ across the experimental campaign. The maximum water vapour concentration in the laboratory air ranged from 2.1% to 2.9% in this temperature range for a relative humidity of 100%. According to a thermodynamic model of the scramjet, the static pressure and temperature at the TDLAS test section were of the order of $10 - 30$ kPa and 700 K respectively for shots with air as a test gas. Figure F.1 shows the modelled absorbance through the scramjet flow at the TDLAS wavenumber range for these conditions. The absorbance by the feature at 7181.15578 cm^{-1} is approximately 14 times that of the feature at 7185.599 cm^{-1} but is still less than 0.25%. This small amount of absorption was expected to be very difficult to detect using TDLAS. Figure F.2 shows static pressures at the TDLAS test area for air test gas without hydrogen injection. Each test could be broken into four time segments: pre-test,

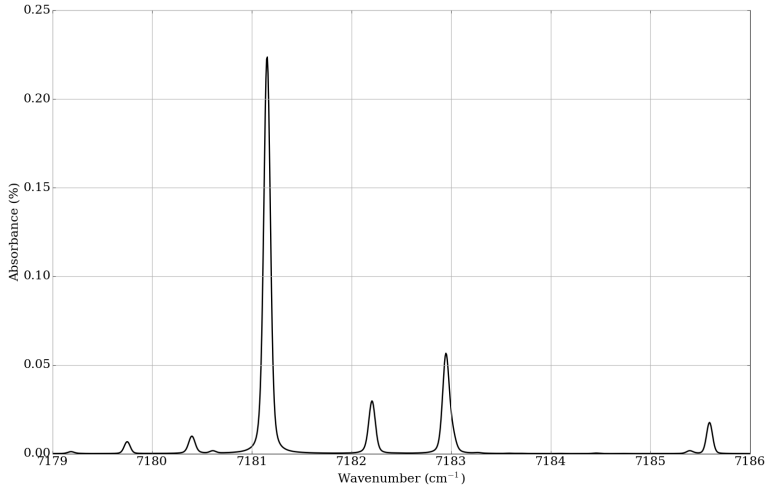

Figure F.1.: Absorbance through scramjet flow with air test gas and no fuel injection. The test section temperature is 700 K, pressure is 20 kPa and water vapour concentration is 3%.

flow establishment, test and post-test. Pre-test time occurs before the acceleration tube gas reaches the model. Flow establishment time is when the acceleration gas impacts the model and relatively steady state conditions are established. Flow establishment typically took 0.5 ms. Test time lasted for $1-2$ ms after the flow established and before contaminated gas arrived at the model. During post-test, large flow variations were observed as the shock-processed test gas and driver gas flowed through the scramjet. The static pressure at the test section with air as a test gas was $15-21$ kPa. Based on the

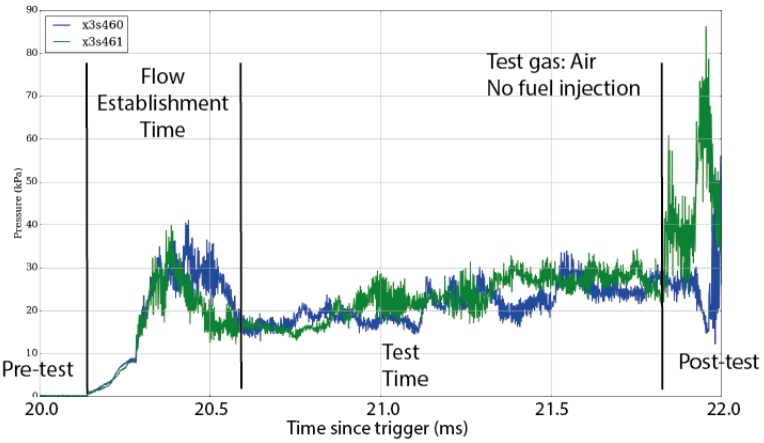

Figure F.2.: Measured static pressure at TDLAS test area for air test gas without fuel injection. Data has been filtered using a Butterworth filter of length 5 and with a cut-off frequency of 5% of the Nyquist frequency.

measured pressure at the test section, the peak absorption for the feature at 7181.15578 cm^{-1} may have varied from 0.07% at a static pressure of 10 kPa to 0.22% at 30 kPa pressure. Provided the flow temperature was constant, the strength ratio for the two target features would also be constant. As Sancho found from CFD modelling of the scramjet [141], temperature was unlikely to be constant across the scramjet. Thus, variations in the feature strength ratios may be expected both spatially and as test time progresses.

F.2. Nitrogen test gas with fuel injection

The second set of conditions used nitrogen as a test gas with gaseous hydrogen fuel injected into the scramjet. The expected result was no absorption of the TDLAS signals because there was no combustion and, therefore, no water vapour in the scramjet exhaust. The test section pressure was expected to rise above that for air as a test gas without injection because of the gaseous hydrogen being injected into the flow.

This test condition was undertaken to verify that TDLAS did not falsely detect water vapour. Theoretically, the TDLAS signals should be constant and show zero absorption throughout the pre-test and test time when nitrogen is used as a test gas. Practically, absorption due to humidity in the laboratory

air could be observed if the laser paths are not correctly purged with dry nitrogen gas. Also, residual water vapour in the acceleration tube after evacuation may cause combustion, particularly during flow establishment and at the start of the test time.

Two experiments were conducted with nitrogen as a test gas with gaseous hydrogen fuel injection. The injection pressure was 1.0 MPa for one shot (x3s463) and 800 kPa for the other (x3s464). Figure F.3 shows the combustor exit pressure at transducer TR27 for the latter shot. In this figure, the trigger was a pressure rise at the primary diaphragm station associated with diaphragm rupture. Flow establishment began at the combustor exit approximately 20 ms after trigger. The pressure was approximately constant at 25 ± 10 kPa during the test time with pressure spikes due to transient shock waves propagating through the combustor. The absence of a pressure rise during the test time indicates that there was no combustion during the test time. From the pressure measurement, the test time was approximately 1.3 ms at the combustor exit. Figure F.4 shows the photo detector signal for

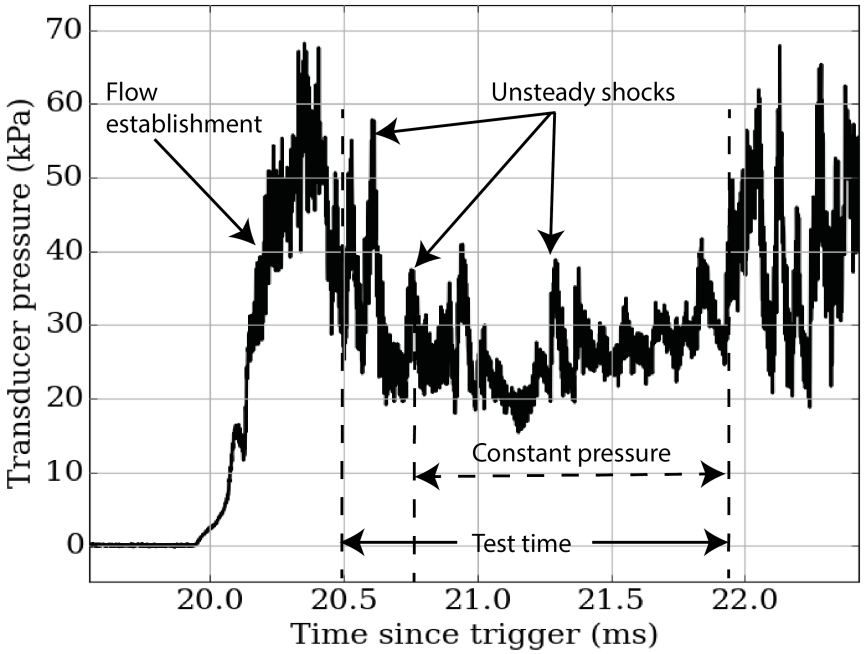

Figure F.3.: Combustor exit pressure versus time since primary diaphragm rupture for nitrogen test gas with 800 kPa hydrogen fuel injection pressure.

channel 1 around the test time for this test case. The trigger for this data was the scramjet leading edge pressure rise associated with the end of test time there. Prior to arrival of the test gas, the TDLAS signal amplitude is large (± 0.3 V) indicating absorption by room temperature water vapour in the dump tank and scramjet. When the nitrogen test gas arrives, the TDLAS amplitude decreases to less than ± 50 mV indicating no absorption by the nitrogen. Figure F.5 shows three levels of increasing detail around the test time. The upper plot contains $45,000$ samples from 0.25 ms before trigger to 0.5 ms after trigger.The centre plot contains more detail for a section of test time between 167 μs and 33 μs prior to trigger. The lower plot shows a further expansion of the signal between 100 μs and 67 μs prior to trigger. According to the TDLAS data, the test time duration at the TDLAS window is 350 ± 50 μs compared with 1.3 ms measured using a pressure transducer at the combustor exit. Table

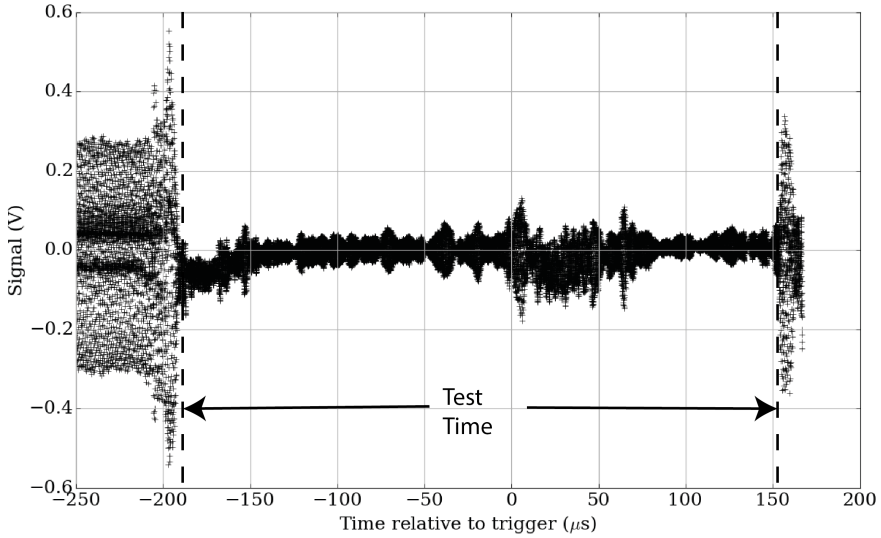

Figure F.4.: Channel 1 photo detector signal near test time for a shot with nitrogen as a test gas with 800 kPa gaseous hydrogen fuel injection pressure.

Table F.1.: Scramjet pressure transit times. Transit time 1 - time between pressure rises at TR01 and TR16. Transit time 2 - time between pressure rises at TR01 and TR27.

Test Gas	**Fuel Pressure** (kPa)	**Transit Time 1** (μs)	**Transit Time 2** (μs)
Air	0	210 ± 6	236 ± 17
Air/Nitrogen	800	152 ± 11	180 ± 6
Air/Nitrogen	1000	161 ± 17	177 ± 6
Air	1600	161 ± 17	206.6
Air	2000	155 ± 17	193 ± 15

F.1 lists the transit times for pressure rises from the scramjet inlet, the centre of the combustor and the combustor exit. When hydrogen was injected, the pressure rise transit time reduced from 236 μs to $177 - 206$ μs due to the sonic speed increasing in hydrogen. The TDLAS signal shows no sign of combustion or increase water vapour concentration during test time for a shot with fuel into nitrogen. This is in stark contrast with the earlier air only shot. Also, the injection of hydrogen into the flow did not affect the TDLAS signals.The gradual rise in laser signal ratio during test time may indicate an increase in dump tank pressure without any coincident change in water vapour concentration. There is a clear difference in TDLAS signals during shots with air as a test gas and those with hydrogen gas injected into nitrogen test gas. This proves the concept that TDLAS may be able to detect temperature and water vapour concentration changes in scramjet exhausts.

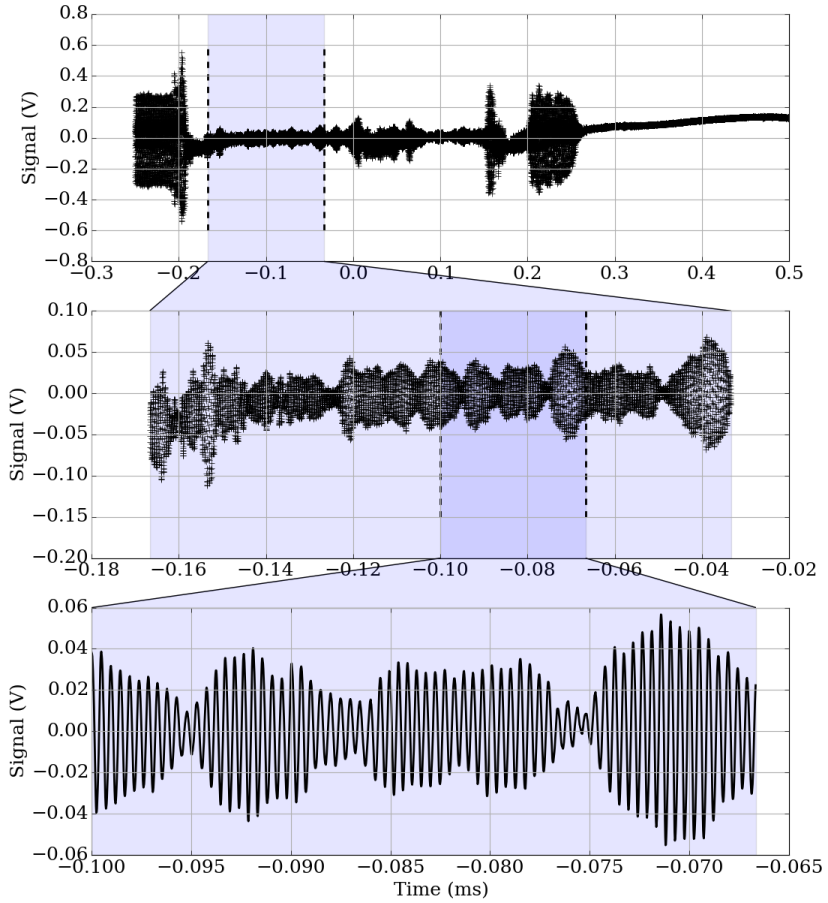

Figure F.5.: Channel 1 photo detector signal near test time for a shot with nitrogen as a test gas with 800 kPa gaseous hydrogen fuel injection pressure.

F.3. Air as a test gas with fuel injection

The final set of experiments used laboratory air as a test gas with gaseous hydrogen fuel injection at four different injection pressures. In these conditions, TDLAS was expected to detect the presence of water vapour in the scramjet exhaust. Appendix G describes the fuel injection methodology and calibration process. The major focus of these experiments was the injection of hydrogen into air with the aim of detecting combustion. Four levels of injection pressure were used: 0.8 MPa, 1.0 MPa, 1.6 MPa and 2.0 MPa. Table F.2 lists the thermodynamic properties at the TDLAS test point for the different test conditions. The saturated vapour pressure of water at 298 K is 3.167 kPa making the partial pressure at 80% relative humidity 2.53 kPa. Assuming complete combustion of hydrogen in air, the molar concentration of water vapour in the scramjet exhaust χ_{H_2O} is related to the equivalence ratio ϕ by:

$$\chi_{H_2O} = \frac{2\phi}{4.76 + \phi} \tag{F.1}$$

Table F.2.: Calculated thermodynamic properties at the TDLAS test point for various test conditions. The water concentration with no fuel injection was calculated assuming a relative humidity of 80% at a temperature of 298 K.

Fuel Pressure (kPa)	Mass Flow Rate (gs^{-1})	ϕ	Static Pressure (kPa)	Static Temperature (K)	Water Concentration ($\%$)
0	0	0	9.3	735	2
800	2.7	0.47	16.1	1250	19
1000	3.3	0.58	17.7	1370	22
1600	5.1	0.91	22.8	1740	32
2000	6.4	1.13	26.4	1980	35

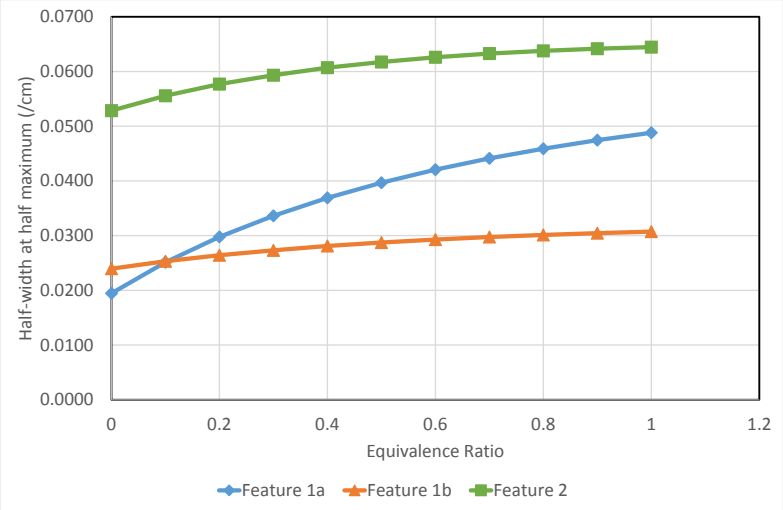

Figure F.6.: Calculated half-widths at half maximum for water features versus equivalence ratio at the TDLAS test point

The partial pressure of water vapour in the exhaust Pp_{H_2O} is related to the static pressure P by:

$$Pp_{H_2O} = \chi_{H_2O} P \tag{F.2}$$

The collision broadened half-width at half maximum for feature i at temperature T (γ_i) is given by:

$$\gamma_i = \left[\chi_{H_2O}\gamma_{\text{self}_i} + (1 - \chi_{H2O})\,\gamma_{\text{air}_i}\right]\left(\frac{T_0}{T}\right)^{r_i} \tag{F.3}$$

where γ_{self_i} and γ_{air_i} are the self- and air-broadened HWHMs for feature i, $T_0 = 296$ K and r_i is the temperature coefficient for feature i. Figure F.6 shows the calculated variation of the HWHMs for the three features used in these experiments versus equivalence ratio.

F.3.1. 0.47 equivalence ratio

Figure F.7 shows static pressures at the TDLAS test area for 800 kPa hydrogen injected into air and nitrogen test gases. The fuel into air data covers four shots whilst the fuel into nitrogen data is from one shot only. All data has been shifted so that the initial pressure rise times coincide. The maximum

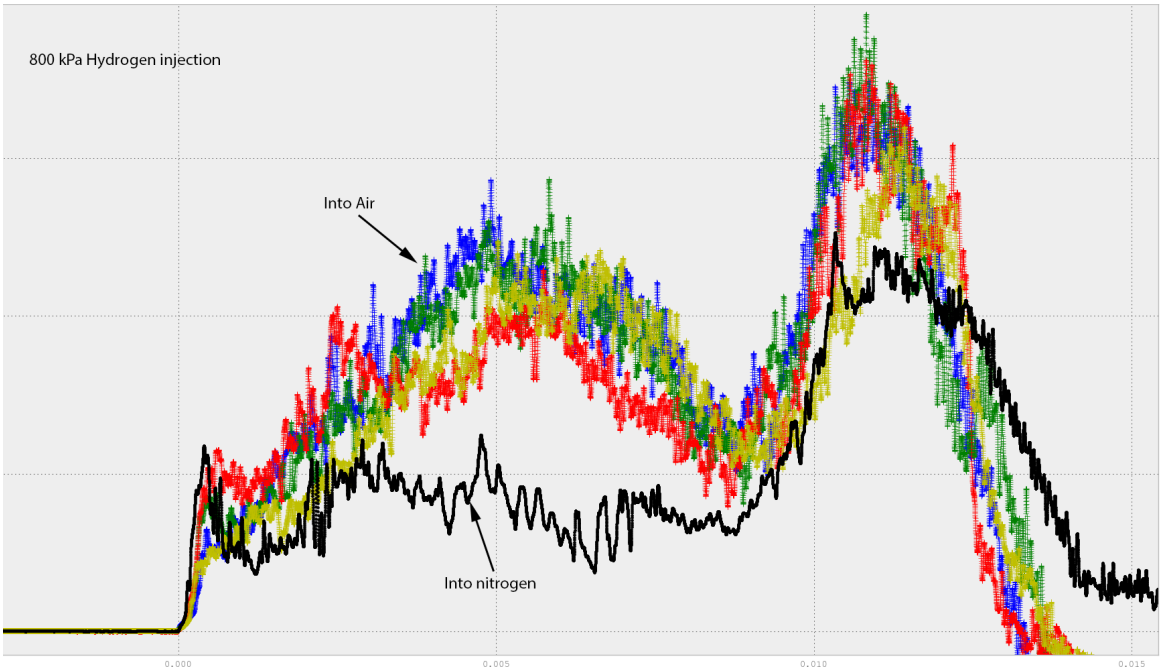

Figure F.7.: Measured static pressure at TDLAS test area for 800 kPa hydrogen injected into air and nitrogen test gases. Data has been filtered using a Butterworth filter of length 5 and with a cut-off frequency of 5% of the Nyquist frequency.

pressure achieved for the fuel into nitrogen shot was 55 ± 30 kPa at 2.88 ms after pressure rise (APR). The pressure then fell to 35 ± 100 kPa at 6.9 ms APR. The pressures in the fuel into air shots increased approximately linearly after the initial pressure rises until they were 115 ± 15 kPa at 5 ms APR. The pressures then decreased linearly to 55 ± 10 kPa at 8.8 ms APR. The pressure rises for the fuel into air shots are indicative of combustion. Unfortunately, the test time was anticipated to be of the order of 1 ms whilst the maximum pressure was reached at 5 ms APR.

Figure F.8 shows the fuel injection pressure trace for this shot. The maximum measured pressure was 525 kPa and the injection time was 226.5 ms. The time base for this measurement was determined by compression tube recoil when the piston was launched. Injection began well before the test time and continued until after the test time.

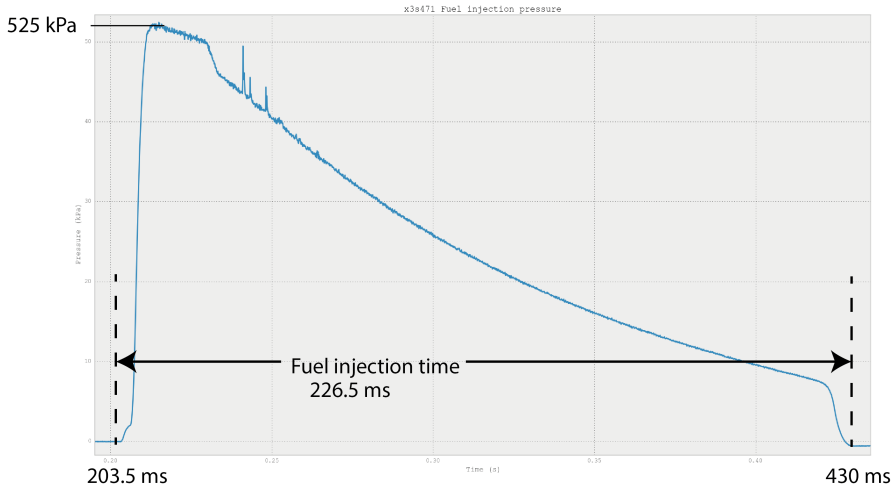

Figure F.8.: Fuel injection pressure trace for shot with fuel injection at an equivalence ratio of 0.47.

G. Fuel system and calibration

The fuel system and triggering system is described in detail in Sancho's thesis [141]. Figure G.1 is a schematic diagram of the fuel system showing the major pneumatic and hydraulic components [141]. The system was designed to deliver 25 gs^{-1} of H_2 to the fuel port. To achieve this, a 12 m long by 18 mm internal diameter Ludwieg tube was used to hold pressurised gas and an ASCO SCB223A10NV stainless steel solenoid valve controlled the flow of fuel to the scramjet. This valve had a 20 ms opening and closing time [141]. Considering that typically 15 ms passed between the pressure rises at sensor ST1 and arrival of the test gas at the scramjet, the fuel solenoid valve had to be triggered before the primary diaphragm burst. The fuel trigger system comprised a Recoil Trigger Box, a Fuel Solenoid Control Trigger Box, a Fuel Solenoid Trigger and the solenoid valve. Figure G.2 is a schematic diagram of the system showing the interfaces between the components. The Fuel Solenoid Control Box was armed via an RS232 interface from the NI databox. This allowed the user to set the delay time and trigger level prior to an experiment. When the expansion tube piston was launched, the tunnel upstream of the recoil damper recoiled. Upon recoil, a photodiode in the Recoil Trigger Box was exposed to light and sent a $3-4$ VDC trigger signal to the Fuel Solenoid Control

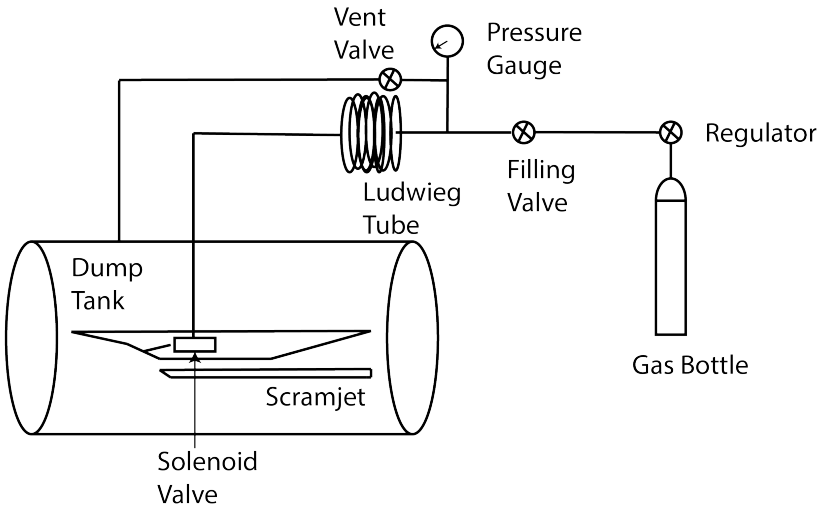

Figure G.1.: Schematic diagram of fuel system.

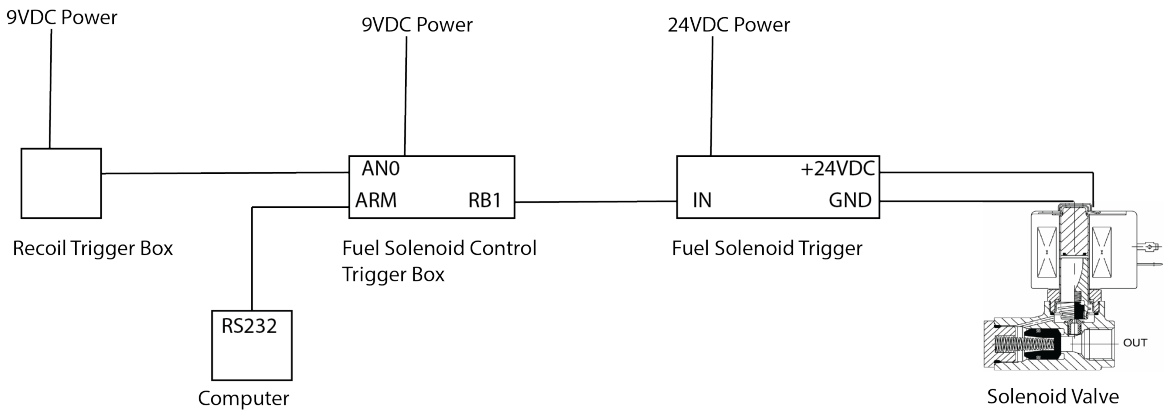

Figure G.2.: Fuel control system schematic

Trigger Box input. When the trigger box was armed and received the input signal, it waited for the programmed delay time then sent a $3-4$ VDC signal to the Fuel Solenoid Trigger. This, in turn, sent a 24 VDC signal to open the fuel solenoid valve. After the pre-programmed time, the fuel solenoid control trigger box signal fell to 0 VDC. On receiving this signal, the solenoid valve trigger removed the 24 VDC signal and closed the fuel solenoid. The fuel injection point was on the second inlet ramp 125 mm upstream of third ramp. The mass flow of hydrogen through the injectors was calculated using the data and formula given in Table 5.4 of reference [141]. The mass flow $\dot{m}_f$ was:

$$\dot{m}_f \approx 0.58 C_d A P_f \sqrt{\frac{\gamma_f}{R_f T_f}} \tag{G.1}$$

where C_d is the injector discharge coefficient, A is the injector area, P_f is the fuel stagnation pressure, γ_f is the ratio of specific heats for gaseous hydrogen, R_f is the gas constant for hydrogen, and T_f is the fuel stagnation temperature. Data in reference [156] was used to model the specific heat and ratio of specific heats for hydrogen gas.

Figure G.3 shows the plotted data and a trend line fitted using linear regression. The correlation coefficient of 99.73% indicates strong correlation between the data and trend line. The mass of air injected m_{air} in grams is related to the air fill pressure p_{air} in kPa by:

$$m_{air} = 0.0355 p_{air} - 4.7276 \tag{G.2}$$

The fuel calibration was repeated using hydrogen gas. To avert risk of explosion, hydrogen was injected into the scramjet when the dump tank pressure was approximately 120 Pa. After each test, the dump tank was vented with laboratory air until the outside of the explosive limits for hydrogen in air. The Lower Explosive Limit (LEL) and Upper Explosive Limit (UEL) for hydrogen are 4.0% and 75.0% respectively [174].

Figure G.4 shows the integrated mass flow of hydrogen and fitted trend line. The mass of hydrogen injected m_{H_2} in grams is related to the hydrogen fill pressure p_{H_2} in MPa by:

$$m_{H_2} = 0.7 p_{H_2} + 0.0167 \tag{G.3}$$

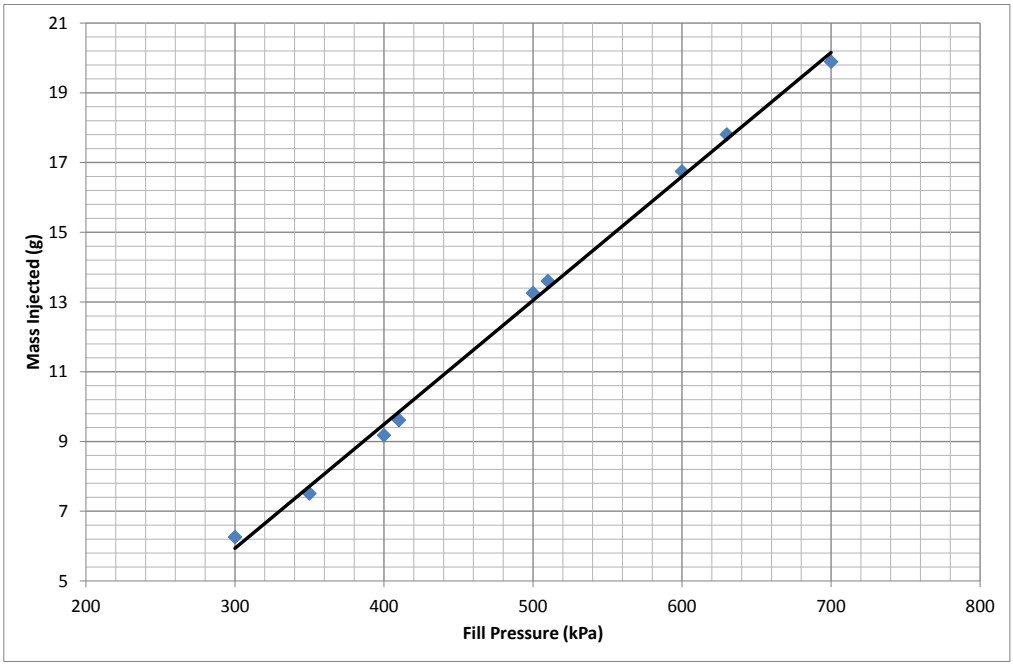

Figure G.3.: Fuel system calibration using instrument air

The correlation for hydrogen was similar to that for instrument air. The mass of hydrogen injected at each fill pressure was divided by the measured injection time to obtain the mass flow rate of hydrogen as a function of fill pressure.

$$\dot{m}_{H_2} = 3.111 p_{H_2} + 0.1615 \tag{G.4}$$

where $\dot{m}_{H_2}$ is the mass flow rate in gs^{-1} and p_{H_2} is the fill pressure in MPa. The correlation coefficient for this fit was over 99.9%. The chemical equation for stoichiometric combustion of gaseous hydrogen in air is:

$$\mathrm{H_2} + \frac{1}{2}\left[\mathrm{O_2} + 3.76\mathrm{N_2}\right] \rightarrow \mathrm{H_2O} + \frac{3.76}{2}\mathrm{N_2} \tag{G.5}$$

The fuel-air ratio (F/A) is defined as the mass of fuel divided by the mass of air in the reactants. The mass-based stoichiometric fuel-air ratio for hydrogen in air $\left(F/A_{\text{stoic}}\right)$ is 0.0291. The molar concentration of water vapour in the exhaust for stoichiometric combustion was 0.347. The equivalence ratio (ϕ) is defined as:

$$\phi = \frac{F/A}{F/A_{\text{stoic}}} \tag{G.6}$$

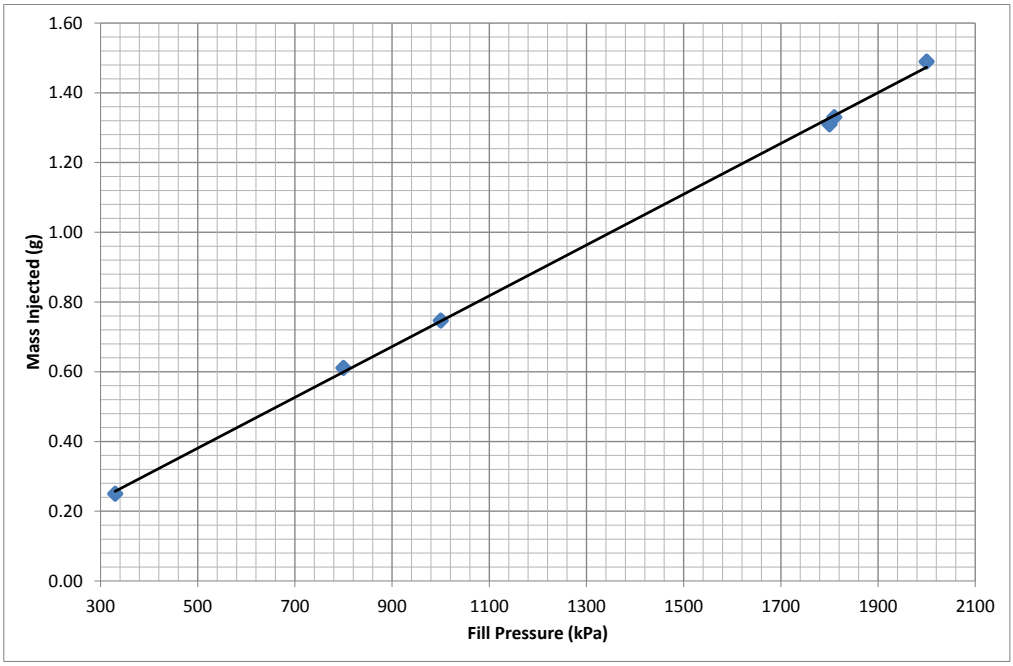

Figure G.4.: Fuel system calibration using gaseous hydrogen

Lean burning occurs when excess air is present and $\phi < 1$. In this case:

$$\phi \mathrm{H_2} + \frac{1}{2}\left[\mathrm{O_2} + 3.76\mathrm{N_2}\right] \rightarrow \phi \mathrm{H_2O} + 0.5\left(1-\phi\right)\mathrm{O_2} + 1.88\mathrm{N_2} \tag{G.7}$$

and the molar concentration of water vapour in the exhaust is:

$$\chi_{H_2O} = \frac{2\phi}{4.76+\phi} \tag{G.8}$$

Rich burning occurs when excess fuel is present and $\phi > 1$. The chemical equation for this reaction is:

$$\phi \mathrm{H_2} + \frac{1}{2}\left[\mathrm{O_2} + 3.76\mathrm{N_2}\right] \rightarrow \mathrm{H_2O} + \left(\phi-1\right)\mathrm{H_2} + 1.88\mathrm{N_2} \tag{G.9}$$

and the molar concentration of water vapour in the exhaust is:

$$\chi_{H_2O} = \frac{1}{1.88+\phi} \tag{G.10}$$

The partial pressure of water vapour in the exhaust Pp_{H_2O} is related to the static pressure P by:

$$Pp_{H_2O} = \chi_{H_2O} P \tag{G.11}$$